IntechOpen

Structural Health Monitoring from Sensing to Processing

Edited by Magd Abdel Wahab, Yun Lai Zhou and Nuno Manuel Mendes Maia

STRUCTURAL HEALTH MONITORING FROM SENSING TO PROCESSING

Edited by **Magd Abdel Wahab, Yun Lai Zhou** and **Nuno Manuel Mendes Maia**

Structural Health Monitoring from Sensing to Processing
http://dx.doi.org/10.5772/intechopen.73069
Edited by Magd Abdel Wahab, Yun Lai Zhou and Nuno Manuel Mendes Maia

Contributors

Fei Du, Chao Xu, Huaiyu Ren, Changhai Yan, Daniela Enciu, Ioan Ursu, Mihai Tudose, Zenghua Liu, Honglei Chen, Inka Mueller, Claus-Peter Fritzen, Francesc Pozo, Yolanda Vidal, Tomasz Galka, Md Tawhidul Islam Khan

Notice

First published in London, United Kingdom, 2018 by IntechOpen
eBook (PDF) Published by IntechOpen, 2019
IntechOpen is the global imprint of INTECHOPEN LIMITED, registered in England and Wales, registration number: 11086078, The Shard, 25th floor, 32 London Bridge Street
London, SE19SG – United Kingdom
Printed in Croatia

British Library Cataloguing-in-Publication Data
A catalogue record for this book is available from the British Library

Additional hard and PDF copies can be obtained from orders@intechopen.com

Structural Health Monitoring from Sensing to Processing
Edited by Magd Abdel Wahab, Yun Lai Zhou and Nuno Manuel Mendes Maia

p. cm.

Print ISBN 978-1-78923-787-0

Online ISBN 978-1-78923-788-7

eBook (PDF) ISBN 978-1-83881-713-8

Meet the editors

Professor Magd Abdel Wahab is a full-time professor of applied mechanics in the Faculty of Engineering and Architecture at Ghent University, Belgium, and an adjunct professor of computational mechanics at Ton Duc Thang University, Vietnam. He received his B.Sc., 1988, in Civil Engineering and his M.Sc., 1991, in Structural Mechanics, both from Cairo University. Professor Wahab completed his Ph.D. in Fracture Mechanics in 1995 at KU Leuven, Belgium. He was awarded the degree of Doctor of Science from the University of Surrey in 2008. He has published more than 350 scientific papers in solid mechanics and dynamics of structures, and edited more than 12 books and proceedings. His research interests include fracture mechanics, damage mechanics, fatigue of materials, durability, structural health monitoring, and dynamics and vibration of structures.

Dr. Yun Lai Zhou is a research fellow in the Department of Civil and Environmental Engineering at the National University of Singapore, Singapore. He received his B.Sc., 2010, in Mechanical Engineering from Northwestern Polytechnical University, China, and completed his M.Sc. in 2011 and PhD in 2015, both in Civil Engineering, from the Technical University of Madrid (UPM), Spain. He was awarded the honor of International Ph.D. from UPM in 2015. He has published more than 40 scientific papers, conference proceedings, and technical reports in structural health monitoring, transmissibility-based damage identification, machine learning, and structural dynamics. His current research interests include structural health monitoring, sensing techniques, data processing, fracture mechanics, damage mechanics, coupling, and structural vibrations.

Professor Nuno Manuel Mendes Maia had his habilitation in Mechanical Engineering in 2001 from Instituto Superior Tecnico (IST), University of Lisbon. Professor Maia has authored and co-authored two textbooks and about 200 scientific publications in international journals and conference proceedings on the subject of modal analysis and structural dynamics. He obtained his first degree in 1978 and his master's degree in 1985, both in Mechanical Engineering, from Instituto Superior Tecnico IST, University of Lisbon. He received his Ph.D. in Mechanical Vibrations (1989) from Imperial College London, UK. His current research interests are modal analysis and modal testing, updating of finite element models, coupling and structural modification, damage detection in structures, modeling of damping, transmissibility in multiple degree-of-freedom systems, and force identification.

Contents

Preface

Structural health monitoring (SHM) has attracted more attention during the last few decades in many engineering fields with the main aim of avoiding structural disastrous events. This aim is achieved by using advanced sensing techniques and further data processing. SHM is a multidisciplinary technique that has undergone decades of development. It has experienced booming advancements during recent years due to the developments in sensing techniques such as wireless sensing systems, embedded sensing systems, fiber optical sensing systems, etc. The reliable operation in current sophisticated man-made structures, e.g. dams, bridges, and wind turbines in civil engineering applications, and vehicles, trains, and aircraft in mechanical and aerospace applications, drives the development of incipient reliable damage diagnosis and assessment. This book aims to illustrate the background and applications of SHM from both sensing and processing approaches. Its main objective is to summarize the advantages and disadvantages of SHM methodologies and their applications, which may provide a new perspective in understanding SHM for readers from diverse engineering fields.

This book contains eight chapters that cover SHM methodologies and applications. The chapters concerned with methodologies include topics on aspects of reliability of piezoelectric actuators and sensors, the acoustic emission technique for SHM, and selection of diagnostic symptoms for condition assessment and prognosis. The chapters concerned with applications include topics on applications and challenges of signal processing techniques for Lamb wave structural integrity, the use of piezoelectric wafer active sensor technology in SHM for space applications, application of SHM to wind turbine structures using univariate and multivariate hypothesis testing, and application of SHM to bolted joints using guided waves.

The editors would like to express their thanks to the authors of the chapters presented in this book for their invaluable contributions.

Professor Magd Abdel Wahab
Ghent University
Ghent, Belgium

Dr. Yun Lai Zhou
Department of Civil and Environmental Engineering
National University of Singapore, Singapore

Prof. Nuno Manuel Mendes Maia
University of Lisbon
Lisbon, Portugal

Chapter 1

Failure Assessment of Piezoelectric Actuators and Sensors for Increased Reliability of SHM Systems

Inka Mueller and Claus-Peter Fritzen

Additional information is available at the end of the chapter

http://dx.doi.org/10.5772/intechopen.77298

Abstract

In the chain from sensing to information extraction, there are many traps where errors can occur, which might lead to false alarms and therefore leave us with the impression of an unreliable system. In this chapter, we deal with the important first element of the chain, the sensor, which can undergo various faults and defects during its lifetime. Especially for the use of acousto-ultrasonic (AU)-based methods or the electro-mechanical impedance (EMI) method, piezoelectric transducers are frequently used. Subsequent steps within the chain of SHM rely on the quality and reliability of these measurements. An overview is given on the usage of piezoelectric transducers within SHM systems, their electro-mechanical coupling and its modeling as well as frequent faults of these devices and methods on how to inspect them and diagnose defects. The authors show the effects of different transducer faults on the excited wave field, used for AU. It is shown how a sensor fault can be detected before the SHM system indicates a (false) alarm. With the help of application scenarios—including temperature variations—the advantages and disadvantages of the introduced methods of transducer inspection are presented, enabling an increased reliability of SHM systems.

Keywords: piezoelectric transducers, piezoelectric wafer active sensors, faults, defects, electro-mechanical impedance, acousto-ultrasonics, guided waves, lamb waves, structural health monitoring, system reliability

1. Introduction

Aspects of reliability play a major role for the development of structural health monitoring (SHM) systems in working industrial applications. This reliability has to be ensured for all

steps of the SHM process, which are, according to Farrar and Worden, (1) operational evaluation, (2) data acquisition, (3) feature selection and (4) statistical modeling for feature discrimination [1]. Within this chapter, the second step "data acquisition" is focused. It is closely linked to the third step, which aims at extracting the damage relevant information from the measured data via data analysis. Within the toolbox of methods used for SHM, the two groups vibration-based methods and wave-based methods have emerged. Vibration-based methods are based on the fact that modal parameters like eigenfrequencies, mode shapes and modal damping are functions of physical properties like the distribution of stiffness or of mass. In case of damage, physical properties are changed, leading to a change of the modal parameters, which are monitored by vibration-based SHM systems. Moreover, we can go to the higher frequency range and evaluate the time data directly. For their monitoring, excitation is necessary, which is often achieved by using ambient excitation, e.g., cars crossing a bridge to be monitored. Wave-based SHM methods either use the fact that a damage, e.g., cracks or breaking fibers within a composite component, will result in an emitted acoustic signal or use the fact that a wave will interfere with a possible damage. For the first, the acoustic signal will travel through the component and be detected by members within a net of listening sensors. Data evaluation will identify these single events and might locate the crack's position via triangulation. While this method is a passive method, the wave-based acousto-ultrasonics method is characterized as an active method. A well-defined excitation is used, creating a wave, which travels through the structure, interferes with specific geometric features of the structure, like edges, thickness, changes but also damages and is sensed after these interferences, e.g., at a different point of the structure. When traveling through thin-walled plates or rods, waves often appear as guided waves. They are reflected, can convert into different modes or the transmitted part is changed by discontinuities, like damages. Therefore, a change of the evaluated signal is interpreted as an indicator for damage.

For all SHM systems, it has been shown that the influence of environmental and operational conditions cannot be neglected. If we ignore a change of temperature, it might be interpreted as damage or a temperature change might decrease or even reverse the effect of damage. Depending on the SHM method, different approaches to tackle especially temperature changes have been proposed. For methods using acousto-ultrasonics, in [2] an overview of different methods for the compensation of temperature changes is given and the use of the local temporal coherence to cope with the changes of temperature and effects of surface wetting is detailed. Similar to this approach, for methods based on the signature of the electro-mechanical impedance (EMI) spectrum, in [3], a correlation coefficient-based method is used, which compensates frequency and magnitude shifts, caused by temperature changes, while changes of the shape, caused by damages within the structure, are identified. This method is applicable if the effects of damage can be clearly separated from effects of temperature variation. This is not the case for all applications. Therefore, in [4, 5], a physics-based compensation of the influences of temperature changes is used for EMI and acousto-ultrasonics (AU)-based methods. The effort for this method is large, as the temperature dependence of all significant parameters has to be included within the model. Other efforts to compensate for varying environmental and operational conditions for signal-based techniques within wave- and

vibration-based SHM systems use statistical damage classification [6, 7] including, e.g., fuzzy classification [8], the use of neural networks [9] and self-organizing maps [10].

For vibration-based SHM systems, the used sensors are often based on well-approved measurement sensors, which have been used in the past for different purposes, measuring strain, acceleration or displacement. The special requirements of SHM systems regarding the continuous monitoring on-site over long periods are achievable and the measurement systems might include a self-check and transducer electronic data sheets (TEDS) to increase the reliability, e.g., ICP compatible accelerometers. Wave-based methods often use a distributed sensor network and the included sensors are just starting to enter more into commercial products, e.g., PICeramic P-876.SP1 and Acellent SMART Layer [11, 12]. This chapter focuses on the wave-based methods, which use piezoelectric transducers for data acquisition, including actuation and sensing purposes.

Using guided waves, an SHM system identifies damages via comparing signals from different states. While the current state which should be evaluated is always based on measurements, the reference state, often taken from the pristine structure, can either be based on measurement data or set up by physics-based models. Occasionally, the comparison is also based on assumptions like the linear material behavior of the system in pristine state. The different methods of feature selection and feature discrimination are not within the focus of this chapter, as there are a multitude of possibilities. Nevertheless, the consideration of reliability on these steps is highly important and is a major research area to enable certification processes, necessary for the use of SHM systems in industrial applications.

Focusing the inspection of sensors and its self-test, different approaches can be found. Simple systems check, if the sensor signal is different from zero. More advanced data-driven methods are based on hardware redundancy [13]. Typical faults are bias, complete failure, drifting and precision degradation, see [14], as well as gain, noise and constant with noise [13]. For networks of wireless sensor nodes, these methods are used to find faulty nodes to be able to either replace those nodes or simply remove them from the network, which is only possible with sufficient redundancy, see e.g., [15]. The use of hardware redundancy, which tests if the sensor signal fits the assumed signal, when only using all other sensors, has been used for SHM systems, too. In [16], a modal filtering approach is used, and [17] uses a PCA-model to represent the signal in a lower-dimensional space and compare it with the original signal. The effect of temperature change and structural damage is considered in [18] using the mutual information concept. All these methods use the measurement data for a mathematical procedure not based on physical quantities. While it is an advantage that no additional measurements are needed, this also leads to difficulties in distinguishing between structural damage and sensor fault, especially for the case of small defects and in widespread sensor network. Depending on the type of sensor, physics-based methods of self-diagnosis using additional measurements can be found. Ref. [19] describes the use of electrical impedance spectroscopy measurement to enable self-monitoring of semiconductor gas sensor systems. In [20], methods to enable a validation of the sensor functions under operational conditions are suggested, which include the use of a magnetostrictive coated fiber. For piezoelectric wafer active sensors (PWAS), self-diagnosis capabilities exist, which are mainly based on the transducers physics.

For these transducers, the typical classification into gain, drifting, and so on does not represent the effects of faulty PWAS. The importance of reliable sensor data cannot be overestimated to achieve a reliable output of an SHM system over long monitoring periods.

Within this chapter, a short overview on the usage of piezoelectric transducers within AU-based SHM systems, their electro-mechanical structure and its modeling is given in Section 2. The effects of different transducer faults on the generated wave field, used for AU, as well as on the electro-mechanical impedance spectrum are described in Section 3. Section 4 shows a variety of methods for transducer inspection including model-based and data-based methods with different requirements on the available knowledge about the system and material parameters. Using application scenarios—also including temperature variations—the advantages and disadvantages of the introduced methods of transducer inspection, enabling an increased reliability of SHM systems, are presented in Section 5.

2. Tasks of piezoelectric transducers

In many applications, piezoelectric material is used purely for actuating or sensing purposes. The use of PWAS for SHM purposes is mostly including both, the inverse and the direct piezoelectric effect. In general, the piezoelectric effect is not linear. Nevertheless, the effect can be modeled linearly in a certain strain range for most piezoelectric materials. Moreover, the temperature needs to stay well below the Curie point. The actuation (inverse piezoelectric effect) can be described by

$$D_i = d_{ikl} T_{kl} + \varepsilon_{ik}^{T} E_k \tag{1}$$

$$S_{ij} = s_{ijkl}^{E} T_{kl} + d_{kij} E_k \tag{2}$$

with stress T, strain S, elastic compliance s, dielectric constant ε, electric field E, dielectric displacement D, defined by charge Q per unit area A at given stress T, and piezoelectric constants d, linking dielectric displacement with stress as well as strain with electric field.

Although these equations already fully describe the direct and inverse piezoelectric effect, for sensing purposes (direct piezoelectric effect) the most familiar description uses g as piezoelectric voltage coefficient to connect stress with electric field.

$$E_i = -g_{ikl} T_{kl} + \beta_{ik}^{T} D_k \tag{3}$$

$$S_{ij} = s_{ijkl}^{D} T_{kl} + g_{kij} D_k \tag{4}$$

These equations can be simplified especially in their dimension, when using Voigt notation and assuming multiple symmetry in the piezoelectric materials as well as in the strain and stress tensors.

$$\begin{bmatrix} D_1 \\ D_2 \\ D_3 \end{bmatrix} = \begin{bmatrix} 0 & 0 & 0 & 0 & d_{15} & 0 \\ 0 & 0 & 0 & d_{15} & 0 & 0 \\ d_{31} & d_{31} & d_{33} & 0 & 0 & 0 \end{bmatrix} \begin{bmatrix} T_{11} \\ T_{22} \\ T_{33} \\ T_{23} \\ T_{13} \\ T_{12} \end{bmatrix} + \begin{bmatrix} \varepsilon_{11}^T & 0 & 0 \\ 0 & \varepsilon_{11}^T & 0 \\ 0 & 0 & \varepsilon_{33}^T \end{bmatrix} \begin{bmatrix} E_1 \\ E_2 \\ E_3 \end{bmatrix} \tag{5}$$

$$\begin{bmatrix} S_{11} \\ S_{22} \\ S_{33} \\ 2S_{23} \\ 2S_{13} \\ 2S_{12} \end{bmatrix} = \begin{bmatrix} S_{11}^E & S_{12}^E & S_{13}^E & 0 & 0 & 0 \\ S_{12}^E & S_{11}^E & S_{13}^E & 0 & 0 & 0 \\ S_{13}^E & S_{13}^E & S_{33}^E & 0 & 0 & 0 \\ 0 & 0 & 0 & S_{55}^E & 0 & 0 \\ 0 & 0 & 0 & 0 & S_{55}^E & 0 \\ 0 & 0 & 0 & 0 & 0 & 2\left(S_{11}^E - S_{12}^E\right) \end{bmatrix} \begin{bmatrix} T_{11} \\ T_{22} \\ T_{33} \\ T_{23} \\ T_{13} \\ T_{12} \end{bmatrix} + \begin{bmatrix} 0 & 0 & d_{31} \\ 0 & 0 & d_{31} \\ 0 & 0 & d_{33} \\ 0 & d_{15} & 0 \\ d_{15} & 0 & 0 \\ 0 & 0 & 0 \end{bmatrix} \begin{bmatrix} E_1 \\ E_2 \\ E_3 \end{bmatrix} \tag{6}$$

A huge variety of piezoelectric materials exist—well known are barium titanate ($BaTiO_3$) and lead zirconate titanate ($Pb(Zr, Ti)O_3$), known as PZT, as well as more flexible materials like polyvinylidene fluoride (PVDF). Most common are PWAS, made of PZT. They are separated into hard and soft PZTs by their coercive field. Hard PZTs exhibit a large linear drive region, showing small strain magnitudes and a relatively high Curie point ($T_C \approx 250^\circ$C); soft PZTs exhibit larger induced strain, while having a smaller linear region. Most soft PZTs have a Curie point above 150°C, but below those of hard PZTs. Examples of soft PZTs are PIC255, PSI 5A4E —Navy Type II, PIC151, PIC155, PZT5A-3195STD and PSI-5H4E Navy Type VI; examples for hard PZTs are PIC 181 and PIC 300, depending on the manufacturers naming (e.g., PICeramic, Piezo systems Inc.). In [21], a threshold of E_c =1 kV/mm to divide those two groups is mentioned.

For AU-based SHM systems, the use of PZT discs has proven to be useful. Different types of transducers exist. The simple form is a piezoceramic disc with a wrap-around electrode, which enables the soldering of both contacts on the top surface of the transducer, see **Figure 1a**. Alternatively, one might use PZT discs, which are already capsulated in embedding material. Depending on the application, the connecting cables are also embedded as conducting paths within a layer of embedding material. Examples are Acellent SMART layer© and DuraAct

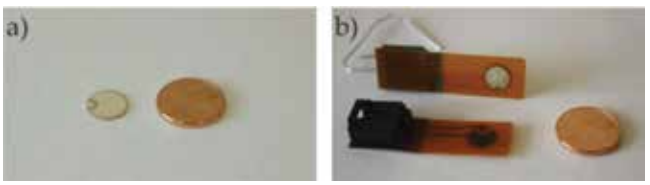

Figure 1. Types of transducers, (a) single transducer with wrap-around electrode from PICeramic, (b) embedded transducer, Acellent SMART layer©.

from PICeramic (see **Figure 1b**). Within this chapter, the first type is named single transducer/PWAS, while the second type is called embedded transducer/PWAS.

The generated wave field depends on the excitation frequency and the orientation of the transducer itself. In [22] it is shown that the orientation of the wrap-around electrode has significant influence on the generated wave field.

The use of PWAS for AU purposes has been described in a multitude of publications. An excellent overview is given in [21]. Herein, the interested reader will also find an extensive description of the governing equations for AU and EMI. In this chapter, only main results are cited.

For free disc-shaped transducers, the model is based on axial symmetry, leading to uniform radial and circumferential expansion. Using Eqs. (1) and (2) in cylindrical coordinates, the derivation of the induced strain and displacement—used for AU—as well as the electrical displacement, finally leading to the EMI spectrum, can be derived. As soon as the PWAS is attached to the structure, stress-free boundary conditions have to be replaced by a force equilibrium at the PWAS edges. Moreover, a shear layer coupling between PWAS and structure, achieved by the adhesive layer, needs to be considered. Based on [21, 23], in [4], a model was developed, which includes these effects and focuses on the PWAS signature, including resonances and antiresonances of the EMI spectrum $Z(\omega)$.

$$Z(\omega) = \left(i\omega C \left(1 - k_p^2 \left(1 - \frac{(1+\nu_a) J_1(\varphi_a)}{\varphi_a J_0(\varphi_a) - (1-\nu_a) J_1(\varphi_a) + \chi(\omega)(1+\nu_a) J_1(\varphi_a)} \right) \right) \right)^{-1} \tag{7}$$

It includes the Bessel functions of the first kind J, Poisson's ratio of the PWAS's material ν_a, the capacitance C, the coupling factor k_p, the frequency dependent stiffness quotient $\chi(\omega)$ and the abbreviation φ_a which can be derived by

$$C = \varepsilon_{33} \frac{\pi r_{pwas}^2}{h_{pwas}} \tag{8}$$

$$k_p^2 = \frac{2 d_{31}^2}{\varepsilon_{33} s_{11}^E (1-\nu_a)} \tag{9}$$

$$\varphi_a = \frac{\omega}{c} r_{pwas} \tag{10}$$

$$\chi(\omega) = \frac{k_{str\&adh}}{k_{pwas}} \tag{11}$$

When including the frequency dependent stiffness of the adhesive layer and a simple model for the stiffness of PWAS and structure, this can be included into $\chi(\omega)$.

$$k_{pwas} = \frac{h_{pwas}}{r_{pwas} s_{11}^E (1-\nu_a)} \tag{12}$$

$$\mathrm{k_{str\&adh}} = \frac{1}{\frac{1}{k_{str}} + \frac{1}{k_{adh}}} \tag{13}$$

$$k_{str} = \frac{2h_{str}E_{str}}{r_{pwas}(1-\nu_{str}^2)} \tag{14}$$

$$k_{adh} = \frac{G_{adh}}{2}\frac{\left(\frac{\omega}{c\sqrt{\alpha}}\right)^2}{\sinh^2\left(\frac{\omega h_{adh}}{c\sqrt{\alpha}}\right)}\left(\frac{\sinh\left(\frac{\omega h_{adh}}{c\sqrt{\alpha}}\right)}{2\frac{\omega}{c\sqrt{\alpha}}}+h_{adh}\right)\cdot\frac{1}{2}\frac{\frac{\omega}{c}r_{pwas}J_0^2\left(\frac{\omega}{c}r_{pwas}\right)^2-2J_0\left(\frac{\omega}{c}r_{pwas}\right)J_1\left(\frac{\omega}{c}r_{pwas}\right)+J_1^2\left(\frac{\omega}{c}r_{pwas}\right)}{\frac{\omega}{c}J_1^2\left(\frac{\omega}{c}r_{pwas}\right)} \tag{15}$$

This includes the geometry parameters $r_{PWAS}, h_{PWAS}, h_{str}, h_{adh}$, the material parameters elastic modulus E_{str}, Poisson's ratio ν_{str} and the wave speed for axially symmetric radial motion in the PWAS c.

It must also be kept in mind that many of the parameters used have complex values as damping has to be taken into account, e.g., $s_{11}^E = \hat{s}_{11}^E(1-i\eta)$.

The frequency dependency of the characteristic structural stiffness was neglected. This model is therefore useful for analyzing the PWAS itself and its bonding condition, while it cannot be used for the modeling of changes respecting damages within the structure.

From Eq. (7), the susceptance B as the imaginary part of the admittance which is the inversion of the impedance can be calculated.

$$Y(\omega) = \frac{1}{Z(\omega)} \tag{16}$$

$$\mathrm{B}(\omega) = \mathrm{Im}\{\mathrm{Y}(\omega)\} \tag{17}$$

If neglecting the factor multiplied with k_p^2, the simple model of a PWAS as a capacitor gets visible. The capacitance C describes the slope, when plotting B over ω. This line is interrupted by the effects of the PWAS eigenfrequencies and its coupling with the structure. As the model does not include the frequency dependency of the structures stiffness, the peaks of eigenfrequencies of the stiffness are not visible. Other models include this frequency dependency of the structures stiffness, see [21]. Due to the necessary simplicity of these models, the applicability for SHM based on the EMI spectrum is limited, but they lead to a better understanding of its characteristic features.

3. Classification of transducer faults

Different types of PWAS faults result from different causes. Due to the continuous or periodical monitoring with permanently installed sensors, PWAS used for SHM need to be tested against degradation issues. Nevertheless, early faults within the PWAS service life have to be taken into account. Production deficiencies can lead to an insufficient bonding quality between structure and PWAS before the PWAS can be used for the first time. Depending on the type of fault, the effects on the generated wave field as well as on the EMI spectrum differ.

3.1. Cracks

When describing the fault type crack within this chapter, this refers to macro-size cracks. Different causes can lead to these cracks. During production or later use, falling objects, which hit the transducer itself, cause cracks and spalling. Two examples of single transducers impacted twice by falling mass (m = 53.5 g, h = 350 mm for (a), 450 mm for (b)) are shown in **Figure 2**.

Due to the nonsymmetric characteristic of the fault, the effects on the wave field are also nonsymmetric. **Figure 3** shows the signal, recorded by two neighboring transducers (PWAS 1 and PWAS 3), generated by a cracked PWAS (PWAS 2). The two signals differ significantly, showing the nonsymmetric characteristic of the fault. Single transducers as well as embedded transducers show decreased output when being cracked. The effect of spalling is not present for embedded transducers, as the embedding material holds the separated parts together. If a PWAS inspection system does not indicate these faults, the SHM system is based on corrupted signals and will most likely give alarm, although not the structure but the PWAS is damaged.

The effects of this type of fault on the EMI spectrum differ significantly depending on the type of transducer, see **Figure 4**. Due to the changed stiffness of the cracked PWAS, the resonance frequency changes. These changes are larger for the single transducers, while the effect is

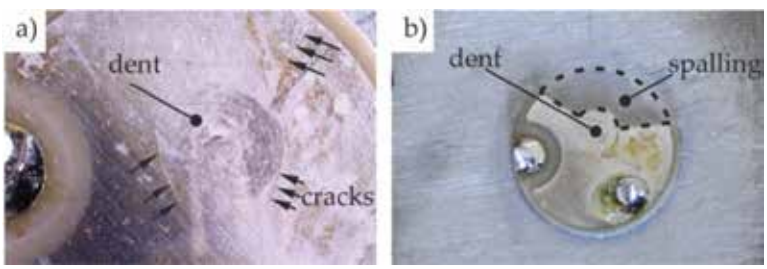

Figure 2. Micrographs of transducer fault type, (a) crack (b) crack and spalling.

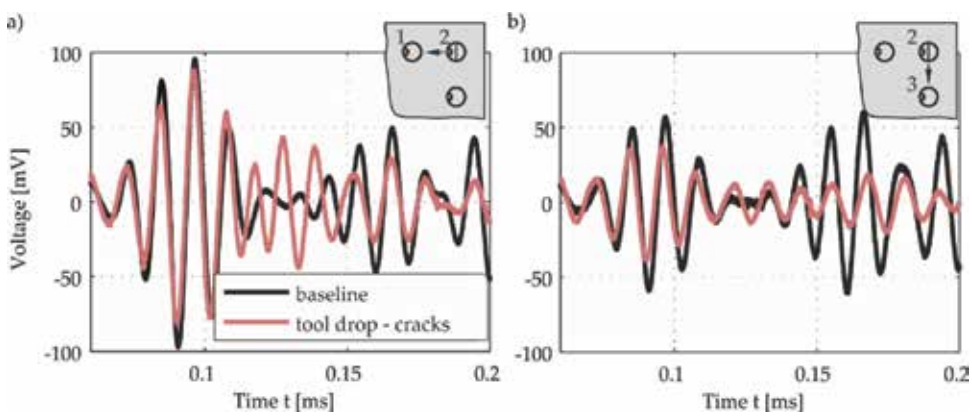

Figure 3. Change of wave propagation depending on the orientation of damage, (a) PWAS2-PWAS1, (b) PWAS2-PWAS3.

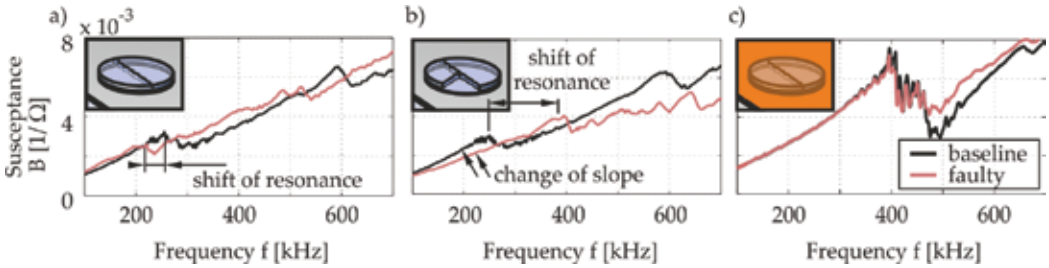

Figure 4. Change of EMI spectra depending on PWAS type and type of fault, (a) single transducer with crack, (b) single transducer with crack and spalling, (c) embedded transducer with crack.

decreased for the embedded transducers, where the embedding material leads to remaining stiffness between the cracked parts. A drop of capacitance, which will lead to a decreased susceptance slope is visible for the case of spalling. As the capacitance is proportional to the area, the reason for this drop is the missing piece of transducer, which is only the case for single transducers.

3.2. Degradation

Degradation of the piezoelectric transducer and its bonding to the structure is a major transducer fault especially for long-term monitoring, favored in structural health monitoring. It can be caused, e.g., by elevated temperatures. Depending on the selected adhesive (e.g., Hysol EA9394 by Henkel, Z70 by HBM) and the chosen PWAS material (e.g., PIC 255, PIC 151), either the adhesive or the piezoelectric material is prone to degrade. It has been shown in [24] that the pure exposure to outdoor conditions can also lead to minor degradation, which is visible in the generated wave field by a slightly decreased signal. Its level decreases uniformly. In **Figure 5**, the degradation, caused by elevated temperature, is shown.

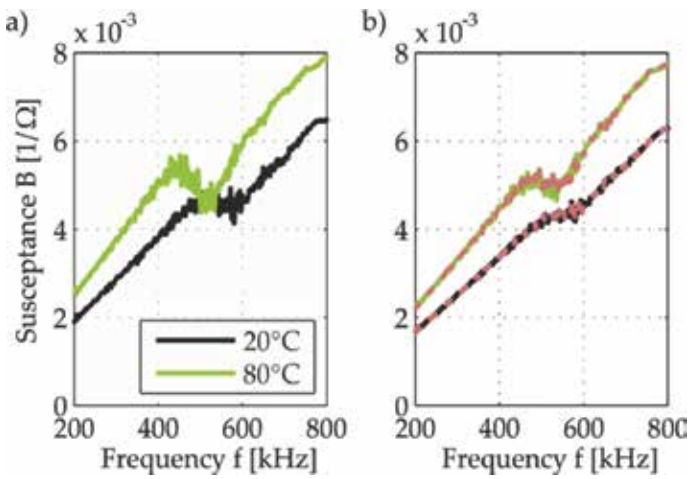

Figure 5. EMI spectra for 20 and 80°C, (a) baseline and (b) degraded state.

It led to a slight decrease of the susceptance slope, which is not caused by a change of the surface area but the degrading of the PWAS material and a change of its adhesive stiffness, see Eq. (15). If the temperature is unknown, degradation might be interpreted as temperature change.

3.3. Debonding

Debonding is a fault type, located at the adhesive zone between PWAS and structure. While a contaminated surface of the structure during the bonding process will lead to deficiencies of the bonding quality and debonding effects right from the beginning, fatigue of the bonding layer, e.g., under bending moments, might also lead to a debonding of the PWAS from the structure. The latter has a defined orientation of the fault, while a contamination might be local or evenly distributed over the bonding area. **Figure 6** shows the maxima of the out-of-plane component of the velocity field of a perfectly bonded transducer compared to the fields, generated by two PWAS, which were bonded on an aluminum plate, being contaminated with wax before bonding.

The out-of-plane velocity has been measured on the structure, from the back-site of the plate using a Laser Doppler Vibrometer CLV1000 with CLV700 head. The generated wave field of the debonded transducers is far from being symmetric and the generated amplitudes are smaller, compared to the perfectly attached transducer.

The debonding due to bending has been modeled by partial bonding of a PWAS to an aluminum plate. **Figure 7** shows the out-of-plane velocity, measured at the surface of the PWAS itself and from the back-site. A vibration of the debonded section is visible in **Figure 7a**. This energy is stored and transferred to the structure with a delay. The amplitude on the back is decreased in the debonded area.

The partial debonding also changes the frequency characteristic of a bonded PWAS. It has been shown that with some frequencies used as input frequency, the amplitudes, measured at a distance of 20 mm to the PWAS center, are larger for the debonded case; see **Figure 8**.

The debonding also leads to a changed EMI spectrum, the effects depend on the severity of debonding. **Figure 9** shows the effect of a 20% debonded surface, with four different orientations of the debonded area, relative to the wrap-around electrode.

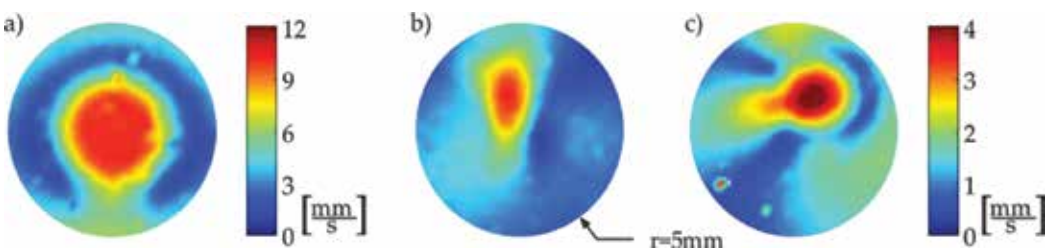

Figure 6. Maximum values of the out-of-plane velocity time signal, generated by the PWAS and transferred to the structure, measured by a laser vibrometer at the back of the structure, (a) perfectly attached PWAS, (b), (c) two PWAS attached on a plate with wax-contaminated surface.

http://dx.doi.org/10.5772/intechopen.77298

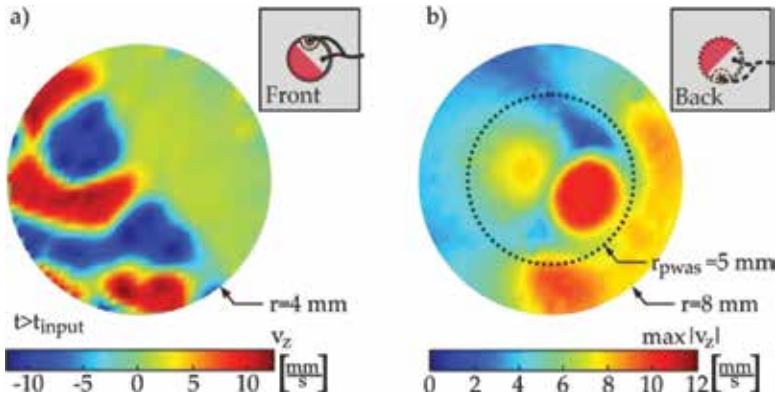

Figure 7. Out-of-plane velocity of a debonded PWAS, (a) measured at the top surface of the PWAS after the decay of the input signal, the radius of the circular measurement area is 4 mm, (b) measured at the back of the plate, the maxima of out-of-plane velocity are plotted, the dotted circle marks the PWAS location, the radius of the circular measurement area is 8 mm.

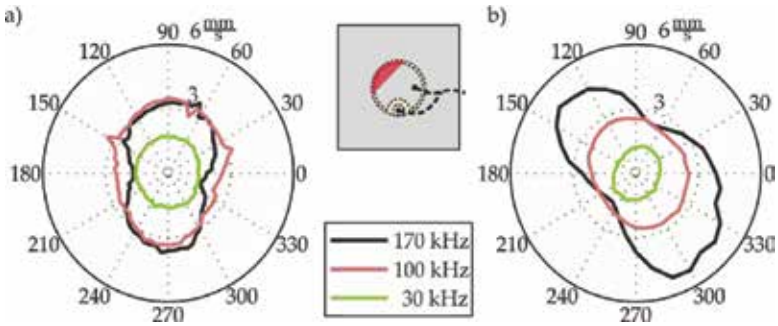

Figure 8. Maximum out-of-plane velocity at different angles for 30 kHz, 100 kHz and 170 kHz, measured at 20 mm distance, (a) for the fully bonded PWAS, (b) for the partially debonded PWAS.

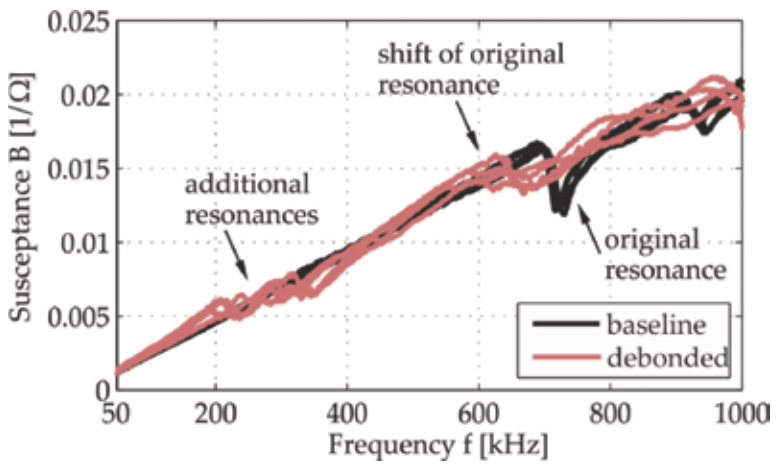

Figure 9. Effects of 20% debonded area on the susceptance spectrum. Four completely bonded PWAS are compared with four partially debonded PWAS. The orientation of the bonding relative to the wrap-around electrode has been changed.

4. Methods of transducer inspection

To achieve an increased reliability of SHM systems, a check of the systems' piezoelectric transducers and a good knowledge about the component itself is necessary. Refs. [24–28] pay attention to durability and long-term integrity as well as investigations on typical damage patterns. These investigations include stereomicroscopy [26], monitoring a possible change of the slope of electric charge over strain [26–28] and near-field scanning interferometry [24]. These methods are useful under laboratory conditions but cannot be transferred to the inspection of transducers during their employment and operation.

In [29], a method of transducer inspection based on a time reversal index, a symmetry index and a Lamb wave energy ratio index is suggested. Herein, the capacitance is used as a first indicator to finally separate structural damage, changes of environmental conditions and PWAS faults. The systems are partially based on analytical and hardware redundancy.

Using a second, independent measurement quantity, the EMI spectrum was discussed as a side issue in [30, 31] and later is focused in [32, 33]. They concentrate on the susceptance slope, which is increased by debonding and decreased if the PWAS breaks. As it can be seen in **Figure 4**, this is possible for some fault types and severe damages but does not detect, e.g., minor cracks and central debonding [34]. Further work in this regard can be found in [29, 35–39]. Using more information like the resonance behavior included in the EMI-spectrum enables the detection of minor PWAS faults and is especially valuable for the inspection of embedded transducers [40–42]. This is possible with the use of a physical model [4] or by utilizing purely data-driven approaches [43]. A simplified measurement of the EMI spectrum suggested in [44] and implemented, e.g., in [45] enables a quick measurement of the EMI spectrum with the same equipment as used for AU-based SHM systems. Based on the results of a PWAS inspection system, in [46, 47], signal correction factors are suggested to enable the exploitation of the signals in case of minor damage.

Within this section, the most used and elevated methods of transducer inspection based on the EMI spectrum, resp. the susceptance spectrum, are described. They are categorized into data-based and model-based methods. If a method allows to waive the explicit use of the temperature information for temperature compensation, this will be highlighted.

4.1. Model-based methods

For the inspection of PWAS with model-based methods, the analytical model, introduced in Section 2 can be used. The idea is to adapt the model to the experimental data via fitting of the parameters. The fitted parameter vector is used to separate the healthy state. Using principal component analysis (PCA), they can be aggregated to a damage index DI_{model}. For details, the reader is referred to [4, 42].

An advantage of this method is the nonnecessity to include temperature information for the test in application, also if the influence of environmental conditions should be compensated. Nevertheless, during training, temperature information is necessary.

As already shown in Eqs. (7-17), the model itself includes a bunch of parameters. Although most of them cannot be changed due to damage (e.g., nominal radius of the PWAS), these parameters will have some variations resulting from different batches, different bonding procedures, and so on. Therefore, the model needs to be adapted to the experimental baseline first. With this updated model, the model-based transducer inspection procedure can start.

The major disadvantage of this procedure is the high correlation of the different parameters on the influence on the susceptance spectrum. The adaptation of the parameters is based on optimization procedures, which do not necessarily result in physically meaningful parameters. Moreover, the user needs to know a multitude of parameters about the applied PWAS before being able to use this method.

4.2. Data-based methods

The avail of the EMI spectrum started from using the susceptance slope coefficient SC as the damage indicator [33, 37, 39]. As the capacitance is a linear factor for the susceptance, it can be seen as an advanced alternative to solely measure the PWAS capacitance. It is measured in a frequency range up to a small share of the eigenfrequency, which interrupts the constant slope. Although it has been shown that not all faults can be detected with this method, it is a simple method, which can be applied easily, and which detects severe damages like fracture of the PWAS.

The employment of more information from the susceptance spectrum than only using the slope is also possible with data-based methods. In [48], 12 parameters, which can be extracted from the susceptance spectrum, have been listed. After extraction from the spectrum, they are used for PCA. The first principal component (PC) can be taken as damage indicator for degradation and breakage. While data-based models in general are less numerically expensive than model-based methods, one difficulty of this method is to extract the parameters, depending on the data quality.

The inclusion of more information of the spectrum is also possible by using the correlation coefficient and subtracting its absolute value from 1 to achieve a damage index. This way, no additional extraction of features is necessary.

$$DI_{CC} = 1 - |CC| \text{ with } CC = \frac{V_{12}}{\sqrt{V_{11}V_{22}}}, \tag{18}$$

V_{kl} being the entries within the covariance matrix V. The correlation coefficient CC is 1 for two susceptance spectra, which only differ by a proportional change This way, the slope is an insensitive parameter for this method. Nevertheless, PWAS faults change the characteristic shape of the spectrum at resonance also for small faults. This is focused, when using the damage index based on the correlation coefficient DI_{CC}.

4.3. Transducer inspection in the context of the whole SHM system reliability

The quality of the inspection methods has to be assured not only by checking if specific damaged can be found; Moreover, the combination of SHM system and transducer inspection

needs to be checked. This is especially the case as most operators of SHM systems are not able to define specific types of transducer defects and its sizes to assess the quality of performance of a transducer inspection method. It therefore has to be ensured that the transducer inspection will find a faulty PWAS, before the signal deterioration will lead to a changed output of the SHM system. The authors emphasize that it is necessary to consider the algorithm of the SHM system as well as the PWAS inspection method to assess its performance. This way it is also possible to reconsider if data of a degraded transducer might still be used or has to be neglected.

A possible approach for this is described in [49, 42] and suggests using statistical methods, based on the probability of detection (POD) approach: it enables increased knowledge of the combination of transducer inspection and SHM system, including the value, which the structural damage detection indicator reaches, before a defective transducer can be detected with a probability of 90% at a confidence level of 95% (SDI_90|95). A complete reliability analysis needs to incorporate the interaction of SHM system and transducer inspection system.

5. Application scenarios

In this section, several application scenarios, including a comparison of different methods of transducer inspection, as described in Sections 4.1 and 4.2, are presented. Moreover, the results of these methods have to be evaluated taking into account the effects of the different defects of the results of the SHM system, which is implemented, as discussed in Section 4.3.

5.1. Detection of cracks in and debonding of transducers

To detect cracks and debondings, two data-based methods are compared in the following application scenarios. The most proposed method to inspect piezoelectric transducers is the monitoring of the susceptance slope. This is compared with the correlation coefficient-based method.

Cracks in an embedded transducer, bonded in central position on a CFRP strip, have been caused by four-point-bending of the strip (see **Figure 10a**) left down. First cracks started on reaching a strain level of 0.5%.

The EMI spectrum was always measured at unloaded condition after deforming the specimen at the following strain levels: 0.15, 0.3, 0.45, 0.5, 0.6, and 0.7%. **Figure 10b** shows that the multiple cracks of the embedded transducer after 0.7% strain led to a slight decrease of the susceptance slope, while the first two fault levels exhibit similar behavior like the undamaged states. For the correlation coefficient-based method, all three stages of fault can be clearly identified and separated from the undamaged state (see **Figure 10c**). For detailed information about the experimental setup, see [43, 42].

The debonding scenario is achieved by preventing the contact between adhesive and PWAS at approximately 20% of the surface area. This area was covered with Teflon tape during the process of gluing. Four different orientations of the debonded area relative to the wrap-around electrode have been tested (**Figure 11**).

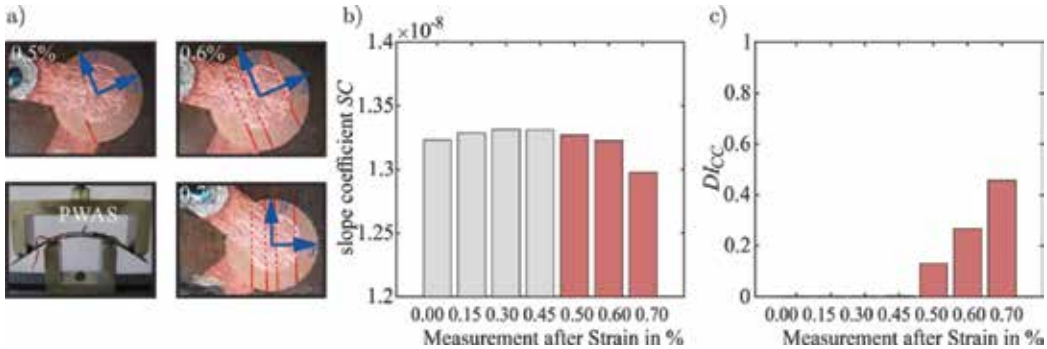

Figure 10. (a) Experimental setup with a four-point-bending test and micrographs of the three different crack states of an embedded DuraAct transducer caused by different strain levels (0.5, 0.6 and 0.7%), (b) slope coefficient *SC* of the impedance spectrum, (c) correlation coefficient-based damage index DI_{CC}, evaluated for measurements of four uncracked and three cracked states.

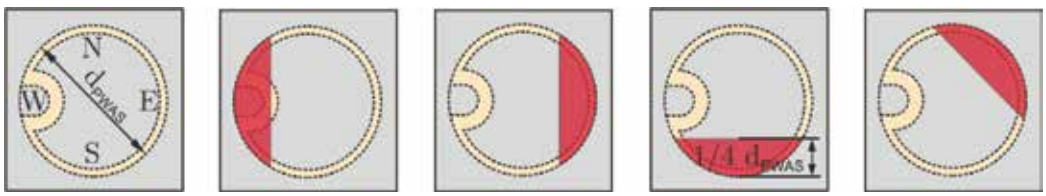

Figure 11. Debonding scenario and orientation of debonded area relative to the wrap-around electrode.

As this procedure makes it difficult to have a baseline measurement of each sensor, four fully bonded transducers are used as a baseline. For all eight transducers, the EMI spectrum has been recorded five times within an interval of 10 m. **Figure 12** shows the resulting damage indices.

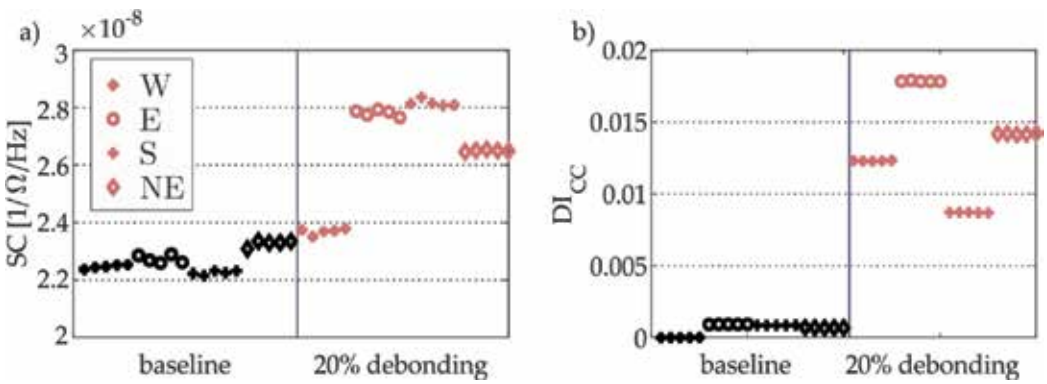

Figure 12. (a) Slope coefficient SC, (b) correlation coefficient-based damage indicator DI_{CC} for four fully bonded and four partially debonded transducers.

While the slope coefficient values are not normalized with a reference value, the reference for the correlation coefficient-based method is the first measurement of the first transducer. Using the slope coefficient, the difference between debonded and healthy state is small, especially for the debonding beneath the wrap-around electrode. For the correlation coefficient-based method, the debonding can be clearly separated from the fully bonded state. Moreover, the variation between the measurements of the same state is higher for the slope coefficient.

An analysis of the resulting wave propagation for these debonded PWAS can be found in [50]. For detailed information about the experimental setup and other debonding levels, see [42].

5.2. Inspection of transducers after system setup

The difficulty of transducer inspection after system setup is the absence of a proper reference. In many cases, this can be overcome with the help of a model-based approach. Nevertheless, in this application, a whole batch of transducers as a reference within the batch is used. Building the mean correlation coefficient for all combinations of all transducers, except a single one, and subtracting the mean correlation coefficient of all transducers with the single one from this value, this can be used as an indicator for the similarity of the single one with the whole batch. Another procedure without using a reference is described in [37], the use of correlation blocks is suggested in [14].

In this application, 16 transducers have been mounted on a plate structure. The plate has been contaminated with wax at two positions so that PWAS 12 and 16 are insufficiently bonded. Using the correlation coefficients of all combinations, the two contaminated PWAS could be clearly identified, see **Figure 13**, showing significantly higher indicator values than the rest of the sensors.

5.3. Inspection of transducers under changing temperature conditions

The influence of environmental and operational conditions is known to be nonnegligible for the automated continuous monitoring of structures in general. The effect on the inspection of piezoelectric transducers using the EMI spectrum therefore needs to be considered. In this

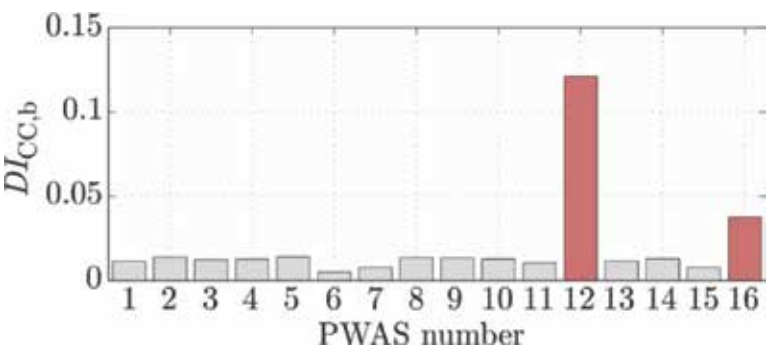

Figure 13. Damage indices, based on the comparison of correlation coefficients for all 16 PWAS after system setup. PWAS 12 and 16 are insufficiently bonded due to contamination with wax.

application scenario, a model-based and a purely data-based method are used for the detection of degradation faults within a temperature range of 20–85°C.

As defect, a degradation of the adhesive as well as of the piezoelectric material was introduced to a PWAS by heat exposure for 32 h at 130°C. Fourteen measurements, equally distributed over the whole temperature range, have been used as reference data for the data-based approach to train the model for the model-based approach. Twenty-six measurements distributed over the whole temperature range are used as test data and 42 measurements over the whole temperature range have been recorded after degradation took place.

Figure 14 shows the results for the model- and data-based methods in (b) and (c) as well as the temperature present during the specific EMI measurement in (a).

Both methods clearly distinguish between the degraded and the healthy state. The results show that the model fits best for medium temperatures, although the whole temperature range was used for training. The model-based approach allows to waive the explicit use of the

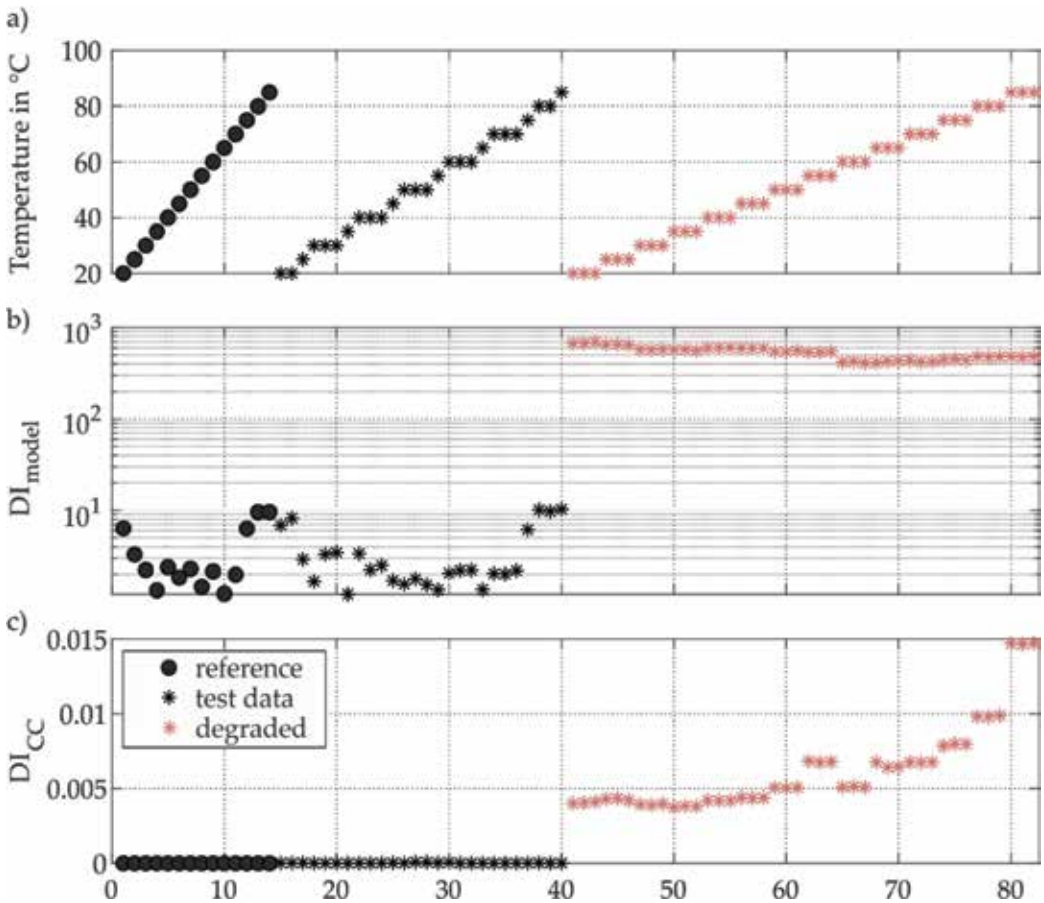

Figure 14. (a) Temperature, (b) DI_{model} and (c) DI_{CC} for several measurements of a single transducer before and after degradation of adhesive and piezoelectric material.

temperature information after the training is completed. The data-based approach employing the correlation coefficient needs the temperature information to select the correct baseline. For more information on the experimental setup and the estimated model parameters, see [4], on the data-based method, see [42].

6. Conclusion

Piezoelectric transducers are used within several SHM systems for a multitude of applications. For the system reliability, the proper functionality of the permanently installed transducers must be secured. This chapter proposes a system self-check, similar to other measurement equipment. For its realization, a detailed analysis of possible fault types and their effects on the generated wave field and the EMI spectrum is necessary. Moreover, it is tremendously important to incorporate the effects of possible PWAS faults on the SHM system to know if a faulty transducer will be identified before it will have an influence on the SHM system output and a false alarm will be produced. To enable the reader to increase the reliability of SHM systems, within this chapter several methods for transducer inspection have been presented. Their usage was demonstrated for different applications, showing disadvantages and advantages of the different methods. While model-based methods are linked to the necessity of an expert knowledge about the transducer and its bonding conditions, data-based approaches, using the correlation coefficient, need a temperature measurement to incorporate temperature changes. Especially for small cracks without spalling, using more aspects of the EMI than just the susceptance slope is advantageous.

Acknowledgements

Most of this work has been conducted during 2012–2016 within the framework of national and international cooperation, leading to the PhD thesis [42]. The authors would like to acknowledge Maria Moix-Bonet (DLR) and Martin Bach (Airbus), who have been a great help in identifying the need of research within this area and supported the research with samples and fruitful discussions especially regarding the damage types of degradation and crack. Moreover, the authors would like to acknowledge Alisa Shpak and Mikhail Golub from Kuban State University, Krasnodar, Russia, with whom they have worked on the modeling of the debonding fault and its experimental validation within the last years and enjoyed fruitful discussions.

Parts of this work are based on research activities within the EU 7th framework project SARISTU under grant agreement No. 284562 which is thankfully acknowledged.

Conflict of interest

The authors declare no conflict of interest. The founding sponsors and employers had no role in the design of the study; in the collection, analyses, or interpretation of data; in the writing of the manuscript and in the decision to publish the results.

Author details

Inka Mueller[1]* and Claus-Peter Fritzen[2]

*Address all correspondence to: inka.mueller@rub.de

1 Institute for Structural Engineering, Ruhr-Universität Bochum, Germany

2 Institute for Mechanics and Control Engineering—Mechatronics, University of Siegen, Germany

References

[1] Farrar CR, Worden K. Structural Health Monitoring: A Machine Learning Perspective. Chichester, West Sussex, United Kingdom: John Wiley & Sons Ltd; 2012

[2] Michaels JE, Michaels TE. Detection of structural damage from the local temporal coherence of diffuse ultrasonic signals. IEEE Transactions on Ultrasonics, Ferroelectrics and Frequency Control. 2005;**52**:1769-1782

[3] Baptista FG, Vieira Filho J, Inman DJ. Real-time multi-sensors measurement system with temperature effects compensation for impedance-based structural health monitoring. Structural Health Monitoring-an International Journal. 2012;**11**:173-186

[4] Buethe I, Eckstein B, Fritzen CP. Model-based detection of sensor faults under changing temperature conditions. Structural Health Monitoring. 2014;**13**:109-119

[5] Roy S, Lonkar K, Janapati V, Chang FK. A novel physics-based temperature compensation model for structural health monitoring using ultrasonic guided waves. Structural Health Monitoring. 2014;**13**:321-342

[6] Sohn H, Worden K, Farrar CR. Statistical damage classification under changing environmental and operational conditions. Journal of Intelligent Material Systems and Structures. 2002;**13**(9):561-574

[7] Figueiredo E, Park G, Farrar CR, Worden K, Figueiras J. Machine learning algorithms for damage detection under operational and environmental variability. Structural Health Monitoring-an International Journal. 2011;**10**:559-572

[8] Fritzen C-P, Kraemer P, Buethe I. Vibration-based damage detection under changing environmental and operational conditions. Advances in Science and Technology. 2013;**83**: 95-104

[9] Sepehry N, Shamshirsaz M, Abdollahi F. Temperature variation effect compensation in impedance-based structural health monitoring using neural networks. Journal of Intelligent Material Systems and Structures. 2011;**22**:1975-1982

[10] Buethe I, Kraemer P, Fritzen C-P. Applications of self-organizing maps in structural health monitoring. Key Engineering Materials. 2012;**518**:37-46

[11] PI Ceramic GmbH. https://www.piceramic.com/en/products/piezoceramic-components/

[12] Acellent Technologies Inc. http://www.acellent.com/en/products/sensors/

[13] Kullaa J. Detection, identification and quantification of sensor fault. In: Proceedings of ISMA 2010 Including USD2010; 2010

[14] Dunia R, Qin SJ, Edgar TF, McAvoy TJ. Identification of faulty sensors using principal component analysis. AICHE Journal. 1996;**42**:2797-2812

[15] Guo S, Zhong Z, He T. FIND: Faulty node detection for wireless sensor networks. In: Proceedings of the 7th ACM Conference on Embedded Networked Sensor Systems, New York, NY, USA; 2009

[16] Friswell MI, Inman DJ. Sensor validation for smart structures. Journal of Intelligent Material Systems and Structures. 1999;**10**:973-982

[17] Worden K. Sensor validation and correction using auto-associative neural networks and principal component analysis. In: IMAC-XXI: Conference and Exposition on Structural Dynamics; Orlando, USA. 2003

[18] Kraemer P, Fritzen C-P. Sensor fault identification using autoregressive models and the mutual information concept. Damage Assessment of Structures VII. 2007;**347**:387-392

[19] Reimann P, Dausend A, Schutze A. A self-monitoring and self-diagnosis strategy for semiconductor gas sensor systems. IEEE Sensors. 2008;192-195

[20] Köppe E, Bartholmai M, Daum W, Gong X, Holmann D, Basedau F, Schukar V, Westphal A, Sahre M, Beck U. New self-diagnostic fiber optical sensor technique for structural health monitoring. Materials Today: Proceedings. 2016;**3**:1009-1013

[21] Giurgiutiu V. Structural Health Monitoring: With Piezoelectric Wafer Active Sensors. Oxford (Academic Press): Elsevier Science; 2007

[22] Moll J, Golub MV, Glushkov E, Glushkova N, Fritzen C-P. Non-axisymmetric lamb wave excitation by piezoelectric wafer active sensors. Sensors and Actuators A-Physical. 2012; **174**:173-180

[23] Dugnani R. Dynamic behavior of structure-mounted disk-shape piezoelectric sensors including the adhesive layer. Journal of Intelligent Material Systems and Structures. 2009; **20**:1553-1564

[24] Blackshire JL, Giurgiutiu V, Cooney A, Doane J. Characterization of Sensor Performance and Durability for Structural Health Monitoring Systems. In: proceedings of SPIE's 12th International Symposium on Smart Structures and Materials. San Diego, CA. March 2005

[25] Blackshire S, Cooney A. Characterization and Modeling of Bonded Piezoelectric Sensor Performance and Durability in Simulated Aircraft Environments. 2006

[26] Gall M, Thielicke B, Schmidt I. Integrity of piezoceramic patch transducers under cyclic loading at different temperatures. Smart Materials and Structures. 2009;**18**:104009

[27] Gall M. Experimentelle und numerische Untersuchungen zur Lebensdauer von flächigen ppiezokeramische Sensor-/Aktor – Modulen [PhD thesis]; 2012

[28] Bach M, Dobmann M, Eckstein B, Moix-Bonet M, Stolz M. Reliability of co-bonded piezoelectric sensors on CFRP structures. In: 9th International Workshop on Structural Health Monitoring; 2013

[29] Lee SJ, Sohn H, Hong JW. Time reversal based piezoelectric transducer self-diagnosis under varying temperature. Journal of Nondestructive Evaluation. 2010;**29**:75-91

[30] Giurgiutiu V, Zagrai A, Bao JJ. Piezoelectric wafer embedded active sensors for aging aircraft structural health monitoring. Structural Health Monitoring. 2002;**1**:41-61

[31] Pacou D, Pernice M, Dupont M, Osmont D. Study of the interaction between bonded piezo-electric devices and plates. In: 1st European Workshop on Structural Health Monitoring; 2002

[32] Park G, Farrar CR, Rutherford AC, Robertson AN. Piezoelectric active sensor self-diagnostics using electrical admittance measurements. Journal of Vibration and Acoustics. 2006;**128**: 469-476

[33] Park G, Farrar CR, Scalea FL, Coccia S. Performance assessment and validation of piezoelectric active-sensors in structural health monitoring. Smart Materials & Structures. 2006; **15**:1673-1683

[34] Rugina C, Enciu D, Tudose M. Numerical and experimental study of circular disc electromechanical impedance spectroscopy signature changes due to structural damage and sensor degradation. Structural Health Monitoring. 2015;**14**:663-681

[35] Bach M, Fritzen B, Eckstein B, Speckmann H. Self-diagnostic capabilities of piezoelectric transducers using the electromechanical impedance. In: International Workshop of Structural Health Monitoring; 2007

[36] Park S, C-BY, Inman DJ. Structural health monitoring using electro-mechanical impedance sensors. Fatigue & Fracture of Engineering Materials & Structures. 2008;**31**:714-724

[37] Overly TG, Park G, Farinholt KM, Farrar CR. Piezoelectric active-sensor diagnostics and validation using instantaneous baseline data. IEEE Sensors Journal. 2009;**9**(11): 1414-1421

[38] Lee SJ. Development of Smart Piezoelectric Transducer Self-Sensing, Self-Diagnosis and Tuning Schemes for Structural Health Monitoring Applications. Pittsburgh, Pennsylvania, USA: Carnegie Mellon University; 2009

[39] Taylor SG, Park G, Farinholt KM, Todd MD. Diagnostics for piezoelectric transducers under cyclic loads deployed for structural health monitoring applications. Smart Materials and Structures. 2013;**22**:025024

[40] Buethe I, Fritzen CP. Sensor performance assessment based on a physical model and impedance measurements. Key Engineering Materials. 2013;**570**:751-758

[41] Mueller I, Fritzen C-P. Inspection of piezoceramic transducers used for structural health monitoring. Materials. 2017;**10**(1):17

[42] Mueller I. Inspection of piezoelectric transducers used for structural health monitoring systems [PhD thesis]; 2016

[43] Buethe I, Moix-Bonet M, Wierach P, Fritzen CP. Check of piezoelectric transducers using the electro-mechanical impedance. In: EWSHM—7th European Workshop on Structural Health Monitoring, Nantes; 2014

[44] Overly TGS. Development and integration of hardware and software for active-sensors in structural health monitoring [MSc thesis]; 2007

[45] Fritzen CP, Moll J, Chaaban R, Eckstein B, Kraemer P, Klinkov M, Dietrich G, Yang C, Xing KJ, Buethe I. A multifunctional device for multi-channel EMI and guided wave propagation measurements with PWAS. In: EWSHM—7th European Workshop on Structural Health Monitoring, Nantes; 2014

[46] Mulligan KR, Quaegebeur N, Masson P, Brault L-P, Yang C. Compensation of piezoceramic bonding layer degradation for structural health monitoring. Structural Health Monitoring. 2014;**13**:68-81

[47] Masson P, Quaegebeur N, Mulligan K, Ostiguy PC. Increasing the roburobust in damage imagin for SHM. In: International Symposium on SHM and NDT; 2013

[48] Xing K. Experiments and simulation in structural health monitoring systems using the E/M impedance and cross transfer function methods [PhD thesis]; 2015

[49] Buethe I, Fritzen CP. Quality assessment for the EMI-based inspection of PWAS. In: International Workshop on Structural Health Monitoring, Stanford; 2015

[50] Golub MV, Shpak AN, Buethe I, Fritzen CP, Jung H, Moll J. Continuous wavelet transform application in diagnostics of piezoelectric wafer active sensors in Days on Diffraction; 2013

Chapter 2

Structural Health Monitoring by Acoustic Emission Technique

Md. Tawhidul Islam Khan

Additional information is available at the end of the chapter

http://dx.doi.org/10.5772/intechopen.79483

Abstract

Elastic wave, which is formed due to sudden rearrangement of stresses in a material, is called acoustic emission (AE). It is widely used in nondestructive testing (NDT) of materials and structures especially in health monitoring of structures for damage detection. When a body is subjected to an external force (in the form of changing pressure, load, or temperature), any micro fracture inside the body releases energy in the form of AE wave, which is received by sensor and later on is converted to electrical signal for inspection. In early stage, major importance was given on studying the AE characteristics during the deformation and fracture on various materials (by J. Kaiser in Germany in 1950 and B. H. Schofield in the USA in 1954). Nowadays, lots of research are conducting on formulating the theories behind AE formation, propagation, and inspection in various fields as an important health monitoring tool for NDT. In this chapter, I would like to elaborate a "feature outlook of AE" based on past, present, and future perspectives; "AE monitoring" procedure based on theoretical and experimental perspectives; and smart applications in structural health monitoring based on industrial and biostructural perspectives with related figures and tables.

Keywords: structural health monitoring, nondestructive testing, acoustic emission technique, industrial applications, biomedical engineering application

1. Introduction

Structural health monitoring (SHM) refers to the theme of damage detection, evaluation, and characterization strategy of an engineering structure through time ranging feature extraction by sensors. Analytical and statistical representations, periodic forms in most cases, of damage-sensitive features of the structure focus on the monitoring system about the present status of structural health condition.

1.1. Acoustic emission (AE) in SHM

Many conventional techniques are proposed by many engineers and scientists for health monitoring of structures, and maximum of them is nondestructive testing (NDT) type methods. Again, in many NDT systems, testing loadings are applied before or after the testing and are widely used as an active method, where signals or energy is delivered from the outside to the testing body. Contrary to active NDT, acoustic emission is widely used as passive NDT method in structural health monitoring, where external energy is not needed to supply the testing structure. The stimulated internal energy of the structure is received in this acoustic emission technique as health monitoring features. Due to this unique characteristic, acoustic emission technique has become very simple; however, accuracy or acquisition sensitivity is very high. Therefore, acoustic emission technique is becoming popular day by day in all types of structural monitoring fields [1–4].

A dominating attribute of acoustic emission technique is its application ability in its loading condition. Therefore, it provides instant damage information within a short period of time. Thus, acoustic emission monitoring tests are often performed in the operating conditions of the structure. As a result, adequate damage information even in minute state triggers the acoustic emission technique as a valuable health monitoring method. Dynamic characterization of any structural damage has become advantageous in this unique monitoring system. Furthermore, since acoustic emission technique is applied in dynamic feature, early stage of any damage can be characterized in this technique. Therefore, easy and adequate measures against any matured fracture or damage can be adopted in the presented fault detection technique [5–8].

Among many important features of acoustic emission technique, source location ability of involved damage inside the material attracts people in application of this technique as well. Following the traveling information of AE hits and applying to preferable algorithms, source location of AE event is performed. Based on the availability of sensors, dimension of source location is defined. For example, if two AE sensors are available, a single degree of source location is applicable; if three sensors are available, two-dimensional source location is applicable; if four or more sensors are available, three-dimensional source location is applicable. Since signal velocity influences the source location very much, velocity modes greatly affect the source location technique as well [9–12].

Present acoustic emission technique can quantify qualitative measure of the defects of a structure. For getting quantitative information of the damage, it often prefers to get supports of ultrasonic testing method. However, ultrasonic technique is necessary to apply in static condition, which is contradictory to the basic principle of acoustic emission. Therefore, pre- or postquantitative diagnosis is suitable for getting damage sizing inside the structure [13].

In addition to many advantages of AE applications in nondestructive testing environment, entire structural damage evaluation can be obtained under whole loading conditions by single or several sensors only. No replacement or cleaning of sensor placements is necessary for that purpose. Furthermore, a noisy environment except structural vibrations, and so on, does not influence to the data acquisition system too much. Therefore, acoustic emission technique in structural health monitoring system is widely applied as a preferable nondestructive tool in various fields of industrial to biomedical engineering fields.

1.2. Onward features and prospective of present topic

According to the strategy of the present writing, acoustic emission technique will be elaborated perspective to its historical criteria in structural health monitoring statistics. Following to its historical elongation, theoretical and experimental applications will be strategically approached. Afterward, some classical applications will be discussed before an elaborate discussion and conclusions of the technique to the structural health monitoring system.

2. Fundamentals of AE technique to SHM applications

2.1. History of AE

Historically, the application of AE to structural health monitoring is not so new; however, the challenges of this monitoring strategy are still facing and progressing on time. Technologically, AE was investigated in the middle of twentieth century. In early stage, AE phenomena were realized in Germany by Forester [14] in transforming mechanical vibration into electrical voltage by electrodynamic transmitter-receiver system. They measured tiny voltage change due to resistance variations caused by martensite transformations in metallurgical experiments. However, AE experiments were officially founded by Kaiser [15] through the publication of his historical irreversibility theory, known as the "Kaiser effect" in 1950. The terminology "AE" was first in history published by Kaiser's pioneering work "Acoustic Emission" in 1961. Later on, Obert, Schofield, Drouillard, Yokomichi, Ikeda, Matsuoka, and Kishinoue did enormous efforts to apply AE in various fields until the end of twentieth century [16–20]. Thus, the application of AE became familiar as a well-known nondestructive tool to different fields in structural health monitoring applications.

2.2. AE technique

Acquisition of transient elastic wave generated due to the sudden change of material stress for any external stimulus locally or globally to the material generates acoustic emission waves. The generated waves propagate through the surface of the material, and therefore, acquisition of these elastic waves and conversion of these waves to electrical signals for visualization and analysis refer to the fundamentals of AE testing. In AE testing, a piezoelectric transducer, generally called as AE sensor, is placed on the surface of the material to be tested. The transducer responds to the dynamic motion generated by the elastic wave as mechanical motion and converts it to an electrical voltage signal, which is often called as AE signal. AE sensor is selected based on the operating frequency. Therefore, different types of AE sensors are commercially available based on their applicable frequencies and sensitivities [21–23].

A fundamental AE testing system consists of a sensor (AE sensor), a preamplifier, main amplifier with appropriate filters, and data acquisition system along with display (oscilloscopes, personal computer with data acquisition software, and data transferring devices like AD conversion system). As AE signals are very small, it is boosted by preamplifier to gain at low signal-to-noise ratio. Later on, AE signals are amplified again and passed through band

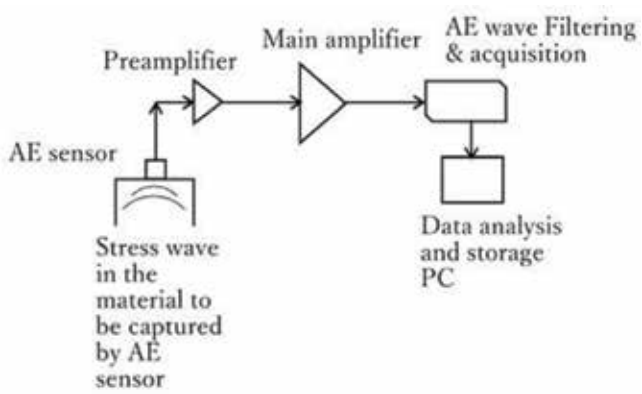

Figure 1. Fundamentals of AE technique.

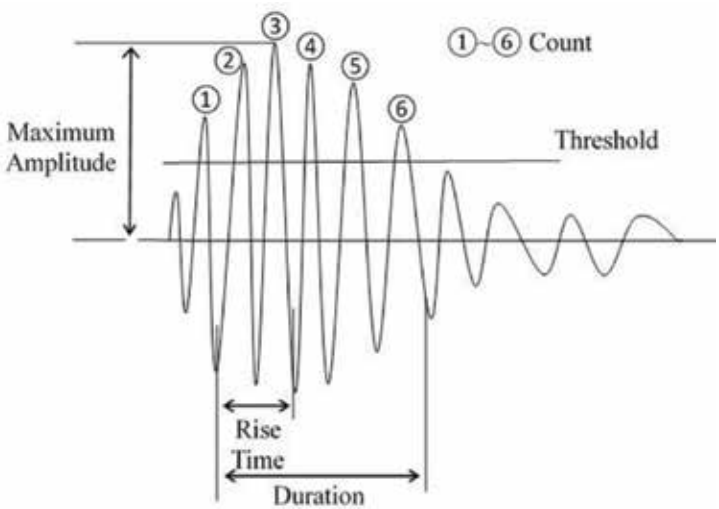

Figure 2. Common parametric features in an AE hit.

pass filters before storing to the mainframe of personal computer (PC) for analysis to any of desired features. The abovementioned AE technique is explained by the following schematic diagram as shown in **Figure 1** [24–26].

2.3. Important AE parametric features

In AE testing, as shown in **Figure 1**, AE signals are received and visualized to the display of the acquisition device when AE sensor is attached to the material surface (object to be tested) by adhesives or tape and is excited by the generated stress wave at the material. AE waves are then saved to PC for further synthesis to characterize the damage inside the test object. Then, parametric features are widely used in analyzing or monitoring damage inside an object by AE NDT, as shown in **Figure 2** [13, 27].

AE event: The time domain or frequency domain of acoustic emission signals represents parametric features due to the elastic wave generated inside the material. It is the total AE wave representation during the AE testing.

AE hit: It is represented as the AE signal from one channel and crosses the user-defined threshold. There can be multiple hits in an AE event or an AE test of multiple channels.

Maximum amplitude: Maximum amplitude (amplitude) is the greatest amplitude of an AE hit measured in voltage or in decibels (dB). AE signals with maximum amplitude below the user-defined threshold line are not recorded as AE signals.

Counts: Counts are referred to the numbers of pulses of an AE hit, which cross the user-defined threshold value.

Rise time: Rise time is defined as the time span of an AE hit from its first threshold crossing amplitude to its maximum amplitude.

Duration: Duration is defined as the time span of an AE hit from its first threshold crossing amplitude to its last threshold crossing amplitude.

Energy: It is the area below the detection envelope within the duration of an AE hit.

Peak frequency: It is the frequency component (kHz) corresponding to the maximum amplitude in an AE wave spectrum.

Average frequency: It is the average frequency in an AE hit. It is associated with duration and count and can be calculated from dividing "count" by "duration." It can roughly represent the signal frequency (when AE waveform is not possible to record). It represents complete acoustic emission impact signal.

Center frequency: It is the frequency component (kHz) corresponding to the center of gravity in an AE wave spectrum.

Initial frequency: It indicates the initial condition of an AE spectrum. It is calculated from dividing "counts" until peak by "rise time."

Reverberation frequency: It is calculated from the relation derived from total count to initial count divided by the relation derived from duration to rise time.

RA value: It is calculated from rise time divided by maximum amplitude (amplitude). It is the reciprocal of gradient in AE signal waveform and represents the type of cracks in the unit of ms/V.

2.4. AE sensors and data acquisition

In a practical AE experiment, generally piezoelectric sensor is widely used as AE sensor. It is normally a contact-type sensor consisted of piezoelectric element protected by hard metal housing and connected by an electric connector for transmitting the generated electric effects. The sensing system is based on the piezoelectric effect out of lead zirconate titanate (PZT). This type of sensor is relatively cheap and highly sensitive and converts the mechanical movement to electrical voltage in AE experiments efficiently.

Figure 3. A typical AE sensor with connecting cable.

Selection of an appropriate AE sensor depends on the demanded frequency in the experiment. As the propagation of elastic wave is heavily affected by the property of the propagation path and the propagation mechanism to the AE sensor, the frequency content of the propagating elastic wave plays a very important role in the selection of the suitable AE sensor in AE tests (**Figure 3**).

Appropriate sensors for AE testing to pressure vessels, storage tanks, heat exchangers, piping, reactors, aerial lift devices, nuclear power plants, and biomedical fields are well prepared based on their required frequency range. In general, based on the frequency range for AE tests, sensors are classified accordingly as low-frequency range sensor (20–100 kHz), middle or standard range sensor (100–400 kHz), and high-frequency range sensor (~400 kHz). Different companies such as Physical Acoustic Corporation (PAC), Vallen Systeme Company, and so on produce their sensors regarding the type of commercial AE sensor with high sensitivity [25, 28–30].

3. AE source location

Source location plays a significant role in AE technique. It is an advantageous facility in AE technique when compared with many other NDTs. It makes the characterizing of damage propagation behavior and the overall damage monitoring system well understandable and well predictable.

It is already mentioned that many AE hits can be taken in one AE event by placing many AE sensors in AE testing. One channel (one AE sensor) can record one AE hit, and thus, multiple channels (multiple AE sensors) can record multiple AE hits. When AE sensors place at different places at a suitable sensor to sensor distance (sometimes carefulness in signal wavelength is necessary) according to the desired inspection area, all AE hits are recorded by the system with different signal traveling times based on the different distances of sensors to the signal source. This traveling time is termed as "arrival time" in AE source location. Knowing the traveling time or arrival time of each hit from the signal acquisition system and multiplying it with the AE signal traveling velocity in that material, signal traveling distance from the

source to each AE sensor is calculated. For simplicity, wave velocity for a particular material is assumed constant in general AE source location technique. However, considering different geometric or traveling effects, like wave reflection due to material inhomogeneity, various wave modes (p-mode, s-mode, etc.) precise velocity calculation is necessary for improving the accuracy of AE source location technique. Based on the number of AE sensors connected to the acquisition system, several source location techniques have been developed already. Several AE source location techniques are discussed later.

3.1. Linear source location technique

A fundamental and very commonly used technique is the linear type of AE source location technique. At least two AE sensors (minimum required number of AE sensors in AE source location technique) are necessary in this technique. Linear type of structures such as bridge and pipe is used for measurements by this technique. This technique is very simple and easy to apply. It is also called as one degree AE source location technique [13].

In linear source location technique, two sensors are placed to an appropriate distance, and therefore, the time of arrivals from two sensors is collected. Based on the difference in signal arrival time, source location is defined. For example, if the source location is located at the middle point of two sensors, the difference between two arrival times is zero. Otherwise, the arrival time will be different. It is considered in this technique that shorter arrival time is the closer source to the receiving sensor. Thus, the source length is calculated by multiplying the arrival time with wave traveling velocity. The schematic of a linear source location technique is shown in **Figure 4**, where AE source is mentioned by s. Similarly, s_1, s_2 and t_1, t_2 indicate as the AE sensor 1, AE sensor 2 and time of arrival to sensor 1, time of arrival to sensor 2, respectively. Furthermore, l, l_2, and l_1 indicate the distance between two sensors (s_1, s_2), axial distance of AE source to sensor 1, and axial distance between AE source and the midpoint (l/2) of two AE sensors, respectively.

The mathematical relations of the linear source location algorithm are explained as the following equations, where Δt indicates the time difference between two arrival times to sensor 1 and sensor 2 and v indicates the AE wave velocity [31].

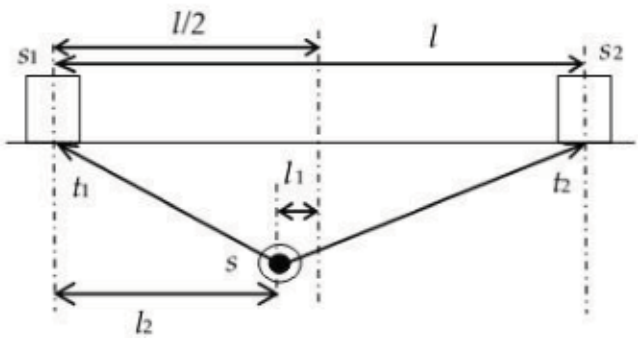

Figure 4. Schematic of linear source location technique.

$$l_1 = \frac{1}{2}(t_1 - t_2).v = \frac{1}{2}\Delta t.v \tag{1}$$

$$l_2 = \frac{1}{2}l - l_1 = \frac{1}{2}(l - \Delta t.v) \tag{2}$$

3.2. Two-dimensional source location technique

Planner or two-dimensional source location technique requires three or more AE sensors to be placed on a plane for identifying AE source. Three sensors generate three hyperbolae, which intersect each other on the monitoring plane at a common interceding point or cross-sectional point, and the point is termed as the AE source. Theoretically, three sensors are sufficient for identifying the source in two-dimensional technique; however, another extra sensor, which is called as reference sensor, improves the accuracy of the source location technique. Therefore, the placement of four sensors in a rectangular sensor array generates six sensor pairs. Calculating time of arrival from each sensor pair and correlating according to the following relations planner or two-dimensional AE source location are done.

The simple algorithm for calculating two-dimensional AE source location is based on the following relations [32].

$$x_s^{\,2} + y_s^{\,2} = r_s^{\,2} \tag{3}$$

$$(\Delta x)_i^{\,2} + (\Delta y)_i^{\,2} = r_i^{\,2} \tag{4}$$

$$(\Delta x)_j^{\,2} + (\Delta y)_j^{\,2} = r_j^{\,2} \tag{5}$$

where $\Delta x = x_s - x$ and $\Delta y = y_s - y$, when x and y indicate the coordinates of sensor positions; however, for the source indication, the suffix s is used. However, s_0 indicates the reference sensor. Furthermore, suffixes i and j indicate the general number of positioning and measuring sensors, respectively, for example, in **Figure 5**, s_i indicates for sensor 1, and s_j indicates for sensor 2. Similarly, r_i, r_j, and r_s indicate the distances from the corresponding sensors to source. Applying simple solutions of above Eqs. (3)–(5), the source distance, r_s can be calculated as follows:

$$r_s = \frac{1}{2}\left[\frac{U_i}{x_i\cos\theta + y_i\sin\theta + d_i}\right] = \frac{1}{2}\left[\frac{U_j}{x_j\cos\theta + y_j\sin\theta + d_j}\right] \tag{6}$$

In Eq. (6), U_i, U_j, d_i, and d_j are defined as follow:

$$U_i = x_i^2 + y_i^2 - d_i^2 \tag{7}$$

$$U_j = x_j^2 + y_j^2 - d_j^2 \tag{8}$$

$$d_i = r_i - r_s = v \cdot \Delta t_{io} \tag{9}$$

$$d_j = r_j - r_s = v \cdot \Delta t_{jo} \tag{10}$$

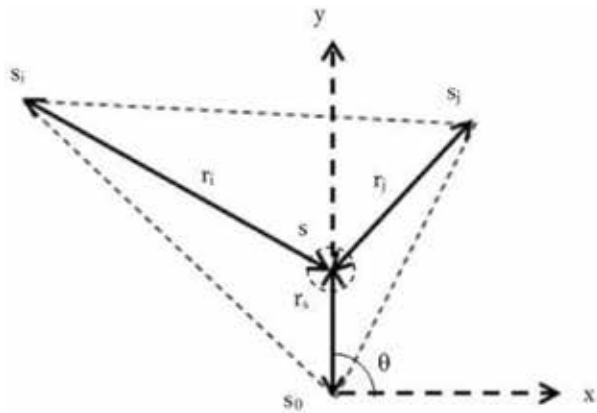

Figure 5. Geometrical representation of two-dimensional source location algorithm.

Similarly, the source angle (θ) can be calculated as follows:

$$\theta = \phi + \psi \tag{11}$$

In Eq. (11), the parameters ϕ and ψ can be calculated by rearranging Eq. (6), and thus, the two-dimensional source location can be found.

Similarly, three-dimensional source location is also possible to calculate in AE source location technique by increasing the number of sensors. Many other modern source location techniques are available [10, 13] and are still introducing to AE fields by AE researchers from all over the world.

4. Smart applications of AE technique

The application of acoustic emission for fault detection or condition monitoring in structural health monitoring (SHM) field is versatile. Since it is a noninvasive technique, it is widely applied in different fields of nondestructive testing (NDT), nondestructive evaluation (NDE), and nondestructive monitoring (NDM) for many engineering applications. Similar application of AE in seismology is well known from its beginning of implementations. Further, recently, applications of AE in biomedical engineering field have attracted many scientists and engineers for its smart applications in condition monitoring as well. Several examples of AE applications are mentioned later.

4.1. Industrial applications in SHM

Out of many industrial applications of AE technique, several are mentioned as monitoring of pressure vessel, storage tank, structural materials, composites, concrete structure, steel structure, bridge, aircraft, gear, ceramics, ceramic components, and so on. In maximum cases of inspection,

standard AE features are evaluated experimentally under satisfactory experimental environments to practical application and correlated with standard values. For example, pressure vessel or other high-pressure tanks are evaluated under cyclic loading pressure [8] up to lifetime number of loading. AE sensors are attached to the tank to be tested and connected to the data acquisition components such as preamplifier and filters, and finally, the digital acquisition system saves the data to the computer where the required AE parameters are evaluated for crack or damage evaluation. Multiple sensors are placed for evaluating the damage source as well. Pipe line or drill pipe fatigue damage is also evaluated frequently by AE technique. Although fatigue loading is a complex mechanism in operation, however, it is defined by cycle number in all fatigue tests, and therefore, fatigue damage is normally evaluated based on crack propagation under certain range of applied cyclic loads. Based on application criteria, drill pipe is subjected to cyclic stress in tension, compression, torsion, and bending. Bending and rotation produce alternation between states of loading at a localized point, which is most concern to damage under fatigue loading. In drilling test rig monitoring, frequent fatigue failures are tested based on critical rotary speed, maximum tension load, notch fatigue load, etc. [33].

Most bridges are tested based on their welded joints and connections under the combinations of loading and loading environments. The general frequency of monitoring bridges is 2 years. Under visual inspection, the necessity of shutting down of its weight capacity is done when damage is found. However, in AE inspection, lane closer is not necessary as it monitors data continuously for real-time forecasting of any damage. Therefore, bridge monitoring by AE technique has increased as well [34].

Material testing by AE technique is also widely applicable. Structural materials, ductile materials, brittle materials, and many other materials including composite materials are tested to evaluate their cracking, breaking, and damaging characteristics for different industrial and biomedical applications. Furthermore, microstructural studies including metallurgical characteristics of many materials are also tested by different smart AE tests.

Different aerospace structures are monitored by AE technique as well. Many sensors are possible to attach to different parts of aerospace structures easily, and therefore, damage monitoring even in minute level and damage location in multidimensional features are performed by AE technique. In many smart AE techniques, real-time wireless monitoring is done by applying wireless AE sensing systems. For example, NASA installed AE sensor-based alert system on the inside of the space shuttle Discovery's wing structure for avoiding the damage of its leading edge during the reentry to the Earth atmosphere [35].

4.1.1. AE parametric analysis

A material test result was conducted for showing the parametric analysis of AE technique [36]. The experiment was conducted for a cast iron specimen (ferrite) under tensile loading in an autograph tensile machine. Four AE sensors (R15α, Physical acoustics Ltd.), placed to the specimen for getting AE data due to crack damage, were connected to four preamplifiers and to a main amplifier with a gain of 40 dB. AE data were collected by a digital oscilloscope, and the collected data were analyzed for the characterization inside a personal computer. For avoiding noise, appropriate threshold values were used. All the recorded AE hits were saved,

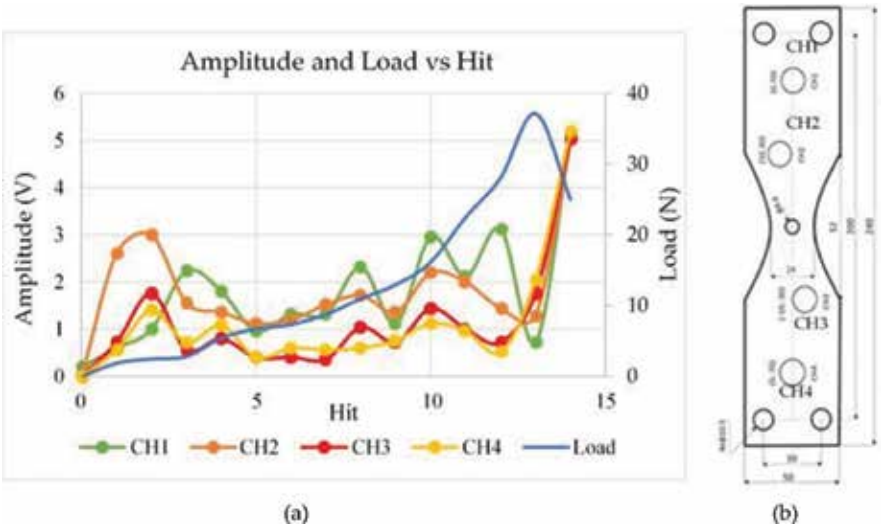

Figure 6. (a) Graphical representation of AE parametric distribution and (b) AE sensor positions in the specimen.

and AE parametric features were calculated to represent the characteristics of crack propagation in a ferrite material under tensile loads. Applied tensile loads were simultaneously saved to the computer for evaluation as well. One experimental result showing AE parametric distribution (amplitude distribution versus tensile loads compared to AE hits) is shown in **Figure 6**. In this experiment, according to the sensor positions, oscilloscope channels (CH in figure) were defined. Furthermore, sensors 2 and 3 were placed near to the crack initiation position; sensor 1 was placed near to the loading chuck; sensor 4 was placed near to the specimen supporting chuck. Accordingly, sensor 2 (CH2) and sensor 3 (CH3) represented the maximum AE excited values in signal amplitude, whereas sensor 1 (CH1) showed the AE amplitude along with noise contamination from the loading chuck. Similarly, sensor 4 (CH4) represented the minimum value as it was the farthest from the cracking position and far from loading nose. Furthermore, amplitude excitation and distribution values of CH2 and CH3 showed that at the initiation of cracking, amplitude excitations were high due to the tensile cracking at its early stage of AE hits, and after that, as cracking took the shear loading, the amplitude values went down until it gained the maximum values at the fracture stage at their end stage of AE hits.

4.1.2. AE source location

An experiment of two-dimensional source location technique as explained in Section 3.2 was conducted on a steel plate with generated artificial AE source based on Hsu-Nielsen [31, 37] technique. The arrival time was calculated according to the first signal recognition in AE hit as shown in **Figure 7**. Three experiments were conducted with three sensor distances, where sensor-to-sensor distance was kept constant among three sensors in each experiment. Accordingly, the source location represented by source distance (r_s) and source angle (θ), as shown in **Figure 4**, was calculated. The results were compared with its actual measured data (known before for comparison) and found good agreement as well. The results are summarized in **Table 1**.

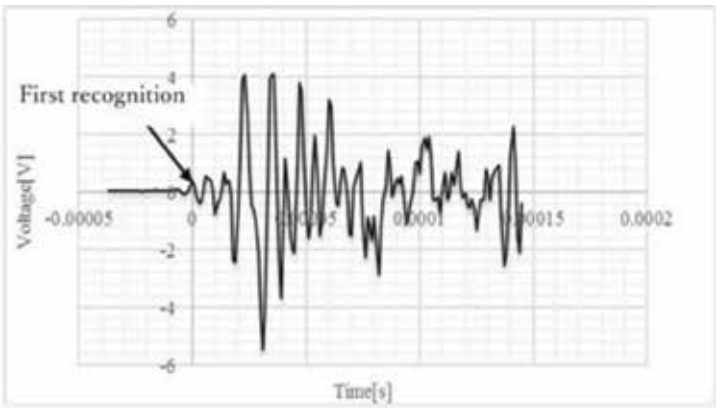

Figure 7. AE hit showing its initial recognition position of arrival signal.

Distance	Actual, θ	Experimental, θ′	Actual, r_s	Experimental, r_s	Error of r_s (%)	Error of θ (%)
200	90	89.42	0.1414	0.1424	0.69	0.64
250	90	89.67	0.1768	0.1775	0.41	0.37
300	90	89.68	0.2121	0.2130	0.41	0.36

Table 1. Results of AE two-dimensional source location.

4.2. AE applications in biomedical health monitoring

A successful history of AE technique in fault detection and condition monitoring encourages research to apply it to biomedical engineering field as well. Since AE technique perfectly evaluates and monitors any discontinuity and internal damage of a structure, it is successfully applied in detecting the integrity condition of human bones and joints, particularly knee joints. As detailed functional assessment of knee joint includes to identify any irregularity among its internal anatomical structures, AE sensors are installed to the knee joint and internal damages are evaluated. A common knee disease, particularly of elderly people, is osteoarthritis. It causes due to the damage of internal cartilage of knee joint. This disease causes the disability of people, and therefore, its prevalence is predicted to increase as a result of aging people in an aging society. The damage of cartilage brings the raw bone-end in contact and causes several knee diseases. In the worst case of osteoarthritis, operation is needed to replace by artificial joint with mixed satisfaction of the patient. Application of AE technique in diagnosis of cartilage damage is interestingly applied as well.

Accordingly, experiments of AE technique for identifying the integrity of knee joint were conducted [38]. Four AE sensors were placed to the knee joint, and AE data (AE features) were collected as shown in **Figure 8**. AE parameters from the knee were collected under the dynamic loading condition of knee joint by several stand-sit-stand motions of participants. Both

http://dx.doi.org/10.5772/intechopen.79483

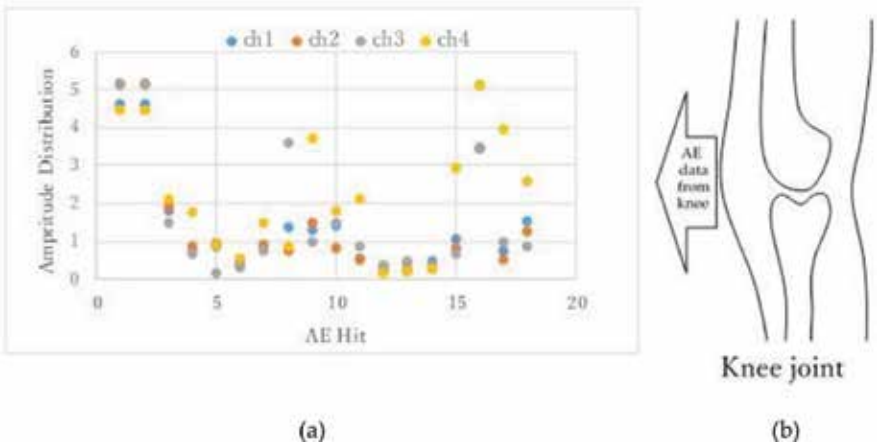

Figure 8. (a) Sample result of AE amplitude distribution for four sensors from the knee joint experiments and (b) schematic of knee joint from AE sensor data were collected.

healthy participants and patients of knee osteoarthritic disease joined to the experiments. A sample result of AE amplitude distribution compared with AE hit is presented in **Figure 7**. Acquisition of AE data is perfectly specified in the figure. All channels received sufficient AE data for identifying the internal conditions of knee joint. Thus, experimental results showed that monitoring of knee condition is possible by applying the AE technique successfully to knee joint and to others.

5. Conclusions

A feature outlook of acoustic emission (AE) technique related to the structural health monitoring has been presented in this chapter. A brief history and chronology of AE monitoring are discussed with adequate references. Basic understandings about AE technique, its experimental methodology, and applications are also summarized in this chapter. A list of frequently used AE parameters is also added here. Useful definitions of AE parameters are provided in this parametric list for understanding the theme of AE parametric analysis. Almost all of the structural health monitoring based on AE technique are conducted by the mentioned parameters. Three examples covering three important applications of AE technique are summarized at the end of the chapter. Two major wings of AE technique in structural health monitoring are AE parametric analysis and AE source location. Both of these applications are explained with appropriate examples along with experimental results in material damage and crack propagations. A smart application of AE technique in biomedical engineering field is also mentioned in this chapter as a promising scope of AE technique for the future versatile solutions. Extension of this work can be found in the future publications as well. Thus, the chapter has made easier for wider and fruitful understanding of AE technique in structural health monitoring to all of its readers.

Acknowledgements

The author expresses his sincere thanks and gratitude to all funding organizations including MEXT, Collaborating Company, Daishin Co. Ltd., and Saga University as well as to all graduate and undergraduate students of his laboratory for their continuous supports to continue all of his research topics. The author is particularly indebted to his biomedical research partner, Dr. Suya Ide (M.D.), for his enormous supports and guidance in continuing the research. The author is also obliged to all of his friends and colleagues, particularly to all participants of his research for having successful goal.

Author details

Md. Tawhidul Islam Khan

Address all correspondence to: khan@me.saga-u.ac.jp

Department of Mechanical Engineering, Saga University, Saga, Japan

References

[1] Miller RK, McIntire P, editors. Acoustic Emission Testing. Nondestructive Testing Handbook. 2nd ed. Vol. 5. American Society for Nondestructive Testing. p. 603

[2] Ono K. Trends of recent acoustic emission literature. Journal of Acoustic Emission. 1993;**12**:177-198

[3] Sachse W, Kim KY. Quantitative acoustic emission and failure mechanics of composite materials. Ultrasonics. 1987;**25**:195-203

[4] Meyendorf N, Frankenstein B, Schubert L. Structural health monitoring for aircraft, ground transportation vehicles, wind turbine and pipes-prognosis. In: Proceedings of 18th World Conference on Nondestructive Testing; 16-20 April 2012; Durban, South Africa

[5] Holroyd TJ, Randall N. Use of acoustic emission for machine condition monitoring. British Journal of Non-Destructive Testing. 1993;**35**:75-78

[6] Gorman M, Prosser WH. Application of normal mode expansion to acoustic emission waves in finite plates. Journal of Applied Mechanics. 1996;**63**:555-557

[7] Hamstad MA, Ogallagher A, Gary J. A wavelet transform applied to acoustic emission signals: Part 2: Source location. Journal of Acoustic Emission. 2002;**20**:62-82

[8] Laksimi A, Herve C, Ennaceur C, Cherfaoui M. AE Study of damage evolution in pressure vessels under cyclic loading. In: Proceedings, 30th European Conference on

Acoustic Emission Testing & 7th International Conference on Acoustic Emission; 12-15 September 2012; Granada, Spain

[9] Gorman MR, Prosser WH. AE source orientation by plate wave analysis. Journal of Acoustic Emission. 1991;**9**:283-288

[10] Christian UG, Ohtsu M, editors. Acoustic Emission Testing. Springer; 2008. DOI: 10.1007/978-3-540-69972-9

[11] Rindorf HJ. Acoustic Emission Source Location in Theory and in Practice. Vol. 2. Bruel and Kjaer Technical Review; 1981. pp. 3-44

[12] Kaita I, Enoki M. Acquisition and analysis of continuous acoustic emission waveform for classification of damage sources in ceramic fiber mat. Materials Transactions. 2007;**48**:1221-1226

[13] https://www.nde-ed.org/EducationResources/CommunityCollege/Other%20Methods/AE/AE_Intro.htm [Accessed: May 22, 2018]

[14] Forster F, Scheil E. Akustische Untersuchung der Bildung von Martensitnadeln (acoustic study of the formation of matensile needels). Zeitschrift für Metallkunde. 1936;**28**:245-247

[15] Kaiser J. A study of acoustic phenomena in tensile tests. [Dr.-Ing. dissertation]. Technical University of Munich; 1950

[16] Obert L, Duvall W. The microseismic method of predicting rock failure in underground mining, Part II: Laboratory experiments. Report of Investigations 3803. Washington D.C.: U. S. Bureau of Mines. 1945

[17] Obert L. The microseismic method: Discovery and early history. In: Hardy Jr, Leighton FW, editors. Proceedings 1st Conference on AE/MS. Geologic Structures and Materials. Clausthal, Germany: Trans Tech Publication; 1977

[18] Schofield BH. Acoustic emission under applied stress. Report ARL-150. Boston: Lessels and Associates; 1961

[19] Kishinoue F. An experiment on the progression of fracture (a preliminary report). Jishin 6:24-31 (1934) translated and published by Ono K. Journal of Acoustic Emission. 1990;**9**:177-180

[20] Yokomichi H, Ikeda I, Matsuoka K. Elastic wave propagation due to cracking of concrete. Cement Concrete Japan. 1964;**212**:2-6

[21] Ohtsu M, Ono K. A generalized theory of acoustic emission and Green's functions in a half space. Journal of Acoustic Emission. 1984;**3**:124-133

[22] Beatttie AG. Acoustic emission, principles and instrumentation. Journal of Acoustic Emission. 1983;**2**:95-128

[23] Nishinoiri S, Enoki M. Development of in-situ monitoring system for sintering of ceramics using laser AE technique. Progress in AE XII:69-76, JSNDI; 2004

[24] Ohtsu M. Acoustic emission characteristics in concrete and diagnostic applications. Journal of Acoustic Emission. 1987;**6**:99-108

[25] MISTRAS Group Inc. Express-8 AE System user's Manual, Rev 0, Part#: 7050-1000. Physical Acoustic Corporation; 2014

[26] Khan M, Islam T, Nagao T, Kondo Y, Teramoto K, Hattori N. Monitoring the fatigue damage in ductile cast iron by AE technique. International Journal of COMADEM. 2015;**18**:27-33

[27] Shiotani T, Nakanishi Y, Iwaki K, Luo X, Haya H. Evaluation of reinforcement in damaged railway concrete piers by means of acoustic emission. Journal of Acoustic Emission. 2006;**23**:260-271

[28] Hatano H, Watanabe T. Reciprocity calibration of acoustic emission transducers in Rayleigh wave and longitudinal wave sound field. The Journal of the Acoustical Society of America. 1997;**101**:1450-1455

[29] Hsu NN, Breckenridge FR. Characterization and calibration of acoustic emission sensors. Materials Evaluation. 1981;**39**:60-68

[30] Vallen Systeme GmbH. Acoustic Emission Sensors Specification; 2015. Available from: http://www.vallen.de/zdownload/pdf/sov1507.pdf [Accessed 2018-07-03]

[31] Khan M, Islam T, Nagafuchi S, Hassan M. Structural damage localization by linear technique of acoustic emission. Open Journal of Fluid Dynamics. 2014;**4**:425-432

[32] Khan TI, Hassan M, Takata R. Effect of wave velocity in two-dimensional AE damage locationon a steel plate. International Journal of COMADEM. 2017;**20**:1-5

[33] Gomera VP, Sokolov VL, Fedorov VP, Okotnikov AA, Saykova MS. Inspection of the pressure vessel used in petrochemical with AE examination. In: Proceedings, EWGAE2010; 8-10 September 2010; Vienna

[34] Shiotani T, Aggelis DG, Makishima O. Global monitoring of concrete bridge using acoustic emission. The Journal of the Acoustical Society of America. 2007;**25**:308-315

[35] Chlada M, Prevorovsky Z. Remote AE monitoring of fatigue crack growth in complex aircraft structures. In: Proceedings, 30th European Conference on Acoustic Emission Testing & 7th International Conference on Acoustic Emission; 12-15 September 2012; Granada, Spain

[36] Rashid AA, Khan Md TI, Hidaka R. Analysis of acoustic emission and crack propagation in ductile cast iron. In: Proceedings, 21th Acoustic Emission Symposium; 9-10 November 2017; Tokushima, Japan

[37] Mostofapour A, Davoodi S. A method for acoustic source location in plate-type structure. Mechanical Systems and Signal Processing. 2017;**93**:92-103

[38] Islam KT, Harino Y. Integrity analysis of knee joint by acoustic emission technique. Journal of Multimodal User Interfaces. 2015;**10**:319-324

Chapter 3

Evaluation of Diagnostic Symptoms for Object Condition Diagnosis and Prognosis

Tomasz Gałka

Additional information is available at the end of the chapter

http://dx.doi.org/10.5772/intechopen.77264

Abstract

For complex objects, condition assessment is usually based on indirect symptoms related to residual processes such as vibration, noise, heat generation, etc. The number of available symptoms is often large, and it is necessary to select those which are most representative (i.e., sensitive to condition parameters). Such selection may be based on singular value decomposition (SVD). An alternative approach is proposed that employs information content measures. In order to obtain a reliable condition assessment and prognosis of its evolution (in particular, remaining useful life estimation), certain preprocessing of experimental data is necessary. This involves, among others, issues such as life cycle normalization or identification and removal of outliers. Suitable procedures are proposed and discussed. Example is presented for vibration-based symptoms of steam turbine technical condition.

Keywords: diagnostic symptom, technical condition, prognosis, information content

1. Introduction

Terms like *condition assessment* (which is basically equivalent to *diagnosis*) and *prognosis* are commonly used in technical sciences and have been defined in several ways. For any given class of diagnostic objects, there is a logical sequence of activities which may be summed up including four consecutive stages [1, 2]:

- Measurement (acquisition of data that contain information on object condition)
- Qualitative diagnosis (or recognition-identification and localization of failures and malfunctions)

- Quantitative diagnosis (estimation of damage advancement)
- Prognosis (forecast for object operation in future)

In structural health monitoring and condition-based maintenance, the third and fourth steps are of particular importance. Quantitative diagnosis is in fact an estimation of the current object condition. Once this has been accomplished, a prognosis may follow, which basically means remaining useful life (RUL) estimation on the basis of certain criteria. This is extremely important for proper and safe operation and cost-effective maintenance of complex and critical machinery.

Evolution of object condition may be described in terms of the *hazard function* [3, 4], which typically takes the form of the bathtub curve (**Figure 1**). Initially hazard function decreases with time; this may be interpreted as "running-in." During normal operation period, hazard function increase is so weak that it may be treated as constant. Finally, during the final stage of the object service life, hazard function increases with time—in theory to infinity and in practice until the highest acceptable value is attained. For a wide range of objects, reliability is well described by three-parameter Weibull distribution. In such case, hazard function in its classic form is given by [5, 6]

$$h(\theta;\beta,\eta,\gamma) = \frac{\beta}{\eta}\left(\frac{\theta-\gamma}{\eta}\right)^{\beta-1}, \tag{1}$$

where θ denotes time and β, η, and γ are parameters; γ is the location parameter (set to zero if $\theta = 0$ corresponds to the beginning of object life—in such case, two-parameter distribution is obtained); η denotes characteristic life; and β is the shape factor. Cases $\beta < 1$, $\beta = 1$, and $\beta > 1$ correspond to three consecutive periods shown in **Figure 1**.

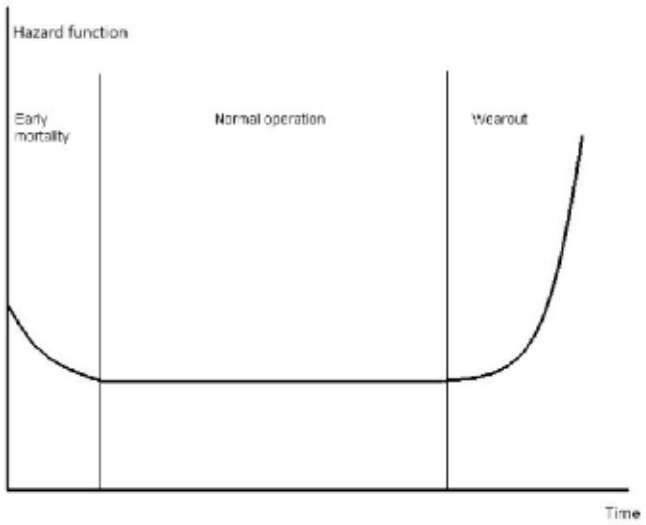

Figure 1. Typical shape of the hazard function (bathtub curve).

For many objects it is impracticable or inconvenient to describe condition evolution in terms of the hazard function (or failure density). An alternative approach is based on the analysis of energy transformation and dissipation mechanisms, which leads to the energy processor model [1, 7]. This model implies that object condition is estimated in an indirect manner, from measurable physical quantities referred to as *diagnostic symptoms*. Each symptom is related to the power $V(\theta)$ of residual processes that accompany the principal process of energy transformation. In the simplest case, the ith symptom $S_i(\theta)$ is given by

$$S_i(\theta) = \Phi\left(\frac{V_0}{1-\theta/\theta_b}\right) \tag{2}$$

where $V_0 = V(\theta = 0)$ and Φ is the symptom operator and θ_b denotes time to breakdown. Detailed description can be found in literature; several modifications have been proposed [1, 8], but basic principles have remained unchanged. The $S_i(\theta)$ given by Eq. (2) and referred to as *symptom life curve* is a monotonically increasing function with a vertical asymptote at $\theta = \theta_b$. As for the symptom operator, Weibull and Fréchet functions have been shown to give consistent results; they yield $S_i(\theta)$ in the forms of

$$S_i(\theta) = S_{i0}\left(\ln\frac{1}{1-\theta/\theta_b}\right)^{1/\gamma} \tag{3}$$

for the former and

$$S_i(\theta) = S_{i0}(-\ln\theta/\theta_b)^{-1/\gamma} \tag{4}$$

for the latter; in both cases, $S_{i0} = S_i(\theta = 0)$ and γ is the shape factor. For a given object, if sufficient database is available, it is possible to estimate θ_b by relatively simple fitting procedure. This, in turn, allows to estimate RUL. It has to be kept in mind that θ_b is obviously not equivalent to RUL, unless the most primitive "run-to-breakdown" operational policy is employed.

Large and complex objects usually generate many diagnostic symptoms, and their number in fact has no upper limit. It has to be kept in mind that values of these symptoms depend not only on condition parameters. If all symptoms S_i are expressed in the form of a vector $\mathbf{S}(\theta)$, then the following general relation holds [1, 9]:

$$\mathbf{S}(\theta) = F[\mathbf{X}(\theta), \mathbf{R}(\theta), \mathbf{Z}(\theta)], \tag{5}$$

where **X**, **R,** and **Z** denote vectors of condition parameters, control parameters, and interference, respectively. Obviously individual symptoms differ in their sensitivity to the components of all these vectors; it is thus necessary to select those which can be regarded "the best." The problem of selection was addressed at early stages of technical diagnostic development (see, e.g., [9]). Initially, at the stage of qualitative diagnosis, the principal criterion was symptom sensitivity to condition parameters. Quantitative diagnosis and prognosis imply a need to follow object condition evolution with time; thus, the symptom which best represents this process should be considered the most suitable one.

This chapter is devoted mainly to symptom evaluation and selection methods based on the analysis of information content measures. Some attention shall, however, also be paid to the method employing the singular value decomposition, the first that has been used for this purpose.

Suitability of symptom evaluation methods has been verified for a number of vibration-based symptoms generated by steam turbines operated at utility power plants. Details on symptom generation mechanisms may be found, e.g., in [1, 10, 11]. Absolute vibration velocity was recorded in the form of 23% constant percentage bandwidth (CPB) spectra, at points located at bearings and low-pressure turbine casings. Piezoelectric accelerometers were used with magnetic mountings, which allows for a frequency range well above 10 kHz. This implies that both "harmonic" (i.e., resulting directly from rotational motion) and "blade" (i.e., generated by the fluid flow system) components are recorded. Vibration amplitudes in frequency bands determined from turbine vibrodiagnostic models [1, 11] are the diagnostic symptoms to be evaluated. It has to be stressed here that presented methods are valid for a broad class of various diagnostic symptoms, irrespective of their physical origin.

2. Singular value decomposition

Singular value decomposition (SVD) is well known from linear algebra; concise description can be found, e.g., in [12]. To the author's best knowledge, the idea to employ this method in technical diagnostics goes back to the late 1990s [13]. Application for vibration-based symptoms has shown this method to give consistent results [14].

The first step is to represent symptom value database in the form of an $m \times n$ matrix $\mathbf{O}$, where m denotes the number of symptoms and n is the number of symptom value readings. In principle, symptoms of different physical origins are compared, so all are normalized with respect to their values at $\theta = 0$; moreover, 1 is subtracted from all normalized values, so they start from zero and are dimensionless. In accordance with general SVD rules, matrix $\mathbf{O}$ can be expressed as the following product:

$$\mathbf{O} = \mathbf{U} * \mathbf{\Sigma} * \mathbf{V}^T \tag{6}$$

where $\mathbf{U}$ and $\mathbf{V}$ are orthogonal matrices ($n \times n$ and $m \times m$, respectively) and $\mathbf{\Sigma}$ is a diagonal $m \times n$ matrix, $\mathbf{\Sigma} = \mathrm{diag}(\sigma_i)$. If σ_i components are arranged in the descending order, which is conventionally accepted, the representation given by Eq. (6) is unique. Components σ_i correspond to generalized faults, so that the sum given by

$$F(\theta) = \sum_{i=1}^{p} \sigma_i(\theta), \tag{7}$$

where $p = \min(m, n)$ represents the total damage advancement or lifetime consumption degree. Columns of $\mathbf{U}$ and $\mathbf{V}$ matrices are left-singular and right-singular vectors, denoted by $\mathbf{u}_t$ and $\mathbf{v}_t$, respectively, with $1 \le t \le n$. Eq. (6) can thus be rewritten as

$$\mathbf{O} = \sum_{t=1}^{p} \sigma_i \cdot \left(\mathbf{u}_t * \mathbf{v}_t{}^T\right) \tag{8}$$

According to [15] and following notation used herein, the tth fault can be described by two discriminants, namely

$$\mathbf{SD}_t = \mathbf{O} * \mathbf{v}_t = \sigma_t \cdot \mathbf{u}_t \tag{9}$$

$$\mathbf{AL}_t = \mathbf{u}_t^T * \mathbf{O} = \sigma_t \cdot \mathbf{v}_t^T \tag{10}$$

This means that this fault can be expressed in terms of left-singular or right-singular vectors, which are generally interpreted as "input" and "output" [13, 15]. In the case of system condition evolution, "input" represents condition parameters and "output" represents symptoms. Obviously, the second discriminant, given by Eq. (10), is of practical use here, as condition parameters are typically nonmeasurable.

SVD analysis may be performed using one of available software packages. In practical applications the first step is to analyze individual singular values. For a comparatively new object, the descent of consecutive singular values is rather slow; this means that dominant failure mode has not yet appeared. On the other hand, with considerable lifetime consumption degree, the first singular value dominates. Examples are shown in **Figure 2**. They refer to vibration-based symptoms generated by steam turbine fluid flow systems. In both cases illustrated in **Figure 2**, there are six such symptoms. For a turbine with a few dozen thousand hours logged (**Figure 2a**), contributions of the first three singular values into generalized damage are 36, 29, and 17%, respectively. For the second turbine (**Figure 2b**), which has logged well over 200,000 hours, corresponding values are 48, 24.5, and 10%—the difference is clearly seen. The second step is to calculate contributions of individual symptoms into several (e.g., three) first singular values. Corresponding graphs are shown in **Figure 3**. For the first turbine,

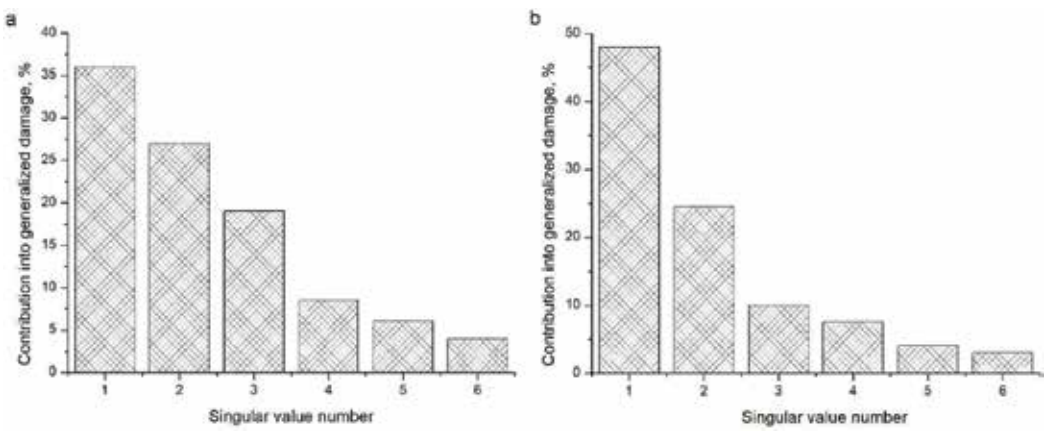

Figure 2. Contributions of singular values into generalized damage; (a) 260 MW unit, low-pressure turbine casing, rear part left; (b) 200 MW unit, low-pressure turbine casing, front part right (see main text for details).

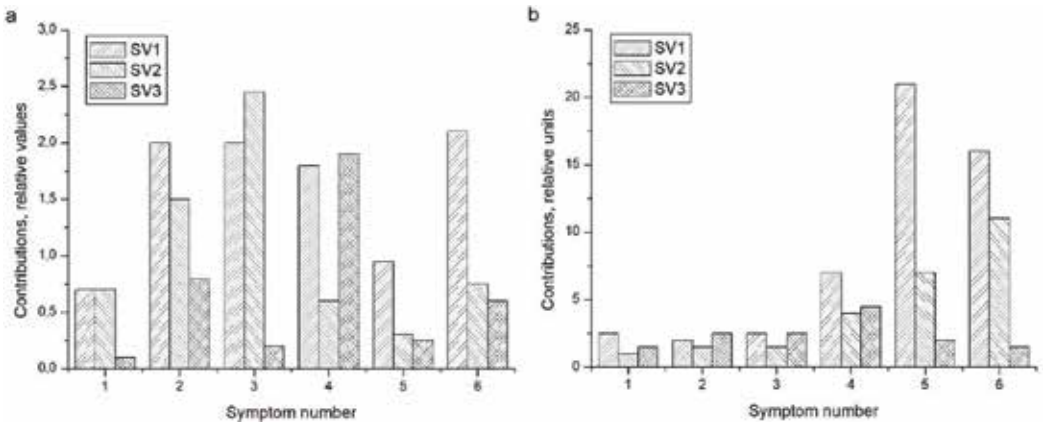

Figure 3. Contributions of individual symptoms into the first three singular values: (a) as in **Figure 2a** and (b) as in **Figure 2b**.

dominant symptoms cannot be identified, although we may infer that symptom numbers 1 and 5 can be skipped. For the second turbine, however, dominance of symptom numbers 5 and 6 is clearly seen, and they may be judged most sensitive to the fluid flow system lifetime consumption.

3. Information content measures

3.1. The idea

The abovementioned energy processor model is, by its very nature, deterministic. From Eq. (5), however, it is clearly seen that symptom values depend not only on deterministic condition parameters $X_i(\theta)$ but also on control parameters $R_i(\theta)$ and interferences $Z_i(\theta)$, which are random variables. Therefore, any symptom $S_i(\theta)$ should in principle be treated as a random variable with time-dependent parameters.

For a given object operated at a given location, it is reasonable to assume that $R_i(\theta)$ and $Z_i(\theta)$ are characterized by statistical distributions with time constant parameters. At the same time, from Eq. (2) it is clearly seen that the influence of lifetime consumption θ/θ_b (or, more generally, of *deterministic* condition parameters) will increase as $\theta \to \theta_b$. This means that $S_i(\theta)$ will become more deterministic or, to put it in a different way, more predictable. As pointed out in [16], this corresponds to information content decrease, in the sense of Shannon entropy [17]. Therefore, a symptom with the highest rate of an information content measure which decreases with time is the one that is most sensitive to lifetime consumption mechanisms.

Investigations of information content and its measures were pioneered by Claude E. Shannon. In his fundamental work [17], he introduced an information content measure $H(p_1, p_2, \ldots, p_n)$, later termed *Shannon entropy,* where p_i is the probability of the ith event, and showed it to have the following form:

$$H = -K\sum_{i=1}^{n} p_i \log_b p_i, \tag{11}$$

where K is a constant depending on units used (irrelevant if only decrease rate is of interest). Logarithm base b is typically set at 2, Euler constant, or 10, H being expressed in bits, nats, and dits, respectively. Obviously

$$\bigwedge_i 0 \le p_i \le 1, \tag{12}$$

$$\sum_{i=1}^{n} p_i = 1. \tag{13}$$

Shannon entropy was originally introduced for verbal communication; hence, a discrete random variable is involved. A diagnostic symptom in the sense of the energy processor model is in general continuous, so a derivative of H known as *continuous* or *differential entropy* should be used. It is given by (see, e.g., [18])

$$h = -K\int_{-\infty}^{\infty} p(S_i)\log_b p(S_i)dS_i, \tag{14}$$

where $p(S_i)$ is the probability density function. Despite formal similarity, Eq. (14) is not just a limiting case of Eq. (11) for $n \to \infty$. Contrary to H, continuous entropy is not invariant under change of variables [19]. Moreover, h can be negative, although a satisfactory physical explanation of the negative information content is still lacking. From the practical point of view, continuous entropy is very convenient, as for widely employed statistical distributions it is given by relatively simple analytical expressions.

It may be added here that several other entropy types have been proposed, e.g., by Hartley [20], Rényi [16], or Tsallis [21]. Their use, however, has been limited. Hartley entropy is a specific case of the Shannon entropy, while Rényi entropy may be viewed by its generalization. Both Rényi and Tsallis entropies involve certain adjustable parameters of rather unclear physical meanings, which are generally difficult to estimate.

For the purpose of condition symptom evaluation, the time window procedure may be employed. A window containing sufficient number of $S_i(\theta)$ readings is moved along the time axis; for each position, statistical distribution parameters within it are determined, and in this way the $h(\theta)$ curve is obtained. This in turn allows for estimation of the information content measure (ICM) decrease rate. In practice this involves certain problems which shall be discussed in the following section.

3.2. Shortcomings

3.2.1. Distribution type

Obviously, in order to employ the abovementioned procedure, symptom distribution type has to be determined. In general, distributions of diagnostic symptom values are of the right-hand

tailed type [1]. Weibull and gamma distributions are commonly used, with the probability density functions given by

$$f_W(x) = \frac{k}{\lambda^k} x^{k-1} \exp\left(-\frac{x^k}{\lambda^k}\right) \tag{15}$$

and

$$f_G(x) = \frac{x^{k-1}\exp\left(-\frac{x}{\lambda}\right)}{\lambda^k \Gamma(k)}, \tag{16}$$

respectively, where k is the shape factor, λ denotes the scale factor, and Γ is the gamma function. It has been shown for a number of cases [1, 22, 23] that results obtained with these two distributions are quantitatively similar. Moreover, although this might seem strange, normal distribution given by

$$f_N(x) = \frac{1}{\sqrt{2\pi\sigma^2}} \exp\left(-\frac{(x-\mu)^2}{2\sigma^2}\right) \tag{17}$$

(μ and σ denote mean value and standard deviation, respectively) yields very similar results; this greatly simplifies calculations. Continuous entropy for these three distributions is given by the following relations [24]:

$$h_W(x) = \frac{(k-1)\gamma_E}{k} + \ln\frac{\lambda}{k} + 1, \tag{18}$$

$$h_G(x) = \ln(\lambda\Gamma(k) + (1-k)\psi(k) + k, \tag{19}$$

$$h_N(x) = \ln\left(\sigma\sqrt{2\pi e}\right), \tag{20}$$

where γ_E is the Euler-Mascheroni constant and $\psi(x)$ is the digamma function. An example of comparison of results obtained with gamma, and Weibull and normal distributions is shown in **Figure 4**.

3.2.2. Outliers

Diagnostic symptom time histories often exhibit a considerable number of outliers. According to [25], "an outlying observation, or outlier, is one that appears to deviate markedly from other members of the sample in which it occurs"; there is no generally accepted precise definition. From the point of view of information theory, outliers are equivalent to noise. As with the definition, there is no universal method for removing outliers. The "three-sigma rule," which is often used for this purpose, is not applicable to distributions with long right-hand tails [26]. Three-point averaging [27] merely flattens outliers instead of removing them. The author has suggested a procedure referred to as "peak trimming" [1], based on comparison of a data point with two adjacent points. If for the $S_i(\theta_k)$ symptom value reading one of the following criteria is met:

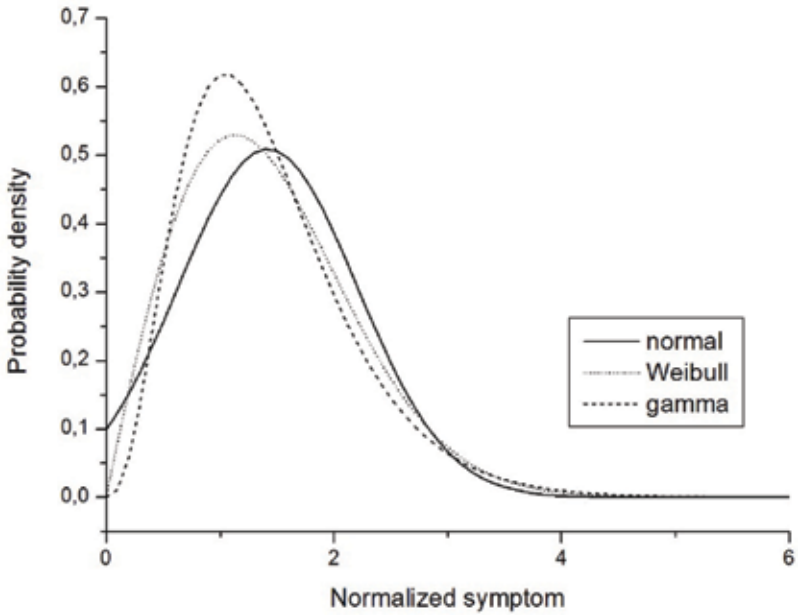

Figure 4. Comparison of distribution fitting results (260 MW steam turbine, vibration component generated by high-pressure fluid flow system—after [23], © JVE Journals).

$$\frac{S_i(\theta_k)}{S_i(\theta_{k-1})} > c_h \quad \text{and} \quad \frac{S_i(\theta_k)}{S_i(\theta_{k+1})} > c_h, \tag{21}$$

$$\frac{S_i(\theta_k)}{S_i(\theta_{k-1})} < c_l \quad \text{and} \quad \frac{S_i(\theta_k)}{S_i(\theta_{k+1})} < c_l, \tag{22}$$

then $S_i(\theta_k)$ is considered as an outlier and replaced by the average of two adjacent readings. Upper and lower thresholds, c_h and c_l, are adjusted experimentally and depend on the object. In practice, situation described by Eq. (21) is much more frequent, mainly as a result of the influence of control parameters and/or interference (cf. Eq. (5)). Very low symptom value readings, as in Eq. (22), are usually caused by plain measurement errors. Effect of peak trimming is illustrated in **Figure 5**.

3.2.3. Stationarity

Fitting continuous distributions to experimental symptom value histograms within the time window limits require at least weak stationarity. This implies that for every symptom S_i mean value and autocovariance must not change with time. In view of the fact that $S_i(\theta)$ has a vertical asymptote at θ_b, this may be considered valid only for $\theta << \theta_b$. As already mentioned, it may be assumed that control and interference (Eq. (5)) are represented by stationary stochastic processes. Therefore, $S_i(\theta)$ may be viewed a trend stationary process, and, if the deterministic trend is removed, what is left is a stationary process [28]. In fact over a hundred years ago, it was pointed out that, in time series analysis, a measure of deviation from trend and not from

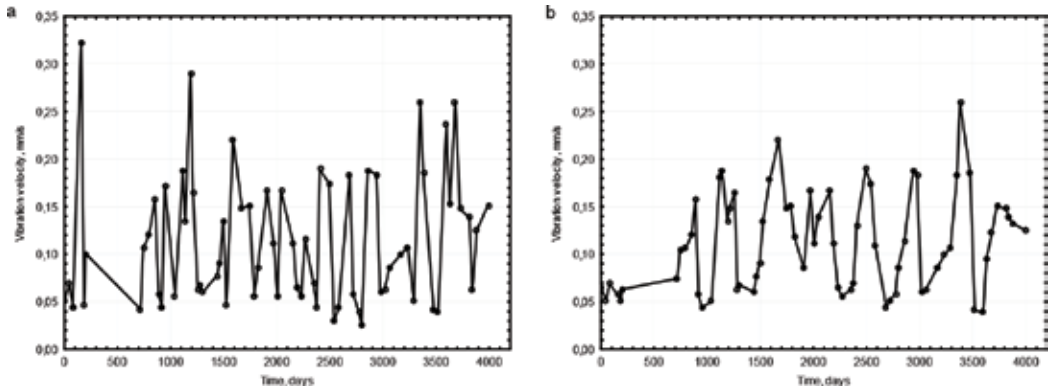

Figure 5. Effect of peak trimming: raw (a) and peak-trimmed (b) symptom time histories. Data refer to the intermediate-pressure turbine of a 260 MW unit.

some "mean" or "average" should be taken into account [29]. In other words, trend normalization should be performed prior to ICM analysis.

Trend may be determined by fitting a suitable function to experimental symptom time history. Weibull and Fréchet functions may be used for this purpose; for low values of θ, exponential function may be a good approximation. An obvious prerequisite is lack of abrupt (stepwise) changes; this issue shall be discussed in detail in the following section. Once this is performed, a procedure may be employed wherein each symptom value reading $S_i(\theta)$ is replaced by trend-normalized value given by [23]

$$S_i'(\theta) = S_i(\theta)\frac{S_{it}(0)}{S_{it}(\theta)}, \tag{23}$$

where subscript t denotes value determined from the estimated trend. An example of trend normalization (Weibull function fitting) is shown in **Figure 6**.

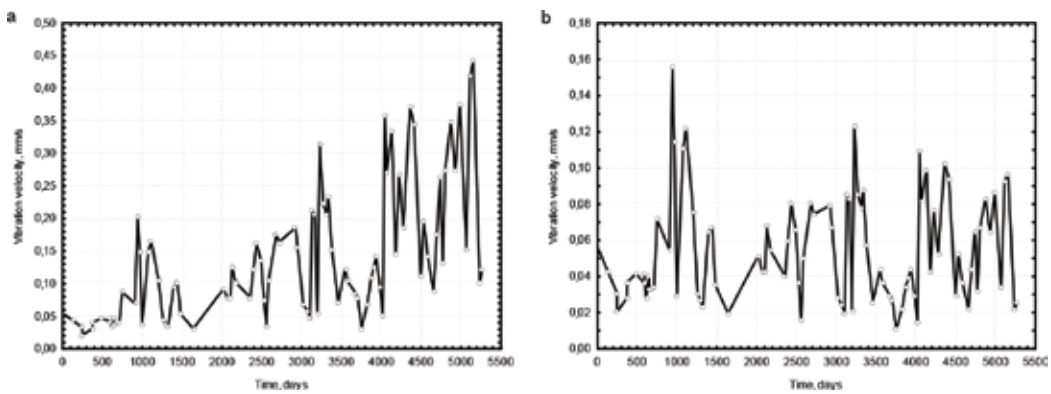

Figure 6. An example of standard peak-trimmed (a) and trend-normalized (b) time histories; data refer to the high-pressure turbine of a 230 MW unit.

3.2.4. Abrupt changes

Complex and costly machines like, for example, power-generating units are usually designed for long service life. During the period between commissioning and final withdrawal from use, they are usually subject to various processes of maintenance, repair, and overhaul. Each of them introduces changes of object properties, which influence both diagnostic symptom generation mechanisms and their propagation from origin to measurement points. So far, it has been assumed (tacitly) that each $S_i(\theta)$ function, or symptom life curve, is a superposition of a monotonic and continuous trend $S_{it}(\theta)$ and random fluctuations. In general this is not the case. Deterministic trend is in fact a sequence of symptom life curves, each being characterized by some specific values of $S_i(0)$ and θ_b. Of course repair or overhaul is performed before the breakdown, so of each curve is represented by a section of the length of $\theta_0 < \theta_b$. This is shown schematically in **Figure 7**.

Figure 7 clearly shows that, if fitting continuous function to experimental data is expected to yield consistent results, abrupt changes should be eliminated. In principle this is relatively simple. Each life cycle and hence each symptom life curve are characterized by the so-called logistic vector [7], which describes its "quality." This vector may be replaced by its scalar measure L, which influences both $S_i(0)$ and θ_b. For a sequence such as shown in **Figure 7**, one cycle is chosen as a reference; it may be convenient to use the one with the lowest initial value for this purpose, but this is not mandatory. Its value for $\theta = 0$ is taken as a reference $S_r(0)$. Then, for each other cycle, a normalizing factor $F_i = S_i(0)/S_r(0)$ is determined, and normalization is obtained by simple multiplication of all symptom readings in this cycle by $1/F_i$.

This idea may seem simple, but precise determination of the moment of transition from a life cycle to the next one may be problematic. Sufficient operational documentation is not always available, and transitions are often masked by random fluctuations. A method for their

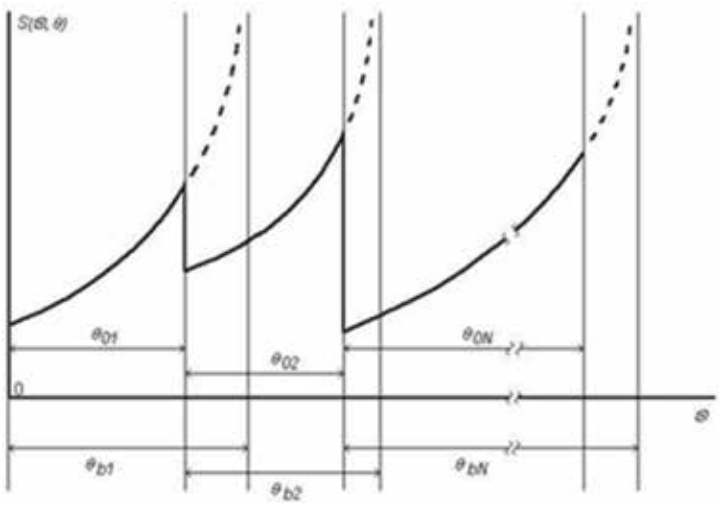

Figure 7. Schematic representation of the symptom life curve sequence.

detection is thus necessary. Such method may be based on techniques originally developed for statistical process control.

In the 1920s Walter A. Shewhart developed a tool for determining whether a process (e.g., manufacturing) is under control, known as the process control chart. If that was the case, no modifications of process or control were needed; otherwise, an intervention was necessary, in order to restore stable and controlled operation [30]. In 1954 E.S. Page proposed a more sensitive process control chart, employing cumulative sum and consequently named CUSUM [31]. His approach consisted in introducing a quantity originally referred to as a "quality number," developing an algorithm to estimate its changes and establishing a quantitative criterion. In general this quality number is a statistical parameter. If this procedure is employed for mean value, it can be used for detecting abrupt changes [32].

Let us assume that a variable x characterizes the process under consideration; its consecutive readings are $x_1, x_2, \ldots, x_N$. Each sample $\langle x_1, \ldots, x_i \rangle$ has a probability density function given by $p_i(x_i, \varphi)$; φ is a parameter which changes from φ_0 to φ_1 when an abrupt change occurs. The log-likelihood ratio c_i given by

$$c_i = \ln \frac{p(x_i, \ \varphi_1)}{p(x_i, \varphi_0)} \tag{24}$$

defines the figure of merit. Cumulative sum C_m is then defined by

$$C_m = \sum_{i=1}^{m} c_i \tag{25}$$

If φ is sample mean, then C_m time history can be used for abrupt change detection. If there is no continuous trend, i.e., the process is stationary, C_m will fluctuate around zero and exhibit an upward or downward drift when an abrupt increase or decrease, respectively, has occurred. As already mentioned, in the case of a diagnostic symptom, there will always be such trend which can be neglected only for $\theta << \theta_b$. Thus, C_m does not fluctuate around zero, but exhibits a continuous trend. An abrupt change, if sufficiently large, will then be indicated by a reversal of the $C_m(\theta)$ trend. This method can be employed for detecting transitions between consecutive life cycles. For normal distribution which, as noted earlier, is often a good approximation, C_m is given by a simple expression:

$$C_m = \sum_{i=1}^{m} (x_i - \mu_0), \tag{26}$$

where μ_0 denotes sample mean. It is easily understood by intuition that, in order to obtain a reliable result, removal of outliers is mandatory [33]. Examples are shown in **Figures 8** and **9**.

3.2.5. Representativeness factor

It may be said, in a descriptive manner, that ICM is a measure of the degree of process organization around a monotonically increasing trend. However, the rate of this increase should also be

http://dx.doi.org/10.5772/intechopen.77264

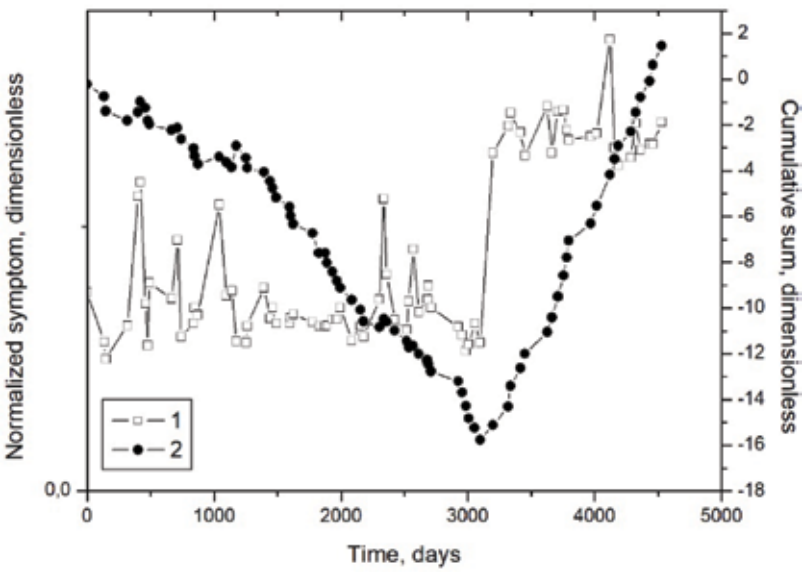

Figure 8. Example of CUSUM method application: normalized symptom (1) and cumulative sum (2) plotted against time. Data refer to vibration generated by high-pressure fluid flow system of a 200 MW steam turbine.

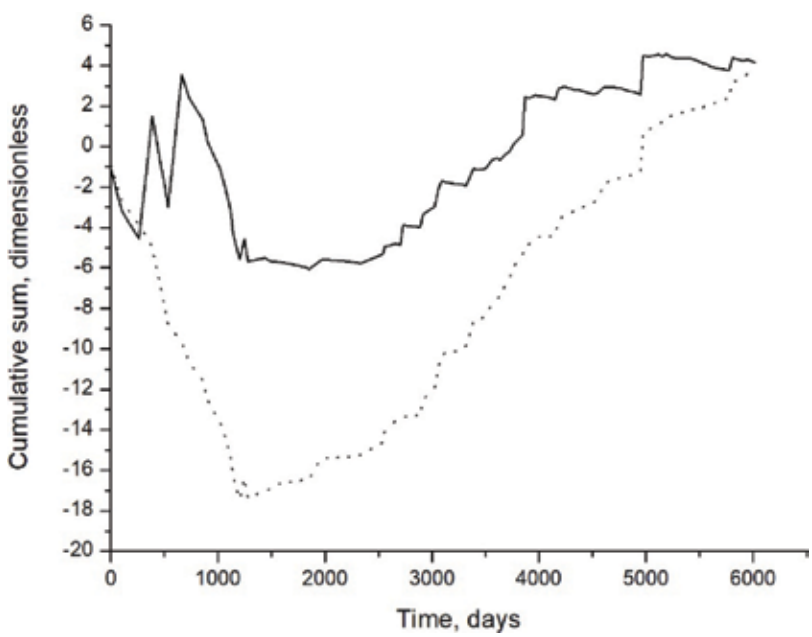

Figure 9. Cumulative sum time history obtained without (solid line) and with (dotted line) outlier removing (after [33], © British Institute of Non-Destructive Testing).

taken into account in symptom evaluation. Organization may take place around a weakly increasing curve; such symptom is only weakly sensitive to object condition evolution and as such is of little use, despite marked ICM decrease. A measure is thus required that would combine *both* sensitivity to condition parameters *and* a degree of process organization [23, 33]. Such measure, termed *representativeness factor R*, is proposed in the following manner. Linear approximation is used for continuous entropy:and Weibull approximation for normalized symptom:

$$h(\theta) \approx h(\theta = 0) - A \cdot \theta \quad (A > 0) \tag{27}$$

$$s_i(\theta) \approx \left[\ln \frac{1}{1 - \theta/\theta_b} \right]^{1/\gamma}; \tag{28}$$

representativeness factor is then defined as

$$R = \frac{A}{\gamma}. \tag{29}$$

Obviously, R should be positive: the larger the R, the more representative is the symptom under consideration. Alternative approach may be adopted for Fréchet approximation; the choice of either of these approximations does not influence qualitative results of symptom assessment.

4. Examples

Measurement data for the first example were obtained with the intermediate-pressure turbine of a 260 MW power-generating unit; the first measurement was performed shortly after commissioning, and available data cover the period of almost 10 years. Vibration velocity was recorded at the front and rear bearings, in three mutually perpendicular directions. Components generated by turbine fluid flow system are contained in four 23% CPB bands, which give 24 available symptoms. Of these, as many as 13 symptoms have revealed no increasing trend; this may be attributed to comparatively short period of operation, as evolution of the fluid flow system condition is usually rather slow. For the remaining 11 symptoms, measured values were normalized, and peak trimming was performed (Eqs. (21) and (22), with $c_h = 1.5$ and $c_l = 0.7$). It was followed by CUSUM analysis, which revealed an abrupt change at about 2200 days (see **Figure 10**). Normalization was thus performed according to the procedure outlined in Section 3.2.4. Trend normalization was based on the Weibull function assumption. Data processed in this manner were used for ICM analysis, with time window length of 25 points and normal distribution assumption (cf. Section 3.2.1).

Continuous entropy time histories are in some cases rather irregular, but nonetheless six of them exhibit a decreasing trend; an example is shown in **Figure 11**. For these six cases, representativeness factor was calculated in accordance with Eq. (29). Results are shown in **Table 1**. It is easily seen that the values of R vary within broad limits. Without doubt symptoms numbered 1 and 2

http://dx.doi.org/10.5772/intechopen.77264

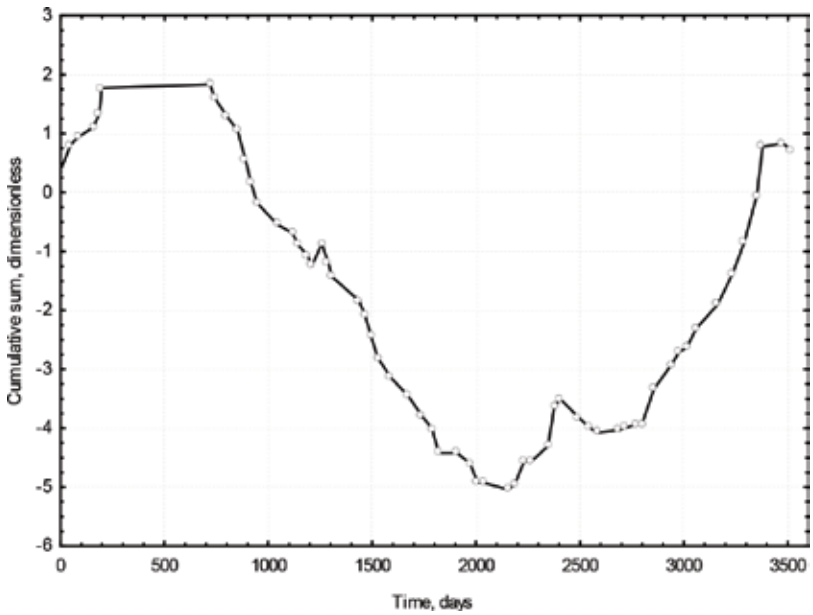

Figure 10. Cumulative sum time history: 260 MW unit, front intermediate-pressure turbine bearing, axial direction, 4 kHz band.

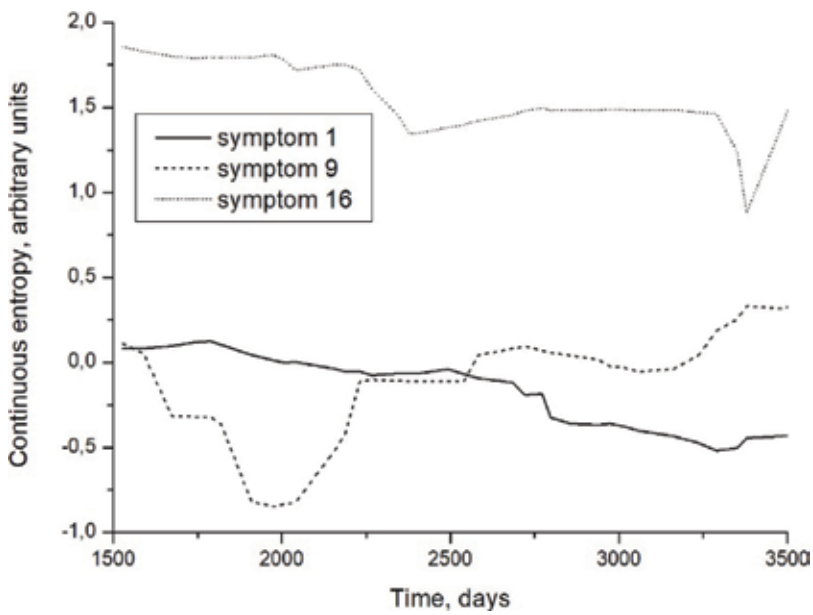

Figure 11. Examples of continuous entropy time histories: for symptoms 1 and 16, entropy is decreasing, while for symptom 9, there is an increasing trend accompanied by large irregularities.

Symptom number	Symptom description (kHz)	Value of γ	Entropy decrease rate	Representativeness factor
1	FB-V 3.15	11.24	0.960	85.44×10^{-3}
2	FB-V 4	10.64	0.905	85.07×10^{-3}
5	FB-H 3.15	500.0	0.010	0.02×10^{-3}
16	RB-V 6.3	52.63	0.775	14.73×10^{-3}
18	RB-H 4	52.63	0.497	9.44×10^{-3}
24	RB-A 6.3	55.56	0.637	11.47×10^{-3}

FB and RB denote the front and rear bearings, respectively; V, H, and A correspond to measurement directions (vertical, horizontal, and radial) (260 MW unit, intermediate-pressure turbine).

Table 1. Results of calculations for six symptoms; γ is dimensionless, and entropy decrease rate and representativeness factor are given in arbitrary units.

are the most representative ones. Symptoms 16, 18, and 24 are certainly inferior, while representativeness of symptom 5 is weak. In this manner, symptoms may be identified that are most suitable for fluid flow system condition assessment.

Figure 12 shows contributions of all 11 symptoms that exhibit an increasing trend into the first three singular values. It may be noted that results are basically consistent with those shown in **Table 1**. The main differences are:

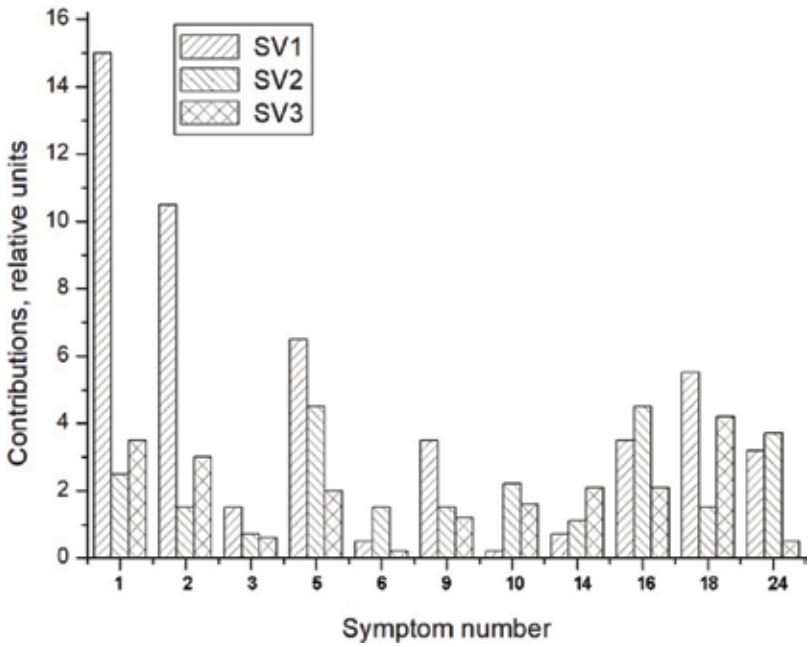

Figure 12. Contributions of individual symptoms into the first three singular values (260 MW unit, intermediate-pressure turbine (only symptoms that reveal an increasing trend have been included)).

- Comparatively high contributions of symptom number 5, which has a low representativeness factor
- Better result for symptom number 18
- Comparatively high contributions of symptom number 9, which is absent in **Table 1** (lack of entropy decreasing trend)

Before commenting on these findings, a second example will follow, this time for a comparatively old 200 MW unit with over 200,000 hours logged; available database covers over 16 years. Fluid flow system of the high-pressure turbine generates vibration components that are contained in ten 23% CPB frequency bands. Given two bearings and three directions, this means that as many as 60 symptoms have to be analyzed. In order to simplify the picture, a two-stage procedure was employed [33]. First, for every measurement point and direction, two dominant symptoms were selected using the SVD approach. Twelve symptoms selected in this manner were then analyzed with both SVD and ICM methods. Results are shown in **Figure 13** and **Table 2**.

In **Table 2**, cases with $R < 0$ have been deliberately included, in order to demonstrate that symptoms with comparatively good rating based on the SVD analysis—in this case, symptom No. 2—sometimes have to be rejected. On the other hand, symptoms with rather high values of R—e.g., numbers 5, 10, and 12—are poorly rated by the SVD method. In fact, only symptom numbers 3 and 4 are chosen on the basis of *both* methods.

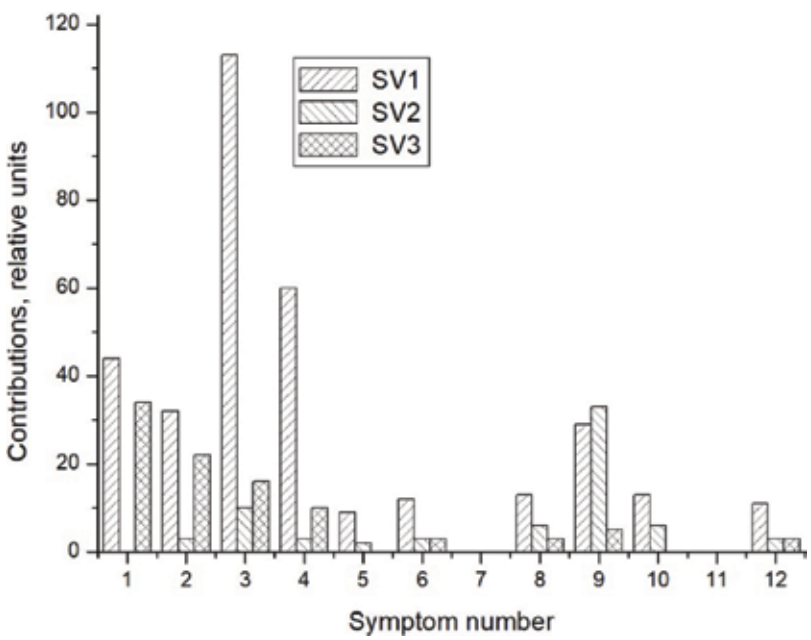

Figure 13. Contributions of individual symptoms into the first three singular values (200 MW unit, high-pressure turbine (after [33], © JVE journals)).

Symptom number	Symptom description (KHz)	Representativeness factor
1	FB-V 6.3	-0.63×10^{-3}
2	FB-V 8	-15.30×10^{-3}
3	FB-H 5	6.97×10^{-3}
4	FB-H 6.3	5.57×10^{-3}
5	FB-A 6.3	8.84×10^{-3}
6	FB-A 8	3.77×10^{-3}
7	RB-V 5	-1.93×10^{-3}
8	RB-V 8	1.17×10^{-3}
9	RB-H 6.3	0.20×10^{-3}
10	RB-H 8	4.14×10^{-3}
11	RB-A 2	-2.52×10^{-3}
12	RB-A 8	5.69×10^{-3}

Table 2. Representativeness factor values calculated for 12 symptoms from **Figure 13** (after [33], © JVE Journals).

In order to comment on these two examples, it has first to be noted that neither SVD nor ICM approach can be considered a reference one. It seems that discrepancies between the results obtained with both may be attributed to at least two possible causes. First, preprocessing of measurement data is based on relatively simple procedures, and their inherent deficiencies—such as inadequate robustness—may influence the final result. Second, the SVD method does not disqualify cases with entropy increase, which are rejected within the ICM approach. This question requires further study. As pointed out in [33], it seems justified to state that symptoms selected on the basis of *both* methods can be safely labeled as the most suitable ones for object condition assessment and prognosis.

5. Conclusions

In this chapter, a relatively straightforward and simple method is presented for evaluation of diagnostic symptoms from the point of view of their suitability for assessment and prognosis of technical condition evolution. For this purpose, the proper choice of symptoms is of prime importance. This is particularly important for complex objects that generate a large numbers of various symptoms. In most cases it is very difficult, or even impossible, to make such choice in a direct manner, even with extensive knowledge on object layout and operation. The proposed method is based on an analysis of an information content measure as a function of time, and the basic assumption is that the greater is general damage advancement, the more deterministic, and hence predictable the symptom becomes. It turns out, however, that in order to obtain reliable results certain preprocessing of measurement data is mandatory. Results of this method have been compared with those obtained from singular value analysis, which had been earlier proposed

and tested. This approach has been applied for vibration-based symptoms of steam turbines operated by power plants and shown to give consistent results. In general it can be applied to any symptom, irrespective of its physical origin, as well as for other machines or structures. In the author's view, possible further development should be concentrated on the preprocessing of measurement data and improvement of the representativeness factor. Other information content measures might also be worth considering; however, the best results have so far been obtained with continuous entropy.

Conflict of interest

The author of this text has no conflict of interest to declare.

Author details

Tomasz Gałka

Address all correspondence to: tomasz.galka@ien.com.pl

Institute of Power Engineering, Warsaw, Poland

References

[1] Gałka T. Evolution of Symptoms in Vibration-Based Turbomachinery Diagnostics. Radom: Publishing House of the Institute for Sustainable Technologies; 2013. 186 p

[2] Randall RB. State of the art in monitoring rotating machinery. Sound and Vibration. 2004, 2004;**3, 5**:14, 10-20 (part 1), 16 (part 2)

[3] Chestnut H. Systems Engineering Tools. New York: Wiley; 1965. 646 p

[4] Vachtsevanos G, Lewis FL, Roemer M, Hess A, Wu B. Intelligent Fault Diagnosis and Prognosis for Engineering Systems. New York: Wiley; 2006. 434 p

[5] Weibull W. A statistical distribution function of wide applicability. Journal of Applied Mechanics. 1951;**18**:293-297

[6] Zhai LY, Lu WF, Liu Y, Li X, Vachtsevanos G. Analysis of time-to-failure data with Weibull model in product life cycle management. In: Nee AYC, Song B, Ong SK, editors. Re-engineering Manufacturing for Sustainability. Singapore: Springer; 2013. pp. 699-704

[7] Cempel C, Natke HG. The modeling of energy transforming and energy recycling systems. Journal of System Engineering. 1996;**6**:79-88

[8] Gałka T, Tabaszewski M. An application of statistical symptoms in machine condition diagnostics. Mechanical Systems and Signal Processing. 2011;**25**:253-265

[9] Cempel C, Haddad SD. Vibroacoustic Condition Monitoring. New York: Ellis Horwood; 1991. p. 212

[10] Orłowski Z, Gałka T. Vibrodiagnostics of steam turbines in the blade frequency range. In: Proceedings of the COMADEM'98 International Conference. Australia: Monash University. pp. 683-692

[11] Gałka T. Vibration-based diagnostics of steam turbines. In: Gökçek M, editor. Mechanical Engineering. Rijeka: InTech Open; 2012. pp. 315-340

[12] Golub GH, Reinsch C. Singular value decomposition and least square solutions. Numerische Mathematik. 1970;**14**:403-420

[13] Natke HG, Cempel C. The symptom observation matrix for monitoring and diagnostics. Journal of Sound and Vibration. 2001;**248**:597-620

[14] Gałka T. Application of the singular value decomposition method in steam turbine diagnostics. In: Proceedings of the CM2010/MFPT Conference, Stratford-upon-Avon, UK. 2010. Paper No. 107

[15] Cempel C. Multidimensional condition monitoring of mechanical systems in operation. Mechanical Systems and Signal Processing. 2003;**17**:1291-1303

[16] Rényi A. On some measures of entropy and information. In: Proceedings of the 4th Berkeley Symposium on Mathematics, Statistics and Probability; 1961. p. 547-561

[17] Shannon CE. A mathematical theory of communication. The Bell System Technical Journal. 1948, 1948;**27, 27**:379, 623-423 (part 1), 656 (part 2)

[18] Ihara S. Information Theory for Continuous Systems. Singapore: World Scientific; 1993. 313 p

[19] Jaynes ET. Prior probabilities. IEEE Transactions on Systems Science and Cybernetics. 1968;**4**:227-241

[20] RVL H. Transmission of information. The Bell System Technical Journal. 1928;**7**:535-563

[21] Tsallis C. Possible generalization of Boltzmann-Gibbs statistics. Journal of Statistical Physics. 1988;**52**:479-487

[22] Schömig AK, Rose O. On the suitability of the Weibull distribution for the approximation of machine failures. In: Proceedings of Industrial Engineering Research Conference, Portland, USA; 2003

[23] Gałka T. A comparison of two symptom selection methods in vibration-based turbomachinery diagnostics. Journal of Vibroengineering. 2015;**17**:3505-3514

[24] Lazo A, Rathie P. On the entropy of continuous probability distributions. IEEE Transactions on Information Theory. 1978;**24**:120-122

[25] Hodge VI, Austin J. A survey of outlier detection methodologies. Artificial Intelligence Review. 2004;**22**:85-126

[26] Maronna RA, Martin RD, Yohai VJ. Robust Statistics. Theory and Methods. Chichester: Wiley; 2006. 403 p

[27] Cempel C, Tabaszewski M. Multidimensional condition monitoring of the machines in non-stationary operation. Mechanical Systems and Signal Processing. 2007;**21**:1233-1247

[28] Nielsen HB. Non-stationary time series and unit root tests [Internet] 2005. Available from: http://www.econ.ku.dk/metrics/econometrics2_05_ii/slides/08_unitroottests_2pp.pdf [Accessed: 2018-02-28]

[29] Yule GU. The applications of the method of correlation to social and economic statistics. Journal of the Royal Statistical Society. 1909;**72**:721-730

[30] Wheeler DJ. Understanding Variation: The Key to Managing Chaos. Knoxville: SPC Press; 2000. 157 p

[31] Page ES. Continuous inspection scheme. Biometrika. 1954;**41**:100-115

[32] Basseville M, Nikiforov IV. Detection of Abrupt Changes: Theory and Application. Upper Saddle River: Prentice-Hall; 1993. 528 p

[33] Gałka T. On the problem of abrupt changes detection in diagnostic symptom time histories. In: Proceedings of the 1st World Congress on Condition Monitoring, London, UK; 2017. Paper No. 122

Chapter 4

Application and Challenges of Signal Processing Techniques for Lamb Waves Structural Integrity Evaluation: Part A-Lamb Waves Signals Emitting and Optimization Techniques

Zenghua Liu and Honglei Chen

Additional information is available at the end of the chapter

http://dx.doi.org/10.5772/intechopen.78381

Abstract

Lamb waves have been widely studied in structural integrity evaluation during the past decades with their low-attenuation and multi-defects sensitive nature. The performance of the evaluation has close relationship with the vibration property and the frequency of Lamb waves signals. Influenced by the nature of Lamb waves and the environment, the received signals may be difficult to interpret that limits the performance of the detection. So pure Lamb waves mode emitting and high-resolution signals acquisition play important roles in Lamb waves structural integrity evaluation. In this chapter, the basic theory of Lamb waves nature and some environment factors that should be considered in structural integrity evaluation are introduced. Three kinds of typical transduces used for specific Lamb waves mode emitting and sensing are briefly introduced. Then the development of techniques to improve the interpretability of signals are discussed, including the waveform modulation techniques, multi-scale analysis techniques and the temperature effect compensation techniques are summarized.

Keywords: Lamb waves, plate, transducers, signal optimization techniques, structural integrity evaluation

1. Introduction

Plate-like structures made with metallic and composite materials have been widely used in various of engineering fields including aerospace and civil engineering. During the manufacturing, processing and usage, various type of damage may be induced in these structures. For

example, corrosion and fatigue cracks are common defects in metal plates, while the main defects in composite plates are delamination, debonding, etc. Thus, it is important to develop defects detection and monitoring techniques to ensure the integrity of plate structures. Lamb waves have multi-modes, full cross-section distribution and low-attenuation nature in plates and can be used for multi-type defects detection in large scale. Combined with modern signal detection instruments and signal processing techniques, there are a lot of research and application of Lamb waves for off-line and on-line structure integrity evaluation [1–3].

Lamb waves are a type of elastic waves that remain the constraint between two parallel free surfaces, such as the upper and lower surfaces of a plate or shell, which contribute both longitudinal and shear partial wave components, as shown in **Figure 1(a)**. According to the particle vibration mode, mainly two kinds of Lamb waves modes are formed as the interaction of longitudinal and shear partial waves, symmetric (S) modes and anti-symmetric (A) modes shown in **Figure 1(b)**. Lamb waves theory, which is fully documented in literatures [4–6], assumes the derivation formula in a cylindrical coordinate of the three-dimensional (3D) waves as

$$\begin{cases} \dfrac{\partial^2\phi}{\partial x^2}+\dfrac{\partial^2\phi}{\partial y^2}+\dfrac{\omega^2}{c_l^2}\phi=0 \\ \dfrac{\partial^2\psi}{\partial x^2}+\dfrac{\partial^2\psi}{\partial y^2}+\dfrac{\omega^2}{c_s^2}\psi=0 \end{cases}, \tag{1}$$

where ϕ and ψ are potential functions, $c_l^2=\left(\lambda+2\mu\right)/\rho$ and $c_s^2=\mu/\rho$ are the longitudinal and shear wave velocities, respectively, λ and μ are the Lamé constants and ρ is the mass density.

Under the stress-free boundary conditions at the upper and lower surfaces, Lamb waves equation can be obtained with the separation variable solution method

$$\frac{\tan\beta d}{\tan\alpha d}=-\left[\frac{4k^2\alpha\beta}{\left(k^2-\beta^2\right)^2}\right]^{\pm1}, \tag{2}$$

where d is the half thickness of plates, k is the wavenumber, $k^2=\omega^2/c_p^2$, c_p is the phase velocity, $\alpha^2=\omega^2/c_l^2-k^2$, $\beta^2=\omega^2/c_s^2-k^2$. The plus sign corresponds to symmetric vibration and the minus to anti-symmetric vibration. A series of eigenvalues k_i^S and k_i^A corresponding various Lamb waves mode shapes are obtained by solving Eq. (2). The S modes and A modes are denoted with S_i and A_i, respectively, where the subscript i indicates the order of the modes and equals 0,1,2…. The relationship $c_p = \omega/k$ yields the dispersive wave velocity which is a function of the product between the frequency and the plate thickness. The wavelength is defined as $\lambda = c_p/f$. The group velocity, c_g, can be derived from the phase velocity with

$$c_g=c_p^2\left(c_p-fd\frac{\partial c_p}{\partial(fd)}\right)^{-1}. \tag{3}$$

Figure 1(c) and **(d)** shows dispersion curves of Lamb waves in an aluminum plate drawn with DISPERSE. The mechanical property of the plate is defined as: the density is 2.7 g/cm^3,

http://dx.doi.org/10.5772/intechopen.78381

Young's module is 70.753 GPa and Poisson's ratio is 0.33. It is easy to find that the particle vibration show out anti-symmetric and symmetric forms for A modes and S modes, respectively. As shown in **Figure 1(c)** and **(d)**, there are at least four modes under the frequency-thickness 8.0 MHz-mm including the fundamental modes (A_0 and S_0). The group velocities and the wavenumbers change with frequency for these Lamb waves modes, termed the dispersion nature of Lamb waves.

Defects in structures induce the scattering profiles and cause the change of the velocity and attenuation in the magnitude of Lamb waves signals. Besides the defects, there are still many other factors may induce the vibration, interpretability of the received Lamb waves signals in structural integrity evaluation. These factors are the Lamb waves nature, the property of transducers and plate structures, the environmental and operational conditions. Some of the influence by these factors is expressed below.

1. Dispersion of Lamb waves complexes the received signals that induce the signals extension in both spatial and temporal domain; multi-modes of Lamb waves and echoes from the multi-defects cause the waveform overlapping in received signals.

2. Property of the transducers influences the performance of Lamb waves signals and the wavefield, such as the disk-wrapped electrode induces the non-axisymmetric wavefield [7], signal amplitude variation with a different type of adhesive and PZT thickness effects

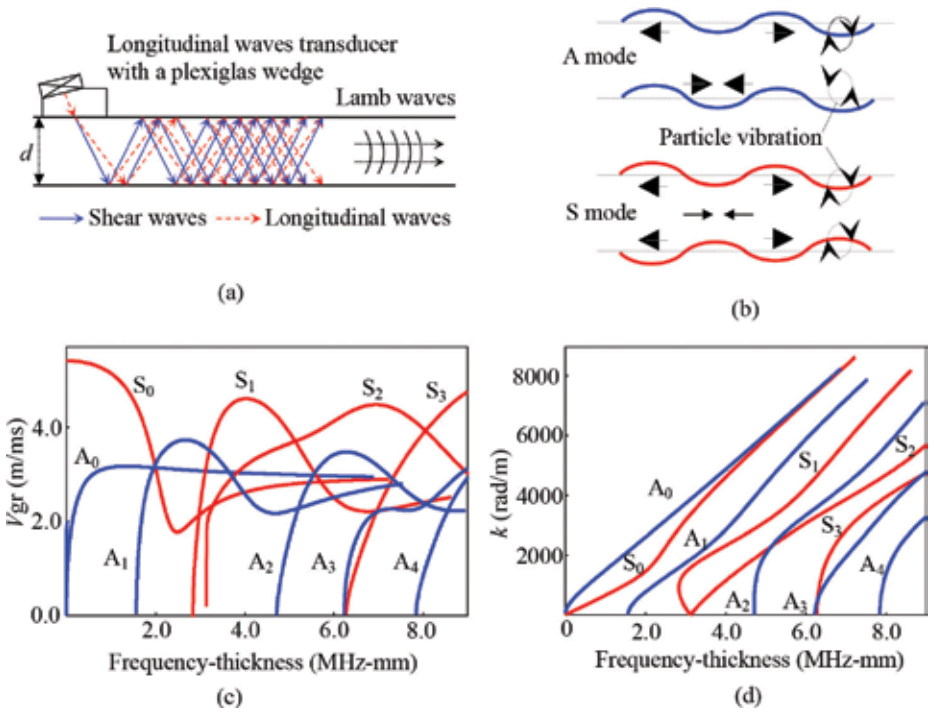

Figure 1. Characteristic of Lamb waves in an aluminum plate drawn with DISPERSE. (a) Oblique incidence method for Lamb waves generation; (b) vibration property of Lamb waves; (c) group velocity dispersion curves; (d) wavenumber dispersion curves.

[8], Lamb waves signals emitted with the laser beam and PZT show non-stationary and stationary property, respectively.

3. Material and structure of plates yield the wavefield, such as anisotropic property of composite plates leading the inhomogeneity distribution of wavefield in spatial and temporal dimensions [9, 10], echoes from the edges, stiffeners, bolts and rivets in the complex structure reduce the interpretability of the received Lamb waves signals [11].

4. Environmental and operational condition change the material properties and further influence the emitting, propagation and the sensing of Lamb waves [12, 13], typically the temperature and the local concentrated stress. The temperature changes (a) the plate material stiffness affects the waves phase/group velocity [14, 15]; (b) the dielectric permittivity and piezoelectric coefficient of piezoelectric transducers [16] and (c) the adhesive stiffness and then modifies the transducer-plate bonding shear stress transmission and minor thermal expansion/contraction occurring within the adhesive layer can yield to a slight shift in the peak frequency response [17]. The variation of the loads during usage changes resulting a slight anisotropy of the structure and further induces the velocity directionality [18]. Meanwhile, it also induces the time shifts effect under loads conditions that are of the same order as those caused by temperature change.

As illustrated in the above content, the factors influencing signals features, the environmental and operation condition, Lamb waves, transducers, plate-like structures and the defects are combined and form a close detection/monitoring ecosystem in which the transducers realize the energy conversion between the systems and the structures. Meanwhile the properties of transducers have influence on the detection/monitoring systems setting strategies and the emitting and sensing of Lamb waves. All these have decided that transducers play a very important role in structure integrity evaluation. Signal processing technologies are adopted to optimize and analysis the acquired data and finally realize structure state evaluation. When the received data have relatively high resolution and interpretability, defects imaging techniques and the intelligent recognition techniques are directly applied for structure integrity evaluation; otherwise, the signals should be pre-processed with signal optimization techniques to improve their resolution and interpretability through modulating waveforms, multi-scale analysis and temperature effect compensation. Considering the importance roles of transducers and the signal processing strategies used in Lamb waves based structure integrity evaluation, the structure of this chapter is setting as: Section 2 introduces several kinds of transducers used for Lamb waves emitting and sensing. Then some signal processing technologies for dispersion compensation, time-frequency analysis and overlapping waveform decomposition, and illuminating the influence temperature effects are briefly reviewed in Section 3. Finally, a short summary and conclusions are provided.

2. Transducers and specific Lamb wave mode emitting

There are mainly three kinds of transduction mechanism used for the design of the transducers in structure integrity evaluation, including piezoelectric effect, electromagnetic ultrasonic coupling mechanisms and laser thermodynamics. In this section, we will briefly review some

http://dx.doi.org/10.5772/intechopen.78381

typical transducers and their application for specific mode of Lamb waves emitting and sensing.

2.1. Piezoelectric transducers

Piezoelectric materials have piezoelectric effect that can be used to achieve energy conversion between mechanical energy and electrical energy. As shown in **Figure 2(a)**, when the piezoelectric material is loaded with an alternating voltage, it may produce an oscillatory mechanical vibration, and form pressure at its surface or sound waves in the around air. Vice versa, an oscillatory expansion and contraction of the material produce an alternating voltage at the terminal. This phenomenon is named as the piezoelectric effect. The geometry size, polarization direction and the voltage frequency have influence on the vibration mode of the piezoelectric materials. Many kinds of piezoelectric transducers have been designed in laboratories and corporations.

Piezoelectric wafer active transducers (PWATs) have relative simple round or rectangle geometrical shapes. Typically, these transducers have electrodes on the top and bottom surfaces as plotted in **Figure 2(b)**. With the piezoelectric effect, PWATs actuate and sense Lamb waves signals in the structure directly through in-plane strain coupling. More differences between the PWATs and conventional ultrasonic transducers are listed in Ref. [19]. Interdigital transducers (IDTs) have electrodes shaped in a comb pattern that are designed with traditional piezoelectric ceramics or the novel piezoelectric materials, such as macro-fiber composite (MFC) [20] and poly vinylidene fluoride (PVDF) piezoelectric polymer film [21–23]. **Figure 2(c)** plots an interdigital transducer. Through adjusting the space between adjacent interdigital electrodes, IDTs are able to generate Lamb waves with a specific wavelength. Comparing with the piezoelectric ceramics, the novel piezoelectric materials feature better flexibility, higher dimensional stability and more stable piezoelectric coefficients over time. They can be of various shape to cope with curved surfaces for signal sensing in low frequency range due to their weak driving. The tunable IDTs have a series of density distributed discrete electrode stripes that are connected in various configurations [24]. In the application, Lamb waves with different wavelengths can be emitted through adjusting the configuration of the interdigital electrodes. As shown in **Figure 2(d)**, air-coupled ultrasonic transducers [25] are often used for non-contact

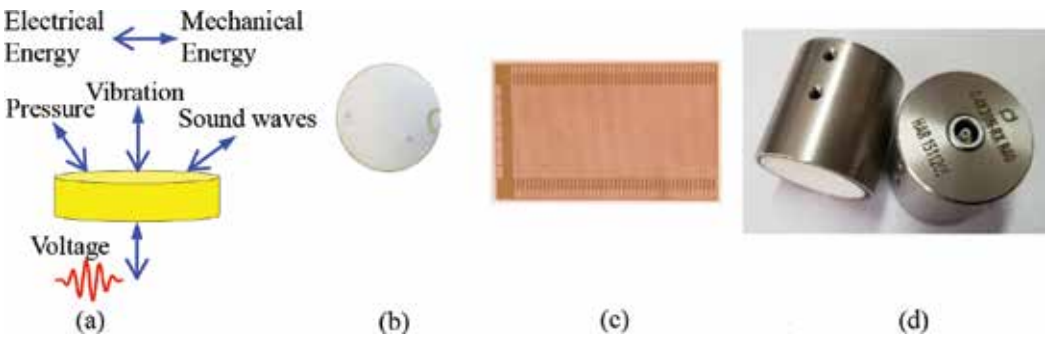

Figure 2. Typical piezoelectric effect-based transducers. (a) Piezoelectric effect; (b) PWAT; (c) Interdigital transducer; (d) air-coupled transducers.

and non-contaminating ultrasonic scanning detection. The proportion of the ultrasonic energy transmitted through an interface depends on the acoustic impedance match ratio of the two materials. The higher match ratio, the more energy is transmitted into the plates. Thus, it is important to minimize these losses to obtain an acceptable signal to noise ratio. With the development of micro-electro-mechanical technology, micro-machined ultrasonic transducers are researched [26] that have many advantages over conventional ultrasonic transducers, including miniature size, low power consumption and the ability to create one-dimensional (1D) and two-dimensional (2D) array structures.

The techniques for pure mode emitting and sensing have been studied with the piezoelectic transducers. Theoretical models researches of PWATs [27] show that the displacements at the plate surface is a function of an interelement distance for a specific Lamb waves mode. With the theory, dual-element transducers are placed at a specific distance on the same surface of a plate for pure A_0 mode emitting, or two dual PZTs (concentric disc and ring) structure is adopted to tune the excitated signal properly for specific mode emitting, or to decompose both mode contributions in the received signals [28]. The IDTs can realize pure mode emitting by adjusting the interspace between individual electronic elements of the piezoelectric array or adding backing materials to the elements [29]. While the interaction between individual elements may have a significant influence on the performance of the IDTs, these effects cannot be neglected even in the case of low frequency excitation. Researchers deposited symmetrical transducers on both sides of the plate to generate pure Lamb waves mode [30], in which for electric symmetrical connection to the two transducers, S_0 mode is generated, vice versa, for the anti-symmetrical electric connection, A_0 mode is strong and S_0 mode is suppressed. Degertekin et al. [31] added hertzian contacts between the plates and the end of specially designed quartz rods, which guide anti-symmetric modes generated by PZT-5H transducers bonded at their other end. For an angle beam transducer, a low-attenuation Lamb waves mode was generated by setting the incidence angle [32]. Other literatures studied theoretical model of the PWAS-related Lamb waves to identify the single mode emitting frequency, then adopted the post-process technique, such as time reversal, to enhance the mode purity [33, 34]. As the symmetric modes have more energy components in the out-of-plane direction, air-coupled ultrasonic transducer can be very suitable for pure A_0 mode emitting and sensing [35]. The high-order or high frequency-thickness Lamb waves have more complex wave structure and shorter wavelength, while more sensitive to the characteristic change of plates. Higher Order Mode Cluster (HOMC) is proposed by Jayaraman et al. [36], it used the nature that multiple modes concentrate together to form a cluster. Khalili et al. [37] realized single Lamb waves mode emitting at 20 MHz-mm with the HOMC method.

2.2. Electromagnetic acoustic transducer

Electromagnetic acoustic transducer (EMAT) consists of permanent magnets, coils and a metal material in which the magnets introduce the static magnetic field. The principle of the electromagnetic ultrasonic coupling mechanisms is shown in **Figure 3(a)**. When the current is loaded on the coils, eddy currents will be generated in the conductive structure and form three kinds of electromagnetic coupling mechanisms for ultrasonic waves emitting and sensing: Lorentz

http://dx.doi.org/10.5772/intechopen.78381

force, magnetostriction mechanism and magnetizing force. In addition, Lorentz force mechanism exists in all conductive materials, whereas the magnetostriction mechanism only exists in ferromagnetic materials. Compared with the other two mechanisms, the magnetizing force is very weak and is often neglected in studies. Various types of EMAT can be designed by changing the configuration of the permanent magnet and coil to realize easily the attenuation of pure Lamb waves mode. **Figure 3(b)** shows the EMAT with solenoid sensing coils and a cylindrical magnet; **Figure 3(c)** shows the Panametrics E110-SB EMAT developed by OLYMPUS.

By adjusting the spacing of meandered line coils equal to the half wavelength of Lamb waves, EMAT can easily realize Lamb waves emitting and sensing at specific frequency. Meanwhile, researchers have developed many kinds of EMATs through specific design of the geometry and the position of the magnets and coils [38], including omnidirectional S_0 mode EMAT [39], omnidirectional A_0 mode EMAT [40] and directional magnetostrictive patch transducer [41]. While the EMAT is difficult to generate a pure Lamb wave mode when dispersion curves of several modes are close together; however, by narrowing the frequency bandwidth via a large number of cycles in the excitation signal, pure mode generation via an EMAT is shown to be possible even in areas of closely spaced modes [42]. Experimentally, the EMAT can scan along the surface, while the loading voltage is often very high compared with that of piezoelectric transducers. EMATs are also used for high-order Lamb waves emitting and sensing in a 6mm-thick steel plate [43].

2.3. Laser ultrasonic systems

Laser ultrasonic systems (LUS) have three basic functional components: a generation laser, a detection laser and a detector. The generation laser emits a laser beam that irritates on the surface of plates to generate ultrasonic waves based on thermoelastic regime or ablation regime. In the thermoplastic regime, the ultrasonic waves are generated from the thermoelastic

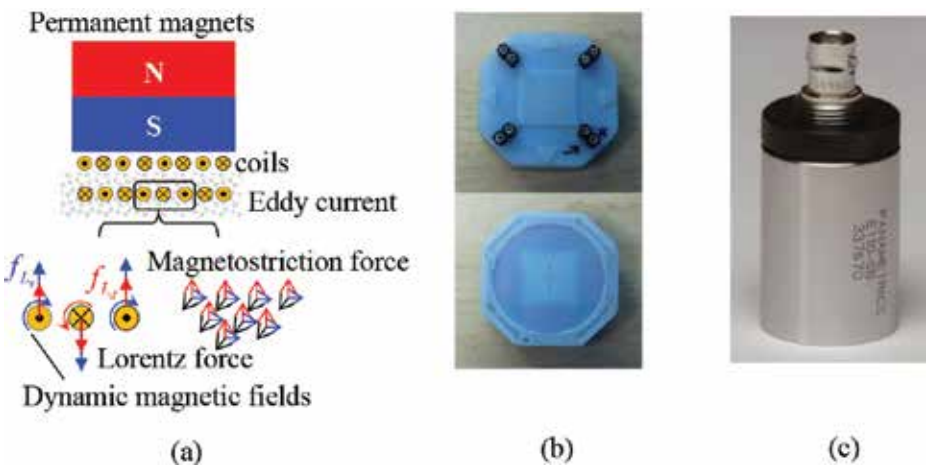

Figure 3. Electromagnetic ultrasonic coupling mechanisms transducers. (a) Principle of the electromagnetic ultrasonic coupling mechanism; EMAT with four solenoid sensing coils and a cylindrical magnet [43]; Panametrics E110-SB EMAT.

expansions of materials. While, in the ablation regime, the ultrasonic waves are generated from the material removal that will induce damage to the surface of plates. The laser ultrasonic systems are carefully set to work in the thermoelastic regime in Lamb waves integrity evaluation. Additionally, the laser-generated Lamb waves signal is a broad bandwidth signal in which several Lamb wave modes can be acquired in a single measurement, providing more opportunities to selectively generate the desired modes. **Figure 4(a)** plots the elastic waves generated by laser beam under thermoelastic regime.

The detection laser and detector are used for ultrasonic waves detection based on various principle including Doppler frequency shift, speckle interferogram and Fabry-Pérot detection schemes. A laser vibrometer principle of operation allows for measuring velocity of a point along the axis of laser beam incidence onto the surface based on the Doppler frequency shift principle. In 1997, researchers started sensing the out-of-plane displacements of Lamb waves with an optical fiber Michelson interferometer. The progress in the development of equipment related to scanning laser Doppler vibrometry (SLDV) resulted in the availability of the full wavefield measurements of Lamb waves propagating in metallic specimens. Shearography is an interferometric technique for surface vibration measurement. In a digital shearography system, the inspected object is illuminated by an expanded laser beam, forming a speckle pattern. The speckle patterns are optically processed by a shearing device, and the resultant interferogram is recorded by a charge-coupled device camera. Speckle interferogram, recorded before and after object deformation, are correlated to yield correlation fringes. The phase of these fringes can represent the displacement gradient of the specimen. More detail information about the system is introduced in Ref. [44]. The elastic waves generate a change in the index of refraction of the surface, incident laser beams will deflect slightly and thus change course. This detected change is converted into an electrical signal. **Figure 4(b)** plots the laser ultrasonic principle.

As the laser beam is irritated on the normal direction of the out-of-plane that is the main displacement components of anti-symmetric modes. In the detection process, people can adjust the shape and the spatial distribution of the laser beams to reduce the energy loss and further form a specific modes wave. Many types optical path adjusting elements are adopted for specific Lamb waves mode emitting, including Fresnel lens, rectangular cylinder lens [45, 46], marks for creating predetermined spatial laser light distributions [47] and periodic spatial array of laser sources [48]. The interference pattern of two high power laser beams on a sample surface produces periodic heating and then generating anti-symmetric Lamb waves [49]. By

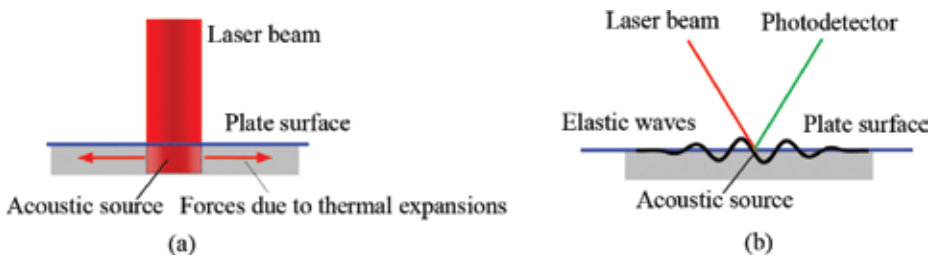

Figure 4. Principle and systems for laser ultrasonic inspection. (a) Elastic waves generated by laser beam under thermoelastic regime; (b) laser ultrasonic principle.

varying the interface fringe spacing, the acoustic frequency is easily and continuously tunable from 2.5 to 23 MHz.

Other transducers used in structural integrity evaluation but not just piezoelectric ceramic fibers, fiber optic transducers [50] and microelectronic transducers. Piezoelectric fibers having a metal core can activate Lamb waves in composite plates transverse to the fibers with radial displacement components originating from the d_{33} coupling coefficient. They can also generate Lamb waves in the direction of the piezoelectric fibers using the d_{31} coupling coefficient. The fiber optic transducers are used for Lamb wave sensing, through connecting a fiber Bragg gratings (FBG) filter with a photodetector, the light intensity induced by the Lamb waves, rather than strain itself, can be sensed at a high sampling rate. The FBG has strong directivity in sensing Lamb wave signals.

3. Signal optimization techniques

The signal processing techniques for improving the resolution and the interpretability of Lamb wave signals are termed as the signal optimization techniques in this section. There are waveform modulation techniques such as multi-scale analysis techniques and temperature effect compensation techniques. These techniques are adopted for Lamb waves dispersion compensation, high-resolution signal emitting and sensing, overlapping waveforms decompensation, time-frequency analysis and temperature effect compensation.

3.1. Waveform modulation techniques

When an excitation signal, $f(t)$, is emitted into a plate at original position, the received signal, $u(x,t)$, at x position can be expressed as

$$u(x,t) = \frac{1}{2\pi}\int_{-\infty}^{\infty} F(\omega)e^{j(\omega t - kx)}d\omega, \tag{4}$$

where $F(\omega)$ is the Fourier transform of the excitation signal and k is the angular wavenumber. In Eq. (4), there are several parameters that decide the signal resolution and interpretability, including the amplitude, phase and frequency variation with the duration. The signal processing techniques process through modulating these fundamental signal parameters for adjusting the signal waveforms are termed waveform modulation techniques that are used for Lamb waves dispersion compensation, high-resolution Lamb waves detection and defects information extraction in structural integrity evaluation.

Signal processing techniques for dispersion compensation are realized through modulating the frequency or the wavenumbers of the received Lamb waves signals, because the dispersion nature of Lamb waves is shown as the nonlinear characteristic of signal phase in mathematical form. Time recompression technique [51] compensates the dispersion using spatial phase shift arising at each signal frequency component from the propagation of the waves over a large distance. The back-propagation function in the technique can only provide the first-order phase shift. Time-distance mapping technique [52] compresses dispersive signals by converting the

signals in frequency domain to a specific propagation distance by back-propagating signals to t = 0 using the known dispersion relation. Considering the relationship between the angle frequency ω and the wavenumber, backward Lamb waves of Eq. (4) at x can be expressed as

$$u_b(-x) = \frac{1}{2\pi}\int_{-\infty}^{\infty} U(\omega)e^{jkx}d\omega = \frac{1}{2\pi}\int_{-\infty}^{\infty} U(\omega)c_g(\omega)e^{jkx}dk, \tag{5}$$

where ω_0 is the specific frequency and $U(\omega)$ is the Fourier transform of the original received signal, $u(x,t)$.

Beside interpolating G(ω) and $c_g(\omega)$, the variables in spatial-wavenumber domains in time-frequency domains are needed to ensure the calculation accuracy. Spectral warping technique [53–55] was applied for the removal of dispersion from a signal in time-space domain using frequency transformation. The rescaling is defined mathematically by a composition of the signal spectrum with a function closely related to the dispersion relation that is independent of propagation distances and can be applied to signals consisting of multiple arrivals with the same dispersion characteristics. The wideband dispersion reversal technique [56], as expressed in Eq. (6), makes use of a priori knowledge of the dispersion characteristics to synthesize the corresponding dispersion reversal excitations, which is able to selectively excite the self-compensation pure mode waveforms.

$$\begin{aligned}\mathrm{WDR}[u(\tau_0 - t)] &= \frac{1}{2\pi}\int_{-\infty}^{+\infty} U(-\omega)e^{-j\omega\tau_0}\cdot H'(\omega)e^{j\omega t}d\omega \\ &= \frac{1}{2\pi}\int_{-\infty}^{+\infty} F(-\omega)\cdot H'(-\omega)\cdot H'(\omega)e^{j\omega(t-\tau_0)}d\omega \\ &= \frac{1}{2\pi}\int_{-\infty}^{+\infty} F(-\omega)e^{j\omega(t-\tau_0)}d\omega \\ &= f(\tau_0 - t),\end{aligned} \tag{6}$$

The above-mentioned algorithms are limited in practical application as the propagation distance may be unknown. Wavenumber curves linearization technique [57, 58] uses the first- or second-order Taylor expansion to linearize the nonlinear wavenumber. It is independent on the propagation distance and can be applied to the signals constructed with multiple arrivals with the same wave mode or dispersion characteristics. It has less computation efforts than the time-distance mapping technique. With the idea of nonlinear wavenumber linearization, Cai et al. [59] extended the wavenumber linearization technique and developed the linearly dispersive signal construction and non-dispersive signal construction method these are expressed as

$$\begin{aligned}u_{\mathrm{lin}}(t) &= \frac{1}{2\pi}\int_{-\infty}^{\infty} M(\omega-\omega_c)e^{-i[k_0+k_1(\omega-\omega_c)]x+i\omega t} \\ &= \frac{e^{i\omega_c t-ik_0x}}{2\pi}\int_{-\infty}^{+\infty} M(\omega)e^{-i\omega k_1x+i\omega t}d\omega \\ &= m(t-k_1x)e^{i\omega_c t-ik_0x} \\ &= f(t-k_1x)e^{i(k_1\omega_c-k_0)x},\end{aligned} \tag{7}$$

where τ_0 is a time delay constant, $M(\omega\text{-}\omega_c) = u(\omega)$ is the Fourier transform result of the amplitude modulation function with shift ω_c, ω_c is the center frequency of the excitation,

$k_0 = \omega_c/c_p(\omega_c)$, $k_1 = dk_0/d\omega|_{\omega=\omega_c} = 1/c_g(\omega_c)$, $H(-\omega) = e^{-ik(-\omega)x}$ is the phase spectrum of the dispersion function and $K_0(\omega)$ is the wavenumber that determines the dispersion relation of Lamb waves mode. The above-mentioned techniques are performed with the received Lamb waves signals that can be named as the post-processing dispersion compensation techniques and more detail process of them are introduced in Refs [51–53, 57–60].

The other signal processing strategy for high-resolution detection is realized through modulating the waveform of excitation signals, termed the excitation modulation techniques, in which the excitations are built based on the dispersion characteristics of Lamb waves, the propagation distance and the travel time [61] or utilize the chirp technique to established effects on the original excitation signal for a given compensation distance, and thus the response extraction and the dispersion compensation can be made simultaneously [62]. For pulse compression (PuC) techniques, a δ-like wave packet can be generated with a broader auto-correlation of a specific waveform including linear chirp signal, nonlinear chirp signal, Barker code and Golay complementary code. The linear chirp has the smallest main lobe width, corresponding to the best inspection resolution; the nonlinear chirp and Golay complementary code are with smaller sidelobe level, corresponding to the better performance in terms of side lobe cancelation [63], and the waveform comparisons are still effective with small errors in dispersion compensation. Malo et al. [64] presented a 2D compressed analysis, which combines pulse compression and dispersion compensation techniques in order to improve the SNR, temporal-spatial resolution and extract accurate time of arrival of responses. Yücel et al. [65] utilizes maximal length sequence (MLS) signals to produce a brute-force search-based dispersion compensation and cross-correlation for defects location. Compared with a linear broadband chirp, the technique using MLS combined with cross-correlation can improve SNR and facilitate the accurate extraction of time-of-flight (ToF), even in complex multimode situation. Marchi et al. [66] proposed a code division strategy based on the warped frequency transform. In the first, the proposed procedure encodes actuation pulses using Gold sequences. Then for each considered actuator, the acquired signals are compensated from dispersion by cross-correlating the warped version of the actuated and received signals. Compensated signals from the base for a final wavenumber imaging meant at emphasizing defects and/or anomalies by removing incident wavefield and edge reflections. Hua et al. [67] proposed pulse energy evolution method for high-resolution Lamb wave inspection. Some conclusions were obtained as follows. Linear chirp signal combined with pulse compression provides a δ-like excitation with a high signal-to-noise ratio. By the application of dispersion compensation with systemically varied compensation distances, an evolution of compensation degree curve can be obtained to estimate the actual propagation distance of the interested wave packet.

Time reversal (TR) technique can focus the elastic waves to its original shape by time-domain reversal of the received signal with the reciprocity principle. **Figure 5** shows the principle diagram of time reversal technique that consists of the forward propagation and backward propagation. In the forward propagation, a signal, $f(t)$, is emitted into the plate by the transducer A, and received by transducer B. Then received signal is reversed in time domain and reemitted by the transducer A in the backward propagation process. The final TR processed result is received signal at transducer B. To avoid the inconvenience in the process of classical time reversal, a pure numerical signal process technique for TR technique is developed, termed the virtual time reversal technique, and can be expressed as

$$f_{\mathrm{TR}}(t) = \mathrm{ifft}\left\{ \mathrm{fft}[u(-t)] \frac{\mathrm{fft}[u(t)]}{\mathrm{fft}[f(t)]} \right\}, \tag{8}$$

where $f(t)$ is the excitation signal, $u(t)$ is the original received Lamb waves signal, $u(-t)$ is the time reversal result of signal of $u(t)$, $f_{\mathrm{TR}}(t)$ is the time reversal result, fft and ifft are the fast Fourier transform and its inverse transform.

It has been studied for dispersed compression [60, 68] and defects information extraction [69, 70]. Zeng et al. [70] carefully designed the amplitude of the input signal before the time reversal process. Huang et al. [71] used a weight vector to modulated the signal in both the forward and backward processes, the vector is obtained as the product of the reciprocal of amplitude dispersion and a window function that varies with the excitation signal adaptively, and its shape is also determined by a threshold. The advantages of single mode tuning in the application of time reversal damage detection are highlighted in Refs. [33,71]. The adhesive, host plate, transducer and excitation parameters are also influenced on the performance of time reversibility of Lamb waves.

3.2. Multi-scale analysis techniques

Multi-scale analysis techniques map a 1D signal into a high dimensional space with transform based on a kernel function, including short-time Fourier transform (STFT), Wavelet transform (the continue wavelet transform (CWT), the discrete wavelet transform (DWT) and wave packet transform), Gabor transform [72], Chirplet transform [73] and asymmetric Gaussian Chirplet transform [74, 75]. When the mapping data space express the changing frequency of the signal parameters, the algorithm can be used for time-frequency analysis [76]. In other case, the mapping data space indicates the inner product between the signal and a kernel function, the algorithm can be used for Lamb waves mode identification and overlapping waveforms decomposition. The formula of STFT and CWT can be expressed as Eq. (9) and Eq. (10), respectively.

$$y(\omega, \tau) = \int_{-\infty}^{+\infty} u(t) w(t-\tau) e^{-j\omega t} dt, \tag{9}$$

$$y(s, \tau) = \frac{1}{\sqrt{s}} \int_{-\infty}^{+\infty} u(t) \psi^* \left(\frac{t-\tau}{s} \right) dt, \tag{10}$$

where $w(t)$ is the window function, commonly a rectangle window, Hanning window or Gaussian window; $u(t)$ is the sensing Lamb waves signal, ψ is the mother wavelet, τ is the shift step in time-axis, s is the scale and * indicates the complex conjugate operation.

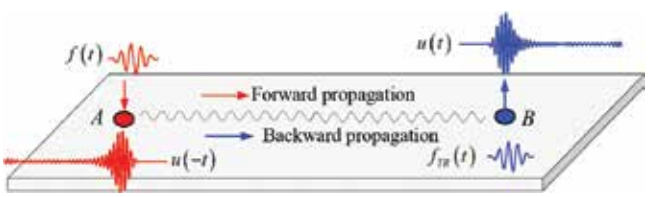

Figure 5. Principle diagram of time reversal technique.

http://dx.doi.org/10.5772/intechopen.78381

STFT divides a signal into blocks with fixed window width that controls the trade-off of bias and variance. Shorter window leads to poor frequency resolution, while longer window improves the frequency resolution but compromises the stationary assumption within the window. Thus researchers adopted variable window width instead of constant-width [77, 78] into the STFT to deal with the local resolution requirement. CWT projects a signal into a class of kernel function, termed mother wavelet, that usage of scale factor that is inversely proportional to the frequency of the given signal. Limited by the Heisenberg uncertainty principle that can be briefly described as the time-frequency windows have constant area, its results have higher frequency resolution and lower time resolution for lower frequency components, while have lower frequency resolution and higher time resolution for higher frequency components. Meanwhile the frequency resolution at the same scale level cannot be adaptively adjusted. The time-frequency representation concentration cannot be significantly improved for non-stationary signal with rapidly time-varying frequency component with the STFT and CWT. Reassignment method is a post-processing technique putting forwards to improve the readability of time-frequency representation. Through assigning the average of energy in a domain to the gravity center of these energy contributions, the reassignment technology reduces energy spread of time-frequency representation at the cost of greater computational complexity. However, it is sensitive to the noise, and inevitably introduces interference terms since the computed gravity center unnecessarily represents the real energy distribution of the interested signal. Wigner-Ville distribution (WVD) is a representative of bilinear time-frequency analysis in which the process is based on the Fourier transform of instantaneous auto-correlation function of the signal. WVD could generate time-frequency representation with the high concentration, while it also introduces plenty of cross-terms. Hilbert-Huang transform uses empirical mode decomposition (EMD) to decompose a signal into several intrinsic mode functions (IMF) along with a trend and obtain instantaneous frequency [79]. EMD is a data-driven signal decomposition technique that sequentially extracts zero-mean regular/distorted harmonics from a signal, starting from high- to low- frequency components, and it is a dyadic filter equivalent to an adaptive wavelet. While the end effects influence the performance of the signal decomposition and distort the results. For this case, researchers proposed various signal extension technique to solve the problem of end effects, including feature-based extension, mirror images, prediction methods and pattern comparison [80].

The general formula of Gabor transform, Chirplet transform and asymmetric Gaussian Chirplet transform can be expressed as Eqs. (11) and (12). Their results are the inner product between the signal $u(t)$ and the complex conjugate of kernel function $g_{\tau,\omega,\Theta}$.

$$y(\tau,\omega;\Theta)=\int_{-\infty}^{+\infty}u(t)g^{*}_{\tau,\omega,\Theta}(t)dt, \tag{11}$$

$$g(t)=\begin{cases} e^{-\pi\left(\frac{t-\tau}{s}\right)^2}\cos\left[\omega(t-\tau)+\phi\right], & \text{Gabor} \\ \left(\sqrt{2\pi}s\right)^{-1/2}e^{-\pi\left(\frac{t-\tau}{s}\right)^2}\cos\left[\omega(t-\tau)+\zeta(t-\tau)^2+\phi\right], & \text{Gaussian Chirplet} \\ ae^{-\alpha(1-r\tanh(\kappa(t-\tau)))(t-\tau)^2}\cos\left[\omega(t-\tau)+\zeta(t-\tau)^2+\phi\right], & \text{asymmetric Gaussian Chirplet,} \end{cases} \tag{12}$$

where ζ is the linear chirp rate, ϕ is the phase, a is the amplitude, α is the decay rate controlling the signal bandwidth, r is the asymmetry factor controlling the skewness of the window and $\tanh(\kappa t)$ is hyperbolic tangent function of order κ, a positive constant integer. The detail description of Eq. (11) is given in Refs [81, 82]. Gabor transform and the Chirplet transform projects a signal energy distribution in a time-frequency plane, which does not induce interference terms [83]. An important advantage of such analysis is to provide highly concentrated time-frequency representation with signal-dependent resolution. Especially for the latter one, there are many parameters adaptively adjusted for an accuracy mapping the signal features, including the center frequency, arrival time, duration and frequency-varying characteristics. These two algorithms can also be used for decomposition of the overlapping waveforms.

The signal decomposition is based on a reasonable assumption that a signal can be expressed as a sum of several wave packets, as shown in Eq. (14).

$$u(t) = \sum_{n=0}^{N-1} \left\langle R^n u, g_{\gamma n} \right\rangle g_{\gamma n} + R^N u, \tag{13}$$

where $u(x,t)$ is the signal received at x that contains the first arrival waves, the echoes from the edges of plates and the defects; $R^N u$ is the residual term; N is the number of iterations; $g_{\gamma n}$ is the matching atoms that fit to the residual term $R^n u$, which is the residual left after subtracting results of previous iterations; $g_{\gamma i}$ is the atoms in a pre-built over-complete dictionary or a sub-type of a kernel function. The derivation processes of parameters $R^n u$ and $g_{\gamma n}$ can be expressed as

$$\begin{cases} R^0 u = u(t) \\ R^{n+1} u = R^N u - \left\langle R^n u, g_{\gamma n} \right\rangle g_{\gamma n} \\ g_{\gamma n} = \arg \max\limits_{g_{\gamma i} \in D} \left| \left\langle R^n u, g_{\gamma i} \right\rangle \right| \end{cases}. \tag{14}$$

In the process of the wave packets decomposition, the atoms can be selected from a pre-built dictionary or sub-type of a kernel function. The dictionary can be built based on the pre-analysis of the excitation [84], the interaction between Lamb waves and defects [85], etc. Mallat et al. [86] introduced the matching pursuit with time-frequency dictionaries. The decomposition based the Gabor transform and the Gaussian Chirplet transform are suitable for the signals with symmetric envelops, while the sensing signals often have asymmetric envelops induced by the dispersion nature of Lamb waves. Thus, the asymmetric Gaussian Chirplet is designed for decomposition the dispersive Lamb waves signal benefiting from its specific designed windows.

Matching pursuit algorithm is a highly adaptive signal decomposition and approximation method for de-noising, wave parameter estimation and feature extraction [86, 87], while it does not provide the best approximation to signal by a linear combination of atoms from a dictionary or a sub-type of kernel function. Actually, many parameters need to be estimated in each iteration step to get a best approximant, it is an NP-hard problem. Therefore, a suitable parameter evaluation algorithm is very important for signal decomposition algorithms. The successive parameters estimation algorithm [88] and the fast ridge pursuit algorithm [82] are most used algorithms for estimation of the atom parameter. In each iteration of the pursuit, the

best atom is first selected, and then, its scale and the chirp rate are locally optimized so as to get a 'good' chirp atom. While the successive parameter estimation is a suboptimal method. The error in one parameter estimate due to noise will induce errors in estimation of other parameters. Zeng et al. [89] combined the adaptive Chirplet transform and the time-varying band-pass filtering provides a methodology for extracting interest waveforms from the overall Lamb wave signals.

3.3. Temperature effect compensation techniques

The signals received under a vibration of temperature condition can be expressed as [90, 91].

$$u(t; T_0 + \delta T) = \sum_{j=1}^{N} a_j s_j \left[t - t_j \beta(\delta T)\right], \tag{15}$$

where a_j, s_j and t_j are the amplitude, the waveform and the arrival time of the j^{th} wave packet respectively, $\beta(\delta T)$ is the shift in arrival times of wave packets in each time-trace with respect to their values at an arbitrary fixed temperature, $\beta = 1 - \delta T \cdot c_g k_p / c_p^2$, k_p is the change in phase velocity with temperature.

The optimal baseline selection (OBS) and the baseline signal stretch (BSS) are widely studied [92] for elimination the temperature effect in Lamb waves based structure integrity evaluation. In OBS technique, a pre-built database under different temperatures is built. The process for OBS includes (1) recording a set of baseline waveforms from the intact specimen at temperatures spanning the expected operating range; (2) selecting a waveform from the baseline set, which the temperature is the closest to the measured signal; (3) adjusting the baseline waveform to best match the signal, then calculating an error parameter between the signal and the adjusting waveform and (4) comparing these parameters with a threshold to determine the structural status. A large number of baselines data are needed even for small temperature steps to ensure the accuracy of the extracted defects waveforms that increase computational and memory costs. Meanwhile the damage manifests itself and the noise will rise the OBS error [93]. Wang et al. [94] combined the OBS and the adaptive filter to compensate the temperature variations. The simplistic representation of the signal and the choice of activation function are the main limitations of this technology. BSS modified a single baseline time-trace to match the field time-trace to compensate the temperature effect. In BSS, the time-axis of the baseline time-trace is stretched by a stretch factor to yield a new time-trace, while the BBS is strongly dependent on the mode purity and structural complexity. The OBS and the BBS can be combined to form a robust temperature compensation strategy [90, 95]. The reduction in the number of baselines in the database is limited by the maximum temperature gap between baselines, which can be compensated for by the optimal stretch without loss of sensitivity; this is a function of mode purity, signal complexity and the maximum propagation distance to cover the whole structure expressed in wavelengths [96]. Their formula are

$$u_m(t; T_m) = \sum_{j=1}^{N} a_j^m s_j^m \left[t - t_j^m \beta(\delta T_m)\right], \quad \text{(OBS)} \tag{16}$$

$$\widehat{u}\left(t;T_0,\widehat{\beta}\right)=u\left(t/\widehat{\beta};T_0\right)=\sum_{j=1}^{N}a_j s_j\left(t/\widehat{\beta}-t_j\right),\quad \text{(BSS)} \tag{17}$$

where u_m is the m^{th} time-trace from the baseline dataset, T_{m}= T_0+δT_m refers to as the baseline dataset and $\beta(\delta T_m)$ is the fractional shift in arrival times of wave packets in each time-trace with respect to their values at an arbitrary fixed temperature. $\widehat{\beta}$ is a stretch factor to yield a new time-trace $\widehat{u}\left(t;T_0,\widehat{\beta}\right)$.

Other techniques have been proposed for compensation the temperature effect. Physics-based approach builds the compensation data through analyzing the temperature effect on the structures and transducers [97]. This approach needs to train with prior data, which are always unavailable. Fendzi et al. [98] presented a data-driven temperature compensation approach, which considers a representation of the piezo-sensor signal through its Hilbert transform that allows one to extract the amplitude factor and the phase shift in signals, while its compensation accuracy depends on the length of the time window that should be considered in the temperature compensation parameters estimation. Liu et al. [99] proposed a baseline signal reconstruction technique in which the Hilbert transform is used to compensate the phase of baseline signals and the orthogonal matching pursuit is used to compensate the amplitude of baseline signal. Dao et al. [100] combined the cointegration technique and fractal signal processing to effective removal of undesired multiple temperature trends in Lamb waves signals. The former technique relies on the analysis of non-stationary behavior, whereas the latter brings the concept of multi-resolution wavelet decomposition of time series. While the self-similar pattern of cointegration residuals will be broken when damage is present.

4. Summary and conclusions

Lamb waves are a type of elastic waves propagating in plate-like structures that have been widely studied for defects location, sizing and recognition during the past decades. The detection or monitoring system settings, the transducers, the nature of Lamb waves, the environment and operational condition are three key factors influence Lamb waves emitting and sensing, and further decide the design and the performance of signal processing techniques. Considering the important roles of transducers and the signal processing techniques in Lamb waves based structure integrity evaluation, various transducers and signal processing technologies are proposed and developed, and that are briefly reviewed in this chapter.

1. The transducers for Lamb waves emitting and sensing in structure integrity evaluation are mainly based on three types of transduce mechanisms, including piezoelectric effect, electromagnetic acoustic transducer mechanism and laser ultrasonic technique. Piezoelectric transducers, EMAT and laser ultrasonic systems are mostly used for Lamb waves emitting and sensing in structure integrity evaluation. The PWAT, IDTs, the air-coupled transducers are designed with the piezoelectric materials that has high energy conversion efficiency. EMATs are working under electromagnetic acoustic transducer mechanism,

http://dx.doi.org/10.5772/intechopen.78381

including Lorentz force, magnetostriction mechanism and magnetizing force. Through adjusting the configuration of the permanent magnets, coils, EMATs can used for relatively pure Lamb waves modes emitting and sensing at specific frequency, including the A modes, S modes. Laser ultrasonic systems commonly consist of a laser transmitter, a laser receiver and a laser demodulator and are very complex systems that designed with the shearography and the laser vibrometer techniques. In the structure integrity evaluation, the system works under the thermoelastic regime, not the ablation regime, for emitting Lamb waves without the hurt of structure. Through scanning the surface of the plates, the full wavefield Lamb waves can be acquired with the laser ultrasonic system.

2. The waveform modulation techniques, multi-scale analysis techniques and temperature effect compensation techniques are developed to optimize the resolution and interpretability of received Lamb waves signals. Among them, the waveform modulation techniques are used to acquire signals that have more regular waveforms through modulating the phase parameters or the excitation waveforms based on the Lamb waves dispersion principle and the δ-like waveform response of specific waves. After the process, the ToF and the scatterers echoes can be analyzed easily. During the process of the time recompression technique, the time-distance mapping technique, the spectral warping technique and the wideband dispersion reversal technique, the propagation should be known that limits their application potentials. The nonlinear wavenumber linearization technique can realize dispersion compensation without the propagation distance parameter. Pulse compression technique also attracts many attentions for generating that high improve the resolution of the received signals, but it still exists many challenges for field application. TR technique is built with the acoustic reciprocity principle for dispersion compensation and damage feature extraction and is easily realized in applications, while it often cannot get ideal dispersion compensation results. It is more suitable for defects feature extraction in Lamb waves defects detection.

3. Multi-scale analysis techniques are performed through mapping a signal into a multi-parameters data space with a function transform or matching pursuit operation. The transforms based on a kernel function include STFT, CWT, DWT, Gabor transform, Chirplet transform and asymmetric Gaussian Chirplet transform that have been used for time-frequency analysis and overlapping wave packets decomposition. Among them, the wavelet transforms and the Chirplet-based transforms are more attractive as their flexible and more parameter adjusting probability in signal processing. Particularly for the asymmetric Gaussian Chirplet transform has the ability for accuracy decompose the signals with the dispersion characteristics. The dictionary based on overlapping waveforms decomposition techniques is also very attractive. The OBS, the BBS and physics-based approaches are proposed for compensating the temperature effect. OBS is performed with a pre-built database under different temperatures where large number of baseline data are acquired under various temperature conditions. In BSS, the time-axis of the baseline time-trace is stretched by a stretch factor to yield a new time-trace, but it is sensitive to the resolution and the interpretability of Lamb wave signals. The combination of the OBS and BSS can effectively eliminate the shortage in both of the algorithms and have a robust performance in temperature effect compensation. Physics-based approach realizes the

compensation through analysis the temperature effect on the structures and the transducers that is time consuming for field application.

Acknowledgements

This work was supported by the National Natural Science Foundation of China (Grant Nos. 51475012, 11772014, 11527801, and 11272021).

Conflict of interest

We declare that we do not have any commercial or associative interest that represents a conflict of interest in connection with the work submitted.

Author details

Zenghua Liu* and Honglei Chen

*Address all correspondence to: liuzenghua@bjut.edu.cn

College of Mechanical Engineering and Applied Electronics Technology, Beijing University of Technology, Beijing, China

References

[1] Joseph RL. Guided wave nuances for ultrasonic nondestructive evaluation. IEEE Transactions on Ultrasonics, Ferroelectrics, and Frequency Control. 2000;**47**:575-583. DOI: 10.1109/58.842044

[2] Su ZQ, Ye L, Lu Y. Identification of damage using Lamb waves. Journal of Sound and Vibration. 2006;**295**:753-780. DOI: 10.1007/ 978-1-84882-784-4

[3] Willberg C, Duczek S, Vivar-Perez JM, Ahmad ZAB. Simulation methods for guided wave-based structural health monitoring: A review. Applied Mechanics Reviews. 2015; **67**:1-20. DOI: 10.1115/1.4029539

[4] Joseph RL. Ultrasonic Guided Waves in Solid Media. 2nd ed. New York: Cambridge University Press; 2014. pp. 76-106. ch6

[5] Giurgiutiu V. Structural Health Monitoring with Piezoelectric Wafer Active Sensors-Predictive Modeling and Simulation. 2nd ed. New York: Elsevier; 2014. pp. 293-355. DOI: 10.1016/B978-0-12-418691-0.00020-4.ch6

[6] Worden K. Rayleigh and Lamb waves-basic principles. Strain. 2001;**37**:167-172. DOI: 10.1111/j.1475-1305.2001.tb01254.x

[7] Moll J, Golub MV, Glushkov E, Glushkova N, Fritzen CP. Non-axisymmetric Lamb wave excitation by piezoelectric wafer active sensors. Sensors and Actuators, A: Physical. 2012; **174**:173-180. DOI: 10.1016/j.sna.2011.11.008

[8] Ha S, Lonkar K, Mittal A, Chang FK. Adhesive layer effects on PZT-induced Lamb waves at elevated temperatures. Structural Health Monitoring. 2010;**9**:247-256. DOI: 10.1177/1475921710365267

[9] Bratton RL, Datta SK, Shah AH. Anisotropy effects on Lamb waves in composite plates. In: Proceedings of the Review of Progress in Quantitative Nondestructive Evaluation. Berlin: Springer; 1989. pp. 197-204

[10] He CF, Liu HY, Liu ZH, Wu B. The propagation of coupled Lamb waves in multilayered arbitrary anisotropic composite laminates. Journal of Sound and Vibration. 2013;**332**: 7243-7256. DOI: 10.1016/j.jsv.2013.08.035

[11] Wang L, Yuan FG. Group velocity and characteristic wave curves of Lamb waves in composites: Modeling and experiments. Composites Science and Technology. 2007;**67**: 1370-1384. DOI: 10.1016/j.compscitech.2006.09.023

[12] di Scalea FL, Salamone S. Temperature effects in ultrasonic Lamb wave structural health monitoring systems. The Journal of the Acoustical Society of America. 2008;**124**:161-174. DOI: 10.1121/1.2932071

[13] Pei N, Bond LJ. Comparison of acoustoelastic Lamb wave propagation in stressed plates for different measurement orientations. The Journal of the Acoustical Society of America. 2017;**142**:327-331. DOI: 10.1121/1.5004388

[14] Putkis O, Dalton RP, Croxford AJ. The influence of temperature variations on ultrasonic guided waves in anisotropic CFRP plates. Ultrasonics. 2015;**60**:109-116. DOI: 10.1016/j.ultras.2015.03.003

[15] di Scalea FL, Matt H, Bartoli I. The response of rectangular piezoelectric sensors to Rayleigh and lamb ultrasonic waves. The Journal of the Acoustical Society of America. 2007;**121**:175-187. DOI: 10.1121/1.2400668

[16] Marzani A, Salamone S. Numerical prediction and experimental verification of temperature effect on plate waves generated and received by piezoceramic sensors. Mechanical Systems and Signal Processing. 2012;**30**:204-217. DOI: 10.1016/j.ymssp.2011.11.003

[17] Sirohi J, Chopra I. Fundamental understanding of piezoelectric strain sensors. Journal of Intelligent Material Systems and Structures. 2000;**11**:246-257. DOI: 10.1106/8BFB-GC8P-XQ47-YCQ0

[18] Lee SJ, Gandhi N, Michaels JE, Michaels TE. Comparison of the effects of applied loads and temperature variations on guided wave propagation. In: Proceedings of the 37th

Annual Review of Progress in Quantitative Nondestructive Evaluation, 18–23 June 2011; San Diego. Huntington Quadrangle: Amer Inst Physics; 2010. pp. 175-182

[19] Giurgiutiu V. Tuned Lamb wave excitation and detection with piezoelectric wafer active sensors for structural health monitoring. Journal of Intelligent Material Systems and Structures. 2005;**16**:291-305. DOI: 10.1177/1045389X05050106

[20] Manka M, Rosiek M, Martowicz A, Stepinski T, Uhl T. Lamb wave transducers made of piezoelectric macro-fiber composite. Structural Control and Health Monitoring. 2013;**20**: 1138-1158. DOI: 10.1002/stc.1523

[21] Mamishev AV, Sundara-rajan K, Yang F, Du YQ, Zahn M. Interdigital sensors and transducers. Proceedings of the IEEE. 2004;**92**:808-844. DOI: 10.1109/JPROC.2004.826603

[22] Monkhouse RSC, Wilcox PD, Cawley P. Flexible interdigital PVDF transducers for the generation of Lamb waves in structures. Ultrasonics. 1997;**35**:489-498. DOI: 10.1016/S0041-624X(97)00070-X

[23] Stepinski T, Mańka M, Martowicz A. Interdigital Lamb wave transducers for applications in structural health monitoring. NDT and E International. 2017;**86**:199-210. DOI: 10.1016/j.ndteint.2016.10.007

[24] Mańka M, Rosiek M, Martowicz A, Stepinski T, Uhl T. PZT based tunable interdigital transducer for Lamb waves based NDT and SHM. Mechanical Systems and Signal Processing. 2016;**78**:71-83. DOI: 10.1016/j.ymssp.2015.12.013

[25] Castaings M, Hosten B. The use of electrostatic, ultrasonic, air-coupled transducers to generate and receive Lamb waves in anisotropic, viscoelastic plates. Ultrasonics. 1998;**36**: 361-365. DOI: 10.1016/S0041-624X(97)00144-3

[26] Kusano Y, Wang Q, Luo GL, Lu YP, Rudy RQ, Polcawich RG, Horsley DA. Effects of DC bias tuning on air-coupled PZT piezoelectric micromachined ultrasonic transducers. Journal of Microelectromechanical Systems. DOI: 10.1109/JMEMS.2018.2797684

[27] Grondel S, Paget C, Delebarre C, Assaad J, Levin K. Design of optimal configuration for generating A_0 Lamb mode in a composite plate using piezoceramic transducers. The Journal of the Acoustical Society of America. 2002;**112**:84-90. DOI: 10.1121/1.1481062

[28] Emmanuel L, Charles H, Marc R, Nazih M, Christian B. Numerical and experimental study of first symmetric and antisymmetric Lamb wave modes generated and received by dual-PZTs in a composite plate. In: Proceeding of the Eleventh International Workshop on Structural Health Monitoring; 12–14 September 2017, California. Pennsylvania: DEStech Publications, Inc.; 2017

[29] Liu T, Veidt M, Kitipornchai S. Single mode Lamb waves in composite laminated plates generated by piezoelectric transducers. Composite Structures. 2002;**58**:381-396. DOI: 10.1016/S0263-8223(02)00191-5

[30] Mao Y, Shui Y, Jiang W, Yin J. Switchable single mode Lamb wave transduction by means of both side excitation. In: Proceedings of 1995 IEEE Ultrasonics Symposium; 07–10 November, Seattle. New York: IEEE; 1995. pp. 807-810

[31] Degertekin FL, KhuriYakub BT. Single mode Lamb wave excitation in thin plates by Hertzian contacts. Applied Physics Letters. 1996;**69**:146-148. DOI: 10.1063/1.116902

[32] Birgani PT, Sodagar S, Shishesaz M. Generation of low-attenuation Lamb wave modes in three-layer adhesive joints. International Journal of Acoustics and Vibrations. 2017;**22**: 51-57. DOI: 10.20855/ijav.2017.22.1450

[33] Xu BL, Giurgiutiu V. Single mode tuning effects on Lamb wave time reversal with piezoelectric wafer active sensors for structural health monitoring. Journal of Nondestructive Evaluation. 2007;**26**:123-134. DOI: 10.1007/s10921-007-0027-8

[34] Clarke T, Simonetti F, Rohklin S, Cawley P. Development of a low-frequency high purity a(0) node transducer for SHM application. IEEE Transactions on Ultrasonics, Ferroelectrics, and Frequency Control. 2009;**56**:68-1457. DOI: 10.1109/TUFFC.2009.1201

[35] Liu ZH, Yu HT, He CF, Wu B. Delamination detection in composite beams using pure Lamb mode generated by air-coupled ultrasonic transducer. Journal of Intelligent Material Systems and Structures. 2014;**25**:541-550. DOI: 10.1177/1045389X13493339

[36] Jayaraman C, Anto I, Balasubramaniam K, Venkataraman KS. Higher order modes cluster (HOMC) guided waves for online defect detection in annular plate region of above-ground storage tanks. Insight - Non-destructive Testing and Condition Monitoring. 2009;**51**:606-611. DOI: 10.1784/insi.2009.51.11.606

[37] Khalili P, Cawley P. Excitation of single-mode Lamb waves at high-frequency-thickness products. IEEE Transactions on Ultrasonics, Ferroelectrics, and Frequency Control. 2016; **63**:12-303. DOI: 10.1109/TUFFC.2015.2507443

[38] Guo ZQ, Achenbach JD, Krishnaswamy S. EMAT generation and laser detection of single Lamb wave modes. Ultrasonics. 1997;**35**:423-429. DOI: 10.1016/S0041-624X(97)00024-3

[39] Lee JK, Kim YY. Tuned double-coil EMATs for omnidirectional symmetric mode reference Lamb wave generation. NDT&E International. 2016;**83**:38-47. DOI: 10.1016/j.ndteint.2016.06.001

[40] Liu ZH, Hu YN, Xie MW, Wu B, He CF. Development of omnidirectional A_0 mode EMAT employing a concentric permanent magnet pairs with opposite polarity for plate inspection. NDT&E International. 2018;**94**:13-21. DOI: 10.1016/j.ndteint.2017.11.001

[41] Yoo B, Na SM, Flatau AB, Prines DJ. Directional magnetostrictive patch transducer based on Galfenol's anisotropic magnetostriction feature. Smart Materials and Structures. 2014; **23**:95035. DOI: 10.1088/0964-1726/23/9/095035

[42] Khalili P, Cawley P. Relative ability of wedge coupled piezoelectric and meander coil EMAT probes to generate single mode Lamb waves. IEEE Transactions on Ultrasonics, Ferroelectrics, and Frequency Control. DOI: 10.1109/TUFFC.2018.2800296

[43] Tomohiro Y, Uno Y. High-order Lamb waves for flaw detection in steel plates by electromagnetic acoustic transducers. Journal of Solid Mechanics and Materials Engineering. 2007;**1**:355-363. DOI: 10.1299/jmmp.1.355

[44] Ostachowicz W, Radzieński M, Kudela P. Comparison studies of full wavefield signal processing for crack detection. Strain. 2014;**50**:275-291. DOI: 10.1111/str.12098

[45] Costley RD, Berthelot YH, Jacobs LJ. Fresnel arrays for the study of Lamb waves in laser ultrasonics. Journal of Nondestructive Evaluation. 1994;**13**:33-42. DOI: 10.1007/BF00723945

[46] Song MK, Jhang KY. Crack detection in single-crystalline silicon wafer using laser generated Lamb waves. Advances in Materials Science and Engineering. 2013;**2013**:1-6. DOI: 10.1155/2013/950791

[47] Huke P, Schröder M, Hellmers S, Kalms M, Bergmann RB. Efficient laser generation of Lamb waves. Optics Letters. 2014;**39**:5795-5797. DOI: 10.1364/OL.39.005795

[48] Addison RC, Mckie ADW. Laser-based ultrasound arrays for generation and detection of narrowband single mode Lamb waves. In: Proceedings of the 1994 IEEE Ultrasonics Symposium; 01–04 November 1994; Cannes. New York: IEEE; 1994. pp. 1201-1404

[49] Nakano H, Nagai S. Laser generation of antisymmetric Lamb waves in thin plates. Ultrasonics. 1991;**29**(3):230-234. DOI: 10.1016/0041-624X(91)90061-C

[50] Todd MD, Johnson GA, Vohra ST. Deployment of a fiber Bragg grating-based measurement system in a structural health monitoring application. Smart Materials and Structures. 2001;**10**:534-539. DOI: 10.1088/0964-1726/10/3/316

[51] Sicard R, Goyette J, Zellouf D. A numerical dispersion compensation technique for time recompression of Lamb wave signals. Ultrasonics. 2002;**40**:727-732. DOI: 10.1016/S0041-624X(02)00201-9

[52] Wilcox PD. A rapid signal processing technique to remove the effect of dispersion from guided wave signals. IEEE Transactions on Ultrasonics, Ferroelectrics, and Frequency Control. 2003;**50**:419-427. DOI: 10.1109/TUFFC.2003.1197965

[53] De Marchi L, Marzani A, Speciale N, Viola E. A passive monitoring technique based on dispersion compensation to locate impacts in plate-like structures. Smart Materials and Structures. 2011;**20**:35021. DOI: 10.1088/0964-1726/20/3/035021

[54] De Marchi L, Marzani A, Miniaci M. A dispersion compensation procedure to extend pulse-echo defects location to irregular waveguides. NDT and E International. 2013;**54**: 115-122. DOI: 10.1016/j.ndteint.2012.12.009

[55] Fu SC, Shi LH, Zhou YH, Cai J. Dispersion compensation in Lamb wave defect detection with step-pulse excitation and warped frequency transform. IEEE Transactions on Ultrasonics, Ferroelectrics, and Frequency Control. 2014;**61**:2075-2088. DOI: 10.1109/TUFFC.2014.006606

[56] Xu KL, Ta DA, Hu B, Laugier P, Wang WQ. Wideband dispersion reversal of Lamb waves. IEEE Transactions on Ultrasonics, Ferroelectrics, and Frequency Control. 2014; **61**:997-1005. DOI: 10.1109/TUFFC.2014.2995

[57] Xu BL, Yu LY, Giurgiutiu V. Lamb wave dispersion compensation in piezoelectric wafer active sensor phased-array applications. In: Proceedings of the Conference on Health Monitoring of Structural and Biological Systems, 8–12 March 2009, San Diego. California: SPIE Press; 2009. p. 7295: p. 729516. DOI: 10.1117/12.816085

[58] Liu L, Yuan FG. A linear mapping technique for dispersion removal of Lamb waves. Structural Health Monitoring. 2010;**9**:75-86. DOI: 10.1177/1475921709341012

[59] Cai J, Yuan SF, Wang TG. Signal construction-based dispersion compensation of Lamb waves considering signal waveform and amplitude spectrum preservation. Materials. 2016;**10**:4. DOI: 10.3390/ma10010004

[60] Xu CB, Yang ZB, Chen XF, Tian SH, Xie Y. A guided wave dispersion compensation method based on compressed sensing. Mechanical Systems and Signal Processing. 2018; **103**:89-104. DOI: 10.1016/j.ymssp.2017.09.043

[61] Alleyne DN, Pialucha TP, Cawley P. A signal regeneration technique for long range propagation of dispersive Lamb waves. Ultrasonics. 1993;**31**:201-204. DOI: 10.1016/ 0041-624X(93)90007-M

[62] Zeng L, Lin J. Chirp-based dispersion pre-compensation for high resolution Lamb wave inspection. NDT and E International. 2014;**61**:35-44. DOI: 10.1016/j.ndteint.2013.09.008

[63] Lin J, Hua JD, Zeng L, Luo Z. Excitation waveform design for lamb wave pulse compression. IEEE Transactions on Ultrasonics, Ferroelectrics, and Frequency Control. 2016;**63**: 165-177. DOI: 10.1109/TUFFC.2015.2496292

[64] Malo S, Fateri S, Livadas M, Mare C, Gan TH. Wave mode discrimination of coded ultrasonic guided waves using two-dimensional compressed pulse analysis. IEEE Transactions on Ultrasonics, Ferroelectrics, and Frequency Control. 2017;**64**:1092-1101. DOI: 10.1109/TUFFC.2017.2693319

[65] Yücel MK, Fateri S, Legg M, Wikinson A, Kappatos V, Selcuk C, Gan TH. Coded waveform excitation for high resolution ultrasonic guided wave response. IEEE Transactions on Industrial Informatics. 2016;**12**:257-266. DOI: 10.1109/TII.2015.2501762

[66] De Marchi L, Marzani A, Moll J, Kudela P, Radzienski M, Ostachowicz W. A pulse coding and decoding strategy to perform Lamb wave inspections using simultaneously multiple actuators. Mechanical Systems and Signal Processing. 2017;**91**:111-121. DOI: 10.1016/j.ymssp.2016.12.014

[67] Hua JD, Lin J, Zeng L, Gao F. Pulse energy evolution for high-resolution Lamb wave inspection. Smart Materials and Structures. 2015;**24**:65016. DOI: 10.1088/0964-1726/24/6/ 065016

[68] Xu KL, Ta D, Moilanen P, Wang WQ. Mode separation of Lamb waves based on dispersion compensation method. The Journal of the Acoustical Society of America. 2012;**131**: 2714-2722. DOI: 10.1121/1.3685482

[69] Agrahari JK, Kapuria S. Active detection of block mass and notch-type damages in metallic plates using a refined time-reversed Lamb wave technique. Structural Control and Health Monitoring. 2018;**25**:1-18. DOI: 10.1002/stc.2064

[70] Zeng L, Lin J, Huang LP. A modified Lamb wave time-reversal method for health monitoring of composite structures. Sensors. 2017;**17**:955. DOI: 10.3390/s17050955

[71] Huang LP, Zeng L, Lin J, Luo Z. An improved time reversal method for diagnostics of composite plates using Lamb waves. Composite Structures. 2018;**190**:10-19. DOI: 10.1016/j.compstruct.2018.01.096

[72] Hong JC, Sun KH, Kim YY. The matching pursuit approach based on the modulated Gaussian pulse for efficient guided-wave damage inspection. Smart Materials and Structures. 2005;**41**:548-560. DOI: 10.1088/0964-1726/14/4/013

[73] Le Touze G, Nicolas B, Mars JI, Lacoume JL. Matched representations and filters for guided waves. IEEE Transactions on Signal Processing. 2009;**57**:1783-1795. DOI: 10.1109/TSP.2009.2013907

[74] Demirli R, Saniie J. Asymmetric Gaussian chirplet model and parameter estimation for generalized echo representation. Journal of the Franklin Institute. 2014;**351**:907-921. DOI: 10.1016/j.jfranklin.2013.09.028

[75] Demirli R, Saniie J. Asymmetric Gaussian Chirplet model for ultrasonic echo analysis. In: Proceedings of the 2010 IEEE International Ultrasonics Symposium Proceedings; 11–14 October; California. New York: IEEE; 2010. pp. 124-128

[76] Prosser WH, Seale MD, Smith BT. Time-frequency analysis of the dispersion of lamb modes. The Journal of the Acoustical Society of America. 1999;**105**:76-2669. DOI: 10.1121/1.426883

[77] Kwok HK, Jones DL. Improved instantaneous frequency estimation using an adaptive short-time Fourier transform. IEEE Transactions on Signal Processing. 2000;**48**:2964-2972. DOI: 10.1109/78.869059

[78] Pei SC, Huang SG. STFT with adaptive window width based on the chirp rate. IEEE Transactions on Signal Processing. 2012;**60**:4065-4080. DOI: 10.1109/TSP.2012.2197204

[79] Chen B, Zhao SL, Li PY. Application of Hilbert-Huang transform in structural health monitoring: A state-of-the-art review. Mathematical Problems in Engineering. 2014. DOI: 10.1155/2014/317954

[80] Guo W, Huang LJ, Chen C, Zuo HW, Liu ZW. Elimination of end effects in local mean decomposition using spectral coherence and applications for rotating machinery. Digital Signal Processing. 2016;**55**:52-63. DOI: 10.1016/j.dsp.2016.04.007

[81] Xu BL, Giurgiutiu V, Yu LY. Lamb waves decomposition and mode identification using matching pursuit method. In: Proceedings of SPIE, Sensors and Smart Structures Technologies for Civil, Mechanical, and Aerospace Systems 2009; 27–30 March 2009; San Diego. Bellingham: SPIE Press; 2009. pp. 1-12

[82] Demirli R, Saniie J. Asymmetric Gaussian chirplet model and parameter estimation for generalized echo representation. Journal of the Franklin Institute-engineering and. Applied Mathematics. 2014;**351**:907-921. DOI: 10.1016/j.jfranklin.2013.09.028

[83] Kim CY, Park KJ. Mode separation and characterization of torsional guided wave signals reflected from defects using chirplet transform. NDT and E International. 2015;**74**:15-23. DOI: 10.1016/j.ndteint.2015.04.006

[84] Li FC, Su ZQ, Ye L, Meng G. A correlation filtering-based matching pursuit (CF-MP) for damage identification using Lamb waves. Smart Materials and Structures. 2006;**15**:1585-1594. DOI: 10.1088/0964-1726/15/6/010

[85] Rostami J, Tse PWT, Fang Z. Sparse and dispersion-based matching pursuit for minimizing the dispersion effect occurring when using guided wave for pipe inspection. Materials. 2017;**10**:622. DOI: 10.3390/ma10060622

[86] Mallat SG, Zhang ZF. Matching pursuits with time-frequency dictionaries. IEEE Transactions on Signal Processing. 1993;**41**:3397-3415. DOI: 10.1109/78.258082

[87] Agarwal S, Mira M. Lamb wave based automatic damage detection using matching pursuit and machine learning. Smart Materials and Structures. 2014;**23**:85012. DOI: 10.1088/0964-1726/23/8/085012

[88] Lu YF, Demirli R, Cardoso G, Saniie J. A successive parameter estimation algorithm for Chirplet signal decomposition. IEEE Transactions on Ultrasonics, Ferroelectrics, and Frequency Control. 2006;**53**:2121-2131. DOI: 10.1109/TUFFC.2006.152

[89] Zeng L, Zhao M, Lin J, Wu WT. Waveform separation and image fusion for Lamb waves inspection resolution improvement. NDT and E International. 2016;**79**:17-29. DOI: 10.1016/j.ndteint.2015.11.006

[90] Croxford AJ, Moll J, Wilcox PD, Michaels JE. Efficient temperature compensation strategies for guided wave structural health monitoring. Ultrasonics. 2010;**50**:28-517. DOI: 10.1016/j.ultras.2009.11.002

[91] Clarke T, Simonetti F, Cawley P. Guided wave health monitoring of complex structures by sparse array systems influence of temperature changes on performance. Journal of Sound and Vibration. 2010;**329**:2306-2322. DOI: 10.1016/j.jsv.2009.01.052

[92] Lu YH, Michaels JE. A methodology for structural health monitoring with diffuse ultrasonic waves in the presence of temperature variations. Ultrasonics. 2005;**43**:717-731. DOI: 10.1016/j.ultras.2005.05.001

[93] Konstantinidis G, Wilcox PD, Drinkwater BW. An investigation into the temperature stability of a guided wave structural health monitoring system using permanently attached sensors. IEEE Sensors Journal. 2007;**7**:905-912. DOI: 10.1109/JSEN.2007.894908

[94] Wang YS, Gao LM, Yuan SF, Qiu L, Qing XL. An adaptive filter-based temperature compensation technique for structural health monitoring. Journal of Intelligent Material Systems and Structures. 2014;**25**:2187-2198. DOI: 10.1177/1045389X13519001

[95] Moll J, Fritzen CP. Guided waves for autonomous online identification of structural defects under ambient temperature variations. Journal of Sound and Vibration. 2012; **331**:4587-4597. DOI: 10.1016/j.jsv.2012.04.033

[96] Clarke T, Simonetti F, Cawley P. Guided wave health monitoring of complex structures by sparse array systems influence of temperature changes on performance. Journal of Sound and Vibration. 2010;**329**:2306-2322. DOI: 10.1016/j.jsv.2009.01.052

[97] Roy S, Lonkar K, Janapati V, Chang FK. A novel physics-based temperature compensation model for structural health monitoring using ultrasonic guided waves. Structural Health Monitoring. 2014;**13**:321-342. DOI: 10.1177/1475921714522846

[98] Fendzi C, Rebillat M, Mechbal N, Guskov M, Coffignal G. A data driven temperature compensation approach for structural health monitoring using Lamb waves. Structural Health Monitoring. 2016;**15**:525-540. DOI: 10.1177/1475921716650997

[99] Liu GQ, Xiao YC, Zhang H, Ren GX. Baseline signal reconstruction for temperature compensation in Lamb wave-based damage detection. Sensors. 2016;**16**:1273. DOI: 10.3390/s16081273

[100] Dao PB, Staszewski WJ. Lamb wave based structural damage detection using cointegration and fractal signal processing. Mechanical Systems and Signal Processing. 2014;**49**:285-301. DOI: 10.1016/j.ymssp.2014.04.011

Chapter 5

Application and Challenges of Signal Processing Techniques for Lamb Waves Structural Integrity Evaluation: Part B-Defects Imaging and Recognition Techniques

Zenghua Liu and Honglei Chen

Additional information is available at the end of the chapter

http://dx.doi.org/10.5772/intechopen.79475

Abstract

The wavefield of Lamb waves is yielded by the feature of plate-like structures. And many defects imaging techniques and intelligent recognition algorithms have been developed for defects location, sizing and recognition through analyzing the parameters of received Lamb waves signals including the arrival time, attenuation, amplitude and phase, etc. In this chapter, we give a briefly review about the defects imaging techniques and the intelligent recognition algorithms. Considering the available parameters of Lamb waves signals and the setting of detection/monitoring systems, we roughly divide the defect location and sizing techniques into four categories, including the sparse array imaging techniques, the tomography techniques, the compact array techniques, and full wavefield imaging techniques. The principle of them is introduced. Meanwhile, the intelligent recognition techniques based on various of intelligent recognition algorithms that have been widely used to analyze Lamb waves signals in the research of defect recognition are reviewed, including the support vector machine, Bayesian methodology, and the neural networks.

Keywords: Lamb waves, plate, defect imaging techniques, intelligent detection algorithm, structural integrity evaluation

1. Introduction

The propagation characteristic of Lamb waves is yielded by the state of plate-like structures. Defect scattering waveforms are generated as the interaction between Lamb waves and

defects, and that may be contained in received Lamb waves signals during the Lamb waves structural integrity evaluation. To clearly show out the state of the structures, many kinds of defect imaging and recognition techniques are proposed for analyzing the change of the signal parameters based on the settings of detection/monitoring systems during the past decades. In laboratory and practical field applications of Lamb waves based structure integrity evaluation, the detection/monitoring systems have two basic setting strategies. Firstly, Lamb waves signals are emitted and sensed at relatively small number of spatially distributed position by transducers that have the same or different transduction mechanisms. These positions are maybe distributed in sparse (adjacent transducer spacing is larger than the largest wavelength of signals) or compact (adjacent transducer spacing is shorter than the shortest wavelength of signals) array forms. Collaborative with different signal excitation and detection strategies, signal processing techniques are developed for integrity detection/monitoring in the whole structure. The other strategy is a full-scale scanning of the surface of structures with laser ultrasonic systems, air-coupled scanning systems, to obtain the full wavefield of Lamb waves. On the basis of the above detection/monitoring system setting strategies, Lamb waves signals used for damage detection/monitoring are obtained. Then, signal processing techniques are adopted to analyze the change of signal parameters to extract the damage information such as the amplitudes, velocity, phase, frequency, etc. Finally, defect influence maps and intelligent recognition models that indicating defect information are achieved with imaging and recognition techniques.

In this chapter, the defect imaging techniques and intelligent recognition techniques are briefly reviewed. Considering the settings of detection/monitoring system, we roughly divide the defect imaging algorithms into four categories: spare array imaging techniques, tomography techniques, compact array imaging techniques, and full wavefield imaging techniques. The basic principle of them is introduced in Section 2. In Section 3, the intelligent recognition techniques used to process Lamb waves signals and defect feature recognition are introduced. Finally, a short summary and conclusion are provided.

2. Defect imaging techniques

When a set of Lamb waves signals are received at spatially distributed positions, the techniques map the received time-domain signals that have or have not been processed with the signal optimization techniques into a 2D or 3D space-domain based on the ToF or beam directivity for defect location (sizing are termed the defect imaging techniques). Considering the distribution of the signal received position, we roughly divide these techniques into four categories: sparse array imaging techniques, tomography techniques, compact array imaging techniques, and full wavefield imaging techniques.

2.1. Sparse array imaging techniques

In a sparse array, the adjacent transducers are far separated from each other that provide higher coverage with fewer transducers at the cost of imaging resolution. Discrete ellipse

http://dx.doi.org/10.5772/intechopen.79475

imaging technique [1, 2] and the hyperbola imaging technique [3] are ToF imaging algorithms and map the amplitude information of scattering signals to elliptical trajectory and hyperbola trajectory, respectively. Their calculation formulas are expressed as

$$t_{ij} = \begin{cases} \left(\sqrt{(x_i - x)^2 + (y_i - y)^2} + \sqrt{(x_j - x)^2 + \left(y_j - y\right)^2}\right)/c_g, & \text{(Elliptical trajectory)} \\ \left(\sqrt{(x_i - x)^2 + (y_i - y)^2} - \sqrt{(x_j - x)^2 + \left(y_j - y\right)^2}\right)/c_g, & \text{(Hyperbola trajecory)} \end{cases}, \quad (1)$$

In the process, the previously recorded baseline data are subtracted from the field-sensing signals. Then, the pixel intensity is determined by calculating the amplitude information contained in the combined backward signals. Both of the algorithms have full summation form and full multiplication form and can be expressed as

$$I(x,y) = \begin{cases} \frac{1}{N^2}\sum_{i=1}^{N}\sum_{j=1,\, i\neq j}^{N} s_{ij}\left(t_{ij}[x,y]\right), & \text{(Full summation)} \\ \frac{1}{N^2}\prod_{i=1}^{N}\prod_{j=1,\, i\neq j}^{N} s_{ij}\left(t_{ij}[x,y]\right), & \text{(Full multiplicaton)} \end{cases}, \quad (2)$$

where N is the number of transducers, s_{ij} is the amplitude information of scattering signals, t_{ij} is the arrival time of scattering signals. The quality of image produced improves rapidly with the increase of the transducer number.

The window-modulated ellipse imaging algorithm is proposed in Ref. [4]. Many auxiliary signal processing techniques are developed for enhancing the imaging performance, such as the scattering signal normalization to eliminate the different path sensitivity to damage and extract damage information with the complex Morlet wavelet coefficient [5], the temperature effect compensation technique to ensure the detection quality [6], consideration of the velocity directionality [2], and damage information extraction with statistical method [7, 8].

2.2. Tomography techniques

Tomography technique works with specific designed transducer array to reconstruct a physical quantity in a cross-sectional area by analyzing Lamb waves attenuation, velocity, and mode conversion from the projection of the quantity in all directions. There are three classical transducer configuration existed in tomographic detection, parallel tomography, fan beam tomography, and crosshole tomography [9]. **Figure 1** plots the typical spatial distributions of transducers working with different tomography mechanisms in which the parallel array working with a parallel tomography at 0°, circular array working with fan beam tomography at 0°, and square array working with crosshole tomography are shown in **Figure 1(a)**, **(b)** and **(c)**, respectively. In the parallel array, the transducers are scanned along parallel lines. Once the pitch-catch measurements for each ray in an individual orientation have been taken, the sample is rotated by a fixed amount and the measurement is repeated. The ray density is

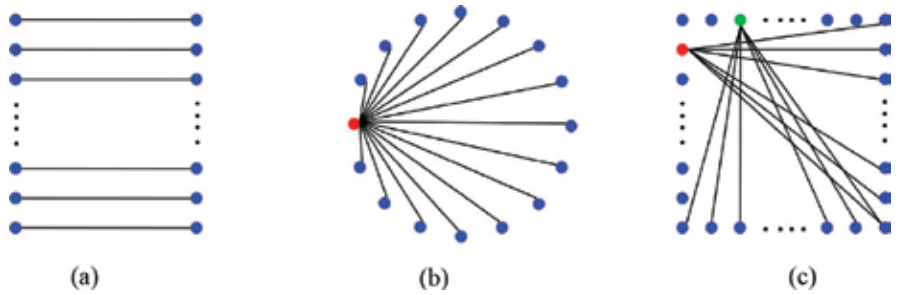

Figure 1. Typical spatial distributions of transducers working with different tomography mechanisms. (a) Parallel array working with a parallel tomography at 0°, (b) circular array working with fan beam tomography at 0°, and (c) square array working with crosshole tomography.

uniform for parallel projection tomography within the scanning region that is critical to the quality of the reconstruction. Crosshole configuration is a fast and practical alternative to the parallel-projection scheme in which transducers surround the detection zone to improve the ray density. The classical tomographic image reconstruction algorithms have the probabilistic reconstruction algorithms, transform methods, and iteration-based algorithms.

The probabilistic reconstruction algorithms (PRAs) are processed with the probabilistic statistical techniques to analyze the difference among the parameters for all the rays, including the ToF, waveforms, and energy [10]. The PRA has the flexibility in array geometry selection that can realize good reconstruction quality in fast speed. In the analysis, the ray theory needs to satisfy two validity criteria: the geometry size of the defect must be larger than the wavelength and larger than the width of the Fresnel zone. The waveform overlapping caused by reflection echoes of multidefects may make the TOF calculation inaccurate and fail the ray theory. The probabilistic inspection of damage (RAPID) [11, 12] method is a typical PRA that has been studied in Lamb waves based structure integrity evaluation in which variable shape factor is used for irregular shape defect imaging [13]. Keulen et al. [14] introduced the damage progression history into RAPID for composite structure detection. Sheen et al. [15] modified the shape factor, β, of RAPID algorithm to quantify a defect area. The expressions of the RAPID algorithm are

$$I_{\mathrm{RAPID}}(x,y) = \sum_{n=1}^{N} \left(1 - \rho_n^{ij}(x,y)\right) W_n\left[R_n^{ij}(x,y)\right], \tag{3}$$

$$W_n\left[R_n^{ij}(x,y)\right] = \begin{cases} 1 - \dfrac{R_n^{ij}(x,y)}{\beta}, & R_n^{ij}(x,y) \le \beta \\ 0 \quad , & R_n^{ij}(x,y) > \beta \end{cases}, \tag{4}$$

$$R_n^{ij}(x,y) = \frac{\sqrt{(x_i - x)^2 + (y_i - y)^2} + \sqrt{(x_j - x)^2 + \left(y_j - y\right)^2}}{\sqrt{(x_i - x_j)^2 + \left(y_i - y_j\right)^2}} - 1, \tag{5}$$

where $I_{\mathrm{RAPID}}(x,y)$ is the pixel value in the imaging zone, ρ is the zero-lag cross correlation between the baseline data and the received signals, W_n is the weighted distribution function, n

is the path number of the pitch-catch transducers numbered as i and j, respectively, $R_n^{ij}(x, y)$ is related to both the distance from point (x, y) to the two transducers for excitation (x_i, y_i) and sensing (x_j, y_j) and the distance between the two transducers, β controls the size of the ellipse and $\beta > 1$. If β is too small, then artifacts will be introduced. If it is too large, the resolution will be lost. Usually, β is setting around 1.05 [16]. The technique for relative relationship calculation algorithms can be used to acquire the value of ρ, such as correlation coefficient method, time reversal method, baseline subtraction method, etc. More damage index calculation methods are reviewed in [17].

Filtered back-projection (FBP) combines the back-projection and the filter based on the Radon transform and Fourier slice theorem. Only with a circular sensor array, FBP method has efficiency of reconstruction and incomplete datasets, and unfortunately is sensitive to noise. It is essential to form a complete set of projections from many directions. Its formulas can be expressed as

$$I_{\mathrm{FBP}}(x, y) = \int_0^{2\pi} \int_{-\infty}^{+\infty} F(\omega, \theta) e^{i2\pi\omega(x\cos\theta + y\sin\theta)} \omega d\omega d\theta = \int_0^{\pi} Q_\theta(t) d\theta, \tag{6}$$

$$Q_\theta(t) = \int_{-\infty}^{+\infty} F(\omega, \theta) e^{i2\pi\omega t} |\omega| d\omega, \tag{7}$$

where $I_{\mathrm{FBP}}(x,y)$ is the pixel value in the imaging zone, $F(\omega,\theta)$ is the spatial Fourier transform of a line integral of the attenuation $f(x,y)$ in a polar coordinate system o-θ, $Q_\theta(t)$ is called a filtered projection because it represents a spatial frequency filtering operation, in which the filter response is $|\omega|$. Every point (x,y) in the image plane is contributed by a value $Q_\theta(t)$ from all direction θ. For a given direction θ, the function $Q_\theta(t)$ is a constant on the line AB, where t is fixed as shown in **Figure 2(a)**. This is equivalent to saying that the filtered projection function $Q_\theta(t)$, which is obtained from angle θ and position t, is back-projected along the initial projection direction over the image plane.

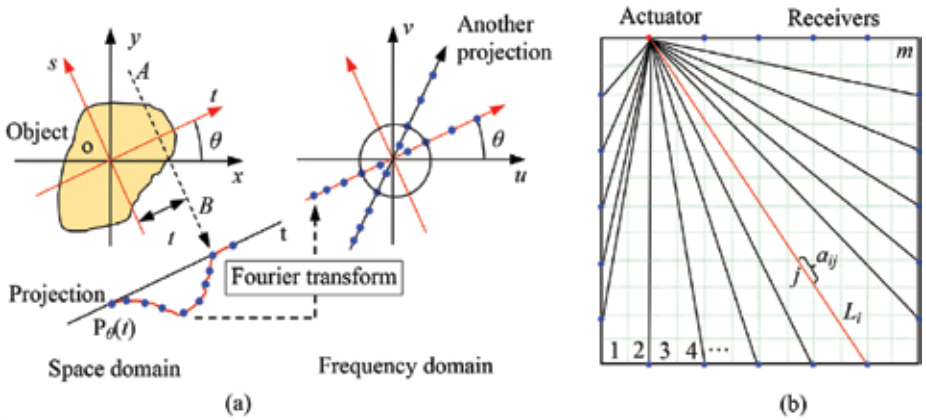

Figure 2. Principle of fan beam projection and algebraic reconstruction technique. (a) Principle of the filtered back-projection method and (b) situation of the ith path crossing the specimen.

The key to FBP tomographic image is the Fourier slice theorem that relates the measured projection data to the 2D Fourier transform of the object cross section. Wright et al. [18] used the FBP technique to image defects in isotropic and anisotropic plates of different materials using air-coupled Lamb wave tomography. Mokhtari et al. [19] proposed a polygon reconstruction technique for polygonal damage shape reconstruction. First, the projections (Radon transform) of the damaged region are generated from a small number of angles with the aid of beamforming method. Then, the damaged region is modeled by a polygon, which its optimal number of vertices is estimated using the minimum description length principle. Finally, using the polygon reconstruction technique, the coordinates of the vertices are determined. While in practice, it is not possible to measure a large number of projections in FBP that may induce the aliasing distortions by insufficiency of the input data, necessary for the transform-based techniques to produce highly accurate results. Researchers developed the interpolated FBP in which interpolations with respect to sample angle and projection angle based on limit measurements are used to generate the required projection data for the number of sampled grid values necessary for displaying a well-balanced reconstructed image. Meanwhile, it should constrain the projection data at a source point to zero when using the interpolation, rather than using extrapolation to generate projection data. **Figure 2(a)** plots the principle of the filtered back-projection method [20]. The formula, $I_{\text{fan\_FBP}}(x,y)$, of the fan beam-based FBP can be expressed as

$$I_{\text{fan\_FBP}}(x,y) = \frac{2\pi}{M}\sum_{i=1}^{M}\frac{Q_{\beta i}(\gamma)}{L^2\left(x,y,\beta_i\right)}, \tag{8}$$

where $Q_{\beta i}(n\alpha)$ is the filtered projection along the fan, M is the number of projections, and L is the distance from the transmitter to the point (x,y). β_i is the i^{th} projection angle and γ is the angle of the fan beam ray passing through the point (x,y).

The algebraic reconstruction technique (ART) starts from an initial guess for the reconstructed object and then performs a sequence of iterative grid projections and correction back-projections until the reconstruction has converged. Its formulae are expressed in Eqs. (9)–(11).

$$A_{i\times j} \times x_{j\times 1} = b_{i\times 1} \tag{9}$$

$$b_{i\times 1} = \int_j X(i,j)dl_{ij} \tag{10}$$

$$\begin{pmatrix} b_1 \\ \vdots \\ b_i \\ \vdots \\ b_m \end{pmatrix} = k \begin{pmatrix} L_{11} & \cdots & L_{1j} & \cdots & L_{1n} \\ \vdots & & \vdots & & \vdots \\ L_{i1} & \cdots & L_{ij} & & L_{mj} \\ \vdots & & \vdots & & \vdots \\ L_{m1} & \cdots & L_{mj} & \cdots & L_{mn} \end{pmatrix} \begin{pmatrix} x_1 \\ \vdots \\ x_i \\ \vdots \\ x_m \end{pmatrix} \tag{11}$$

where $A_{i\times j}$ represents the weight of i^{th} path in j^{th} grid, x represents the image results for each cell, and $b_{i\ \times\ 1}$ represents the change of signal feature (correlation) for each path. $X(i,j)$ is the

http://dx.doi.org/10.5772/intechopen.79475

attenuation coefficient for i^{th} path in j^{th} grid, and the L_{ij} represents the real length for i^{th} projected to j^{th} grid. Here, m represents the number of paths and n represents the number of grids.

In the ART, a weight matrix is constructed as a rectangular array whose size is equal to the number of paths multiplied by the number of grids. From the projections (measured data) and the weight matrix (created from sensor locations and ray geometry), the field value that maps the state of the inspection zone (correlation coefficient) is obtained using the ART method. The iterative solution to the reconstruction problem in ART is constructed by Ladas and Deveaney [21]. The iteration operation of Eq. (9) is expressed as Eq. (12) [23] in which one equation is used in each step, and an iteration consists of m steps.

$$\begin{aligned} x^{k,0} &= x^k \\ x^{k,i} &= x^{k,i-1} + \lambda_k \frac{b_i - a^i x^{k,i-1}}{\|a^i\|_2^2}, \ i = 1, 2, \cdots, m \\ x^{k+1} &= x^{k,m} \end{aligned} \tag{12}$$

Though compared with the FBP technique, ART has many advantages including better noise tolerance and better handling of the insufficiently distributed projection datasets that are induced by the spare and nonuniformly distributed projection data, it has slow speed due to iteration process. Wang et al. [22] used the ART to locate and quantify the corrosion damage at the edge of holes. In order to make the tomographic image describe the real condition of the damage, a homogenization method was designed to make the image smoother. Improved tomograms as a result of ART consider the anisotropic and attenuation characteristics of composite plates [23]. The technique based on the similarity theory is the simultaneous iterative reconstruction technique (SIRT). Malyarenko et al. [24] described the basic principle of SIRT for Lamb waves tomography that working with travel time data. In the research, the bend ray routines of a moderately scattered wavefiled was transformed into straight routines with a ray bending correction technique. The output image from the present straight ray algorithm serves as an input background for the ray tracing routine. The curved-ray ART then reconstructs the updated image and feed the next iteration until the desired quality or asymptotic behavior is observed. Miller et al. [25] used SIRT to process the multiple-mode Lamb wave signals for feature extraction of corrosion thinning for autonomous classification of flaw severity. This technique also termed diffraction tomography (DT) technique incorporates scattering effect into tomographic algorithms in order to improve the image quality and resolution. Mode conversion frequency occurs on defect boundaries, and dispersion makes all quantities frequency dependent.

Figure 3 plots the stages of accuracy thickness mapping tomography algorithms. Inhomogeneity objects are as small as 5% of the background; multiple scattering can introduce severe distortions in multicomponent objects [26]. The hybrid algorithm for robust breast ultrasound tomography (HARBUT) uses the low-resolution bent-ray tomography algorithm as the background for DT [27] in which bent-ray tomography can be applied initially to obtain a low-resolution estimate of the velocity field; this then forms the background for the DT method using the technique outlined above. Meanwhile, the subtraction is not necessary to obtain a

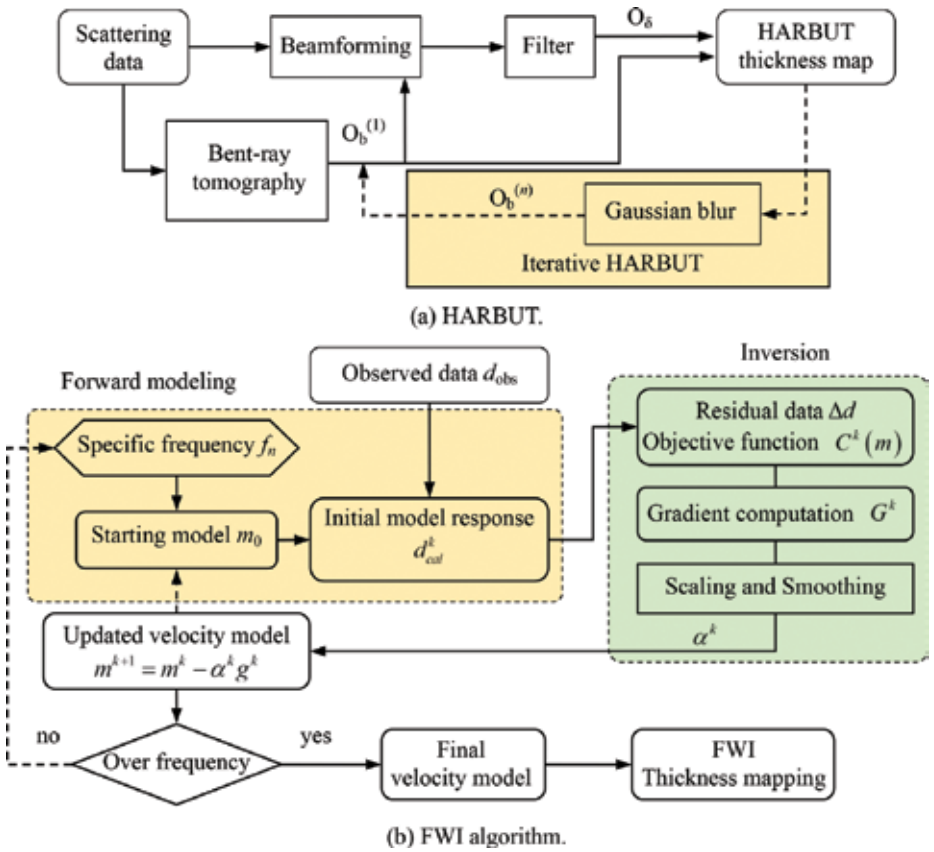

Figure 3. Stages of accuracy thickness mapping tomography algorithms. (a) HARBUT. (b) FWI algorithm.

good reconstruction, simplifying the process and avoiding these errors. The object function in HARBUT is divided into two components, the known background component O_b and the perturbation component O_δ. Since there is no need to run forward models, the speed of the algorithm is also improved. While the traditional HARBUT relies on having a sufficiently accurate background reconstruction that should satisfy the Born approximation assumption, iterating HARBUT uses an existing HARBUT reconstruction as the background for another HARBUT stage in place of bent-ray tomography, as illustrated in **Figure 3(a)**. At each step, O_b becomes more accurate, minimizing O_δ and allowing HARBUT to produce more accurate velocity maps. Through iteration operation of the HARBUT, small and high contrast defects are successfully imaged. A Gaussian filter is used to smooth the background before the next iteration, which is a form of regularization. This filter aims to remove as many of the artifacts from each iteration as possible, while maintaining the true reconstruction values. Full waveform inversion (FWI) technique is first developed in geophysics for seismic wave imaging in which the process also based on a serious of iteration operation. Rao et al. [28] introduced the FWI in Lamb waves tomography for corrosion mapping. The stages for FWI algorithm is plotted in **Figure 3(b)** in which a numerical forward model is used to predict the scattering of

http://dx.doi.org/10.5772/intechopen.79475

Lamb waves through corrosion defects and an iterative inverse model to reconstruct the corrosion profile. The aim of the tomography is to reconstruct the object function, which is a mathematical representation of the defect and is formulated in terms of velocity. The FWI algorithm proceeds from a starting velocity model to refine the velocity model in order to reduce the residual wavefield between the predicted data by the current model and the observed data from FE simulations or experiments. The predicted data are obtained by using frequency-domain finite difference method. It overcomes the limitation imposed by ignoring crucial low-frequency effects in travel time tomography. The FWI can obtain a resolution of around 0.7 wavelengths for defects with smooth depth variations from the acoustic modeling data, and about 1.5∼2.0 wavelengths from the elastic modeling data. The defect abrupt change in the wall thickness has been shown to decrease the reconstruction error of small defects compared to the smoothly varying thickness, for larger defects with sharper change in thickness, they are more likely to lead to overestimation in depth [29]. FWI allows higher order diffraction and scattering to be considered in its numerical solver, thus it has the potential to achieve more accurate inversion results, especially when multiple defects exist.

2.3. Compact array imaging techniques

Phase array (PA) technique and the synthetic aperture (SA) technique are widely performed based on the compact arrays in which the spacing between the adjacent transducers is shorter than the wavelength. **Figure 4** plots the typical compact arrays used for Lamb waves based structure integrity evaluation, such as the linear-phased arrays, circular, square, spiral, and star-shaped arrays [30]. During detection or monitoring, when one of the transducers used as actuator, Lamb waves signals are captured by all the rest transducers, then next transducer is chosen and used as actuator and capture the signal data until all the transducers have been

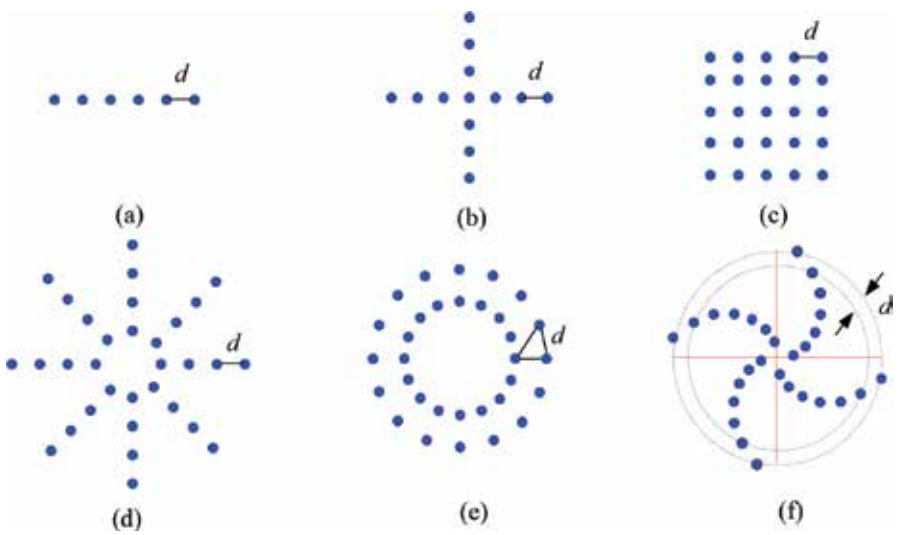

Figure 4. Typical compact arrays used for Lamb waves based structure integrity evaluation. (a) Linear, (b) cross-shaped, (c) rectangular, (d) star-shaped, (e) circular, and (f) spiral.

used for Lamb waves emitting. Through analysis of the amplitudes and phase parameters of the received Lamb waves signals, the imaging is performed in a polar coordinate system where each pixel can be defined with its angular position and the distance from the center.

Total focusing method (TFM), also named as delay-and-sum algorithm, is processed with the amplitude information of signals. Using steered and possibly focused beam improves angular resolution in ultrasonic image but it requires scanning of the full structure. It is sensitive to the wavefield profile, signal-to-noise ratio (SNR), and the dispersion nature of Lamb waves [31]. Meanwhile, TFM suffers from large side lobes that result from overlapping echoes that result in the back-propagation. Adaptive imaging methods [32], where the weights are adjusted for each pixel, can offer a significant improvement to the side lobe behavior of TFM. Vector total focusing method, phase coherence factor (PCF), and the sign coherence factor (SCF) use signal phase information to perform the correction action and defect location. Besides achieving the main goal, these methods obtain improvements in lateral resolution and SNR. Implementation of the SCF technique is quite straight forward, operating in real-time, and can be added to any virtually existing beam former to improve the resolution [33]. Compared with amplitude-based imaging techniques, such as the TFM, the phase information-based techniques are no sensitive to Lamb waves dispersion. For enhancing the defect imaging performance, many imaging combination strategies are proposed, including the combination of the TFM and various polarity images or SCF for enhancing damage detection [34–36], the combination of the TFM, and the multiapodization polarity (MAP) technique [36, 37]. The formulas of the TFM and the SCF algorithms are expressed in Eqs. (13) and (14), respectively.

$$I_{TFM}(x,y) = \frac{1}{N^2}\sum_{i=1}^{N}\sum_{J=1}^{N} a_{ij}u_{ij}\left(\tau_{ij}(x,y)\right), \tag{13}$$

where N is the number of a linear array, a_{ij} corresponds to an apodization applied to individual elements to control some characteristics of the acoustic beam, such as main lobe width and side lobe levels, $u_{ij}(t)$ is the amplitude time domain data from all transmitter and receiver j; $\tau_{ij}(x, y)$ is the ToF from the transmitter i to the receiver j and passes the point (x, y).

$$I_{SCF}(x,z) = 1-\sigma, \qquad \sigma^2 = 1-\left[\frac{1}{N^2}\sum_{i=1}^{N}\sum_{J=1}^{N} b_{ij}\left(\tau_{ij}(x,z)\right)\right]^2, \qquad b_{ij}(t) = \begin{cases} -1 & ,if\ \ v_{ij}(t) < 0 \\ 1 & ,if\ \ v_{ij}(t) \geq 0 \end{cases}, \tag{14}$$

where σ is the standard deviation of the polarity $b_{ij}(t)$ of the aperture data; $b_{ij}(t)$ is the polarity or algebraic sign of the aperture data.

Minimum variance distortionless response (MVDR), also known as Capon's method, divides the signals into several subspaces. It can minimize the mean output power of the noise and interference. Their weights are determined by finding the vector to suppress undesired modes and incident angles [38]. One challenge associated with MVDR imaging is sensitive to the assumed look direction, which depends upon possibly unknown scattering characteristics [33].

Through adding a diagonal loading term, $\alpha\mathbf{I}$, to $\widehat{\mathbf{S}}\ (\omega)$, to obtain a non-singular $\widehat{\mathbf{S}}\ (\omega)$, in which α is proportional to the power of the received signals [39]. The incident angle and wavenumber of

http://dx.doi.org/10.5772/intechopen.79475

the signals are acquired through searching an array steering vectors that is orthogonal to the noise subspace. The MUSIC algorithm can provide the location or the direction-of-arrival of the active sources in the field with its high spatial resolution capability. Han et al. [40] used the time-frequency MUSIC [41] beamforming procedure to eliminate the effects of the direct excitation signals and the boundary-reflected wave signals. It is better than TFM for adjacent defect imaging when the signal-to-noise ratio is lower than 20dB [42]. **Figure 5** plots the comparison of the flow chart of the MVDR and the MUSIC algorithm.

Decomposition of the time-reversal operator (DORT) refocuses the wave energy back on multiple scatters, even for those that are neither small nor perfectly resolved. The whole DORT process is described in detail in Ref. [43]. DORT algorithm has the capability of individually imaging these scatters by back-propagating the eigenvectors obtained from eigenvalue decomposition of the time-reversal operator, providing separate information about each scatterer. When the scatterers are relatively large compared to the excitation wavelength, a single scatterer may generate multiple significant eigenvalues. In this case, the back-propagation of the eigenvectors can provide a certain amount of information about the relatively large scatterers. Time-reversal multiple signal classification algorithm was originally proposed by Schmidt [44]. Lehman and Devaney [45] developed a combined DORT and MUSIC algorithm, termed DORT-MUSIC, to image multiple buried cylinders in the seismo-acoustic application. He et al. [46] adopted the DORT-MUSIC in space-frequency domain for separating imaging from both the actuator-to-damage and the sensor-to-damage. The dispersion, multimode, and multireflection nature of Lamb waves have serious influence on the imaging performance of DORT, MUSIC, and DORT-MUSIC.

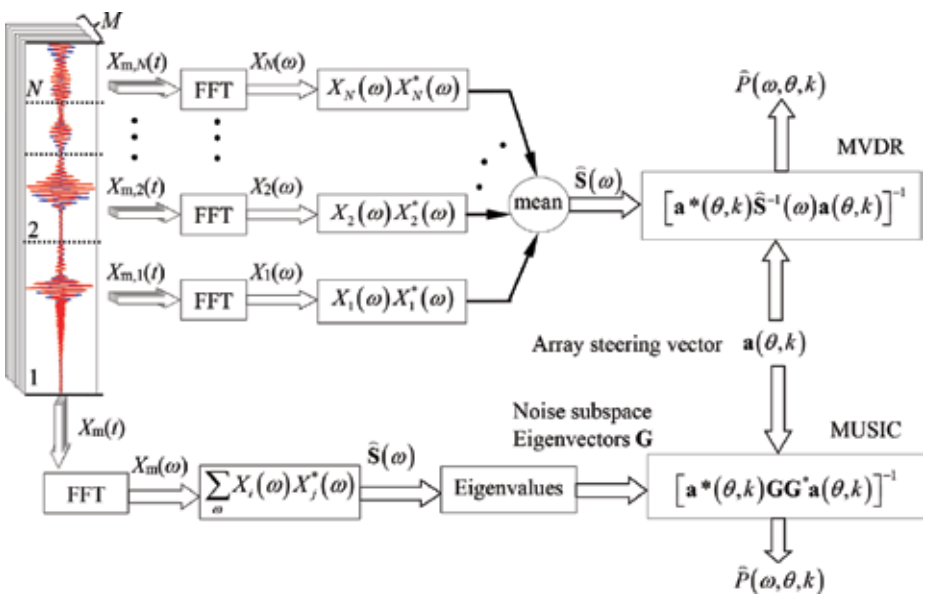

Figure 5. Comparison of the flow chart of the MVDR and the MUSIC algorithm.

Synthetic aperture focusing technique (SAFT) focuses the acoustic field along the 1D linear array toward the location of scatterer based on the angular and the distance information. It is first proposed for body waves defect detection. Sicard et al. [47] presented an F-SAFT algorithm for Lamb waves imaging in which the dispersion nature of Lamb waves is considered. Furthermore, multidefects detection in an isotropic plate was realized. Other algorithms for far-field defect imaging based on the wavenumber analysis have the spatial-wavenumber filter (SWF) [48–50] and wavenumber filtering algorithm [51]. Ren and Qiu [49, 52] proposed a scanning spatial-wavenumber filter-based diagnostic imaging method for online characterization of multi-impact event. The procession does not rely on any modeled or measured wavenumber response. The formulae of SCFT and the SWF are expressed as Eqs. (15)–(18), respectively.

$$I_{\mathrm{SCFT}}(x,d) = \mathit{ifft}\left(\sum_{f\in\Omega} s(k_x,d,f)\right),\ \ s(k_x,d,f) = \mathit{fft}(u(x,t))\exp\left(2\pi d i\sqrt{\frac{f^2}{\left(c_p(f\times 2h)/2\right)^2}-k_x^2}\right), \tag{15}$$

$$I_{\mathrm{SWF}}(k,t_r) = \sum\left|u(x,t_r)\otimes\phi(x)\right| = \sum\left|4\pi^2 A(t_r)\delta(k-k_a\cos\theta_a)\delta(k-k_a\cos\theta)\right|, \tag{16}$$

$$A(t_r) = u(t_r)e^{i\omega t_r}e^{-ik_a l_a}, \tag{17}$$

$$\phi(x) = \left[e^{ik_a x_1\cos\theta}, e^{ik_a x_2\cos\theta}, \ldots, e^{ik_a x_m\cos\theta}, \ldots, e^{ik_a x_M\cos\theta}\right], \tag{18}$$

where I_{SCFT} is the imaging result of SAFT, $u(x,t)$ is the spatial response acquired by the linear array, d is the propagation distance, k_x is the wavenumber in x direction; I_{SWF} is the imaging result of the SWF, $u(x,t_{\mathrm{r}})$ is the response acquired at time t_r, $\otimes$ indicates the convolution operation, $\phi(x)$ is the original spatial-wavenumber filter, a is the number of the transducer, θ_a, l_a are the angle and the distance of the damage respectively, k_a is the wavenumber at direction θ_a.

2.4. Full wavefield imaging techniques

With the aid of the laser ultrasonic system, the strategy used for capturing the full propagation wavefield relies on experiment settings in which one transducer at a fixed position and the second transducer as a movable point, actuator-sensor synchronization and signal registration at one point, in a repetitive manner at various locations. The time delay is introduced between consecutive wave excitations in order to wait until the wave fully attenuates. Researchers adopted the compressive sensing algorithm [53, 54] or combined binary search and compressed sensing [55] to improve the efficiency of full wavefield data acquisition. Once time-space wavefield data are acquired, data analysis can be implemented in time-space domain and frequency-wavenumber domain. The original signal process techniques are used for studying the amplitude information to observe the wave reflection with the root mean square and cumulative kinetic energy methods. Moreover, advanced signal processing techniques with 2D Fourier transform [44], such as wavenumber filtering, frequency-wavenumber analysis, space-frequency-wavenumber analysis, local wavenumber domain analysis, give the possibility

of damage size estimation [56, 57]. Mode separation can be performed similarly for reflection separation [58].

The imaging techniques based on time-domain signal process have the integral mean value (IMV), the root mean square (RMS), and the weighted root mean square (WRMS) [59] that can be expressed as Eqs. (19)–(22), respectively.

$$\mathrm{IMV}(u(t)) = \frac{1}{t_2 - t_1}\int_{t_1}^{t_2} u(t)dt \approx \frac{1}{n}\sum_{k=1}^{n} u_k, \tag{19}$$

$$\mathrm{RMS}(u(t)) = \sqrt{\frac{1}{t_2 - t_1}\int_{t_1}^{t_2}\left[u(t)^2\right]dt} \approx \sqrt{\frac{1}{n}\sum_{k=1}^{n}\left[u_k^2\right]}, \tag{20}$$

$$\mathrm{WRMS}(u(t)) = \sqrt{\frac{1}{t_2 - t_1}\int_{t_1}^{t_2}\left[w(t)u(t)^2\right]dt} \approx \sqrt{\frac{1}{n}\sum_{k=1}^{n}\left[w_k u_k^2\right]}, \tag{21}$$

$$w_k = w(t_k) = k^m, m \geq 0 \tag{22}$$

where $u(t)$ is the received signals at n points. For a discrete signal u_r=$u(t_r)$ sampled at n points with time intervals Δt, following relation can be written as u_k=$u(t_k)$, t_k=t_1+(k-1)Δt, Δt=(t_2-t_1)/(n-1), k=1,2,…,n. $w(t)$ is a weighting factor, which decreases the importance of the time samples closer to the beginning of the sampling process and increases the importance of the samples closer to its end. t_1 and t_2 denote the beginning and the end of the sampling process, respectively. The weighting factor w_k=k (m=1), the importance (weight) of particular time samples, increases linearly with time t; this importance (weight) increases as a square function of time t when the weighting factor is w_k=k^2 (m=2).

The effectiveness of the applied algorithms is strongly dependent on the calculation parameters (weighting factor and time window), excitation frequency, and damage types. The extension of the time window leads to the increase in differences in the WRMS values between the damaged and undamaged areas. The constant weighting factors do not provide efficient results due to the high influence of the incident wave at excitation point. The statistical analysis of the calculated WRMS values was adopted to successfully supplement the visual assessment of the defect imaging [60].

The multidimensional Fourier transform maps the time-space domain signals into the frequency-wavenumber domain and realizes defect imaging; the formula of the transform can be expressed as

$$I(\omega, k_x, k_y) = \int_{-\infty}^{\infty}\int_{-\infty}^{\infty}\int_{-\infty}^{\infty} u(x,y,t)W(x-a, y-b)e^{-i\left(\omega t + k_x x + k_y y\right)}dydxdt, \tag{23}$$

where $u(x,y,t)$ is the full wavefield data; a and b are the coordinates of the window function in x and y dimension; W is the window with various of types, including rectangle window, Gauss window, and Hanning window. For a Hanning window with a diameter of D_r, W can be expressed as

$$W(x,y) = \begin{cases} 0.5\left[1-\cos\left(2\pi\dfrac{\sqrt{x^2+y^2}}{D_r}\right)\right] & if\ \sqrt{x^2+y^2} \le 0.5D_r \\ 0 & \text{otherwise} \end{cases}. \tag{24}$$

The wavenumber adaptive image filtering is introduced in reference [61] and further expanded in reference [62] in which the data are transformed from Cartesian coordinates to polar coordinates. In the frequency-wavenumber domain, the filtering is applied to separate the different modes or forward and backward waves, as shown in Eq. (25).

$$\tilde{S}(\omega, k_r; \theta_i) = I(\omega, k_r; \theta_i) W(k_r, \omega), \tag{25}$$

where $\tilde{S}(\omega, k_r; \theta_l)$ is the separating waves in frequency-wavenumber domain, $I(\omega,k_r;\theta_i)$ is the frequency-wavenumber result of the $u(t,r;\theta)$ in polar coordinates; θ_i is the specific angle index; $W(k_r,\omega)$ is a 2D window function operating as a filter in frequency-wavenumber domain.

Finally, the filtered data are successively transformed back to the time domain in polar coordinates and Cartesian coordinates.

Harley et al. [63] presented a baseline-free, model-driven, statistical damage detection, and imaging framework for guided waves measured from partial wavefield scans in which the sparse wavenumber analysis, sparse wavenumber synthesis, and data-fitting optimization to accurately model damage-free wavefield data. Kudela et al. [64] combined the time-distance mapping technique and novel Lamb waves focusing technique to realize crack detection. Meanwhile, the temperature effect is compensated by using the temperature-dependent dispersion curve. Pai et al. [65] presented a dynamics-based methodology for accurate damage inspection of thin-walled structures by combining a boundary effect evaluation method for space-wavenumber analysis of measured operational deflection shapes and a conjugate-pair decomposition method for time-frequency analysis of time traces of measured points. Li et al. [66] proposed a correlation filtering-based matching pursuit signal processing approach to realize precise value of time of flight and locating and sizing the delamination in composite beams. Through analysis, the reflection intensity of Lamb waves from an elliptical damage realized defect sizing [67]. Perelli et al. [68] combined the wavelet packet transform and frequency warping to generate a sparse decomposition of the acquired dispersive signal. Tofeldt et al. [69] presented a 2D array and wide-frequency bandwidth technique for Lamb waves phase velocity imaging. Through a discrete Fourier transform, a spectral estimate is obtained for the 2D array in the frequency-phase velocity domain. The variation of the phase velocity is then mapped using a stepwise movement of the 2D array within the complete measurement domain.

3. Intelligent recognition techniques

There are mainly two steps for defect recognition in structure integrity evaluation, i.e., feature extraction and classifier design. Time-frequency and time-scale analysis techniques

http://dx.doi.org/10.5772/intechopen.79475

are adopted for feature extraction, including dynamic wavelet fingerprinting, wavelet transform (CWT, DWT, and wavelet packet decomposition), and statistical features [70]. While the processing of the feature extraction with these techniques may be very time consuming [71] and cannot ensure the feature data are optimally suitable for mapping the state of structures. Additionally, overtrain may be induced with the available dataset for these methods. So, many techniques have been developed to optimize the feature extraction process. The principal component analysis (PCA) is one of the most widely used linear mapping techniques for feature reduction [72, 73]. Nonlinear mapping techniques reduce dimensionality following the criterion which minimizes the difference between interpoint distances of the initial and detection/monitoring feature space, including Sammon mapping, self-organizing maps, and the generative topographic maps [74]. In the following part of this section, we focus on the introduction of the pattern recognition model that attracted relatively more attention in structure integrity evaluation, such as support vector machine, Bayesian methodology, and neural networks.

3.1. Support vector machine

Support vector machine (SVM) is a supervised learning classifier that uses a kernel function to form a hypothesis space in a high-dimensional feature space for linear and nonlinear classification. The principle schematic diagram of support vector machine is plotted in **Figure 6**. The kernel function may be a linear, polynomial, sigmoid, or custom kernels. Given a set of training examples that are belonging to two categories, an SVM training algorithm builds a model that assigns the examples to one category or the other. In this case, the SVM is a nonprobabilistic binary linear classifier that is not common in practical application. For nonlinear classification and regression problems, the input data are mapped to another linearly separable space using a nonlinear kernel function ϕ and the normal linear SVM. The least squares support vector machine (LS-SVM) is an improved variant of SVM. It can increase the convergence rate for complex problems [75]. The general formula of the LS-SVM can be expressed as

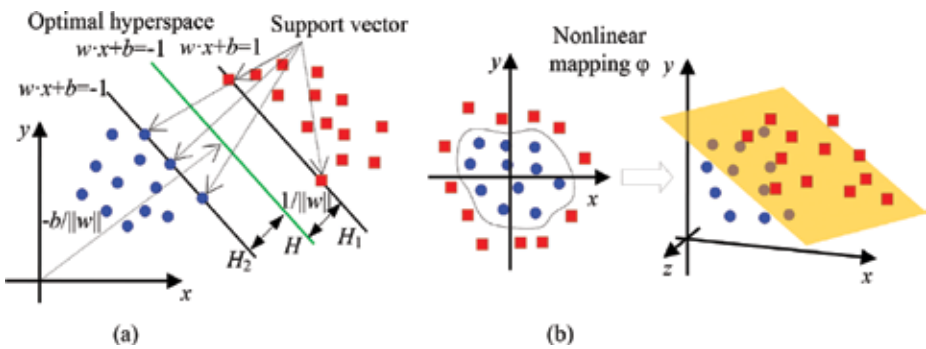

Figure 6. Principle schematic diagram of support vector machine. (a) Linearly separable space with linear function and (b) linearly separable space with nonlinear function.

$$y(x) = w^T \phi(x) + b, \tag{26}$$

where the term $\phi(\cdot)$ is a nonlinear mapping function, $w \in R^n$ and $b \in R$ are the mode parameters.

SVM is a robust classifier in the existence of noise and more computational efficient than artificial neural network (ANN) [76]. Das et al. [77] developed an one-class SVM algorithm to characterize and classify different damage states in composite laminates by measuring the change in the signature of the Lamb waves that propagates through the anisotropic media under forced excitations. Park et al. [78] used SVM to enhance the damage identification with the extracted damage features. In the study, multifeatures were extracted for mapping the state of structures, including TOF, the root mean square deviations (RMSD) of the impedances, and wavelet coefficients (WC) of Lamb waves. Then, in Ref. [79], the same authors proposed a two-step support vector machine (SVM) classifier for railroad track damage identification that forms optimal separable hyperplanes. In the study, a two-dimensional damage feature space was built with the root mean square deviations (RMSD) of impedance signatures and the sum of square of wavelet coefficients for maximum energy mode of guided waves. In the process, the damage detection was accomplished by the first step-SVM, and damage classification was carried out by the second step-SVM. Sun et al. [80] adopted genetic algorithm to optimize the LS-SVM parameters in which normalized amplitude, phase change, and correlation coefficient were proposed to build the damage features.

3.2. Bayesian methodology

The Bayes' theorem combines a prior belief and the observation regarding the related parameters through the likelihood function to update the distribution of the interested parameters in which the model parameters u can be updated using the observation data θ, as expressed as

$$q(u) \propto p(u)p(\theta|u), \tag{27}$$

where $p(u)$ is the prior distribution of the model parameters u that can be a vector for multiple parameters. $p(\theta \mid u)$ is the likelihood function. $q(u)$ is the posterior distribution of updated parameter u.

$$q(\theta|x_1, x_2, \ldots, x_n) \propto p(\theta) \left(\frac{1}{\sqrt{2\pi}\sigma_\varepsilon}\right)^n \times \exp\left\{-\frac{1}{2}\sum_{i=1}^{n}\left[\frac{x_i - M(\theta)}{\sigma_\varepsilon}\right]^2\right\}, \tag{28}$$

where $M(\theta)$ is a parameterized model describing the relationship between the signal features and damage information. σ_ε is the standard deviation of the error term. The posterior distribution of each parameter is estimated by the samples generated with the Markov-Chain Monte-Carlo method.

Bayesian methodology is a probabilistic detection technique that has the ability to consider the uncertainties such as measurement uncertainty, and model parameter uncertainty in damage

detection/monitoring. A multivariate regression model is proposed to correlate damage features, the phase change, and normalized amplitude, to the actual crack size [81]. It is a baseline crack size quantification model can also use for more general and complex structures. Prior distributions of model parameters are obtained using the coupon test data. The posterior distribution of the parameters and the posterior distribution of θ in a multivariate regression model are expressed as Eq. (28). A multilevel Bayesian framework is proposed for identifying the position and the effective mechanical properties of the damaged layers in composite laminates [82] in which the framework is initially applied to a set of synthetic signals with increasing levels of noise and complexity. He et al. [83] employed the Bayesian model to determine the crack number, and then, the Bayesian statistical framework was used to identify the crack parameters and the associated uncertainties in beam-like structures. The proposed method is able to accurately identify the number, locations, and sizes of the cracks, and is robust under measurement noise.

Bayesian imaging method (BIM) is used to build the likelihood function using the differences between the model predictions and the field observations. The structure is discretized into many small cells, and each cell is assigned an associated probability of damage, such as the location and size. Next, the overall posterior distribution of the parameters can be obtained by combining the prior information about the parameters. The marginal posterior distribution of each parameter is estimated by the samples generated using the Markov-Chain Monte-Carlo method. Given the parameter samples, the probability of damage in each cell is computed using the ratio of the number of samples falling into each cell to the total number of samples. Following the damage probability distribution can be used to construct an image that directly represents the damage location and size. Peng et al. [84] presented a Bayesian imaging technique to simultaneously estimate damage location and size, as well as the corresponding uncertainty bounds. Neerukatti et al. [85] used a sequential Bayesian technique to combine a physics-based damage prognosis model with a data-driven probabilistic damage localization approach for effective damage localization and prognosis in complex metallic structures. Sohn et al. [86] proposed an instantaneous damage diagnosis based on the concepts of time reversal acoustics and consecutive outlier analysis to minimize damage misclassification without relying on past baseline data.

Gaussian mixture model (GMM) is a probability static method for characterizing uncertainties based on unsupervised learning. This method organizes itself according to the nature of the input data with probability distributions without any prior knowledge. The GMM has the advantages of better robustness of uncertainties and high efficiency with lower computational complexity with a relatively small number of model parameters. PCA is used to reduce the dimensions of the extracted multistatistical characteristic parameters of the excited Lamb waves, then training the damage identification system using the GMM [73]. Several statistical characteristic parameters, including the root mean square (RMS), variance, skewness, kurtosis, peak-to-peak (PPK), and K-factor, are extracted as the input for the GMM-processed Lamb wave-based identification model. Qiu et al. [72] proposed an online updating Gaussian mixture model (GMM), for aircraft wings par damage evaluation under time-varying boundary conditions in which the formulas are expressed as Eqs. (29) and (30).

$$\phi(f_r|\boldsymbol{\mu},\boldsymbol{\Sigma}) = \sum_{i=1}^{C} w_i \phi_i(f_r|\boldsymbol{\mu}_i,\boldsymbol{\Sigma}_i), \tag{29}$$

$$\phi_i(f_r|\boldsymbol{\mu}_i,\boldsymbol{\Sigma}_i) = \frac{1}{(2\pi)^{d/2}} \exp\left\{-\frac{1}{2}(f_r-\boldsymbol{\mu}_i)^T \sum_i^{-1}(f_r-\boldsymbol{\mu}_i)\right\}, \tag{30}$$

where $f=\{f_1,f_2,\ldots,f_k\}$ is a random sample set composed by k independent random samples. f_r denotes a d-dimensional sample in the sample set, where $f_r=\{f_1,f_2,\ldots,f_d\}^T$ and $r=1,2,\ldots,k$, $\boldsymbol{\mu}_i$, Σ_i and w_i are the mean, the covariance matrix and the mixture weight of the i^{th} Gaussian component, respectively, and $i=1,2,\ldots C$, C is the number of Gaussian components, $\phi_i(f_r|\boldsymbol{\mu}_i, \Sigma_i)$ is the probability density of each Gaussian component is a d-dimensional Gaussian function.

3.3. Neural networks

Neutral network is comprised of layouts that are built with artificial neurons, termed nodes. These nodes in the adjacent layers are connected to each other with various of strengths (weights). The high weights value indicates a strong connection; vice versa, it is a weak connection. **Figure 7** shows the principle diagram of a three-layer neutral network in which the three-layer neural

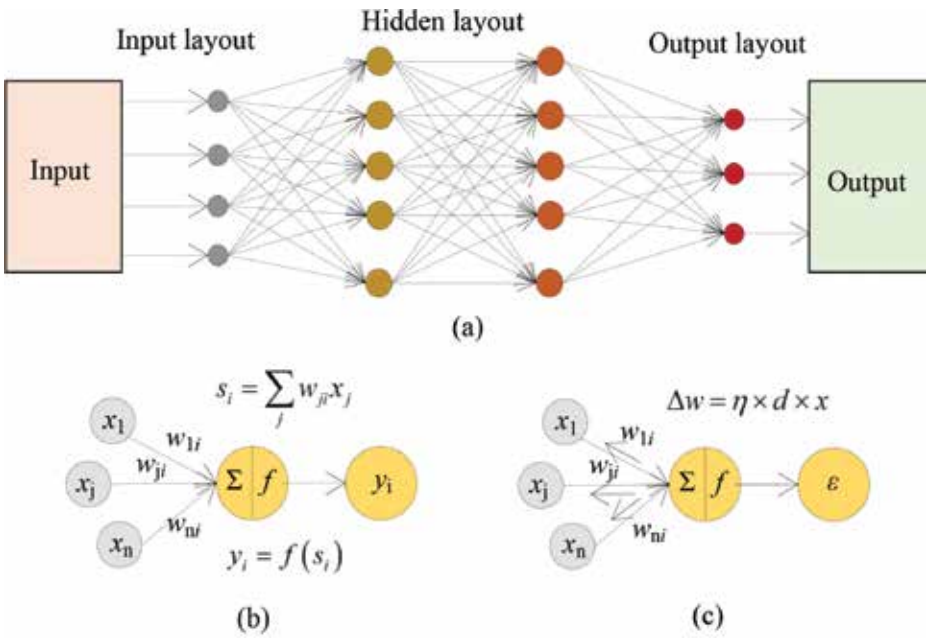

Figure 7. Principle diagram of a three-layer neural network. (a) Three-layer neural network, (b) forward, and (c) backward.

http://dx.doi.org/10.5772/intechopen.79475

network, the forward and the backward principles are plotted in **Figure 7(a)**, **(b)** and **(c)**, respectively. There exists three types of nodes including input nodes, hidden nodes, and output nodes. Except the input layer out, there is a transfer function in each node to transfer input data to the connected nodes in the adjacent layout. The typical transfer function used in a neural network classifier has the unit step (threshold), sigmoid, piecewise linear, and Gaussian. The training of neutral networks consists of the forward propagation and the backward propagation. In the forward propagation process, the input nodes take the feature date into the model. The information is presented as activation values, where each node is given a value, the higher value, the greater activation. Based on the weights, inhibition or excitation, and transfer functions, the activation value is passed from node to node. The activation values at each node are summed. Then, the value is modified based on its transfer function. The activation flows through the network, through hidden layers, until it reaches the output nodes. Then, the difference between the output value and actual value (error) modified with the backward propagation process with gradient descent algorithm until satisfy a stop threshold. The diagnostic efficiency and precision are highly dependent on the network architecture [87]. The traditional artificial neural networks (ANNs) have been adopted in defect recognition such as welding defects [88], delamination in composite structures [89], and composite plates structural health monitoring [90]. De Fenza et al. [91] combined the ANN and the probability ellipse method to determine the location and degree of defects in aluminum and composite plates.

Benefiting from the flexible configuration of neural networks, researcher developed many kinds of neural networks used in structure integrity evaluation. Probabilistic neural network (PNN) combines the Bayes decision strategy with the Parzen nonparametric estimator of the probability density functions in which the interpretation of the neural network is in the form of a probability density function. An accepted norm for decision strategies used to classify patterns is that they minimize the "expected risk." Park et al. [92] adopted the PNN and SVM to online monitoring the state of jointed plates in which the extracted damage feature that constructed with the ToF and the wavelet coefficient obtained from wavelet transforms of Lamb wave signals. Kohonen neural network (KNN) has two layers, input layer and output layer, and is used for honeycomb sandwich and carbon fiber composite structures studied in which the amount of neuron in input layer is determined by input vector dimensions [93]. The neurons of output layer layout form a 2D plane. In regression neural networks for pattern recognition, a trained network produces large errors when some parts of the test pattern are not found in the training pattern. The weight-range selection (WRS) method has a supervised multilayer perceptron operating with one hidden layer of neurons and trained using a back-propagation algorithm to eliminate the large errors induced by the case a test pattern not found in the training set [94]. Anaya et al. [95] adopted an artificial immune system (AIS) and the notion of affinity was used for the sake of damage detection and used a fuzzy *c*-means algorithm is used for damage classification of an aircraft skin panel. Compared with standard Lamb waves based methods, there is no need to directly analyze the complex time-domain traces containing overlapping, multimodal, and dispersive wave propagation. Other kinds of neural networks that have been studied in nondestructive testing have the recurrent neural network (RNN) [96], deep learning network (DLN), and convolutional neural network (CNN).

4. Summary and conclusions

In this chapter, we divided the defects imaging techniques into four categories based on the setting of detection/monitoring system, and the basic principle of them is introduced. Three kinds of intelligent recognition techniques that have been widely studied in Lamb waves structural integrity evaluation are also reviewed.

1. The discrete ellipse imaging algorithm, the hyperbola imaging technique, and the tomography imagine algorithms are processed in the detection/monitoring based on sparse arrays in which the spacing between the adjacent transducers is larger than the wavelength. Discrete ellipse imaging, the hyperbola imaging algorithm, and their optimal type are processed with the defect scattering signals. The pixel intensity is drawn in an elliptical trajectory and the hyperbola trajectory, respectively. Both of the algorithms are imaging with the amplitude information and sensitive to the dispersion and the SNR of signals. The imaging performance is closely related with transducer numbers and the signal resolutions. In the tomography technique, the distribution of sensing points has relative regular forms such as the parallel, square, or circular. The imaging algorithms used in the tomography have PRA algorithms, FBP-based algorithm, the ART-based algorithms, and the novel algorithms such as the HARBUT and FWI. With the dense ray in the detection, defect sizing can be realized with the tomography techniques, particularly for the HARBUT, and FWI has attractive performance in accuracy corrosion defect imaging.

2. Compact array in which the spacing of the adjacent transducers is shorter than the wavelength that with various of shapes have been developed in Lamb waves based defects imaging, including 1D linear array, 2D rectangular, circular, and spiral arrays. The defect imaging algorithms based on compact arrays have PA, SA, and the full wavefield techniques. The TFM, SCF, MVDR, MUSIC, SAFT-based imaging algorithms, and the SWF can be used for full-scale scanning of the plate and realizing defect location. The TFM is an imaging algorithm with the amplitude information that is sensitive to the dispersion nature of Lamb waves. The phase information-based algorithms, PCF, SCF, have relatively more robust imaging performance than TFM. Besides these algorithms, MVDR, MUSIC, SAFT, and SWF have the potential used for baseline-free detection. The full wavefield techniques have the ability for defect accuracy imaging by analyzing the received full wavefield data. Among them, the IMV, RMS, and WRMS are adopted to time-domain analysis for defect location and sizing. With the 2D Fourier transform, the received time-space data are mapped into frequency-wavenumber domain, and defect sizing and thinning quantification are realized through analysis of the spatial wavenumber information. Meanwhile, many optimization techniques with the added windows are adopted to separate the scattering waves in frequency-wavenumber domain for reflection waves separation, defect imaging can be enhanced.

3. SVM, Bayesian methodology, and the neural networks are three kinds of typical classifiers used in Lamb waves based structure integrity evaluation. SVM maps the input data that indicates the state of the structures into a hypothesis space with a kernel function that may be a linear, polynomial, or custom kernel. The classifiers based on SVM have the one-class

SVM, LS-SVM, two-step SVM. Bayesian methodology realizes the observation of data estimation with the prior received data. For the Bayesian methodology, the state of structures is predicated with the prior distributions of model parameters obtained using the coupon test data. The related techniques have the multilevel Bayesian model, Bayesian imaging method, and the GMM. Among them, the GMM is a probability static method with unsupervised learning property. It has the advantages of better robustness of uncertainties and high efficiency with lower computational complexity with a relatively small number of model parameters. Neural networks are a supervise classifier based on the back-propagation algorithm to optimize the model parameters. Benefiting from the flexible configuration of neural networks, researchers developed many kinds of neural networks for structure integrity evaluation. During the past decade, ANN, PNN, KNN, CNN, etc., have been applied for on- or offline structure integrity evaluation with the extracted Lamb waves defect information. These neural networks can realize accurate defect recognition in the case they are trained with enough dataset. Meanwhile, they have low noise tolerance in field applications.

Acknowledgements

This work was supported by the National Natural Science Foundation of China (Grant Nos. 51475012, 11772014, 11527801, and 11272021).

Conflict of interest

We declare that we do not have any commercial or associative interest that represents a conflict of interest in connection with the work submitted.

Author details

Zenghua Liu* and Honglei Chen

*Address all correspondence to: liuzenghua@bjut.edu.cn

College of Mechanical Engineering and Applied Electronics Technology, Beijing University of Technology, Beijing, China

References

[1] Liu ZH, Yu FX, Wei R, He CF, Wu B. Image fusion based on single-frequency guided wave mode signals for structural health monitoring in composite plates. Materials Evaluation. 2013;**71**:1434-1443

[2] Muller A, Robertson-welsh B, Gaydecki P, Gresil M, Soutis C. Structural health monitoring using Lamb wave reflections and total focusing method for image reconstruction. Applied Composite Materials. 2017;**24**:553-573. DOI: 10.1007/s10443-016-9549-5

[3] Croxford AJ, Wilcox PD, Drinkwater BW, Konstantinidis G. Strategies for guided-wave structural health monitoring. Proceedings of the Royal Society A: Mathematical Physical and Engineering Sciences. 2007;**463**:2961-2981

[4] Michaels JE, Michaels TE. Guided wave signal processing and image fusion for in situ damage localization in plates. Wave Motion. 2007;**44**:482-492. DOI: 10.1016/j.wavemoti.2007.02.008

[5] Shan SB, Qiu JH, Zhang C, Ji HL, Cheng L. Multi-damage localization on large complex structures through an extended delay-and-sum based method. Structural Health Monitoring. 2016;**15**:50-64. DOI: 10.1177/1475921715623358

[6] Michaels JE. Detection, localization and characterization of damage in plates with an in situ array of spatially distributed ultrasonic sensors. Smart Materials and Structures. 2008;**17**:35035. DOI: 10.1088/0964-1726/17/3/035035

[7] Flynn EB, Todd MD, Wilcox PD, Drinkwater BW, Croxford AJ. Maximum-likelihood estimation of damage location in guided-wave structural health monitoring. Proceedings of the Royal Society A: Mathematical Physical and Engineering Sciences. 2011;**467**:2575-2596. DOI: 10.1098/rspa.2011.0095

[8] Gao DY, Wu ZJ, Yang L, Zheng YB. Guide waves-based multi-damage identification using a local probability-based diagnostic imaging method. Smart Materials and Structures. 2016;**25**:45009. DOI: 10.1088/0964-1726/25/4/045009

[9] Leonard KR, Malyarenko EV, Hinders MK. Ultrasonic Lamb wave tomography. Inverse Problems. 2002;**18**:1795-1808. DOI: 10.1088/0266-5611/18/6/322

[10] Liu ZH, Yu HT, Fan JW, Hu YN, He CF, Wu B. Baseline-free delamination inspection in composite plates by synthesizing noncontact air-coupled Lamb wave scan method and virtual time reversal algorithm. Smart Materials and Structures. 2015;**24**. DOI: 10.1088/0964-1726/24/4/045014

[11] Liu ZH, Zhong XW, Dong TC, He CF, Wu B. Delamination detection in composite plates by synthesizing time-reversed Lamb waves and a modified damage imaging algorithm based on RAPID. Structural Control and Health Monitoring. 2017;**24**:1-17. DOI: 10.1002/stc.1919

[12] Lee J, Sheen B, Cho Y. Multi-defect tomographic imaging with a variable shape factor for the RAPID algorithm. Journal of Visualization. 2016;**19**:393-402. DOI: 10.1007/s12650-015-0290-1

[13] Lee J, Sheen B, Cho Y. Quantitative tomographic visualization for irregular shape defects by guided wave long range inspection. International Journal of Precision Engineering and Manufacturing. 2015;**16**:1949-1954. DOI: 10.1007/s12541-015-0253-4

[14] Keulen CJ, Yildiz M, Suleman A. Damage detection of composite plates by Lamb wave ultrasonic tomography with a sparse hexagonal network using damage progression trends. Shock and Vibration. 2014;**2014**:1-8. DOI: 10.1155/2014/949671

[15] Sheen B, Cho Y. A study on quantitative Lamb wave tomogram via modified RAPID algorithm with shape factor optimization. International Journal of Precision Engineering and Manufacturing. 2012;**13**:671-677. DOI: 10.1007/s12541-012-0087-2

[16] Zhao XL, Gao HD, Zhang GF, Ayhan B, Yan F, Kwan C, Rose JL. Active health monitoring of an aircraft wing with embedded piezoelectric sensor/actuator network: I. Defect detection, localization and growth monitoring. Smart Materials and Structures. 2007;**16**:1208-1217. DOI: 10.1088/0964-1726/16/4/032

[17] Torkamani S, Roy S, Barkey ME, Sazonov E, Burkett S, Kotru S. A novel damage index for damage identification using guided waves with application in laminated composites. Smart Materials and Structures. 2014;**23**. DOI: 10.1088/0964-1726/23/9/095015

[18] Wright W, Hutchins D, Jansen D, Schindel D. Air-coupled Lamb wave tomography. IEEE Transactions on Ultrasonics, Ferroelectrics, and Frequency Control. 1997;**44**:53-59. DOI: 10.1109/58.585190

[19] Mokhtari AA, Ohadi A, Amindavar H. Polygonal damage shape reconstruction in plates using guided Lamb wave. Structural Control and Health Monitoring. 2017;**24**:e1907. DOI: 10.1002/stc.1907

[20] Nagata Y, Huang J, Achenbach JD, Krishnaswamy S. Lamb wave tomography using laser-based ultrasonics. In: Proceedings of the Annual Review of Progress in Quantitative Nondestructive Evaluation; 31 July–04 August 1994; Snowmass Village. New York: Plenum Press Div Plenum Publishing Corp; 1995. pp. 561-568

[21] Ladas KT, Devaney AJ. Generalized ART algorithm for diffraction tomography. Inverse Problems. 1991;**7**:109-125. DOI: 10.1088/0266-5611/7/1/011

[22] Wang DJ, Zhang WF, Wang XY, Sun B. Lamb-wave-based tomographic imaging techniques for hole-edge corrosion monitoring in plate structures. Materials. 2016;**9**:916. DOI: 10.3390/ma9110916

[23] Prasad SM, Balasubramaniam K, Krishnamurthy CV. Structural health monitoring of composite structures using Lamb wave tomography. Smart Materials and Structures. 2004;**13**:N73-N79. DOI: 10.1088/0964-1726/13/5/N01

[24] Malyarenko EV, Hinders MK. Ultrasonic Lamb wave diffraction tomography. Ultrasonics. 2001;**39**:269-281. DOI: 10.1016/S0041-624X(01)00055-5

[25] Miller CA, Hinders MK. Classification of flaw severity using pattern recognition for guided wave-based structural health monitoring. Ultrasonics. 2014;**54**:247-258. DOI: 10.1016/j.ultras.2013.04.020

[26] Azimi M, Kak AC. Distortion in diffraction tomography caused by multiple scattering. IEEE Transactions on Medical Imaging. 1983;**2**:176-195. DOI: 10.1109/TMI.1983.4307637

[27] Huthwaite P, Simonetti F. High-resolution guided wave tomography. Wave Motion. 2013; **50**:979-993. DOI: 10.1016/j.wavemoti.2013.04.004

[28] Rao J, Ratassepp M, Fan Z. Guided wave tomography based on full waveform inversion. IEEE Transactions on Ultrasonics, Ferroelectrics, and Frequency Control. 2016;**63**:737-745. DOI: 10.1109/TUFFC.2016.2536144

[29] Rao J, Ratassepp M, Fan Z. Investigation of the reconstruction accuracy of guided wave tomography using full waveform inversion. Journal of Sound and Vibration. 2017;**400**: 317-328. DOI: 10.1016/j.jsv.2017.04.017

[30] Stepinski T, Ambrozinski L, Uhl T. Designing 2D arrays for SHM of planar structures: A review. In: Proceedings of the Conference on Nondestructive Characterization for Composite Materials, Aerospace Engineering, Civil Infrastructure, and Homeland Security; 11–14 March 2013; San Diego. Bellingham: SPIE Press; 2013. pp. 86941-86941

[31] Tian ZH, Leckey CAC, Yu LY. Phased array beamforming and imaging in composite laminates using guided waves. In: Proceedings of the SPIE Conference on Health Monitoring of Structural and Biological Systems; 21–24 March 2016; Las Vegas. Bellingham: SPIE Press; 2016. p. 980505

[32] Michaels JE, Michaels TE. Adaptive imaging of damage from changes in guided wave signals recorded from spatially distributed arrays. In: Proceedings of the Conference on Health Monitoring of Structural and Biological Systems, 8–12 March 2009, San Diego, California: SPIE Press; 2009, 7295: p. 729515. DOI:10.1117/12.815849

[33] Camacho J, Parrilla M, Fritsch C. Phase coherence imaging. IEEE Transactions on Ultrasonics, Ferroelectrics, and Frequency Control. 2009;**56**:74-958. DOI: 10.1109/TUFFC.2009.1128

[34] Liu ZH, Sun KM, Song GR, He CF, Wu B. Damage localization in aluminum plate with compact rectangular phased piezoelectric transducer array. Mechanical Systems and Signal Processing. 2016;**70-71**:625-636. DOI: 10.1016/j.ymssp.2015.09.022

[35] Prado VT, Higuti RT, Kitano C, Martinez-Graullera O, Adamowski JC. Lamb mode diversity imaging for non-destructive testing of plate-like structures. NDT&E International. 2013;**59**:86-95. DOI: 10.1016/j.ndteint.2013.06.001

[36] Higuti RT, Martinez-Graullera O, Martin CJ, Octavio A, Elvira L, de Espinosa FM. Damage characterization using guided-wave linear arrays and image compounding techniques. IEEE Transactions on Ultrasonics, Ferroelectrics, and Frequency Control. 2010;**57**:1985-1995. DOI: 10.1109/TUFFC.2010.1646

[37] Prado VT, Higuti RT, Kitano C, Martinez-Graullera Q. Sparse arrays and image compounding techniques for non-destructive testing using guided acoustic waves. Journal of Control Automation and Electrical Systems. 2013;**24**:263-271. DOI: 10.1007/s40313-013-0029-y

[38] Engholm M, Stepinski T. Direction of arrival estimation of Lamb waves using circular arrays. Structural Health Monitoring. 2011;**10**:467-480. DOI: 10.1177/1475921710379512

[39] Li J, Stoica P, Wang ZS. On robust capon beamforming and diagonal loading. IEEE Transactions on Signal Processing. 2003;**51**:1702-1715. DOI: 10.1109/TSP.2003.812831

[40] Han JH, Kim YJ. Time-frequency beamforming for nondestructive evaluations of plate using ultrasonic Lamb wave. Mechanical Systems and Signal Processing. 2015;**54-55**:336-356. DOI: 10.1016/j.ymssp.2014.09.008

[41] Belouchrani A, Amin MG. Time-frequency MUSIC. IEEE Signal Processing Letters. 1999; **6**:109-110. DOI: 10.1109/97.755429

[42] Fan CG, Caleap M, Pan MC, Drinkwater BW. A comparison between ultrasonic array beamforming and super resolution imaging algorithms for non-destructive evaluation. Ultrasonics. 2014;**54**:1842-1850. DOI: 10.1016/j.ultras.2013.12.012

[43] Prada C, Manneville S, Spoliansky D, Fink M. Decomposition of the time reversal operator: Detection and selective focusing on two scatterers. Journal of the Acoustical Society of America. 1996;**99**:2067-2076. DOI: 10.1121/1.415393

[44] Schmidt RO. Multiple emitter location and signal parameter estimation. IEEE Transactions on Antennas and Propagation. 1986;**34**:276-280. DOI: 10.1109/TAP.1986.1143830

[45] Lehman SK, Devaney AJ. Transmission mode time-reversal super-resolution imaging. Journal of the Acoustical Society of America. 2003;**113**:2742-2753. DOI: 10.1121/1.1566975

[46] He JZ, Yuan FG. Lamb wave-based subwavelength damage imaging using the DORT-MUSIC technique in metallic plates. Structural Health Monitoring. 2016;**15**:65-80. DOI: 10.1177/1475921715623359

[47] Sicard R, Goyette J, Zellouf D. A SAFT algorithm for Lamb wave imaging of isotropic plate-like structures. Ultrasonics. 2002;**39**:487-494. DOI: 10.1016/S0041-624X(01)00087-7

[48] Purekar AS, Pines DJ. Damage detection in thin composite laminates using piezoelectric phased sensor arrays and guided Lamb wave interrogation. Journal of Intelligent Material Systems and Structures. 2010;**21**:995-1010. DOI: 10.1177/1045389X10372003

[49] Qiu L, Liu B, Yuan SF, Su ZQ, Ren YQ. A scanning spatial-wavenumber filter and PZT 2-D cruciform array based on-line damage imaging method of composite structure. Sensors and Actuators A: Physical. 2016;**248**:62-72. DOI: 10.1016/j.sna.2016.04.062

[50] Ren YQ, Qiu L, Yuan SF, Bao Q. On-line multi-damage scanning spatial-wavenumber filter based imaging method for aircraft composite structure. Materials. 2017;**10**:519. DOI: 10.3390/ma10050519

[51] Yoo B, Pines DJ. A magnetostrictive phased array sensor using a nickel comb patch for guided Lamb wave-based damage detection. In: Proceedings of the Conference on Sensors and Smart Structures Technologies for Civil, Mechanical, and Aerospace Systems; 26–29 March 2017; Portland. Bellingham: SPIC; 2017. pp. 1-9

[52] Ren YQ, Qiu L, Yuan SF, Su ZQ. A diagnostic imaging approach for online characterization of multi-impact in aircraft composite structures based on a scanning spatial-wavenumber

filter of guided wave. Mechanical Systems and Signal Processing. 2017;**90**:44-63. DOI: 10.1016/j.ymssp.2016.12.005

[53] Esfandabadi YK, De Marchi L, Testoni N, Marzani A, Masetti G. Full wavefield analysis and damage imaging through compressive sensing in Lamb wave inspections. IEEE Transactions on Ultrasonics, Ferroelectrics, and Frequency Control. 2018;**65**:269-280. DOI: 10.1109/TUFFC.2017.2780901

[54] Mesnil O, Ruzzene M. Sparse wavefield reconstruction and source detection using compressed sensing. Ultrasonics. 2016;**67**:94-104. DOI: 10.1016/j.ultras.2015.12.014

[55] Park B, Sohn H, Liu PP. Accelerated noncontact laser ultrasonic scanning for damage detection using combined binary search and compressed sensing. Mechanical Systems and Signal Processing. 2017;**92**:315-333. DOI: 10.1016/j.ymssp.2017.01.035

[56] Tian ZH, Leckey C, Rogge M, Yu LY. Crack detection with Lamb wave wavenumber analysis. In: Proceedings of the Conference on Health Monitoring of Structural and Biological Systems; 11–14 Match 2013; San Diego. Bellingham: SPIE Press; 2013. p. 86952

[57] Yu LY, Tian ZH, Leckey CAC. Crack imaging and quantification in aluminum plates with guided wave wavenumber analysis methods. Ultrasonics. 2015;**62**:203-212. DOI: 10.1016/j.ultras.2015.05.019

[58] Michaels TE, Michaels JE, Ruzzene M. Frequency-wavenumber domain analysis of guided wavefields. Ultrasonics. 2011;**51**:452-466. DOI: 10.1016/j.ultras.2010.11.011

[59] Żak A, Ostachowicz W, Krawczuk M. Damage detection strategies based on propagation of guided elastic waves. Smart Materials and Structures. 2011;**305**:35024. DOI: 10.1088/0964-1726/21/3/035024

[60] Rucka M, Wojtczak E, Lachowicz J. Damage imaging in Lamb wave-based inspection of adhesive joints. Applied Sciences. 2018;**8**:522. DOI: 10.3390/app8040522

[61] Ruzzene M. Frequency-wavenumber domain filtering for improved damage visualization. Smart Materials and Structures. 2007;**16**:2116-2129. DOI: 10.1088/0964-1726/16/6/014

[62] Kudela P, Radzieński M, Ostachowicz W. Identification of cracks in thin-walled structures by means of wavenumber filtering. Mechanical Systems and Signal Processing. 2015;**50-51**:456-466. DOI: 10.1016/j.ymssp.2014.05.041

[63] Harley JB, Chen CC. Statistical partial wavefield imaging using Lamb wave signals. Structural Health Monitoring. 2017. DOI: 10.1177/1475921717727160

[64] Kudela P, Radzienski M, Ostachowicz W, Yang ZB. Structural health monitoring system based on a concept of Lamb wave focusing by the piezoelectric array. Mechanical Systems and Signal Processing. 2018;**108**:21-32. DOI: 10.1016/j.ymssp.2018.02.008

[65] Pai PF, Sundaresan MJ. Space-wavenumber and time-frequency analysis for damage inspection of thin-walled structures. Structural Health Monitoring. 2012;**11**:452-471. DOI: 10.1177/1475921711434860

[66] Li FC, Su ZQ, Ye L, Meng G. A correlation filtering-based matching pursuit (CF-MP) for damage identification using Lamb waves. Smart Materials and Structures. 2006;**15**:1585-1594. DOI: 10.1088/0964-1726/15/6/010

[67] Hu N, Cai YD, Zhu GJ, Tsuji C, Liu YL, Cao YP. Characterization of damage size in metallic plates using Lamb waves. Structural Health Monitoring. 2012;**11**:125-137. DOI: 10.1177/1475921711414230

[68] Perelli A, De Marchi L, Flamigni L, Marzani A, Masetti G. Best basis compressive sensing of guided waves in structural health monitoring. Digital Signal Processing. 2015;**42**:35-42. DOI: 10.1016/j.dsp.2015.04.001

[69] Tofeldt O, Ryden N. Lamb wave phase velocity imaging of concrete plates with 2D arrays. Journal of Nondestructive Evaluation. 2018;**37**(4):13. DOI: 10.1007/s10921-017-0457-x

[70] Staszewski WJ. Advanced data pre-processing for damage identification based on pattern recognition. International Journal of Systems Science. 2000;**31**:1381-1396. DOI: 10.1080/00207720050197776

[71] Maria ML, Kolios AJ, Wang L. Structural health monitoring of off shore wind turbines: A review through the statistical pattern recognition paradigm. Renewable and Sustainable Energy Reviews. 2016;**64**:91-105. DOI: 10.1016/j.rser.2016.05.085

[72] Qiu L, Yuan SF, Chang FK, Bao Q, Mei HF. On-line updating Gaussian mixture model for aircraft wing spar damage evaluation under time-varying boundary condition. Smart Materials and Structures. 2014;**23**. DOI: 10.1088/0964-1726/23/12/125001

[73] Wang Q, Ma SX, Yue D. Identification of damage in composite structures using Gaussian mixture model-processed Lamb waves. Smart Materials and Structures. 2018;**27**:45007. DOI: 10.1088/1361-665X/aaaf96

[74] Staszewski WJ. Intelligent signal processing for damage detection in composite materials. Composites Science and Technology. 2002;**62**:941-950. DOI: 10.1016/S0266-3538(02)00008-8

[75] Suykens JAK, Gestel TV, Brabanter JD, Moor BD, Vandewalle J. Least squares support vector machines. International Journal of Circuit Theory and Applications. 2002;**27**:605-615. DOI: 10.1142/9789812776655

[76] Agarwal S, Mitra M. Lamb wave based automatic damage detection using matching pursuit and machine learning. Smart Materials and Structures. 2014;**23**:85012. DOI: 10.1088/0964-1726/23/8/085012

[77] Das S, Chattopadhyay A, Srivastava AN. Classifying induced damage in composite plates using one-class support vector machines. AIAA Journal. 2010;**48**:705-718. DOI: 10.2514/1.37282

[78] Park S, Yun CB, Roh Y, Lee JJ. PZT-based active damage detection techniques for steel bridge components. Smart Materials and Structures. 2006;**15**:957-966. DOI: 10.1088/0964-1726/15/4/009

[79] Park S, Lee JJ, Yun CB, Inman DJ. A built-in active sensing system-based structural health monitoring technique using statistical pattern recognition. Journal of Mechanical Science and Technology. 2007;**21**:896-902. DOI: 10.1007/BF03027065

[80] Sun FQ, Wang N, He JJ, Guan XF, Yang JS. Lamb wave damage quantification using GA-based LS-SVM. Materials. 2017;**10**:648. DOI: 10.3390/ma10060648

[81] Yang JS, He JJ, Guan XF, Wang DJ, Chen HP, Zhang WF, Liu YM. A probabilistic crack size quantification method using in-situ Lamb wave test and Bayesian updating. Mechanical Systems and Signal Processing. 2016;**78**:118-133. DOI: 10.1016/j.ymssp.2015.06.017

[82] Chiachio J, Bochud N, Chiachio M, Cantero S, Rus G. A multilevel Bayesian method for ultrasound-based damage identification in composite laminates. Mechanical Systems and Signal Processing. 2017;**88**:462-477. DOI: 10.1016/j.ymssp.2016.09.035

[83] He S, Ng CT. Guided wave-based identification of multiple cracks in beams using a Bayesian approach. Mechanical Systems and Signal Processing. 2017;**84**:324-345. DOI: 10.1016/j.ymssp.2016.07.013

[84] Peng TS, Saxena A, Goebel K, Xiang YB, Sankararaman S, Liu YM. A novel Bayesian imaging method for probabilistic delamination detection of composite materials. Smart Materials and Structures. 2013;**22**:125019. DOI: 10.1088/0964-1726/22/12/125019

[85] Neerukatti RK, Hensberry K, Kovvali N, Chattopadhyay A. A novel probabilistic approach for damage localization and prognosis including temperature compensation. Journal of Intelligent Material Systems and Structures. 2016;**27**:592-607. DOI: 10.1177/1045389X15575084

[86] Sohn H, Park HW, Law KH, Farrar CR. Combination of a time reversal process and a consecutive outlier analysis for baseline-free damage diagnosis. Journal of Intelligent Material Systems and Structures. 2006;**18**:335-346. DOI: 10.1177/1045389X06066291

[87] Lu Y, Ye L, Su ZQ, Zhou LM, Cheng L. Artificial neural network (ANN)-based crack identification in aluminum plates with Lamb wave signals. Journal of Intelligent Material Systems and Structures. 2008;**20**:39-49. DOI: 10.1177/1045389X07088782

[88] Legendre S, Massicotte D, Goyette J, Bose TK. Neural classification of Lamb wave ultrasonic weld testing signals using wavelet coefficients. IEEE Transactions on Instrumentation and Measurement. 2001;**50**:672-678. DOI: 10.1109/19.930439

[89] Su ZQ, Ye L. Lamb wave-based quantitative identification of delamination in CF/EP composite structures using artificial neural algorithm. Composite Structures. 2004;**66**: 627-637. DOI: 10.1016/j.compustruct.2004.05.011

[90] Su ZQ, Ye L. Lamb wave propagation-based damage identification for quasi-isotropic CF/EP composite laminates using artificial neural algorithm: Part II - implementation and validation. Journal of Intelligent Material Systems and Structures. 2005;**16**:113-125. DOI: 10.1177/1045389X05047600

[91] De Fenza A, Sorrentino A, Vitiello P. Application of artificial neural networks and probability ellipse methods for damage detection using Lamb waves. Composite Structures. 2015;**133**:390-403. DOI: 10.1016/j.compstruct.2015.07.089

[92] Park SH, Yun CB, Roh Y. PZT-induced Lamb waves and pattern recognitions for on-line health monitoring of jointed steel plates. In: Proceedings of the Smart Structures and Materials 2005 Conference; 07–10 March 2005; San Diego. Bellingham: SPIE Press; 2005. pp. 364-375

[93] Yuan SF, Wang L, Peng G. Neural network method based on a new damage signature for structural health monitoring. Thin-Walled Structures. 2005;**43**:553-563. DOI: 10.1016/j.tws.2004.10.003

[94] Liew CK, Veidt M. Guided waves damage identification in beams with test pattern dependent series neural network systems. WSEAS Transactions on Signal Processing. 2008;**4**:86-96

[95] Anaya M, Tibaduiza DA, Pozo F. Detection and classification of structural changes using artificial immune systems and fuzzy clustering. International Journal of Bio-Inspired Computation. 2017;**9**:35-52. DOI: 10.1504/IJBIC.2017.10002804

[96] Yuan L, Yuan Y, Hernández Á, Shi L. Feature extraction for track section status classification based on UGW signals. Sensors. 2018;**18**:1225. DOI: 10.3390/s18041225

Chapter 6

Qualification of PWAS-Based SHM Technology for Space Applications

Ioan Ursu, Mihai Tudose and Daniela Enciu

Additional information is available at the end of the chapter

http://dx.doi.org/10.5772/intechopen.78034

Abstract

The chapter refers to the results obtained in the framework of a national research project whose novelty was that concomitant outer space constraints, namely extreme temperature variations, radiations and vacuum, were applied to structures specimens to study their effect on the structural health monitoring (SHM) technology based on piezoelectric wafer active sensors (PWAS) and electromechanical impedance spectroscopy (EMIS) method of damages detection and identification. The results, in short, concern (a) the survivability and sustainability of EMIS technique, in fact the PWAS transducers survival, in these harsh conditions and (b) the developing of a methodology to distinguish between the damages of mechanical origin, and the false ones, caused by environmental conditions, which are, basically, harmless. This has resulted by observing that the splitting phenomenon of resonance peaks on EMIS signature can be associated with the occurrence of mechanical damage, making so possible the clear dissociation of the changes determined by the harsh environmental conditions.

Keywords: lab tests, electromechanical impedance spectroscopy (EMIS), piezoelectric wafer active sensor (PWAS), outer space harsh environmental conditions, entropy, real damage versus false damage

1. Introduction

In the beginning, we prefer to appeal to the well-known definitions. In this book chapter, "the process of implementing a damage identification strategy for aerospace, civil and mechanical engineering infrastructure is referred to as structural health monitoring (SHM). […] The damage is defined as changes to the material and/or geometric properties of these systems, including changes to the boundary conditions and system connectivity, which adversely affect the

current or future performance of these systems" [1]. SHM is, properly, an on-line measurement process supposing a sensor system distributed over the monitored structure. This process is complemented by off-line analysis of damage-sensitive features from these measurements, or by an on-line analysis of damages occurrence, as shown in this contribution. SHM technology enjoys special attention over the past two to three decades. The sensors used to damage detection belong to a wide range, such as optical fiber sensors [2, 3], acoustic active and passive sensors [4–6], microelectromechanical systems (MEMS) [7], and wireless sensor systems [8]. The basic SHM methods are the method based on a modal modification of structure dynamic vibrations in a relatively low-frequency register [9] and the electromechanical method of impedance spectroscopy (EMIS) in the high-frequency register, using the active piezo sensors [10–14]. It should be added that SHM methodology has been strongly related during its development to predictive maintenance [15] and fault detection [16] techniques due to safety demands in all areas of activity, especially in aerospace applications, chemical industry, nuclear power plants, and so on. SHM methodology has its obvious relevance to the air and space industry but has become imperious for many other industries due to the increase of the productivity and quality demands (zero-defects manufacturing), cost savings together with enhanced safety, and increased availability. Of course, not all existing damages compromise the good functioning of the structure. Based on a long-time SHM process, one obtains information on the ability of the structure to perform in spite of the inevitable aging and degradation resulting from operational environments [1], with the benefit to managing the structures life prognosis and reducing life-cycle costs. SHM will be one of the major contributions for future smart structures, including space ones [17].

2. PWAS-based SHM technology—EMIS method

The active SHM sensing techniques are based on two different approaches: transient guided waves and standing waves [12]. In such SHM processes, a piezoelectric wafer active sensor (PWAS) is required to generate elastic waves. These travel along the mechanical structure, are reflected by different structural abnormalities, or boundary edges, and they are recaptured by the same sensor in a pulse-echo configuration or by other sensors of same or different type, even passive sensors, and in pitch-catch configuration. If the structural damage or boundary edges are in the close vicinity of the active sensor, their reflections overlap the incident transient wave, and making impossible the interpretation [14]. One of the active SHM sensing techniques is based on standing waves, in the so-called EMIS method; by sweeping the frequency of the input signals to PWAS, some changes appear in the impedance measured by an impedance analyzer connected to the PWAS terminals. By monitoring the changes in the real part of the impedance function, which is most sensitive to structural changes [10], one can evaluate the integrity of the host structure.

The EMIS method uses PWAS high-frequency active sensors and bonded to the structure. The presence of damage in a neighboring zone of the sensor is signaled as its EMIS "signature," respectively, as a modification of the electromagnetic impedance spectrum Z (ω), recorded and online processed, and in principle [10–14]. The pioneering work on using EMIS

in SHM technology is considered [10] (see [11]). The electromechanical impedance spectrum is defined as the ratios between the applied excitation voltage $V(t) \coloneqq V_0 \sin(\omega t)$ [V] and the current $I(t) \coloneqq I \sin(\omega t)$ [A] generated by the piezoelectric effect. Where appropriate, impedance results are obtained based on an analytical relationship, or by dedicated equipment such as the HP 4194A impedance analyzer. Experimentally it has been proven that the real part, Re (Z (ω)), of the EMIS PWAS attached to the structure can be taken as an indication of the presence of damage or defects, due to the fact that this value closely follows the resonance behavior of the structure vibrating under the PWAS excitation [11]. In other words, this measured value is very sensitive to the smallest variations in the high-frequency structural dynamics at local scales (on the order of microns), which are associated with the presence of incipient damage. Of course, these changes cannot be detected by classical modal analysis sensors operating at lower frequencies.

3. Theoretical and experimental framework of qualification PWAS based SHM technology for space applications

Although SHM will be soon, we think, a key technology in the field of space vehicles, it is surprising how few papers can be reported for the time being in this field [4, 5, 18–22]. However, it is becoming clearer that new space programs can no longer ignore the implementation of SHM technologies to monitor and test the health and performance of space structures. The safety of the crew on board and the safety of the spacecraft, especially in critical moments of launch and re-entry into the earth's atmosphere, depend on the onboard existence of a SHM system. Spatial vehicles, but also the satellites, are subject to harsh environmental conditions: strong vibrations at launching and landing, cosmic radiation (with energy up to 1.6×10^{-11} J (1 GeV) [23], extreme temperatures (+120°C for exposed surfaces to the Sun and −230°C for unexposed surfaces [22]), and advanced vacuum.

The premise of a tests program for qualification PWAS-based SHM technology for space applications is that the changes in the EMIS signature will reflect the complex conditions in which the structures are found: overexposure to natural damage, that is, mechanical fatigue and aging, and special operating conditions in an environment defined by outer space (extreme temperatures, radiation, and vacuum). Both kinds of constraints, that is, mechanical and environmental, are to be simulated. The specific problem of the tests relates to the ability of the PWAS transducer to measure the modal behavior of the structure on which it is attached in the simulated harsh environmental conditions and with simulated mechanical damages. Consequently, a considerable amount of testing stages, EMIS records, data processing, and analytical assessments on damage identification were performed [5, 6, 24–28]. The following types of specimens were subjected to the tests: (a) PWAS STEMINC SMD07T02S412WL transducers, (b) M-bond 610 Vishay epoxy adhesive, and (c) STEMINC PWAS transducers [26] (**Figure 1**). The material and geometry data of the disc specimens (DS) were: A2024 aluminum alloy, with a diameter of 100 mm and a thickness of 0.8 mm. To simulate damages, in discs were processed, with laser technology, slits with 10 mm in length and 0.15 mm width, of various geometries, and locations.

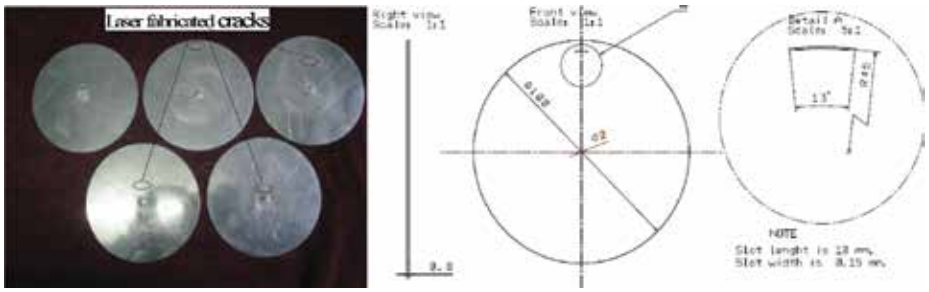

Figure 1. Disc specimens (DS), geometry of damage simulation.

Disc type PWASs with a diameter of 8 mm was bonded in the center of the aluminum disc specimen with epoxy adhesive. The thickness of the adhesive layer was measured with a comparator, and was found to be between 20 and 100 μm. **Figure 2** shows a disc with an arc-type simulated crack damage at 7 mm from the PWAS. The geometry of the simulated cracks (0.15 mm wide and 10 mm long) is the following: crack 1 (curvature):R = 45 mm, θ = 13°; crack 2:R= 25 mm, θ = 23°; crack 3: R = 15 mm, θ=38°; and crack 4: R = 7 mm, θ = 82°. The set of records refer to either PWASs or specimens with bonded PWAS, without and with simulated damages. In **Figure 2c**, the experimental set-up for EMIS recording using the HP 4194A impedance analyzer is presented.

The SHM test protocol involved a lot of operations: records and processing for EMIS, extreme temperature irradiation under high-vacuum, irradiation at room temperature (RT) and atmospheric pressure, optical and acoustic microscopy, scanning laser Doppler vibrometry (SLDV). From the processing of impedance spectrum will result in the characterization of damages. This is done by scalar sizes suitable to capture the differences between the spectra caused by this damage/crack. Ideally, these values should capture only those spectral features that are directly altered by the damage, while the variations caused by normal operating conditions to be neglected.

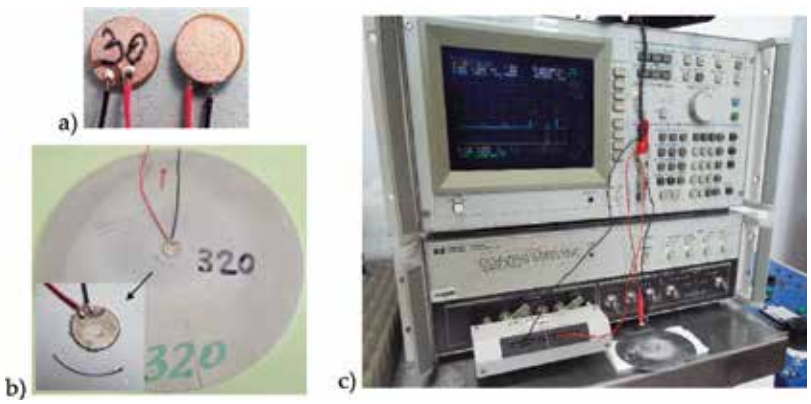

Figure 2. (a) PWAS STEMiNC type SMD 07T02R412WL; (b) DS with simulated damage at 7 mm from the PWAS; and (c) experimental set-up for EMIS recording at RT using the HP 4194A impedance analyzer.

http://dx.doi.org/10.5772/intechopen.78034

The saying "there is nothing more practical than a good theory" is widely known. In a complex tests program with the primary focus of the experiment, it was important to know well the theoretical tools. Indeed, the experiments were based on the concept of EMIS signature, so it was also important to master the theoretical basis of the EMIS method. The graphs summarized in this chapter, to which can be added the numerical analysis in [13, 14] and [29], as well as data, are given in **Table 1**; show that this goal has been met. Detailed analytical solutions are presented in [11–13]. Numerical calculations and experimental validation are widely described in [13, 6, 25, 29]. We cannot fail to notice the excellent monographs [30, 12] that guided the studies and experiments presented in this chapter. As a theoretical foundation, we retain the following equations that provide frequencies of flexural (*f*-indexed) and, respectively, axial (*a*-indexed) modes of a circular pristine disc:

$$\frac{\lambda^2 J_0(\lambda) + (1-v)\lambda J_0'(\lambda)}{\lambda^2 I_0(\lambda) - (1-v)\lambda I_0'(\lambda)} = \frac{J_0'(\lambda)}{I_0'(\lambda)}, \quad \omega_{j,f} := \lambda_{j,f}^2 \sqrt{\frac{D}{\rho h a^4}}, \quad D := \frac{Eh^3}{12(1-v^2)}$$
$$zJ_0(z) - (1-\nu)J_1(z) = 0, \quad z := \gamma a, \quad \omega_j := c_L(z)_{j,a}/a, \qquad c_L^2 := E/\left(\rho(1-v^2)\right) \tag{1}$$

The characteristic Eqs. (1) are obtained as solutions of the equation of motion for the transverse displacement w of a plate [30]:

$$D\nabla^4 w + \rho h \frac{\partial^2 w}{\partial t^2} = 0, \quad D := \frac{Eh^3}{12(1-v^2)} \tag{2}$$

$\nabla^4 = \nabla^2\nabla^2$, where ∇^2 is the Laplace operator. The Eqs. (1) give natural frequencies ω_j associated with solutions (eigenvalues) λ_j or z γ is wavenumber, $\gamma = \omega/c_L$. $J_0(\lambda)$ is the Bessel function of first kind and order zero, whereas $I_0(\lambda)$ is the modified Bessel function of first kind and order zero. D is the transverse (flexural) rigidity, E is Young's modulus, h is the plate thickness, a is the plate radius, v is Poisson's ratio, and ρ is mass density per unit area of the plate. As already mentioned, the DS were fabricated from A2024 aluminum alloy with a diameter of 2*a*=100 mm and a thickness of h =0.8 mm. The properties of the A2024 aluminum plates were: E= 73.146 MPa, ρ = 2780 kg/m^3, and ν = 0.3312. The frequencies values obtained by the experimental method are closer to the theoretical ones. The axial frequencies were noted with an italic font.

Hence, finally electromechanical impedance Z(ω) of a PWAS transducer bonded to disc specimen is:

ν_{th} (kHz)	12.57	19.69	28.38		*35.67*	38.63		50.51	63.95	78.97		*93.95*	95.57	
ν_{exp1} (kHz)	12.48	19.46	28.23		*35.89*	38.51		50.01	62.90	77.02		*92.04*	93.85	
ν_{exp2} (kHz)	12.65	19.91	28.27	28.63	*35.42*	37.35	38.07	38.87	49.32	50.53	63.62	*77.93*	*90.63*	93.73

Table 1. Theoretical (ν_{th}) and measured frequencies on pristine specimen (noted with ν_{exp1}) and on the arc at 15 mm damaged specimen (ν_{exp2}).

$$Z(\omega) = \frac{1}{i\omega C\left(1-k_p^2\right)}\left\{\left[1+\frac{k_p^2}{1-k_p^2}\frac{(1+v_a)J_1(\varphi_a)}{\varphi_a J_0(\varphi_a)-(1-v_a)J_1(\varphi_a)-\frac{a}{r_a}\chi(\omega)(1+v_a)J_1(\varphi_a)}\right]\right\}^{-1}$$
$$k_p^2 \coloneqq \frac{2d_{31}^2}{s_{11}^E(1-\nu_a)\varepsilon_{33}^E}, \varphi_a = \frac{\omega r_a}{c_P}, c_P \coloneqq \sqrt{\frac{1}{\rho s_{11}^E\left(1-v_a^2\right)}}, \quad \chi(\omega) = k_{str}(\omega)/k_{PWAS} \tag{3}$$

$k_{str}(\omega)$ is the dynamic stiffness of PWAS bonded on disc specimen; $k_{PWAS} = t_a/\left[r_a s_{11}^E(1-\nu_a)\right]$ is the PWAS stiffness; k_P is the planar coupling factor; c_P is the sound speed in PWAS disc; $c_L$is the longitudinal wave speed in disc specimen; v_a, r_a, and h_a are corresponding parameters of PWAS. Finally, s_{11}^E, ε_{33}^E, and d_{31} are recognized as PWAS compliance coefficient, dielectric permittivity and, respectively, strain constant.

The issues raised above are primarily qualitative, but at the same time, together with the results of numerical integration and with the measurements made on specimens, will show the capability and resources of the PWAS EMIS SHM technique. For example, spectrum splitting around resonance nominal frequencies of the pristine structure can be considered as an indication of the occurrence of mechanical damage in the monitored structure (**Figure 3**).

The numerical model used in tests program is based on the finite element method (FEM). FEM analysis allowed the study of damaged DSs [13, 14]. There was a good correlation between the analytical method and the experimental method.

The EMIS signature is calculated analytically (for regular geometric shapes, such as discs) and numerically. **Table 1** shows the theoretical natural frequencies described by the analytical model (1), the measured ones corresponding to the pristine DS (noted with ν_{exp1}) and to the "arc at 45 mm from PWAS" damaged DS (ν_{exp2}).

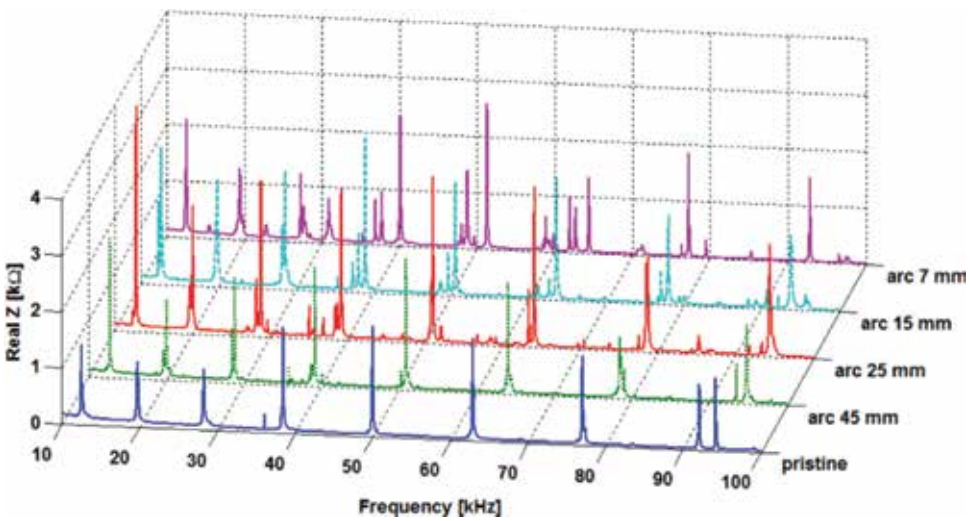

Figure 3. Measurement records for pristine specimen versus damaged one. Changes in RT EMIS signatures for different crack locations.

Relationship (3) is an analytical one. The analytical results are compared with the experimental ones. The statistics of the analytical determinations and the measurements are based on an indicator. In statistics framework, the most available definitions of damages "metrics" could be: "root mean square deviation" (RMSD), mean absolute percentage deviation (MAPD), and "correlation coefficient deviation" (CCD). Expressions of such sizes given in terms of the real part of the impedance, Re (Z), are the following:

$$MAPD = \sum_{N} \left| \left[\mathrm{Re}(Z_i) - \mathrm{Re}\left(Z_i^0\right)\right] / \mathrm{Re}\left(Z_i^0\right) \right|, RMSD = \sqrt{\sum_{N} \left[\mathrm{Re}(Z_i) - \mathrm{Re}\left(Z_i^0\right)\right]^2 / \sum_{N} \left[\mathrm{Re}\left(Z_i^0\right)\right]^2}$$

$$CC = \frac{1}{\sigma_Z \sigma_{Z^0}} \sum_{N} \left[\mathrm{Re}(Z_i) - \mathrm{Re}\left(\overline{Z}\right)\right] \times \left[\mathrm{Re}\left(Z_i^0\right) - \mathrm{Re}\left(\overline{Z}^0\right)\right], CCD = 1 - CC \tag{4}$$

The symbols $\overline{Z}$ and Z^0 means averages in time and σ_Z and σ_{Z^0} represents the standard deviation. Herein, we are interested to "assess a RMS type damage metrics," both for the real fault embodied through cracks or cuts simulated on disk specimens, or to statistical evaluation of EMI changes caused by temperature or irradiation constraints on single PWAS, or DS, constraints generating so-called "virtual (or false) defects".

4. Checks before complex harsh environments tests

The test program started with the establishment of a reference database, with RT EMIS records and processing for each PWAS and DS. It is important to note that the recorded data has been analyzed even from the beginning taking into account the impact that a PWAS improperly glued on DS has on the EMIS graphs. **Figure 4** shows how an inappropriate bonding resulted in the specimen discredit.

Since the EMIS signature does not always clarify the origin of the damages – mechanical or electronic, generated by fatigue and the aging of the structure or by deficiencies of sensors bonding

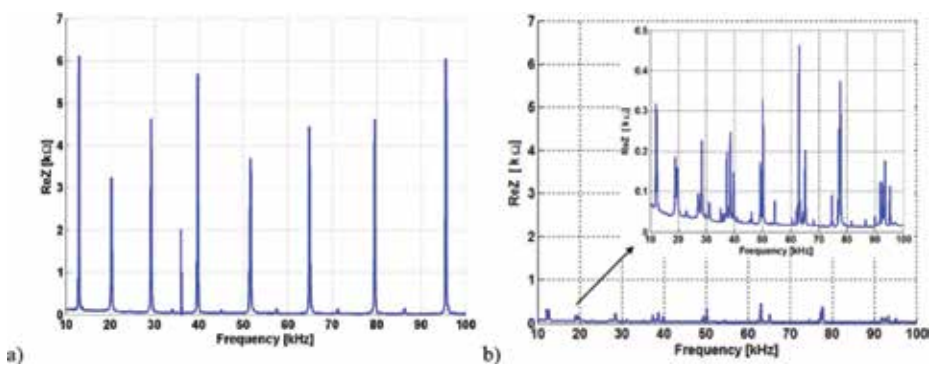

Figure 4. EMI signature for (a) a "good" bonding and (b) a "bad" bonding.

on the specimen and so on, special investigative means were added. This preliminary analysis is correlated with the experimental observation that there can be slight variation of EMIS for nominally identical specimens. It was considered that possible causes of EMIS signature changes were (a) fatigue and aging of the mechanical structure due to vibration, (b) unfulfillment of an adequate bonding of PWAS to the specimen, and (c) damage of PWAS itself.

Figure 5 top shows images obtained with *SAM 300*, at investigating the DS 122, particularly chosen wrong, for study. One can see: cracks in PWAS (red circles) caused by unequal forces applied during the bonding process; a piece of PWAS is broken (green rectangle); areas without glue (yellow rhombs). Another device used was the *digital microscope VHX 5000*. The VHX is an all-in-one microscope that incorporates observation, image capture, and measurement capabilities. **Figure 5** bottom shows two images of the DS 106 obtained with this device. The picture on the right is an enlarged image of the left side; a crack is shown in PWAS.

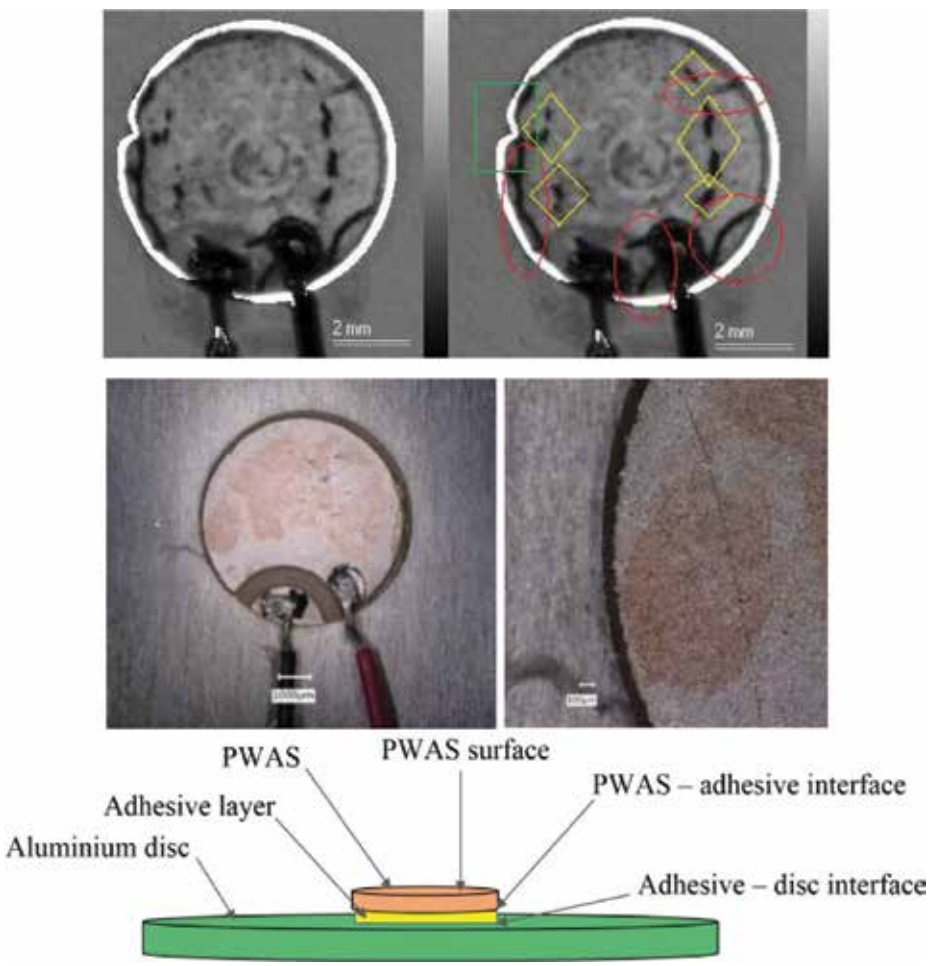

Figure 5. Top: Investigating the DS 122 with 300 scanning acoustic microscope (SAM); middle: Images obtained with digital microscope VHX 5000, DS106; and bottom: Areas of interest PWAS health monitoring.

5. Describing tests protocol and results

5.1. The effects of the harsh environment on PWAS and DS EMIS signature

Two specimens exposed to harsh environmental conditions in the laboratory simulations are free PWAS sensors and circular plates with central bonded PWAS. EMIS was recorded both during exposure to harsh conditions, and in the intervals between these exposures, at RT, see **Table 2**. The technical details of the factors involved in one cycle of harsh environment exposure are presented in **Table 3**. The first stage of the complex test protocol stipulated five cycles of concomitant outer-space condition: high-temperature variation, radiation, and vacuum.

In the test program has been used special harsh environment simulation equipment, starting with the Dewar cryogenic vessel, and the convection oven with the Memmert UFE 400 digital temperature controller. Also, some of the experiments at negative temperatures were performed at INCAS in the environmental chamber INSTRON 5982, and the high temperatures in the thermostatic chamber FD 115 Binder.

The test program also developed experiments at the Horia Hulubei national institute for R and D in physics and nuclear engineering-IFIN-HH, in the gamma irradiation chamber 5000 with 60-Co circular distributed sources. The details are presented in the paper [26]. The measured radiation flow was 4.7 kGy/h. Five consecutive test cycles (**Table 3**) were programmed to provide a full irradiation dose of 23.5 kGy. The premise of the calculations was as follows: (a) the estimated

Tested specimen	Activity	Amount	Working time [h]
PWAS	EMI measuring at RT	30	20
	testing in harsh, space type, conditions	30	200
	EMI measurement after returning to RT	30	20
	EMI changes analysis	30	100
Disc with PWAS	EMI measuring at room temperature	34	20
	testing in harsh, space type, conditions	34	200
	EMI measurement after returning to RT	34	20
	EMI changes analysis	34	100

Table 2. Complex testing protocol for simulation of harsh space type conditions - first stage of complex tests.

Duration	Temperature (°C)	Vacuum (Pa)	Dose per step (kGy)	Dose per cycle (kGy)
Initial EMIS reading – RT				
0.5 h	−196	$1–10^{-2}$	2.35	4.7
1.0 h	RT	—	—	
0.5 h	+100	$1–10^{-2}$	2.35	
EMIS reading after each cycle – RT				

Table 3. Overview of one test cycle of cumulative environmental factors: Radiation, temperature, and vacuum tests.

complete dose for a mission on Mars is 110 mGy/year, which means a dose of about 15 μGy/h; (b) the highest absorbed doses determined by the Pioneer probes 10 and 11 were 15 kGy, and 4.3 kGy, respectively. Consequently, the dose rate determined by the gamma 5000 irradiation chamber has been considered as acceptable. The absorbed dose of 23.5 kGy corresponded to 5 h exposure at the measured dose of 4.7 kGy/h. The usual vacuum in the outer space is 10^{-14} Pa. Vacuum pressures below 10^{-1} Pa were obtained by using a tritium manifold, a high-vacuum plant containing a vacuum pump type TSH-171E Pfeiffer, and pressure vacuum controllers type TPG 262 Pfeiffer.

A reference database is created at the beginning of the tests; for example, see **Figure 6**. The strategy of the program was that, in the first stage of tests, the PWASs and DSs were tested using simultaneous environmental factors that are specific to outer space, see **Figure 7**, the case of disc specimen 127 [25]. Then, to characterize the influence of each factor on the EMIS signature, in the second phase the tests were developed with harsh environmental factors acting successively instead of simultaneously [28], see **Table 4**.

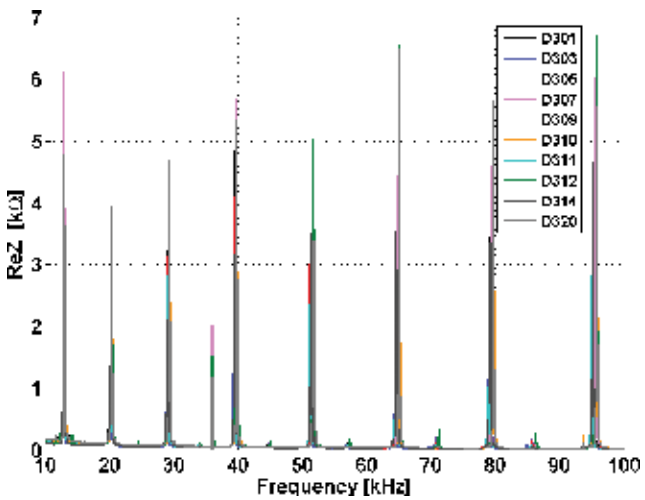

Figure 6. The experimental reference RT for the EMIS method: The signature of the health status of the structure.

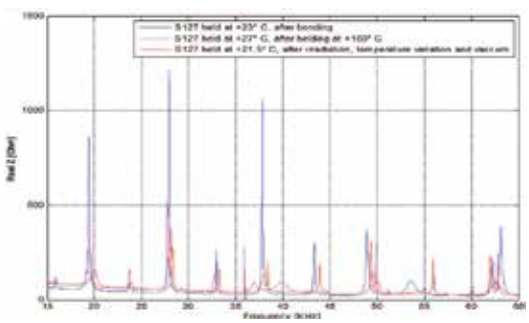

Figure 7. Summary of EMI measurements on S127 disc specimen, without simulated crack.

The effects of harsh environment on PWAS. After performing the tests according to the protocols in **Tables 2** and **3**, it is noted that the resonance frequencies on the EMIS PWAS graphs are constantly moving from left to right when temperatures drop from high (+150°C) to cryogenic values (−70°C), as shown in **Figure 8a**. After completion of the tests at extreme temperatures, measurements were again made at RT.

A compensation technique [26, 28], in fact, a horizontal displacement of graphs, was used to obtain graphs in **Figure 8b**. As far as irradiations are concerned, they cause insignificant changes to EMIS signatures (**Figure 8c**). Thus, we can conclude that EMIS signature changes caused by environmental factors are reversible and consequently do not characterize real damage. The real damages are those of mechanical origin, which produce irreversible changes to the EMIS signature.

The effects on pristine DS. The EMIS behavior at extreme temperatures was analyzed on a set of 4 DS. Initially, the EMIS graph at RT (+25°C) was recorded. Next, tests at low temperatures,

#	Piezoelectric wafer active sensors (PWAS)	Disc specimens (DS)
1	Initial RT EMIS recording of 38 PWAS (26 of them was bonded on the aluminum disc)	Initial RT EMIS recording of 26 DS; 10 of them was eliminated
2	Tests and EMIS recording at high temperatures for 5 PWAS: +50/+200°C, step: +25°C	Fabrication of arc type mechanical damages (MD): arc at 45 mm (2 DS), 25 mm (3 DS), 15 mm (3 DS), and 7 mm (2 DS)
3	RT EMIS recording after high temperatures	RT EMIS recording after MD fabrication
4	Tests and EMIS recording at low temperatures for 5 PWAS: −25, −50, −70°C	Tests and EMIS recording at low temperatures for 4 DS: 0, −25, −50, −70°C
5	RT EMI recording after low temperatures	RT EMI recording after low temperatures
6	Tests and EMIS recording at high temperatures for 5 PWAS: +50/+150°C, step: +25°C	Tests and EMIS recording at high temperatures for 4 DS: +50, +75, +100, +125, and +150°C
7	RT EMIS recording after high temperatures	RT EMIS recording after high temperatures
8	Irradiation tests and EMIS recording for 2 PWAS at 3.71 Gy/h	Irradiation tests and EMIS recording for 2 DS at 3.71 Gy/h
9	RT EMIS recording after irradiation	RT EMIS recording after irradiation

Table 4. Tests summary – Second stage of complex tests.

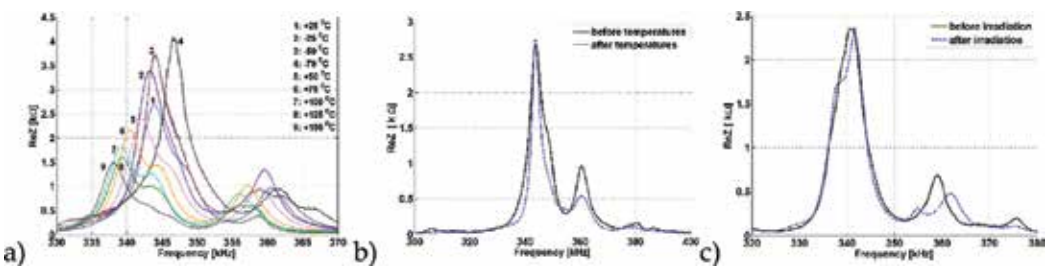

Figure 8. EMIS PWAS signatures: (a) synoptic graph of temperature cycling; (b) initial and after temperature cycling, both at RT, compensated values; and (c) initial and after irradiation tests, both at RT.

0, −25, −50, and −70°C were performed. When returning at the RT, T_1, (+22.4°C), it is noticed that the EMIS chart overlaps the initial one. After that, experiments at high temperatures up to +150°C, with a chosen step of 25°C, followed. When DS is brought to RT, T_2 (+23.6°C), it can be seen that EMIS returns to its original form, see **Figure 9a**.

Results similar to those of the PWAS case were also obtained in the case of 2 DS. The measurements were performed according to protocols before irradiation, during irradiation and after irradiation at RT, with the conclusion that the radiation does not produce splittings of the resonance peaks, but only negligible displacements of the peaks (**Figure 9b**), of the order of dozens of ohms.

5.2. The effects of the mechanical damages on PWAS and DS EMIS signature

Mechanical damages affect the EMIS signature in a well-defined way, namely causing the resonance peaks to split. This phenomenon intensifies in direct proportion to the decrease in distance from the PWAS center. Harsh environmental factors produce only displacements of resonance peaks and variations of amplitude on the EMIS signature, all practically reversible. (**Figure 3**).

The EMIS graphs in **Figure 10a** show, by comparison with the graph in **Figure 10b**, and the impact of the damages on the spectrogram. Of course, this impact is more pronounced when the damage is closer to the PWAS center and is manifested mainly as splittings of resonance peaks in new peaks. This observation generated the idea of developing a method of identifying mechanical damage as well as of dissociating the mechanical damage from the so-called false damage, that induced by environmental factors [31].

Therefore, based on experimental observations, the splitting of resonance peaks on the EMIS signature will be associated with the occurrence of a mechanical deterioration. Instead, the effects of harsh environmental conditions are limited only to reversible movements of resonance peaks with amplitude changes; if the temperatures do not exceed certain limits, the amplitudes are practically reversible, and returning to EMIS signatures in the case of RT. More insignificant are the modifications made on the EMIS graphs by irradiation specific to outer space.

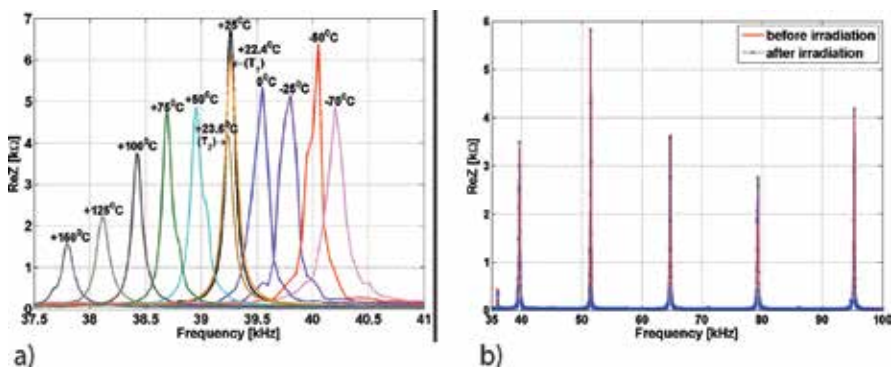

Figure 9. EMIS signature changes for a DS due to: (a) temperatures cycling; (b) irradiation.

http://dx.doi.org/10.5772/intechopen.78034

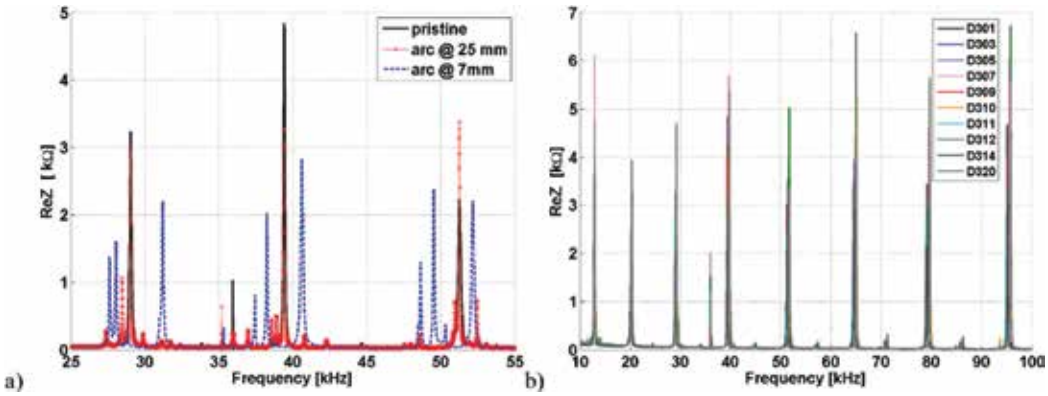

Figure 10. (a) Changes in EMIS signature, without damage versus damage (at 7 and 25 mm); (b) EMIS signature remains unchanged for different DS without damage.

A major tests result to propose a new, simple and effective approach to identifying mechanical damage. This approach allows the algorithmic distinction between real, mechanical damage and false damage, and caused by the harsh environmental factors.

5.3. Entropy method for damage detection and prediction

Figure 11 shows one of the multiple recordings done in the time domain with SLDV. The DS 138, without damage and with arc type defect at 15 mm, is scanned at a frequency of 78.4 Hz, see a 2D and a 3D representation. The position of the laser-cut slit is marked as a red peak. The displacement is given in nanometers depending on time [ms] (vibration measured in the *z*-direction, perpendicular to the disc, takes also negative values). The graph refers to a vibration of a specific point on the surface of the disk otherwise indicated in the picture. It can be seen that the concentric circles are uniformly distributed on the surface of the plate when there is no damage to disturb the wave propagation. In the case with the laser made damage, the amplitudes of the waves in the vicinity of the fabricated crack are much higher than all the other points of the disk producing distinct peak in the EMIS signature. **Figure 12** shows the use of SLDV for records in the frequency domain. For the same DS 138, a 3D image of the vibration at a frequency of 49.56 kHz is shown.

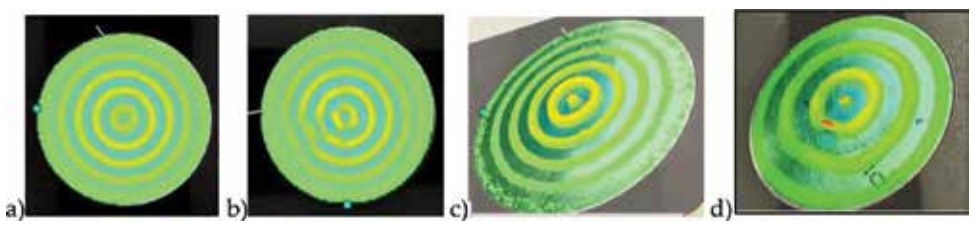

Figure 11. Recordings in time domain done with SLDV on DS 138: (a)disc without damage 2D representation; (b) DS with arc type defect at 15 mm—2D; (c) disc without damage 3D; and (d) DS with arc type defect at 15 mm—3D.

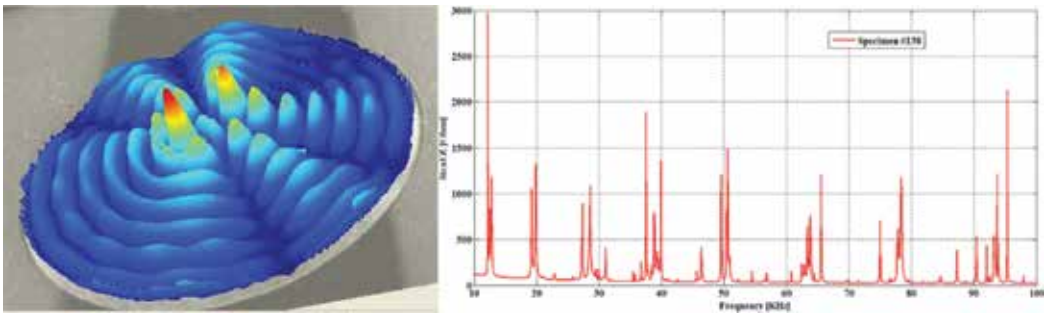

Figure 12. Recordings in frequency domain done with SLDV on DS 138 with mechanical damage; next is given the EMI signature of the disk.

The pattern of vibration in the presence and in the vicinity of the crack shows clear disorder. From here and from the paper [31] came the idea of exploiting the entropy concept in identifying the damage. Thus, an entropy method for damage detection and the prediction was proposed [28, 32]. Since the possible use of SLDV is very costly, we propose a simple method that uses the EMIS global signature. The proposed method can successfully substitute a possible but very expensive use of SLDV that should provide mode shapes for obtaining the global EMIS signature.

Consider the discretized system $Re(Z(\omega_i)) := R_i$, $\omega_i \in [\omega_a, \omega_b]$, $R_i \geq 0, i = 1, \ldots, n$ described by the probabilities $P = (p_1, p_2, \ldots, p_n)$. The complex information contained in EMIS signature measurements, respectively, in $Re(Z(\omega))$ data, is firstly processed in sizes assimilable as probabilities, $p_i \geq 0$, $i = 1, \ldots, n$ and $\sum_{i=1}^{n} p_i = 1$

$$p_i := \frac{Re(Z(\omega_i))}{\sum_{i=1}^{n} Re(Z(\omega_i))} := \frac{R_i}{C} \tag{5}$$

The normalized entropy of the set P is measured as:

$$H(P) = -\frac{\sum_{i=1}^{n} p_i \log_2 p_i}{\log_2 n} \tag{6}$$

The disorder produced in EMIS signature by the mechanical damage will be analyzed based on the investigative capacity of PWAS. This can be deducted from graphs recorded in **Figure 3**, where we find the EMIS signatures of undamaged DS, noted "u," of the DS in which the damage is located at the distance d_1 = 45 mm, noted "d_1", and so on, for the DS "d_2", "d_3", "d_4". This calculation is carried out on frequency intervals $\left[\omega_{a_j}, \omega_{b_j}\right]$, where certain resonance frequencies are present. Define

$$H(P, uu) = -\frac{\sum_{i=1}^{n} p_i \log_2 p_i}{\log_2 n} = -\frac{\sum_{i=1}^{n} \frac{2R_i^u}{2C^u} \log_2 \frac{2R_i^u}{2C^u}}{\log_2 n}$$

$$H(P, uu) = -\frac{1}{\log_2 n}\left[\frac{R_1^u}{C^u}\left(\log_2 R_1^u - \log_2 C^u\right) - \frac{R_2^u}{C^u}\left(\log_2 R_2^u - \log_2 C^u\right) - \ldots - \frac{R_n^u}{C^u}\left(\log_2 R_n^u - \log_2 C^u\right)\right] \tag{7}$$

$$H(P, uu) = -\frac{1}{C^u \log_2 n}\left(\sum_{i=1}^{n} R_i^u \log_2 R_i^u - C^u \log_2 C^u\right)$$

$$C^u := \sum_{i=1}^{n} R_i^u \tag{8}$$

$$p_{i,ud_k} = \frac{R_i^u + R_i^{d_k}}{\sum_{i=1}^{n}\left(R_i^u + R_i^{d_k}\right)} := \frac{R_i^u + R_i^{d_k}}{C^u + C^{d_k}} \tag{9}$$

$$C^{d_k} := \sum_{i=1}^{n} R_i^{d_k} \tag{10}$$

$$\begin{aligned} H(P, ud_k) &= -\frac{1}{\log_2 n}\left[\sum_{i=1}^{n}\frac{R_i^u + R_i^{d_k}}{C^u + C^{d_1}}\left(\log_2\left(R_i^u + R_i^{d_k}\right) - \log_2\left(C^u + C^{d_k}\right)\right)\right] \\ H(P, ud_k) &= -\frac{1}{\left(C^u + C^{d_k}\right)\log_2 n}\left[\left(\sum_{i=1}^{n}\left(R_i^u + R_i^{d_k}\right)\log_2\left(R_i^u + R_i^{d_k}\right)\right) - \left(C^u + C^{d_k}\right)\log_2\left(C^u + C^{d_k}\right)\right] \end{aligned} \tag{11}$$

The relationship (7) gives the entropy, or complexity, or the disorder modifications on the EMIS signatures, of the undamaged u DS in relation with himself, in short uu. We continue with the increased entropy ud_1 of damaged DS having the damage at a distance 45 mm, d_1, versus undamaged u DS, and so on up to ud_4 (**Table 5**).

From exploring the results in **Table 5**, it is noticeable that the PWAS active sensor senses the disorder caused by damage with satisfactory efficiency if this damage is located at a distance close to the sensor center, in this case at distances of 15–7 mm. This conclusion is useful for the

Frequency (kHz)	n for summation	uu	ud_1	ud_2	ud_3	ud_4	Averaged entropy ud_3 + ud_4 increasing vs. uu
26–32	601	0.826	0.850	0.851	0.904	0.905	0.079
36–42.5	651	0.771	0.821	0.805	0.882	0.876	0.108
47–53	601	0.821	0.819	0.830	0.880	0.904	0.071
58–68	1001	0.774	0.811	0.798	0.855	0.882	0.095
78–81.5	551	0.762	0.804	0.811	0.884	0.830	0.095
92.5–98.5	601	0.714	0.799	0.790	0.829	0.833	0.117

Table 5. Entropy values for disc specimens DS: u vs. u (uu), u vs. d_1 (ud_1), …, u vs. d_4 (ud_4) [28].

Frequency (kHz)	n for summation	Before irradiation	During irradiation	Entropy increasing
28–31	121	0.7601	0.7602	0.0001
38–41	121	0.7571	0.7576	0.0005
50–53	121	0.6721	0.6783	0.0062
63–67	121	0.7275	0.7295	0.0020
78–81.5	121	0.7437	0.7450	0.0013
93–97	121	0.7173	0.7183	0.0010

Table 6. Influence of radiations on EMIS signature, type "u" DS [28].

Frequency [kHz]	n for summation	RT	150°C	Entropy increasing
27–30	301	0.754	0.771	0.017
36.5–39.5	301	0.759	0.764	0.005
48–51.5	351	0.808	0.809	0.001
60.5–64.5	401	0.779	0.779	0.000
74–79	501	0.715	0.728	0.013

Table 7. Influence of temperature (after compensation) on EMIS signature, type "*u*" DS [28].

implementation of a SHM system, which should ensure an optimized distribution of monitoring sensors on the surface of the structure.

The fact that irradiation taken separately produces an insignificant change in the EMIS signature is attested in **Table 6**. If a compensation technique is considered and applied as in [26], the same conclusion applies to extreme temperature tests, see **Table 7**.

6. Conclusions

A first conclusion of descriptions and analysis made in this book chapter is that the cumulative impact of severe conditions of temperature and radiation has not generated decommissioning of PWAS sensors, thus confirming the survivability and sustainability of EMIS PWAS based SHM technology, as the first step towards de space vehicles transfer.

A second conclusion is that the splitting phenomenon of resonance peaks on EMIS signature can be associated with the occurrence of mechanical damage, making possible the clear dissociation of the changes determined by the harsh environmental conditions (temperatures and radiations). They are reduced mainly to reversible displacements of the resonance frequencies, with resonance amplitudes modifications, but if the temperatures do not cross certain limits, the amplitudes and frequencies return to those of RT case. Regarding radiations, they do not affect the EMIS graph.

Acknowledgements

The support from National Authority for Scientific Research and Innovation (ANCSI), for Star Space SHM project code ID 188/2012, and for NUCLEU Program project code 18-036/1 PN, "Complex mechatronic systems for procedures of launching systems recovery with active structural health monitoring," is thankfully acknowledged. During these programs, a large amount of experimental data was obtained that ultimately grounded the results and conclusions presented above.

Finally, we express our gratitude to Dr. Cristian Postolache from Horia Hulubei National Institute for R and D in Physics and Nuclear Engineering-IFIN-HH, Bucharest, for developing

the irradiation tests and to Dr. Cristian Rugina from Institute of Solid Mechanics of the Romanian Academy, Bucharest, for FEM applied to DS.

Conflict of interest

The authors declare that they have no conflict of interest.

Author details

Ioan Ursu, Mihai Tudose and Daniela Enciu*

*Address all correspondence to: enciu.daniela@incas.ro

Department of Systems, INCAS – National Institute for Aerospace Research "Elie Carafoli", Bucharest, Romania

References

[1] Farrar CR, Worden K. An introduction to structural health monitoring. Philosophical Transactions of the Royal Society A. 2007;**365**:303-315

[2] Kinet D, Megret P, Goossen KW, Qiu L, Heider D, Caucheteur C. Fiber Bragg grating sensors toward structural health monitoring in composite materials: Challenges and solutions. Sensors. 2014;**14**:7394-7419

[3] Ferdinand P. The evolution of optical fiber sensors technologies during the 35 last year and their applications in structural health monitoring. In: 7th European Workshop on Structural Health Monitoring, La Cité, Nantes, France; July 8–11, 2014

[4] Zagrai A, Doyle D, Gigineishvili V, Brown J, Gardenier H, Arritt B. Piezolectric wafer active sensor structural health monitoring of space structures. Journal of Intelligent Material Systems and Structures. 2010;**21**:921-940

[5] Ursu I, Giurgiutiu V, Toader A. Towards spacecraft applications of structural health monitoring. INCAS Bulletin. 2012;**4**(4):111-124

[6] Toader A, Ursu I, Enciu D. New advances in space SHM project. INCAS Bulletin. 2015; **7**(1):65-80

[7] Caimmi F, Bruggi M, Mariani S, Bendiscioli P. Towards the development of a MEMS-based health monitoring system for lightweight structures. In: International Electronic Conference on Sensors and Applications; 1–16 June, 2014

[8] Lynch JP, Loh KJ. A summary review of wireless sensors and sensor networks for structural health monitoring. The Shock and Vibration Digest. 2006;**38**(2):91-128

[9] Fritzen C-P. Vibration-based structural health monitoring - concepts and applications. Key Engineering Materials. 2005;**293-294**:3-20

[10] Liang C, Sun FP, Rogers CA. Coupled electro-mechanical analysis of adaptive material system – Determination of the actuator power consumption and system energy transfer. Journal of Intelligent Material Systems and Structures. 1994;**5**:12-20

[11] Zagrai A, Giurgiutiu V. Electro-mechanical impedance method for crack detection in thin plates. Journal of Intelligent Material Systems and Structures. 2001;**12**(10):709-718

[12] Giurgiutiu V. Structural Health Monitoring with Piezolectric Wafer Active Sensors. 2nd ed. Amsterdam: Elsevier Academic Press; 2014

[13] Rugina C, Toader A, Giurgiutiu V, Ursu I. The electromechanical impedance method for structural health monitoring of thin circular plates. Proceedings of the Romanian Academy, Series A, Mathematics, Physics, Technical Sciences, Information Sciences. 2014;**15**(3): 272-282

[14] Rugina C, Enciu D, Tudose M. Numerical and experimental study of circular disc electromechanical impedance spectroscopy signature changes due to structural damage and sensor degradation. Structural Health Monitoring - an International Journal. 2015;**14**(6): 663-681

[15] Keith Mobley R. An Introduction to Predictive Maintenance. 2nd ed. Amsterdam: Butterworth Heinemann (Elsevier); 2002

[16] Isermann R. Fault-diagnosis systems. Germany: Springer; 2006

[17] Speckmann H, Roesner H. Structural Health Monitoring: A Contribution to the Intelligent Aircraft Structure, ECNDT 2006 - Tu.1.1.1

[18] Peairs DM, Grisso B, Inman DJ, Page KR, Athman R, Margasahayam RN. Proof-of-concept application of impedance-based health monitoring on space shuttle ground structures. NASA-TM-2003-211193; 2003

[19] Mancini S, Tumino G, Gaudenzi P. Structural health monitoring for future space vehicles. Journal of Intelligent Material Systems and Structures. 2006;**17**:577-585

[20] Pisacane VL. The Space Environment and its Effects on Space Systems. Reston, VA: AIAA Education Series; 2008

[21] Giurgiutiu V, Lin B, Santoni-Bottai G, Cuc A. Space application of piezolectric wafer active sensors for structural health monitoring. Journal of Intelligent Material Systems and Structures. 2011;**22**(8):1359-1370

[22] Ramachandran V, Gadlage M, Ahlbin J, Narasimham B, Alles M, Reed RA, Bhuva B, Massengill L, Black J, Foster CN. Application of a novel test system to characterize single event effects at cryogenic temperatures. Solid State Electronics. 2010;**54**:1052-1059

[23] Nymmik R. Initial conditions for radiation analysis: Models of galactic cosmic rays and solar particle events. Advances in Space Research. 2006;**38**:1182-1190

[24] *** STAR project code ID 188/2012. Structural health monitoring in spacecraft structures using piezoelectric wafer active sensors (PWAS) multimodal guided waves. National Authority for Scientific Research−ANCS, UEFISCDI, STAR Programme

[25] Enciu D, Tudose M, Neculaescu B, Toader A, Ursu I. Damage identification and damage metrics in SHM. Proceedings of AEROSPATIAL 2014, Bucharest, 18–19 September. pp. 349-364. ISSN 2067–8614, 2014

[26] Ursu I, Enciu D, Toader A. Towards structural health monitoring of space vehicles. Aircraft Engineering and Aerospace Technology. 2017;**89**(6):920-927

[27] Ursu I, Toader A, Enciu D, Stefanescu DM. Advanced measurements in star space project on structural health monitoring. Proceedings of XXI IMEKO World Congress. 2015:2084-2087. ISSN 9781510812925

[28] Enciu D, Ursu I, Toader A. New results concerning SHM technology qualification for transfer on space vehicles, Structural Control and Health Monitoring. 2017;**24**(10):e1992. DOI: 10.1002/stc.1992

[29] Rugina C, Giurgiutiu V, Ursu I, Toader A. Finite element analysis of the electromechanical impedance method on aluminum plates in SHM. Proceedings of AEROSPATIAL 2014, Bucharest, 18–19 September, 2014:343-348. ISSN 2067–8614

[30] Leissa A. Vibration of Plates, NASA SP-160. US Gov't Printing Office; 1969

[31] Yang Z-B, Chen X-F, Xie Y, Zhang X-W. The hybrid multivariate analysis method for damage detection. Structural Control and Health Monitoring. 2016;**23**:123-143

[32] Enciu D, Ursu I, Tudose M. Complex method for online identification of mechanical damages using the electromechanical impedance spectroscopy, avoiding the false diagnosis. OSIM Patent no. RO131152B1/29.12.2017. Gold Medal and the Special Prize from the Turkish Patent and Trademark Office for the patent no. RO131152B1/29.12.2017 awarded at the 46th Edition of the International Invention Salon held at Geneva, Switzerland; 11–15 April, 2018

Chapter 7

Condition Monitoring of Wind Turbine Structures through Univariate and Multivariate Hypothesis Testing

Francesc Pozo and Yolanda Vidal

Additional information is available at the end of the chapter

http://dx.doi.org/10.5772/intechopen.78727

Abstract

This chapter presents a fault detection method through uni- and multivariate hypothesis testing for wind turbine (WT) faults. A data-driven approach is used based on supervisory control and data acquisition (SCADA) data. First, using a healthy WT data set, a model is constructed through multiway principal component analysis (MPCA). Afterward, given a WT to be diagnosed, its data are projected into the MPCA model space. Since the turbulent wind is a random process, the dynamic response of the WT can be considered as a stochastic process, and thus, the acquired SCADA measurements are treated as a random process. The objective is to determine whether the distribution of the multivariate random samples that are obtained from the WT to be diagnosed (healthy or not) is related to the distribution of the baseline. To this end, a test for the equality of population means is performed in both the univariate and the multivariate cases. Ultimately, the test results establish whether the WT is healthy or faulty. The performance of the proposed method is validated using an advanced benchmark that comprehends a 5-MW WT subject to various actuators and sensor faults of different types.

Keywords: condition monitoring, wind turbines, principal component analysis, hypothesis testing

1. Introduction

The wind energy cost depends strongly on the performance of the condition monitoring system. Advance in this area would decrease downtime periods, extend the WT lifetime, and ultimately reduce the operation and maintenance (O&M) costs, which is one of the main challenges in wind energy as stated in "20% Wind Energy by 2030" [1].

Usually, condition monitoring comprises different systems (vibration analysis, oil monitoring, etc. [2]) for different parts and different types of faults and makes use of expensive specific sensors that must be installed in the WT. Therefore, the advance in fault detection systems that only make use of already available data from the turbine SCADA system and comprehend different parts and different types of faults is promising (since no additional sensors or data acquisition devices are needed). The SCADA signals provide rich information on the WT performance; thus, with appropriate algorithms, they can be used effectively for condition monitoring, prognostics, and remaining useful life prediction of WTs [3]. There are some success stories about using SCADA data for condition monitoring. For example, Ruiz et al. presented a machine learning approach [4], Zaher and McArthur proposed to use the combination of abnormal detection and data-trending techniques encapsulated in a multiagent framework [5], Pozo and Vidal proposed a fault detection system based on principal component analysis [6].

In this work, following the enhanced benchmark challenge for wind turbine fault detection proposed in [7], a set of eight realistic fault scenarios are considered to develop a WT condition monitoring strategy that combines a SCADA data-driven baseline model—reference pattern obtained from the healthy wind turbine—based on MPCA in combination with uni- and multivariate hypothesis testing. Previous works using MPCA and hypothesis testing to detect structural damage [8] work under the hypothesis of guided waves. That is, the vibration (guided wave) induced to the structure is known and always the same. However, in this work, the vibration is induced by the changeful wind. The used benchmark comprehends different types of faults of a 5-MW WT given by the FAST simulator [9], which has been accepted by the scientific community and is widely used for WT-related research, e.g., [10–12].

The chapter is organized as follows. Section 2 briefly recalls the WT benchmark model. In Section 3, the condition monitoring strategy is stated. Simulation results are discussed in Section 4. Finally, conclusions are drawn in Section 5.

2. Wind turbine benchmark model

The used benchmark model is proposed in [7]. It covers a 5-MW three-bladed, variable speed WT modeled with the FAST simulator, detailed actuator and sensor models, as well as the different fault descriptions. For a complete description of the benchmark, please see reference [7]. Here, a short review is given to introduce the used notation.

The specifications of the 5-MW reference WT is documented in [13]. This model has been used as a reference by research teams throughout the world to standardize baseline on- and offshore wind turbine specifications. The wind turbine typical features are given in **Table 1**, and the assumed available SCADA data are given in **Table 2**. This work copes with the so-called full load region of operation. In order to run the simulations, turbulent wind data sets that cover this region have been generated with TurbSim [14], see **Figure 1**.

The generator-converter system can be approximated by a first-order ordinary differential equation, see [7], which is given by:

Reference wind turbine	Magnitude
Rated power	5 MW
Number of blades	3
Rotor/hub diameter	126, 3 m
Hub height	90 m
Cut-in, rated, and cut-out wind speed	3, 11.4, and 25 m/s
Rated generator speed (ω_{ng})	1173.7 rpm
Gearbox ratio	97

Table 1. WT properties.

Number	Sensor type	Symbol	Units
1	Generated electrical power	$P_{e,m}$	kW
2	Rotor speed	$\omega_{r,m}$	rad/s
3	Generator speed	$\omega_{g,m}$	rad/s
4	Generator torque	$\tau_{c,m}$	Nm
5	First pitch angle	$\beta_{1,m}$	◦
6	Second pitch angle	$\beta_{2,m}$	◦
7	Third pitch angle	$\beta_{3,m}$	◦
8	Fore-aft acceleration at tower bottom	$a^b_{fa,m}$	m/s^2
9	Side-to-side acceleration at tower bottom	$a^b_{ss,m}$	m/s^2
10	Fore-aft acceleration at mid-tower	$a^m_{fa,m}$	m/s^2
11	Side-to-side acceleration at mid-tower	$a^m_{ss,m}$	m/s^2
12	Fore-aft acceleration at tower top	$a^t_{fa,m}$	m/s^2
13	Side-to-side acceleration at tower top	$a^t_{ss,m}$	m/s^2

These sensors are representative of the types of sensors that are available on an MW-scale commercial wind turbine.

Table 2. Assumed available measurements.

$$\dot{\tau}_r(t) + \alpha_{gc}\tau_r(t) = \alpha_{gc}\tau_c(t) \tag{1}$$

where τ_r and τ_c are the real generator torque and its reference (given by the controller), respectively. In the numerical simulations, $\alpha_{gc} = 50$, see [13]. Moreover, the power produced by the generator, $P_e(t)$, is given by (see [7]):

$$P_e(t) = \eta_g \omega_g(t)\tau_r(t) \tag{2}$$

where η_g is the efficiency of the generator and ω_g is the generator speed. In the numerical experiments, $\eta_g = 0.98$ is used, see [7].

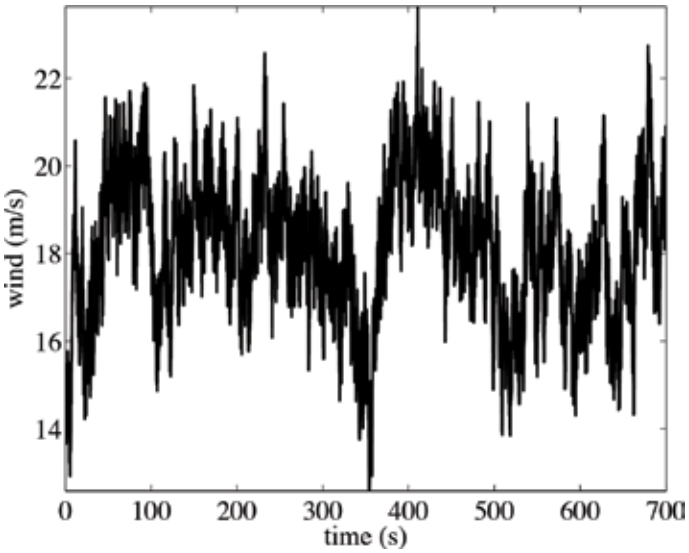

Figure 1. Wind speed signal with turbulence intensity set to 10%.

Each of the three pitch actuators is modeled as a closed loop transfer function between the pitch angle, $\beta(s)$, and its reference $\beta_r(s)$:

$$\frac{\beta(s)}{\beta_r(s)} = \frac{\omega_n^2}{s^2 + 2\xi\omega_n s + \omega_n^2} \tag{3}$$

where ξ is the damping ratio and ω_n the natural frequency that takes the fault-free values $\xi = 0.6$ and $\omega_n = 11.11$ rad/s, see [7].

The fault detection benchmark considers different types of faults at different components (sensors and actuators), as described in **Table 3**.

Fault	Type	Description
F1	Pitch actuator	Change in dynamics: high air content in oil
F2	Pitch actuator	Change in dynamics: pump wear
F3	Pitch actuator	Change in dynamics: hydraulic leakage
F4	Torque actuator	Offset (offset value equal to 2000 Nm)
F5	Generator speed sensor	Scaling (gain factor equal to 1.2)
F6	Pitch angle sensor	Stuck (fixed value equal to 5°)
F7	Pitch angle sensor	Stuck (fixed value equal to 10°)
F8	Pitch angle sensor	Scaling (gain factor equal to 1.2)

Table 3. Fault scenarios.

http://dx.doi.org/10.5772/intechopen.78727

3. Condition monitoring (CM) strategy

The overall CM strategy is based on a three-tier framework:

i. a multiway PCA (MPCA) model is built with the data that are collected from a healthy WT,

ii. when a new WT has to be diagnosed, the SCADA data are projected using the MPCA model created in (i), and

iii. the final decision is based on both univariate and multivariate HT.

3.1. The wind as a source for the excitation: the need for a new paradigm

In general, vibration-based structural health monitoring (SHM) is based on the fact that an alteration or difference in physical properties due to damage or structural change will motivate changes in dynamical responses that may be detected. **Figure 2** represents this paradigm in the sense that a healthy structure is excited according to a prescribed signal to build a pattern. Afterward, the structure that has to be diagnosed is affected by exactly the same signal, where the response is measured, processed, and finally compared with the previous pattern. The strategy presented in **Figure 2** is known as "guided waves in structures for SHM" [15].

In the present chapter, the field of application is wind turbines and a realistic scenario is to consider that the excitation comes from the wind turbulence. The wind turbulence cannot be controlled and it is always different. Therefore, the paradigm of guided waves in WT for SHM as in **Figure 2** cannot be considered. In this case, when the source of the excitation cannot be previously prescribed, a new paradigm is needed, as represented in **Figure 3**. The foundation of the new paradigm is that, even with a constantly different excitation, the CM strategy based on MPCA and univariate and multivariate HT will be able to disclose some hidden damage, misbehavior, or fault. To sum up, the fundamental idea behind the CM strategy is the hypothesis that a variation in the overall behavior of the WT, even with an unprescribed excitation, should be detected.

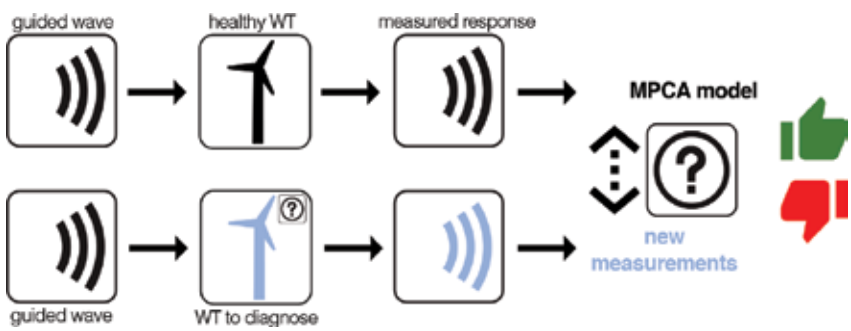

Figure 2. Vibration-based SHM is based on the fact that an alteration or difference in physical properties due to damage or structural change will motivate changes in dynamical responses that may be detected.

Figure 3. The key idea behind the new paradigm of the detection strategy is the assumption that a change in the behavior of the overall system, even with a different excitation, has to be detected.

However, in our application, the only available excitation of the wind turbines is the wind turbulence. Therefore, guided waves in wind turbines for SHM as in **Figure 2** cannot be considered as a realistic scenario. In spite of that, the new paradigm described in **Figure 3** is based on the fact that, even with different wind turbulence, the fault detection strategy based on PCA and statistical multivariate hypothesis testing will be able to detect some damage, fault, or misbehavior. More precisely, the key idea behind the detection strategy is the assumption that a change in the behavior of the overall system, even with a different excitation, has to be detected. Section 4 includes the simulation results of the proposed CM strategy that validates this hypothesis.

3.2. Data-driven baseline modeling based on MPCA

Multiway principal component analysis (MPCA) is a natural extension of classical principal component analysis (PCA) to manage data in multidimensional arrays [16, 17]. A conventional two-dimensional data matrix can be treated as a two-way array, where experiments and variables (or discretization instant times) form the two different ways. Frequently, this arrangement has to be extended to multiway arrays, particularly if several sensors—in different experimental trials—are gathering data at different time instants. Consequently, MPCA is equivalent to the application of standard PCA to an unfolded version of the initial multiway array.

Westerhuis et al. [18] propose six different ways of unfolding a three-way data matrix. Besides, in [18], a critical analysis of several aspects of the treatment of multiway data is provided, including how the matrix is unfolded, but also mean-centering and scaling with respect to the effects on the analysis of batch data. Ruiz et al. [19] assign one of the first six letters of the alphabet to each one of the six different ways of unfolding. In this chapter, as well as in [6, 8, 20, 21], we have considered the so-called type *E*. However, we will present the collected SCADA data arranged in an already unfolded matrix.

The MPCA modeling starts by measuring, from a healthy wind turbine, a sensor during $(nL-1)\Delta$ seconds, where Δ is the sampling time and $n, L \in \mathbb{N}$. The discretized measures of the sensor are a real vector

$$(x_{11}\ x_{12}\ \cdots\ x_{1L}\ x_{21}\ x_{22}\ \cdots\ x_{2L}\ \cdots\ x_{n1}\ x_{n2}\ \cdots\ x_{nL}) \in \mathbb{R}^{nL} \tag{4}$$

where the real number x_{ij}, $i = 1, \ldots, n$, $j = 1, \ldots, L$ corresponds to the measure of the sensor at time $((i-1)L + (j-1))\Delta$ seconds. These collected data can be arranged in matrix form as follows:

$$\begin{pmatrix} x_{11} & x_{12} & \cdots & x_{1L} \\ \vdots & \vdots & \ddots & \vdots \\ x_{i1} & x_{i2} & \cdots & x_{iL} \\ \vdots & \vdots & \ddots & \vdots \\ x_{n1} & x_{n2} & \cdots & x_{nL} \end{pmatrix} \in \mathscr{M}_{n\times L}(\mathbb{R}) \tag{5}$$

where $\mathscr{M}_{n\times L}(\mathbb{R})$ is the vector space of $n \times L$ matrices over $\mathbb{R}$. It is worth noting that n is the number of rows of the matrix in Eq. (5) and L is the number of columns of the same matrix. The effect on the overall performance of the condition monitoring strategy on the choice of n and L is thoroughly analyzed on [21].

Let us assume that the SCADA data are now collected from $N \in \mathbb{N}$ sensors also during the same period of time. In this case, the collected data, for each sensor, can be organized in a matrix as in Eq. (5). Subsequently, all the collected data coming from the whole set of sensors are concatenated and disposed in a matrix $\mathbf{X} \in \mathscr{M}_{n\times(N\cdot L)}$ as follows:

$$\begin{aligned} \mathbf{X} &= \begin{pmatrix} x_{11}^1 & x_{12}^1 & \cdots & x_{1L}^1 & x_{11}^2 & \cdots & x_{1L}^2 & \cdots & x_{11}^N & \cdots & x_{1L}^N \\ \vdots & \vdots & \ddots & \vdots & \vdots & \ddots & \vdots & \ddots & \vdots & \ddots & \vdots \\ x_{i1}^1 & x_{i2}^1 & \cdots & x_{iL}^1 & x_{i1}^2 & \cdots & x_{iL}^2 & \cdots & x_{i1}^N & \cdots & x_{iL}^N \\ \vdots & \vdots & \ddots & \vdots & \vdots & \ddots & \vdots & \ddots & \vdots & \ddots & \vdots \\ x_{n1}^1 & x_{n2}^1 & \cdots & x_{nL}^1 & x_{n1}^2 & \cdots & x_{nL}^2 & \cdots & x_{n1}^N & \cdots & x_{nL}^N \end{pmatrix} \\ &= \left(\underbrace{v_1|v_2|\cdots|v_L}_{\mathbf{X}^1} \underbrace{|v_{L+1}|\cdots|v_{2L}}_{\mathbf{X}^2} |\cdots| \underbrace{v_{(N-1)L+1}|\cdots|v_{N\cdot L}}_{\mathbf{X}^N} \right) \\ &= \begin{pmatrix} \mathbf{X}^1 & \mathbf{X}^2 & \cdots & \mathbf{X}^N \end{pmatrix} \in \mathscr{M}_{n\times(N\cdot L)}(\mathbb{R}) \end{aligned} \tag{6}$$

where the superindex $k = 1, \ldots, N$ of each element x_{ij}^k in the matrix represents the number of sensor. Matrix $\mathbf{X} \in \mathscr{M}_{n\times(N\cdot L)}(\mathbb{R})$—where $\mathscr{M}_{n\times(N\cdot L)}(\mathbb{R})$ is the vector space of $n \times (N \cdot L)$ matrices over $\mathbb{R}$—contains the measures from N sensors at nL discretization instants. Consequently, each row vector $x_i^T = \mathbf{X}(i,:) \in \mathbb{R}^{N\cdot L}$, $i = 1, \ldots, n$ represents the measurements from all the sensors at time instants $((i-1)L + (j-1))\Delta$ seconds, $j = 1, \ldots, L$. Equivalently, each column vector $v_j = \mathbf{X}(:,j) \in \mathbb{R}^n$, $j = 1, \ldots, N \cdot L$ represents measurements from sensor number $\left\lceil \frac{j}{L} \right\rceil$ at time instants $((i-1)L + (j-1))\Delta$ seconds, $1 = 1, \ldots, n$, where $\lceil \cdot \rceil$ is the ceiling function.

The objective of the subsequent analysis is to build the MPCA model, that is, the square orthogonal matrix $\mathbf{P} \in \mathscr{M}_{(N\cdot L)\times(N\cdot L)}(\mathbb{R})$ that has to be used to transform or project the original data matrix $\mathbf{X}$ according to the following matrix-to-matrix product:

$$\mathbf{T} = \mathbf{XP} \in \mathscr{M}_{n\times(N\cdot L)}(\mathbb{R}), \tag{7}$$

where the shape of the variance-covariance matrix of matrix **T** in Eq. (7) is diagonal.

In the proposed approach in this chapter, the model defined in matrix **P** in Eq. (7) is based only on measures that come from a *healthy* wind turbine. Posteriorly, data from the current WT to diagnose will be projected using the matrix-to-matrix multiplication also defined in Eq. (7). However, a different procedure can be considered, particularly, when the goal is not just to detect a damage or a fault but to classify it. In the latter case, matrix **X** in Eq. (6) should contain measures from a WT in its healthy state but also in all the possible fault scenarios. This way, the generated model in matrix **P** in Eq. (7) contains all the possible states of the structure.

3.2.1. Centering and scaling: group scaling (GS) vs. mean-centered group scaling (MCGS)

Considering that the data stored in matrix **X** are affected by a changing wind turbulence, come from different sensors, and could have different magnitudes and scales, some kind of preprocessing step is required to rescale the data [22, 23]. According to Westerhuis et al. [18], the way this preprocessing step is carried out may affect the overall performance of the CM strategy. In the present chapter, we present two possible choices that have some common core. These two alternatives are as follows:

i. group scaling (GS) and

ii. mean-centered group scaling (MCGS).

In the former case (GS), both the arithmetic mean and the variance of all measurements of the sensor are used. More precisely, for $k = 1, 2, \ldots, N$, we define

$$\mu^k = \frac{1}{nL}\sum_{i=1}^{n}\sum_{j=1}^{L} x_{ij}^k, \tag{8}$$

$$\sigma_k^2 = \frac{1}{nL}\sum_{i=1}^{n}\sum_{j=1}^{L}\left(x_{ij}^k - \mu^k\right)^2 \tag{9}$$

where μ^k and σ_k^2 are the arithmetic mean and the variance of the whole set of elements in matrix $\mathbf{X}^k$, respectively. In this case, matrix $\mathbf{X} = \left(x_{ij}^k\right)$ is centered and scaled—using GS—to define a modified matrix $\breve{\mathbf{X}} = \mathbf{X}_{\mathrm{GS}} = \left(\breve{x}_{ij}^k\right)$ as

$$\breve{x}_{ij}^k := \frac{x_{ij}^k - \mu^k}{\sqrt{\sigma_k^2}}, \quad i = 1, \ldots, n, \quad j = 1, \ldots, L, \quad k = 1, \ldots, N. \tag{10}$$

In the latter case (MCGS), the arithmetic of all measurements of the sensor at the same column is considered in the normalization. More precisely, for $k = 1, 2, \ldots, N$, we define

$$\mu_j^k = \frac{1}{n}\sum_{i=1}^{n} x_{ij}^k, \quad j = 1, \ldots, L, \tag{11}$$

where μ_j^k is the arithmetic mean of the measures placed at the same column. In this case, then, matrix $\mathbf{X} = \left(x_{ij}^k\right)$ is centered and scaled—using MCGS—to define a modified matrix $\breve{\mathbf{X}} = \mathbf{X}_{\text{MCGS}} = \left(\breve{x}_{ij}^k\right)$ as

$$\breve{x}_{ij}^k := \frac{x_{ij}^k - \mu_j^k}{\sqrt{\sigma_k^2}}, \quad i = 1, \ldots, n, \quad j = 1, \ldots, L, \quad k = 1, \ldots, N. \tag{12}$$

where σ_k^2 is defined as in Eq. (9) using μ^k as in Eq. (8). It is worth noting that the only difference between the expressions in Eqs. (10) and (12) is how the elements in matrix $\mathbf{X} = \left(x_{ij}^k\right)$ are *centered*. When matrix $\mathbf{X} = \left(x_{ij}^k\right)$ is scaled and centered according to the MCGS strategy described in Eq. (12), the average value of each column vector in the scaled matrix $\breve{\mathbf{X}}$ can be calculated as

$$\frac{1}{n}\sum_{i=1}^{n} \breve{x}_{ij}^k = \frac{1}{n}\sum_{i=1}^{n} \frac{x_{ij}^k - \mu_j^k}{\sigma^k} = \frac{1}{n\sigma^k}\sum_{i=1}^{n}\left(x_{ij}^k - \mu_j^k\right) \tag{13}$$

$$= \frac{1}{n\sigma^k}\left[\left(\sum_{i=1}^{n} x_{ij}^k\right) - n\mu_j^k\right] \tag{14}$$

$$= \frac{1}{n\sigma^k}\left(n\mu_j^k - n\mu_j^k\right) = 0 \tag{15}$$

Taking advantage of the fact that the scaled matrix $\breve{\mathbf{X}}$ is a mean-centered matrix, the variance-covariance matrix can be straightforwardly computed as a matrix-to-matrix product of $\breve{\mathbf{X}}$ and its transpose, divided by $n - 1$, where n is the number of rows of matrix $\mathbf{X}$ in Eq. (6). More precisely,

$$\mathbf{C}\breve{\mathbf{X}} = \frac{1}{n-1}\breve{\mathbf{X}}^T\breve{\mathbf{X}} \in \mathscr{M}_{(N\cdot L)\times(N\cdot L)}(\mathbb{R}) \tag{16}$$

Clearly, GS and MCGS are not the only ways to center and scale data. For instance, feature scaling, also known as unity-based normalization, can also be considered. In this case, data are centered with respect to the minimum value and scaled with respect to the range of the set, that is,

$$\tilde{x}_{ij}^k := \frac{x_{ij}^k - \min\left\{x_{ij}^k\right\}}{\max\left\{x_{ij}^k\right\} - \min\left\{x_{ij}^k\right\}}, \quad i = 1, \ldots, n, \quad j = 1, \ldots, L, \quad k = 1, \ldots, N. \tag{17}$$

However, to easily compute the variance-covariance matrix in the CM strategy that we present in this chapter, the mean-centered group scaling (MCGS) is the method that we have selected

for the centering and scaling. In order to not to use the baroque notation $\breve{\mathbf{X}}$ throughout the rest of this chapter, this centered and scaled matrix is redesignated as $\mathbf{X}$, without the breve sign.

The MPCA model is described by the latent vectors

$$p_j, \quad j = 1, \ldots, N \cdot L, \tag{18}$$

also known as eigenvector or proper vectors, and the latent roots

$$\lambda_j, \quad j = 1, \ldots, N \cdot L, \tag{19}$$

also known as eigenvalues or proper values, of the variance-covariance matrix $\mathbf{C_X}$ as follows:

$$\mathbf{C_X P} = \mathbf{P}\Lambda \tag{20}$$

where

$$\mathbf{P} = \left(p_1|p_2|\cdots|p_{N\cdot L}\right) \in \mathscr{M}_{N\cdot L \times N\cdot L}(\mathbb{R}) \tag{21}$$

$$\Lambda = \left(\Lambda_{ij}\right) \in \mathscr{M}_{N\cdot L \times N\cdot L}(\mathbb{R}) \tag{22}$$

and

$$\Lambda_{jj} = \lambda_j, \quad j = 1, \ldots, N \cdot L \tag{23}$$

$$\Lambda_{ij} = 0, \quad i, j = 1, \ldots, N \cdot L, \quad i \neq j \tag{24}$$

The latent vectors and latent roots in Eqs. (21) and (23) are arranged in descending order with respect to the absolute values of the latent roots, that is,

$$|\lambda_i| \geq |\lambda_{i+1}|, \quad i = 1, \ldots, N \cdot L - 1 \tag{25}$$

The latent vector p_1—corresponding to the largest latent root λ_1 (in absolute value)—is called the first principal component (PC). Likewise, the latent vector p_2—corresponding to the second largest latent root λ_2 (in absolute value)—is called the second principal component. Equivalently, the latent vector $p_j, \quad j = 1, \cdots, N \cdot L$—corresponding to the latent root λ_j—is called the j—th principal component.

Matrix $\mathbf{T}$ in Eq. (7) represents the transformed or projected matrix onto the principal component space and it is also known as score matrix.

When, for the sake of dimensionality reduction, a decreased number of principal components are considered:

$$\ell < N \cdot L, \tag{26}$$

a reduced multiway PCA model is then assembled:

$$P = \left(p_1|p_2|\cdots|p_\ell\right) \in \mathscr{M}_{N\cdot L \times \ell}(\mathbb{R}). \tag{27}$$

3.3. HT-based condition monitoring

As said in Section 3.2, the MPCA model is based only on measures that come from a healthy wind turbine. Posteriorly, data from the current WT to diagnose—and subjected to a different wind turbulence—are gathered from as many sensors as in the modeling phase described in Section 3.2 and during a period of time, $(\nu L-1)\Delta$ seconds, which is not necessarily equal. These new data are arranged in a new matrix $\mathbf{Y}$ in a similar way as in Eq. (6):

$$\begin{aligned}\mathbf{Y} &= \begin{pmatrix} y_{11}^1 & y_{12}^1 \cdots y_{1L}^1 y_{11}^2 \cdots y_{1L}^2 \cdots y_{11}^N \cdots y_{1L}^N \\ \vdots & \vdots \ddots \vdots \vdots \ddots \vdots \ddots \vdots \\ y_{i1}^1 & y_{i2}^1 \cdots y_{iL}^1 y_{i1}^2 \cdots y_{iL}^2 \cdots y_{i1}^N \cdots y_{iL}^N \\ \vdots & \vdots \ddots \vdots \vdots \ddots \vdots \ddots \vdots \\ y_{\nu 1}^1 & y_{\nu 2}^1 \cdots y_{\nu L}^1 y_{\nu 1}^2 \cdots y_{\nu L}^2 \cdots y_{\nu 1}^N \cdots y_{\nu L}^N \end{pmatrix} \in \mathscr{M}_{\nu \times (N \cdot L)}(\mathbb{R}) \\ &= \left(\underbrace{w_1 | w_2 | \cdots | w_L}_{\mathbf{Y}^1} \underbrace{| w_{L+1} | \cdots | w_{2L}}_{\mathbf{Y}^2} | \cdots | \underbrace{w_{(N-1)L+1} | \cdots | w_{N \cdot L}}_{\mathbf{Y}^N} \right) \\ &= \begin{pmatrix} \mathbf{Y}^1 & \mathbf{Y}^2 \cdots \mathbf{Y}^N \end{pmatrix} \in \mathscr{M}_{n \times (N \cdot L)}(\mathbb{R}) \end{aligned} \tag{28}$$

It should be noted that $\nu \in \mathbb{N}$ (the number of rows of matrix $\mathbf{Y}$) does not necessarily need to match the natural number n, which represents the number of rows of matrix $\mathbf{X}$ in Eq. (6). However, the number of columns, represented by the natural number $N \cdot L$, must agree.

The collected data in matrix $\mathbf{Y}$ in Eq. (28) are first centered and scaled to form a matrix $\breve{\mathbf{Y}} = \left(\breve{y}_{ij}^k \right)$ similar to the one in Eq. (12):

$$\breve{y}_{ij}^k := \frac{y_{ij}^k - \mu_j^k}{\sqrt{\sigma_k^2}}, \quad i = 1, \ldots, \nu, \quad j = 1, \ldots, L, \quad k = 1, \ldots, N, \tag{29}$$

where σ_k^2 and μ_j^k are the values of the variance and the arithmetic mean that have been previously calculated in Eqs. (9) and (11), respectively, with respect to $\mathbf{X}$ in Eq. (6). After the preprocessing step, that is, centering and scaling the raw data collected from the current structure to diagnose, the scores related to each row vector

$$r^i = \breve{\mathbf{Y}}(i, :) \in \mathbb{R}^{N \cdot L}, \quad i = 1, \ldots, \nu \tag{30}$$

are computed using a vector-to-matrix product:

$$t^i = r^i \cdot \hat{\mathbf{P}} \in \mathbb{R}^{\ell}, \quad i = 1, \ldots, \nu \tag{31}$$

where matrix $\hat{\mathbf{P}}$ is the reduced MPCA model in Eq. (27).

Let us consider the canonical basis

$$\{\mathbf{e}_1, \mathbf{e}_2, \ldots, \mathbf{e}_\ell\} \subset \mathbb{R}^\ell \tag{32}$$

of the $\ell-$dimensional real vector space $\mathbb{R}^\ell$.

Given a row vector r^i as in Eq. (30), the real number

$$t_1^i = t^i \cdot \mathbf{e}_1 \in \mathbb{R} \tag{33}$$

is called the first score. Likewise, the scalar

$$t_2^i = t^i \cdot \mathbf{e}_2 \in \mathbb{R} \tag{34}$$

is called the second score. In general, the scalar

$$t_j^i = t^i \cdot \mathbf{e}_j \in \mathbb{R} \tag{35}$$

is called the score associated with the principal component p_j, $j = 1, \ldots, \ell$ or, simply, score j.

In addition, an $s-$dimensional vector as can be built if more than one score is considered at the same time. Indeed,

$$\mathbf{t}_s^i = \begin{bmatrix} t_1^i & t_2^i & \cdots & t_s^i \end{bmatrix}^T \in \mathbb{R}^s, \quad s \leq \ell. \tag{36}$$

3.3.1. Scores as a random sample

As said in Section 3.1, the excitation of the WT comes from a changing turbulent wind. Somehow, this turbulent wind can be viewed as a random signal. Therefore, the response of the WT can be also viewed as a random process and so the measurements in the row vector r^i in Eq. (30). As a consequence, the vector t^i receives this random nature and it can be observed as an ℓ-dimensional random vector to construct the statistical approach in this chapter. As a motivating example, in **Figure 4**, two three-dimensional samples are represented: one is the

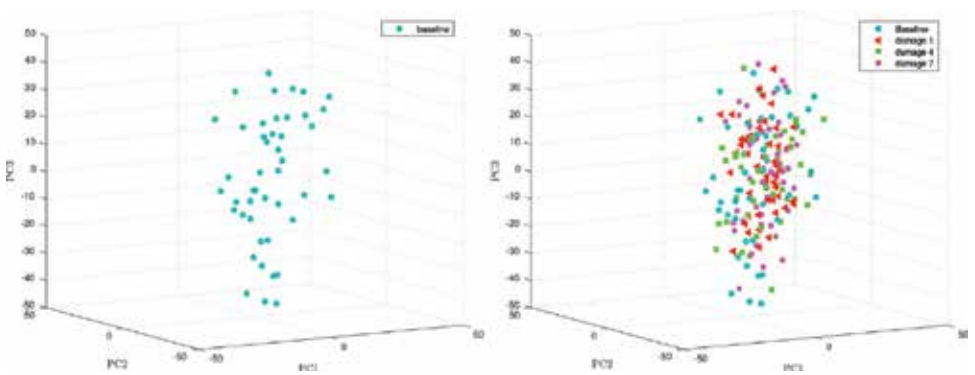

Figure 4. Baseline sample (left) and sample from the wind turbine to be diagnosed (right).

three-dimensional baseline sample (left) and the other is referred to faults 1, 4, and 7 (right). In a classic application of the PCA strategy in the field of SHM, the scores allow a separation, clustering, or visual grouping [24]. However, in this case, it can be clearly monitored in **Figure 4** (right) that a clustering, visual grouping, or separation cannot be performed. Therefore, more powerful and reliable tools are needed to be able to detect a fault in the WT.

In structural health monitoring or condition monitoring applications, the final decision on whether the structure, the actuator and/or the sensor is healthy or not should not depend on graphical approaches. One of the most common approaches to reliable indicators of damage or faults is the use of the powerful machinery of statistical hypothesis testing. The differences in this kind of strategies rely on what is the subject of the test and, of course, how the raw data collected by the sensors are arranged and preprocessed. For instance, in Zugasti et al. [25] the damage detection is based on testing for significant changes in the parameter vector of an AutoRegressive model. A comprehensive three-tier modular structural health monitoring framework is proposed by Hackell et al. [26] where the hypothesis testing is used to declare decision boundaries, control charts, and ROC curves with the ultimate goal of distinguishing between healthy and potentially damaged data on an operational wind turbine. A somehow different approach is presented by Ng et al. [27] that includes a vehicle health monitoring system where several univariate hypothesis tests are considered in parallel. Again in the field of structural health monitoring or condition monitoring of wind turbines, a recent work by Tsiapoki et al. [28] where damage and ice detection is based on data normalization, feature extraction and hypothesis testing (HT).

The use of univariate hypothesis testing as a key element for structural health monitoring or condition monitoring has been increasing in the last years as a reliable method. Variations of these univariate HT for multiple indicators include the use of univariate HT in parallel, that is, testing for each component of a parameter vector rather than testing for the whole multi-dimensional parameter vector. The first approach for the detection of structural changes using a multivariate hypothesis testing has been proposed by Pozo et al. [8]. One of the key results in the work [8] is that multivariate HTs allow to get better results in damage or fault detection that just univariate test. One interesting example presented in the work by Pozo et al. [8] shows that, for a given level of significance α, five independent univariate hypothesis

$$\begin{aligned} H_0: &\quad \mu_{\mathrm{c},i} = \mu_{\mathrm{h},i} \\ H_1: &\quad \mu_{\mathrm{c},i} \neq \mu_{\mathrm{h},i} \end{aligned} \tag{37}$$

where $i = 1, 2, \ldots, 5$ lead to a wrong decision while the single multivariate HT

$$\begin{aligned} H_0: &\quad \boldsymbol{\mu}_{\mathrm{c}} = \boldsymbol{\mu}_{\mathrm{h}} \\ H_1: &\quad \boldsymbol{\mu}_{\mathrm{c}} \neq \boldsymbol{\mu}_{\mathrm{h}} \end{aligned} \tag{38}$$

where

$$\begin{aligned} \boldsymbol{\mu}_{\mathrm{c}}^T &= \begin{bmatrix} \mu_{\mathrm{c},1} & \mu_{\mathrm{c},2} & \cdots & \mu_{\mathrm{c},5} \end{bmatrix} \\ \boldsymbol{\mu}_{\mathrm{h}}^T &= \begin{bmatrix} \mu_{\mathrm{h},1} & \mu_{\mathrm{h},2} & \cdots & \mu_{\mathrm{h},5} \end{bmatrix} \end{aligned} \tag{39}$$

is able to correctly classify the structure. This example shows that multivariate HT is even more reliable than univariate HT. However, these benefits come at a price, in the sense that in order to apply the multivariate HT, the statistical distribution of the data must be multinormal. Of course, it may happen that five sets of 50 samples

$$\{x_1^i, x_2^i, \ldots, x_{50}^i\} \rightarrowtail N(\mu_i, \sigma_i), \quad i = 1, 2, \ldots, 5 \tag{40}$$

are normally distributed, while the sample vector

$$\{\mathbf{x}_1, \mathbf{x}_2, \ldots, \mathbf{x}_{50}\} \not\rightarrowtail N(\mu, \Sigma), \tag{41}$$

where

$$\mathbf{x}_j = \begin{bmatrix} x_j^1 & x_j^2 & \cdots & x_j^5 \end{bmatrix}^T, \quad j = 1, \ldots, 50 \tag{42}$$

and Σ is the variance-covariance matrix, is not multinormally distributed.

3.3.2. Univariate case: testing for the equality of means

In this section, we present how a fault is detected in the WT using univariate HT. To this end, first we have to define what we consider our *baseline*. Given a principal component $j = 1, \ldots, \ell$, the baseline sample is the set of real numbers $\left\{\tau_j^i\right\}_{i=1,\ldots,n}$ defined by

$$\tau_j^i := \left(\mathbf{X}(i,:) \cdot \widehat{\mathbf{P}}\right)(j) = \mathbf{X}(i,:) \cdot \widehat{\mathbf{P}} \cdot \mathbf{e}_j, \quad i = 1, \ldots, n, \tag{43}$$

where $\mathbf{e}_j$ is the j-th vector of the canonical basis in Eq. (32), P is the MPCA model defined in Eq. (27), and $\mathbf{X}$ is the centered and scaled matrix of the collected data from a *healthy* WT as in Eq. (6). Similarly, and given a principal component $j = 1, \ldots, \ell$, the sample of the current WT to diagnose is defined as the set of ν real numbers

$$\left\{t_j^i\right\}_{i=1,\ldots,\nu} \tag{44}$$

as defined in Eq. (35).

Before the univariate HT is applied, the following assumptions must be made:

i. the baseline sample $\left\{\tau_j^i\right\}_{i=1,\ldots,n}$ is a random sample of a random variable (RV) normally distributed with unknown mean μ_X and unknown variance σ_X^2 and

ii. the random sample $\left\{t_j^i\right\}_{i=1,\ldots,\nu}$ in Eq. (44) of the current WT to diagnose follows a normal distribution with unknown mean μ_Y and unknown variance σ_Y^2.

It is worth mentioning that the variances of these two samples are not supposed to be necessary equal.

Let us define

$$\delta\mu = \mu_X - \mu_Y \tag{45}$$

as the difference between these two mean values. Since we want to know if the distribution of these two samples is related, this leads to a test of the hypothesis

$$H_0: \ \delta\mu = 0 \ \text{versus} \tag{46}$$

$$H_1: \ \delta\mu \neq 0 \tag{47}$$

where the null hypothesis H_0 is "the sample of the WT to be diagnosed is distributed as the baseline sample" and the alternative hypothesis H_1 is "the sample of the WT to be diagnosed is not distributed as the baseline sample." In other words, if the result of the test is that H_0 is accepted, the current WT is categorized as healthy. Otherwise, if H_0 is rejected in favor of H_1, this would indicate the presence of some faults in the WT.

Given the assumptions of normality and considering that the two variances are not necessarily equal, the test for the equality of mean is based on the so-called Welch-Satterthwaite method [29], which is outlined below for the sake of completeness. If two random samples of size n and v, respectively, are taken from two normal distributions $N(\mu_X, \sigma_X)$ and $N(\mu_Y, \sigma_Y)$ and the population variances are unknown and not necessarily equal, the random variable

$$\mathscr{WS} = \frac{\left(\overline{X} - \overline{Y}\right) + \left(\mu_X - \mu_Y\right)}{\sqrt{\left(\frac{S_X^2}{n} + \frac{S_Y^2}{v}\right)}} \tag{48}$$

can be approximated with a t-distribution with ρ degrees of freedom (DOF), that is

$$\mathscr{WS} \rightarrowtail t_\rho \tag{49}$$

where

$$\rho = \left\lfloor \frac{\left(\frac{s_X^2}{n} + \frac{s_Y^2}{v}\right)^2}{\frac{\left(s_X^2/n\right)^2}{n-1} + \frac{\left(s_Y^2/v\right)^2}{v-1}} \right\rfloor, \tag{50}$$

S^2 is the sample variance as a random variable, s^2 is the variance of a sample, $\overline{X}, \overline{Y}$ are the sample mean as a random variable, and $\lfloor \cdot \rfloor$ is the standard floor function.

The magnitude of the test statistic using Welch-Satterthwaite method is defined as

$$t_{\text{obs}} = \frac{\overline{x} - \overline{y}}{\sqrt{\left(\frac{s_X^2}{n} + \frac{s_Y^2}{v}\right)}} \tag{51}$$

where $\overline{x}, \overline{y}$ is the mean of a particular sample. The quantity t_{obs} is the fault indicator. We can then construct the following test:

$$|t_{\text{obs}}| \leq t^{\star} \quad \Rightarrow \quad \text{Accept } H_0 \tag{52}$$

$$|t_{\text{obs}}| > t^{\star} \quad \Rightarrow \quad \text{Accept } H_1 \tag{53}$$

where $t^{\star}$ is such that

$$P\left(t_{\rho} \geq t^{\star}\right) = \frac{\alpha}{2}, \tag{54}$$

where α is the level of significance for the test. To sum up,

i. H_0 is rejected if $|t_{obs}| > t^{\star}$ (the WT is classified as not healthy) and

ii. H_0 is accepted if $|t_{obs}| \leq t^{\star}$ (the WT is classified as healthy).

3.3.3. Multivariate case: testing a multivariate mean vector

In Section 3.3.2, for each principal component $j = 1, \ldots, \ell$, a test for the equality of means is performed. This means that for a single sample of the current structure to diagnose, we obtain ℓ decisions on whether the structure is healthy or not. In the present section, more than one principal component will be considered jointly thus defining a vector. Therefore, a test for the plausibility of a value for a normal population mean vector will be performed.

As in Section 3.3.2, the objective of this work is to determine whether the distribution of the multivariate random samples that are obtained from the WT to be diagnosed (healthy or not) is connected to the distribution of the baseline.

Let us define $s \in \mathbb{N}$ as the number of PCs that are considered at the same time. Before the multivariate HT is applied, the following assumptions must be made:

i. the baseline projection is a multivariate random sample (MRS) of a multivariate random variable (MRV) following a multivariate normal distribution (MVND) with known population mean vector $\boldsymbol{\mu}_{\text{h}} \in \mathbb{R}^s$ and known variance-covariance matrix $\sum \in \mathscr{M}_{s\times s}(\mathbb{R})$ and

ii. the multivariate random sample of the WT to be diagnosed also follows an MVND with unknown multivariate mean vector $\boldsymbol{\mu}_{\text{c}} \in \mathbb{R}^s$ and known variance-covariance matrix $\sum \in \mathscr{M}_{s\times s}(\mathbb{R})$.

In this case, opposite to what we have assumed in Section 3.3.2, both multivariate random variables have the same known variance-covariance matrix.

Similarly as in Section 3.3.2, the question that arises here is whether a given s-dimensional vector $\boldsymbol{\mu}_{\text{c}}$ is a reasonable value for the mean of an MVND $N_s\left(\boldsymbol{\mu}_{\text{h}}, \sum\right)$. This leads to the following test of the hypothesis

$$\begin{aligned} H_0 &: \ \boldsymbol{\mu}_{\text{c}} = \boldsymbol{\mu}_{\text{h}} \ \text{ versus} \\ H_1 &: \ \boldsymbol{\mu}_{\text{c}} \neq \boldsymbol{\mu}_{\text{h}}, \end{aligned} \tag{55}$$

where H_0 is "the MRS of the WT to be diagnosed is distributed as the baseline projection" and H_1 is "the MRS of the WT to be diagnosed is not distributed as the baseline projection." In

other words, if the result of the test is that H_0 is accepted, the current WT is categorized as healthy. Otherwise, if H_0 is rejected in favor of H_1, this would indicate the presence of some faults in the WT.

In this case, the multivariate test is based on Hotelling's T^2 statistic and it is outlined below. When an MRS of size $v \in \mathbb{N}$ is taken from an MVND $N_s(\boldsymbol{\mu}_h, \sum)$, the RV

$$T^2 = v(\overline{\mathbf{X}} - \boldsymbol{\mu}_h)^T \mathbf{S}^{-1} (\overline{\mathbf{X}} - \boldsymbol{\mu}_h) \tag{56}$$

is distributed as

$$T^2 \rightarrowtail \frac{(v-1)s}{v-s} \boldsymbol{F}_{s,\, v-s}, \tag{57}$$

where $\boldsymbol{F}_{s,\, v-s}$ denotes an RV with an F-distribution with s and $v - s$ DOF, $\overline{\mathbf{X}}$ is the sample vector mean as a MRV, and $\frac{1}{n}\mathbf{S} \in \mathscr{M}_{s\times s}(\mathbb{R})$ is the estimated variance-covariance matrix of $\overline{\mathbf{X}}$.

The value of the test statistic is defined as

$$t^2_{\text{obs}} = v(\overline{\mathbf{x}} - \boldsymbol{\mu}_h)^T \mathbf{S}^{-1} (\overline{\mathbf{x}} - \boldsymbol{\mu}_h), \tag{58}$$

and is the fault indicator. We can then construct the following test:

$$t^2_{\text{obs}} \leq \frac{(v-1)s}{v-s} \boldsymbol{F}_{s,\, v-s}(\alpha) \quad \Rightarrow \quad \text{Accept } H_0, \tag{59}$$

$$t^2_{\text{obs}} > \frac{(v-1)s}{v-s} \boldsymbol{F}_{s,\, v-s}(\alpha) \quad \Rightarrow \quad \text{Accept } H_1, \tag{60}$$

where $\boldsymbol{F}_{s,\, v-s}(\alpha)$ is the upper (100α)th percentile of the $\boldsymbol{F}_{s,\, v-s}$ distribution, that is,

$$\mathbb{P}(\boldsymbol{F}_{s,\, v-s} > \boldsymbol{F}_{s,\, v-s}(\alpha)) = \alpha, \tag{61}$$

where $\mathbb{P}$ is a probability measure and α is the level of significance for the test. To sum up,

i. H_0 is rejected if $t^2_{obs} > \frac{(v-1)s}{v-s} \boldsymbol{F}_{s,\, v-s}(\alpha)$ (the WT is classified as not healthy) and

ii. H_0 is accepted if $t^2_{obs} \leq \frac{(v-1)s}{v-s} \boldsymbol{F}_{s,\, v-s}(\alpha)$ (the WT is classified as healthy).

4. Simulation results

The results of the CM strategies presented in Sections 3.3.2 and 3.3.3 are organized into three subsections. The absolute value of samples that are correctly identified and the absolute number of false alarms and missing faults are included in Section 4.1. Sections 4.2 and 4.3 show the results, not as absolute values but as a percentage. More precisely, the sensitivity and the specificity are both comprised in Section 4.2, including the false-negative (FNR) and the

false-positive rates (FPR). Besides, the true rate of both false negatives and false positives are contained in Section 4.3.

For the validation of the CM strategies presented in Sections 3.3.2 and 3.3.3, 24 samples of $\nu = 50$ elements each have been examined, in accordance with the following organization:

• 8 samples of a faulty WT (one sample for each one of the different fault scenarios described in **Table 3**) and

• 16 samples of a healthy WT.

All samples are acquired with changing wind data sets with turbulence intensity established to 10% and computed with TurbSim [14]. These wind data have the subsequent features:

i. Kaimal turbulence model,

ii. logarithmic profile wind type,

iii. mean speed of 18.2 m/s simulated at hub height, and

iv. a roughness factor of 0.01 m.

Each sample of $\nu = 50$ elements comes from the measures collected during $(\nu \cdot L - 1)\Delta = 312.4875$ seconds. The values for these parameters are listed in **Table 4**.

We present, in Sections 4.1, 4.2, and 4.3, the results when the collected data are projected into:

i. the *first* principal component,

ii. the *second* principal component,

iii. the *third* principal component,

iv. the first *and* the second principal components, jointly,

v. the first *seven* principal components, jointly, and

vi. the first *twelve* principal components, jointly.

In the three univariate cases, (i)–(iii), we use the test for the equality of means, while in the three multivariate cases, (iv)–(vi), we use the test for the plausibility of a value for a normal population. In both cases, the chosen level of significance is $\alpha = 10\%$.

Parameter	Symbol	Magnitude
Number of rows	ν	50
Number of columns	L	500
Sampling time	Δ	0.0125
Number of sensors	N	13

Table 4. The collected measures are arranged in a $\nu \times (N \cdot L)$ matrix $\mathbf{Y}$ as in Eq. (28)

4.1. Types I and II errors

In this section, each of the 24 samples is classified as follows:

i. number of samples from the healthy WT (healthy sample), which were classified by the hypothesis test as "healthy" (accept H_0) [right decision],

ii. faulty sample classified by the test as "faulty" (accept H_1) [right decision],

iii. samples from the faulty WT (faulty sample) classified as "healthy" [wrong decision/missing fault/type II error], and

iv. healthy sample classified as "faulty" [wrong decision/false alarm/type I error].

The results displayed in **Table 6** are disposed according to the scheme in **Table 5**.

4.2. Sensitivity and specificity

As in [20, 30], two more statistical indicators are analyzed to assess the efficiency of the test. On the one hand, the *specificity* of the test is defined as the fraction of samples from the healthy structure, which are correctly classified. On the other hand, the *sensitivity*—or the power of the test—is defined as the fraction of samples from the faulty wind turbine that are correctly classified as such.

	Healthy sample (H_0)	**Faulty sample (H_1)**
Accept H_0	Correct decision	Type II error (missing fault)
Accept H_1	Type I error (false alarm)	Correct decision

Table 5. Scheme for the presentation of the results in **Table 6**

	H_0	H_1		H_0	H_1
Score 1			Scores 1–2		
Accept H_0	16	1	Accept H_0	12	0
Accept H_1	0	7	Accept H_1	4	8
Score 2			Scores 1–7		
Accept H_0	13	7	Accept H_0	13	0
Accept H_1	3	1	Accept H_1	3	8
Score 3			Scores 1–12		
Accept H_0	16	8	Accept H_0	16	0
Accept H_1	0	0	Accept H_1	0	8

Table 6. Categorization of the samples with respect to the presence or absence of a fault and the result of the test considering the first score, the second score, and the third score (left) and scores 1–2 (jointly), scores 1–7 (jointly), and scores 1–12 (jointly) (right), when the size of the samples to diagnose is $\nu = 50$ and the level of significance is $\alpha = 10\%$

The sensitivity and specificity of both the univariate HT and the multivariate case with respect to the 24 samples displayed in **Table 8** are disposed according to the scheme in **Table 7**.

4.3. Reliability of the results

Finally, the true rate of false negatives and the true rate of false positives can be used to assess the performance of the proposed CM strategy. These two measures—closely related to Bayes' theorem [31]—are described in **Table 9**. On the one hand, the true rate of false negatives is the fraction of samples from the faulty WT that have been wrongly identified as healthy. On the other hand, the true rate of false positives is the fraction of sample from the healthy WT that have been wrongly identified as faulty.

The true rate of false negatives and the true rate of false positives of both the univariate HT and the multivariate case displayed in **Table 10** are disposed according to the scheme in **Table 9**.

	Healthy sample (H_0)	**Faulty sample (H_1)**
Accept H_0	Specificity $(1-\alpha)$	False-negative rate (γ)
Accept H_1	False-positive rate (α)	Sensitivity $(1-\gamma)$

Table 7. Relationship between specificity and sensitivity.

	H_0	H_1		H_0	H_1
Score 1			Scores 1–2		
Accept H_0	1.00	0.12	Accept H_0	0.75	0.00
Accept H_1	0.00	0.88	Accept H_1	0.25	1.00
Score 2			Scores 1–7		
Accept H_0	0.81	0.88	Accept H_0	0.81	0.00
Accept H_1	0.19	0.12	Accept H_1	0.19	1.00
Score 3			Scores 1–12		
Accept H_0	1.00	1.00	Accept H_0	1.00	0.00
Accept H_1	0.00	0.00	Accept H_1	0.00	1.00

Table 8. Sensitivity and specificity of the test considering the first score, the second score, and the third score (left) and scores 1–2 (jointly), scores 1–7 (jointly), and scores 1–12 (jointly) (right), when the size of the samples to diagnose is $\nu = 50$ and the level of significance is $\alpha = 10\%$

	Healthy sample (H_0)	**Faulty sample (H_1)**
Accept H_0	$\mathbb{P}(H_0 \text{accept } H_0)$	True rate of false negatives $\mathbb{P}(H_1 \text{accept } H_0)$
Accept H_1	True rate of false positives $\mathbb{P}(H_0 \text{accept } H_1)$	$\mathbb{P}(H_1 \text{accept} H_1)$

Table 9. Relationship between the proportion of false negatives and false positives.

	H_0	H_1		H_0	H_1
Score 1			Scores 1–2		
Accept H_0	0.94	0.06	Accept H_0	1.00	0.00
Accept H_1	0.00	1.00	Accept H_1	0.33	0.67
Score 2			Scores 1–7		
Accept H_0	0.65	0.35	Accept H_0	1.00	0.00
Accept H_1	0.75	0.25	Accept H_1	0.27	0.73
Score 3			Scores 1–12		
Accept H_0	0.67	0.33	Accept H_0	1.00	0.00
Accept H_1	0.00	0.00	Accept H_1	0.00	1.00

Table 10. True rate of false negatives and true rate of false positives of the test considering the first score, the second score, and the third score (left) and scores 1–2 (jointly), scores 1–7 (jointly), and scores 1–12 (jointly) (right), when the size of the samples to diagnose is $\nu = 50$ and the level of significance is $\alpha = 10\%$

5. Concluding remarks

A multifault detection method based on MPCA through uni- and multivariate hypothesis testing has been presented in this chapter. It is noteworthy to mention the obtained performance through the study of eight realistic different faults in different components of the WT, taking into account that the proposed strategy does not need extra sensors but only uses already available data from the WT SCADA system.

The three main conclusions, which show the benefits of the multivariate statistical hypothesis testing in comparison with the univariate case, for WT condition monitoring, are the following:

1. Given a level of significance $\alpha = 10\%$, when the first 12 scores are considered jointly, an accuracy of 100% is obtained, while in all the other studied cases, misclassifications are present.
2. Multivariate analysis leads to average values of 100% for the sensitivity and 85.33% for the specificity, while for the univariate case, the average values are 33.33 and 93.67%, respectively.
3. Multivariate analysis leads to average value of the true rate of false negatives of 0% and the average value of the true rate of false positives of 20%, while for the univariate case, the average values are 24.67 and 25%, respectively.

Acknowledgements

This work has been partially funded by the Spanish Ministry of Economy and Competitiveness through the research projects DPI2014-58427-C2-1-R and DPI2017-82930-C2-1-R, and by the Generalitat de Catalunya through the research project 2017 SGR 388.

Abbreviations

The following abbreviations are used in this chapter:

DOF	degrees of freedom
CM	condition monitoring
FAST	fatigue, aerodynamics, structures, and turbulence
FD	fault detection
FNR	false-negative rate
FPR	false-positive rate
GS	group scaling
HT	hypothesis testing
MCGS	mean-centered group scaling
MPCA	multiway principal component analysis
MRS	multivariate random sample
MRV	multivariate random variable
MVND	multivariate normal distribution
O&M	operation and maintenance
PCA	principal component analysis
RV	random variable
SCADA	supervisory control and data acquisition
SHM	structural health monitoring
WT	wind turbine

Author details

Francesc Pozo* and Yolanda Vidal

*Address all correspondence to: francesc.pozo@upc.edu

Control, Modeling, Identification and Applications (CoDAlab), Department of Mathematics, Escola d'Enginyeria de Barcelona Est (EEBE), Universitat Politècnica de Catalunya (UPC), Barcelona, Spain

References

[1] Lindenberg S, Smith S, O'Dell K, Demeo E, Ram B. 20% wind energy by 2030: Increasing wind energy's contribution to US Electricity Supply; Technical Report; Oak Ridge, TN, USA: U.S. Department of Energy; 2008. DOE/GO-102008-2567

[2] Tchakoua P, Wamkeue R, Ouhrouche M, Slaoui-Hasnaoui F, Tameghe TA, Ekemb G. Wind turbine condition monitoring: State-of-the-art review, new trends, and future challenges. Energies. 2014;**7**(4):2595-2630

[3] Qiao W, Lu D. A survey on wind turbine condition monitoring and fault diagnosis. Part I: Components and subsystems. IEEE Transactions on Industrial Electronics. 2015;**62**(10): 6536-6545

[4] Ruiz M, Mujica LE, Alférez S, Acho L, Tutivén C, Vidal Y, Rodellar J, Pozo F. Wind turbine fault detection and classification by means of image texture analysis. Mechanical Systems and Signal Processing. 2018;**107**:149-167

[5] Zaher A, McArthur S. A multi-agent fault detection system for wind turbine defect recognition and diagnosis. In: Power Tech. Lausanne: IEEE; 2007. pp. 22-27

[6] Pozo F, Vidal Y. Damage and fault detection of structures using principal component analysis and hypothesis testing. In: Advances in Principal Component Analysis. Springer. 2018. pp. 137-191

[7] Odgaard P, Johnson K. Wind turbine fault diagnosis and fault tolerant control—An enhanced benchmark challenge. In: Proceedings of the 2013 American Control Conference—ACC; Washington DC. USA; 2013. pp. 1-6

[8] Pozo F, Arruga I, Mujica LE, Ruiz M, Podivilova E. Detection of structural changes through principal component analysis and multivariate statistical inference. Structural Health Monitoring. 2016;**15**(2):127-142

[9] Jonkman, J. NWTC Computer-Aided Engineering Tools (FAST); Last modified 28-October-2013; NWTC Information Portal: Washington, DC, USA, 2013

[10] Vidal Y, Tutiven C, Rodellar J, Acho L. Fault diagnosis and fault-tolerant control of wind turbines via a discrete time controller with a disturbance compensator. Energies. 2015;**8**(5): 4300-4316

[11] Ochs DS, Miller RD, White WN. Simulation of electromechanical interactions of permanent-magnet direct-drive wind turbines using the fast aeroelastic simulator. IEEE Transactions on Sustainable Energy. 2014;**5**(1):2-9

[12] Beltran B, El Hachemi Benbouzid M, Ahmed-Ali T. Second-order sliding mode control of a doubly fed induction generator driven wind turbine. IEEE Transactions on Energy Conversion. 2012;**27**(2):261-269

[13] Jonkman JM, Butterfield S, Musial W, Scott G. Definition of a 5-MW reference wind turbine for offshore system development, Technical Report. Golden, Colorado: National Renewable Energy Laboratory; 2009. NREL/TP-500-38060

[14] Kelley, N.; Jonkman, B. NWTC Computer-Aided Engineering Tools (Turbsim); Last modified 30-May-2013; NWTC Information Portal: Washington, DC, USA, 2013

[15] Ostachowicz W, Kudela P, Krawczuk M, Zak A. Guided Waves in Structures for SHM: The Time-Domain Spectral Element Method. Chichester, UK: John Wiley & Sons, Ltd; 2012

[16] Chai Y, Yang H, Zhao L. Data unfolding PCA modelling and monitoring of multiphase batch processes. IFAC Proceedings Volumes. 2013;**46**(13):569-574

[17] Ruiz M, Villez K, Sin G, Colomer J, Vanrrolleghem P. Influence of scaling and unfolding in PCA based monitoring of nutrient removing batch process. In: Fault Detection, Supervision and Safety of Technical Processes 2006. Amsterdam, The Netherlands: Elsevier; 2007. pp. 114-119

[18] Westerhuis JA, Kourti T, MacGregor JF. Comparing alternative approaches for multivariate statistical analysis of batch process data. Journal of Chemometrics. 1999;**13**(3-4):397-413

[19] Ruiz M, Mujica LE, Sierra J, Pozo F, Rodellar J. Multiway principal component analysis contributions for structural damage localization. Structural Health Monitoring. 2017: 1475921717737971

[20] Pozo F, Vidal Y. Wind turbine fault detection through principal component analysis and statistical hypothesis testing. Energies. 2016;**9**(1):1-20

[21] Pozo F, Vidal Y, Serrahima JM. On real-time fault detection in wind turbines: Sensor selection algorithm and detection time reduction analysis. Energies. 2016;**9**(7):520

[22] Anaya M, Tibaduiza D, Pozo F. A bioinspired methodology based on an artificial immune system for damage detection in structural health monitoring. Shock and Vibration. 2015; **2015**:1-15

[23] Anaya M, Tibaduiza DA, Pozo F. Detection and classification of structural changes using artificial immune systems and fuzzy clustering. International Journal of Bio-Inspired Computation. 2017;**9**(1):35-52

[24] Mujica LE, Rodellar J, Fernández A, Güemes A. Q-statistic and t^2-statistic PCA-based measures for damage assessment in structures. Structural Health Monitoring. 2011;**10**(5): 539-553

[25] Zugasti E, González AG, Anduaga J, Arregui MA, Martínez F. Nullspace and autoregressive damage detection: A comparative study. Smart Materials and Structures. 2012; **21**(8):085010

[26] Häckell MW, Rolfes R, Kane MB, Lynch JP. Three-tier modular structural health monitoring framework using environmental and operational condition clustering for data

normalization: Validation on an operational wind turbine system. Proceedings of the IEEE. 2016;**104**(8):1632-1646

[27] Ng HK, Chen RH, Speyer JL. A vehicle health monitoring system evaluated experimentally on a passenger vehicle. IEEE Transactions on Control Systems Technology. 2006; **14**(5):854-870

[28] Tsiapoki S, Häckell MW, Grießmann T, Rolfes R. Damage and ice detection on wind turbine rotor blades using a three-tier modular structural health monitoring framework. Structural Health Monitoring. 2017:1475921717732730

[29] Ugarte MD, Militino AF, Arnholt A. Probability and Statistics with R. Boca Raton, FL, USA: CRC Press/Taylor & Francis Group; 2008

[30] Pozo F, Vidal Y, Salgado Ó. Wind turbine condition monitoring strategy through multiway PCA and multivariate inference. Energies. 2018;**11**(4):749

[31] DeGroot MH, Schervish MJ. Probability and Statistics. London, UK: Pearson; 2012

Chapter 8

Structural Health Monitoring of Bolted Joints Using Guided Waves: A Review

Fei Du, Chao Xu, Huaiyu Ren and Changhai Yan

Additional information is available at the end of the chapter

http://dx.doi.org/10.5772/intechopen.76915

Abstract

Bolted joints are widely applied in engineering structures. Significant advantages of bolted joints are that they can be easily disassembled and the possibility to design for bearing large working load. However, in practical applications, preload loss in pre-tensioned bolts is inevitable. Reliable detection of bolt loosening is significant to ensure structural reliability and safety. In the past decades, the guided wave-based structural health monitoring (SHM) methods have been developed for the detection of bolt loosening, and considerable advancements have been made in this area. This chapter presents a review of the existing studies on bolt preload monitoring method based on guided wave. The basic principle and characteristics of the typical methods are discussed, which involve wave energy dissipation, time reversal guided wave, contact acoustic nonlinearity, and active chaotic ultrasonic excitation-based methods. In addition, this chapter presents an experimental comparison of the detection sensitivity of wave energy dissipation and time reversal method. The results show that the TR method is more sensitive to bolt loosening.

Keywords: bolted joints, bolt-loosening monitoring, structural health monitoring, guided waves, time reversal method

1. Introduction

Bolted joints are widely used in engineering structures such as aerospace and civil structures. Significant advantages of bolted joints are that they can be easily assembled and disassembled and the possibility of bearing large load. In practical applications, bolted joints are subjected to a variety of failure modes including self-loosening, slippage, shaking apart, fatigue cracks, and breaking [1]. Self-loosening is the most common issue among them due to inappropriate

preloads during installation, time varying external loads during service, or other environment factors. Bolts loosening may lead to the failure of the entire structure. Therefore, it is critical to monitor bolt preload to ensure the safety and reliability of structures.

Structural health monitoring (SHM) is generally referred to the process of acquiring and analyzing data from on-board sensors to determine the health of a structure [2]. Several SHM approaches have been reported for the detection of bolt loosening in different structural systems, such as vibration, electromechanical impedance, and guided wave-based techniques. In vibration-based techniques, global dynamic properties, like resonant frequencies, modal shapes, and frequency response functions are utilized for the detection of bolt loosening [3]. However, since an assembled structure usually comprises many bolts and joint interfaces which are known as local structural elements, global structural dynamic properties do not change significantly due to bolt preload loosening at a local position [4]. Consequently, vibration-based SHM techniques are relatively insensitive to changes in bolt preloads and thus lead to poor prognostic capability. Impedance-based techniques monitor variations in mechanical impedance due to damage, which is coupled with electrical impedance of piezoelectric transducers (PZTs) [5]. Previous studies have shown the feasibility of using impedance-based approaches for the detection of bolt loosening [6–8]. A piezoelectric transducer (PZT) is attached to a target bolt-jointed structure, and bolt preload can be identified by monitoring the change of the measured electrical impedance [7]. Although this technique is sensitive to minor changes in the bolt preload, its detection area is limited to the near field of the piezoelectric active sensor [9] and an expensive high-precision impedance analyzer with a high-sampling frequency is required [10].

Guided wave-based damage detection techniques have been intensively developed over the last two decades [11, 12]. Due to their sensitivity to small structural damages and large sensing range [13], guided wave techniques have been increasingly used for structural health monitoring. In recent years, bolt preload detection methods using guided wave have received much interest. In this chapter, bolt preload monitoring methods based on guided waves and the relevant theories are reviewed. The objective is to understand the current technology gaps, future research directions, and areas requiring attention of the researchers. This chapter is organized as follows. Section 2 presents the theoretical backgrounds and numerical modeling approach of guided wave-based SHM methods. Then, linear feature-based detection methods are reviewed and compared in Section 3, which include wave energy dissipation methods and time reversal methods. Section 4 displays nonlinear feature-based methods including contact acoustic nonlinearity (CAN), phase shift, and chaotic ultrasonic excitation methods. Finally, conclusions are summarized in Section 5.

2. Theoretical basis and numerical modeling

2.1. Theoretical backgrounds

A typical bolted joint is illustrated in **Figure 1**. It can be seen that a bolted joint usually consists of one bolt, one nut, and two contact parts. From the view of a micro-scale, the joint interface can be considered to be covered with a large amount of asperities. The real contact area is the summation of the contact area of each asperity. As the bolt preload increases, the contact pressure at

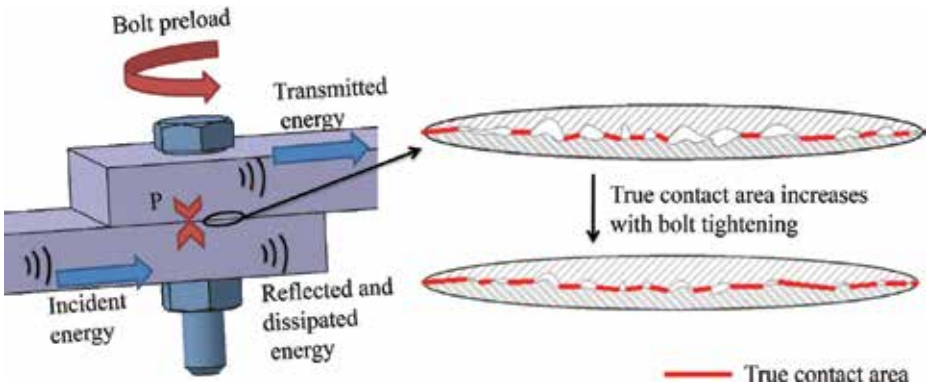

Figure 1. Guided wave transmitted across a bolted joint.

the interface increases. Correspondingly, the real contact area increases as well. When a wave travels through a lap joint, only a part of the incident wave energy can be transmitted, and the other part is reflected and dissipated. Based on Hertz contact theory and the sinusoidal wavy surface model, Yang and Chang [3] establish the relationship between real contact area and contact pressure at a joint interface. Their results show that the energy of transmitted guided wave is proportional to the real contact area of joint interface which increases with bolt preload. Although the topographies of rough contact surfaces are not strictly sinusoidal and the plastic deformation of contact asperities are not considered, Yang's theoretical analysis agrees well with experimental observation. After that, the transmitted wave energy is widely used as the tightness index for bolt-loosening detection. However, based on the theory of rough contact mechanics, the real contact area at an interface reaches a saturation value when the applied contact pressure reaches a certain value [14]. Accordingly, the transmitted energy also saturates when the externally applied load reaches a certain value. In this case, the sensitivity of the transmitted wave energy-based damage detection strategy is reduced considerably.

Nonlinear features of acoustic waves can also be extracted and linked to bolt loosening. Among approaches based on nonlinear features, contact acoustic nonlinearity (CAN) is drawing increasing attention. When the bolt is loosening and the joint is stimulated by acoustic waves or vibration under certain amplitude, joint interface undergoes a certain extent of tension and compression and it opens and closes periodically. This induces asymmetry in the contact restoration forces. Consequently, those forces cause a parametric change of stiffness and lead to structural dynamic nonlinearity, known as contact acoustic nonlinearity [15, 16]. Since the guided wave amplitude excited by a piezoelectric element is generally small, it is difficult to stimulate the nonlinearity of the structure itself. Therefore, impact modulation (IM) and vibro-acoustic modulation (VAM) are two major implementations of CAN-based modulation [17]. The major difference between them is that IM adopts an impact force to excite the natural vibration modes of the inspected structure, while VAM applies a stable vibration to the structure using a harmonic force. The essence of the modulation methods resides on the interaction of the jointed interface with a mixed excitation, like a vibration and a wave. When all the bolts in a jointed structure are fully fastened, the acquired signal spectrum exhibits two peaks at the vibration and wave frequencies, respectively. When bolts

are loosening, there would be additional frequency components around the wave frequency in the spectrum, termed as left and right sidebands. The magnitudes of the sidebands, which are determined by the intensity of CAN, can be linked quantitatively to the bolt preload [18].

In order to quantitatively describe the relation between sidebands of signal spectral features and the residual bolt preload, Zhang et al. [18] established a theoretical modeling of CAN in a joint, as shown in **Figure 2a**. The analysis based on the model demonstrates that the magnitude of the sideband is proportional linearly to the nonlinear contact stiffness K_2 which is dependent on the contact pressure at the jointed interface. The above model is a simplified model with single degree of freedom (DOF). Subsequently, Zhang et al. [19] presented a two-DOF nonlinear model to analyze the physical phenomenon of subharmonics and their generation conditions, as shown in **Figure 2b**. On this basis, analytical prediction was carried out to verify the validity of the loosening detection method for bolted joint structures using the subharmonic resonance.

2.2. Numerical modeling

To understand how guided waves interact with bolted lap joints exactly, theoretical models are essential to describe the propagation behavior of guided wave. Apparently, the above simplified single or two DOF models are not enough. Since the bolted structure is inhomogeneous in the direction of wave propagation, it cannot be modeled by analytical or semi-analytical methods. Finite element method (FEM) can be applied to a variety of complex geometries and has become the most common wave propagation analysis method. Therefore, Clayton et al. [20] established a three-dimensional finite element model of guided wave propagation in bolted joints, but interface contact was not considered in order to reduce computational cost. Then, Doyle et al. [21], and Bao and Giurgiutiu [22] used the same method to establish finite element analysis models. However, they found that these models could not reflect the variation of the guided wave under different bolt preloads. Therefore, in order to consider contact

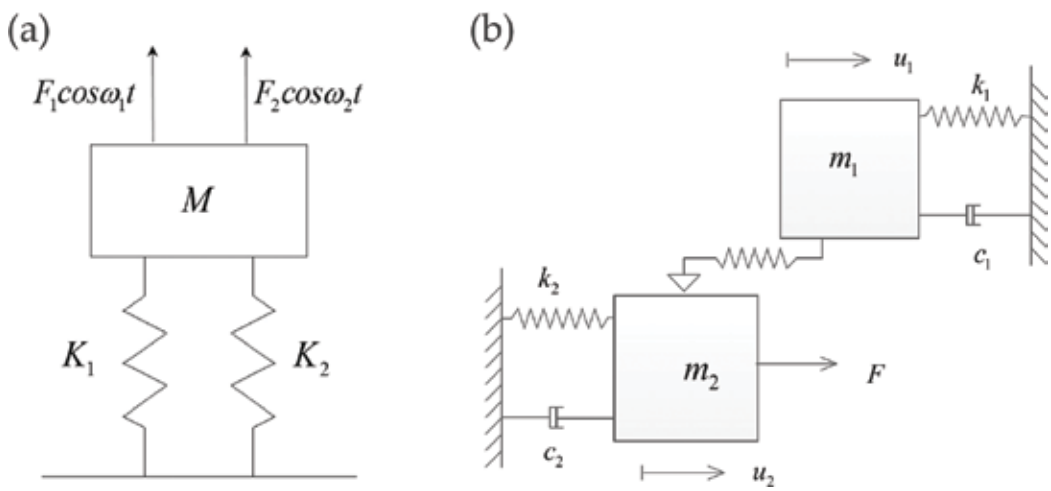

Figure 2. Theoretical modeling of CAN in a joint: (a) single degree of freedom [18] and (b) two degrees of freedom [19].

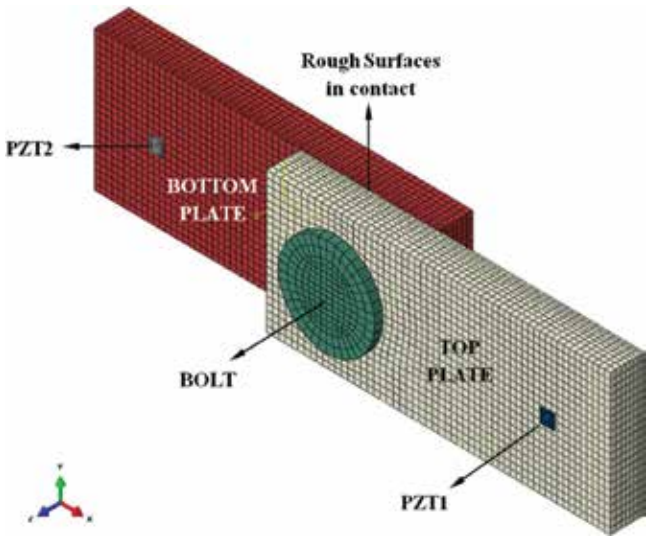

Figure 3. Multi-physics FEM model of bolted lap joint considering rough contact surfaces [10].

behaviors, Bao et al. [23] added contact elements to the finite element model. The improved model can effectively reflect the variation of the guided wave under different preloads, but the wave variations and the measurement results were quite different. The main reason might be that the contact surfaces in the above models are smooth, while the real contact surfaces are rough. In 2016, Parvasi et al. [10] tried to consider rough contact surfaces in finite element model by randomly adjusting node position at the contact surfaces, as shown in **Figure 3**. The simulation results are closer to the experimental measurement results, but the mesh size (1.8 mm) of the contact area is much larger than the size of micro-asperities on rough surfaces.

The above FEM models are mainly used to analyze the relationship between bolt preload and transmitted guided wave energy. Shen et al. [24] built anther 3D multiphysics transient

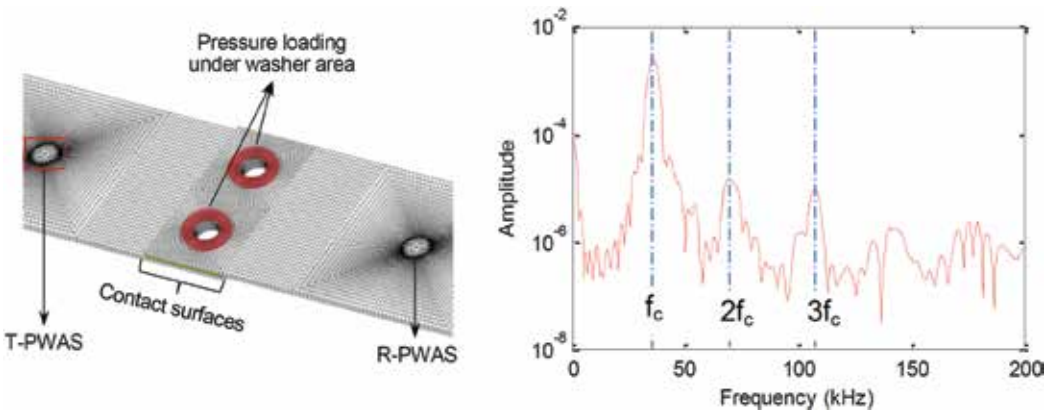

Figure 4. Transient dynamic finite element model and frequency spectrum of simulation signal [24].

dynamic finite element model to analyze the relationship between CAN and bolt load, as shown in **Figure 4a**. The nonlinear higher harmonics (second-order harmonic and third-order harmonic) can be observed clearly in the simulation signal, as shown in **Figure 4b**. The simulation results also displayed that as the bolt preload increases, the ratio of the spectral amplitude at the second harmonic to that at the excitation frequency decreases.

3. Linear feature-based techniques

3.1. Wave energy dissipation

Because ultrasonic wave energy through the bolt joint is strongly tied to the contact status of bolted interface, the transmitted guided wave energy is widely used as tightness index. This type of method is also known as wave energy dissipation (WED) method. In order to detect fastener integrity in thermal protection panels in space vehicles, Yang and Chang [3, 25] used the energy and attenuation speed of guided wave transmitted across jointed interface to assess preload levels and locations of loosening bolt. Subsequently, Wang et al. [26] used only the transmitted guided wave energy to monitor bolt preload. The schematic of the bolt joint monitoring system is displayed in **Figure 5**. The experimental results show that the transmitted energy is basically proportional to torque level. However, the energy does not change with bolt torque when the applied torque reaches a certain value and this is referred to as saturation phenomenon, as shown in **Figure 6a**. Similarly, Amerini and Meo [27] calculated the energy of the transmitted guided wave in frequency domain to assess the tightening state of a bolt lap joint, as shown in **Figure 6b**. Yang et al. [28] extended the WED method to composite bolted joints. With a scanning laser ultrasound system, Haynes et al. [29] acquired the full-field wave data and calculated the wave energy before and after the lap joint to monitor bolt torque levels. Unfortunately, saturation phenomena are also observed in all the above experimental studies. On the other hand, due to multi-mode, dispersion, and boundary reflection of guided waves, the response signal at a joint structure is quite complex [27]. Hence, Kędra et al. [30] investigated the effects of excitation frequency, the time range of received signal, and the position of sensor on the preload detection accuracy of the WED method. They pointed out that these parameters have to be carefully selected.

The above bolt preload detection methods are limited to a flat lap joint with a single bolt. However, in real structures, bolted joints with complex geometry or multiple bolts are more common. In this case, complex signal-processing methods are always needed. In order to

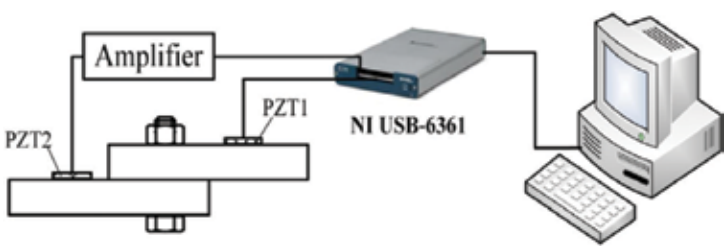

Figure 5. Schematic of the bolt joint monitoring system [26].

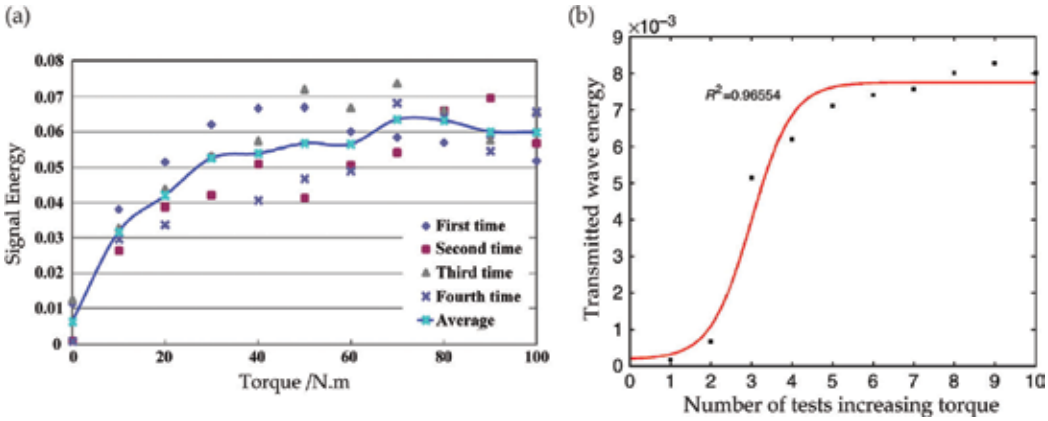

Figure 6. Results of WED methods with saturation phenomenon: (a) result from reference [26] and (b) result from reference [27].

monitor the preload of L-shaped bolt joints, Jalalpour et al. [31] proposed a preload monitoring method using fast Fourier transform, cross-correlation, and fuzzy pattern recognition to process transmitted wave. Nevertheless, the fuzzy sets of torque level were limited. Montoya et al. [32] assessed the rigidity of L-shaped bolt joint using transmitted wave energy. Subsequently, Montoya et al. [33] further extended the method to bolt loosening and preload monitoring of satellite panels jointed by a right angle bracket. Their experimental results display that some measurement parameters, such as the time window of the received signal, have a significant effect on the sensitivity and repeatability of the measurement [33]. With respect to bolt-loosening monitoring in multi-bolt-jointed structures, Mita et al. [34] proposed to use support vector machine to recognize different loosening patterns. Their results show that the proposed method could identify the location and the level of preload of loosened bolts. Moreover, Liang and Yuan [35] developed a decision fusion system for multi-bolt structure, as shown in **Figure 7**. This system consists of individual classification, classifier selection, and decision fusion. The results demonstrate that the proposed method can accurately and rapidly identify the bolt loosening by analyzing the acquired wave signal.

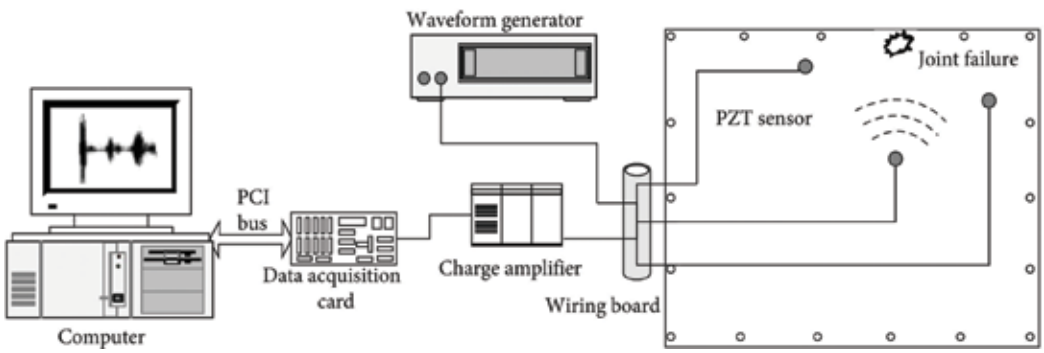

Figure 7. Sensor layout and joint failure position on the specimen [35].

3.2. Time reversal method

Since guided wave signals are always very complex because of multi-mode, dispersion, and scattering at any discontinuity, Fink et al. [36] extended time reversal concept (TR) to a guided wave monitoring technique. In time reversal approach, a received signal is reversed and reemitted as an excitation signal, and then a reconstruction of the input signal can be obtained at the source position. Hence, the time reversal method can effectively reduce the influences of dispersion and multi-modal of the guided wave. In recent years, time reversal-based guided wave monitoring methods have been widely applied to damage detection in various structures, such as metallic plates [37], composite plates [38–40], and rebar-reinforced concrete beams [41]. Recently, Parvasi et al. [10] proposed to use time reversal method to focus guided wave energy transmitted through bolted joint, and then the refocused amplitude peak was selected as the tightness index for preload detection. The experimental results show that the proposed tightness index increases with bolt torque. The TR method for bolt preload monitoring can be divided into four steps, which is shown in **Figure 8**. Step 1, a tone burst input e(t) is applied to transducer A, which activates wave propagation in the plate. Step 2, a wave response signal u(t) is captured by transducer B. Step 3, the recorded signal u(t) is reversed in time domain and is restimulated using transducer B. Step 4, a guided wave signal is captured by transducer A again, and the original signal is reconstructed. Finally, the reconstructed signal peak is used as the tightness index for preload detection [10]. One of the main advantages of TR method is that there is no need to take efforts to select time window of received signal as the WED method.

Actually, the refocused amplitude peak is strongly related to the transmitted wave energy. Hence, when bolt preload is relatively high and the real contact area does not increase with preload, the focused signal peak amplitude changes very slowly. Therefore, Tao et al. [42] experimentally investigated the saturation phenomenon of TR method for bolted preload detection. The results demonstrate that with the increase of the surface roughness of bolted

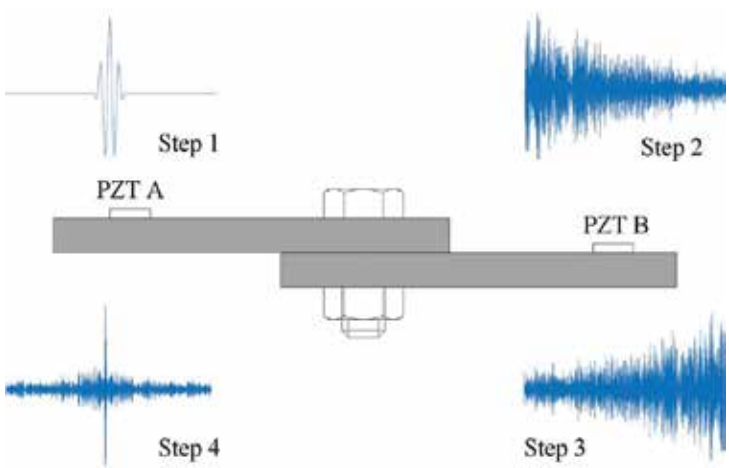

Figure 8. Illustration of the time reversal method in a lap jointed beam.

interface, the saturation phenomenon becomes insignificant. Huo et al. [43] studied guided wave propagation across contact interface based on fractal contact theory and finite element method. They concluded that the saturation phenomenon is linked to the plastic deformation of interacting asperities under a heavy axial load.

3.3. Comparison of TR and WED methods

Until now, the difference in monitoring sensitivities of WED and TR methods is not clear. Hence, the monitoring sensitivities of the two methods are compared in this section. The experimental setup and specimens are displayed in **Figure 9**. The metallic bolted lap joint consists of two flat aluminum 2024-T3 beams, one M6 bolt, one nut, and two washers. The length of each beam is 400 mm, the width is 50 mm, and the thickness 2 mm. The normal torque is selected to be 10 Nm. A torque wrench with a resolution of 0.2 Nm is used to apply bolt preload. A data acquisition (DAQ) system NI USB-6366 with a sampling frequency of 2 MHz is used to generate wave excitation and record responses. A program is built in the LabVIEW environment to control the process of data acquisition. A high voltage amplifier PINTEK HA-400 is used to amplify the excitation signal and provides voltage to PZT actuators. In addition, the specimen is mounted on a foam support to simulate a free-free boundary condition. Two PZT patches are bonded on the specimen. The patch on the left beam, 100 mm, away from the bolt is numbered as PZT 1 PZT. Another one on the right beam, 100 mm, from the jointed bolt is numbered as PZT 2.

The bolt preload is evaluated by both WED and TR methods at the same time. **Figure 10** presents the results of tightness indexes TI_{Ω}(WED) and TI_{Ω}(TR) obtained by $TI_{\Omega}(WED)$, the WED and TR methods, respectively. $TI_{\Omega}(TR)$ It can be seen that TI_{Ω}(WED) increases with bolt preload when the preload is smaller than 6 Nm. However, an obvious saturation trend can be seen, and only the lowest 0.1-Nm torque case can be clearly identified. By contrast, TI_{Ω}(TR) increases with bolt preload in the entire preload range, and the 0.1-, 2-, and 4-Nm cases can be clearly identified. On the other hand, TI_{Ω}(TR) cannot be used to identify torque cases larger than 6 Nm. It can be concluded that the detection sensitivity of TR $TI_{p}(MTR)$ method is better than that of $TI_{\Omega}(WED)$ WED method $TI_{\Omega}(TR)$ especially at the early stage of bolt loosening. The

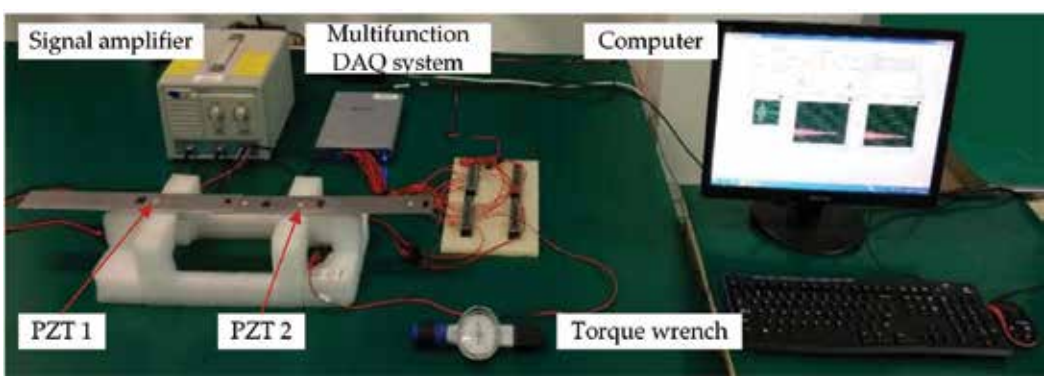

Figure 9. Experimental setup and specimens.

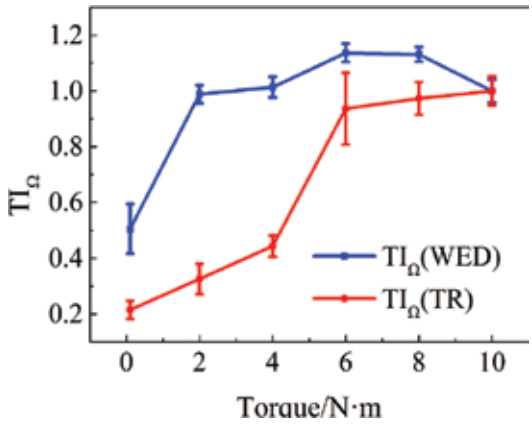

Figure 10. Preload detection results of the WED and TR methods.

main reason is that guided waves traveled twice (from PZT1 to PZT2, and then PZT2 to PZT1) through the jointed interface in the TR technique. The interface affects the waves twice and thus makes the TI_{Ω}(TR) more sensitive to the bolt preload [10].

4. Nonlinear feature-based techniques

4.1. Contact acoustic nonlinearity

Contact acoustic nonlinearity (CAN) is shown to increase with the decrease in contact load, so the second-order harmonics, subharmonic, and spectral sidebands caused by CAN have also been used for bolt preload detection. Usually, the second-order harmonic and subharmonic can be generated by a single frequency excitation, and spectral sidebands are generated by both low- and high-frequency excitations. For the second-order harmonic-based method, the ratio between the second harmonic amplitude and the carrier frequency signal amplitude provided a reliable index for bolt load assessment. Under multi-frequency excitation, the loosening/tightening index proposed is the difference in dB between the carrier frequency amplitude and a mean of the two sideband amplitudes [27]. Zhang M et al. [19] presented a subharmonic resonance method for the detection of bolt looseness, and the bolted joint was excited by a single frequency-guided wave. CAN features are more likely to be excited by adding vibration excitation. Thereby, Zhang Z et al. [17, 18] proposed a vibro-acoustic modulation (VAM)-based method and developed a sideband index for metal and composite bolted joints. The experimental setup and the corresponding detection results for composite bolted joints are shown in **Figure 11**.

In **Figure 11**, the label β is the sideband index in VAM method, and the label energy is the transmitted energy of Lamb waves in WED method. Zhang Z et al. [17] compared the proposed VAM method with WED-based linear method, and the results show that the proposed sideband index β effectively enhanced measurement sensitivity. In addition, Amerini and Meo [27] developed

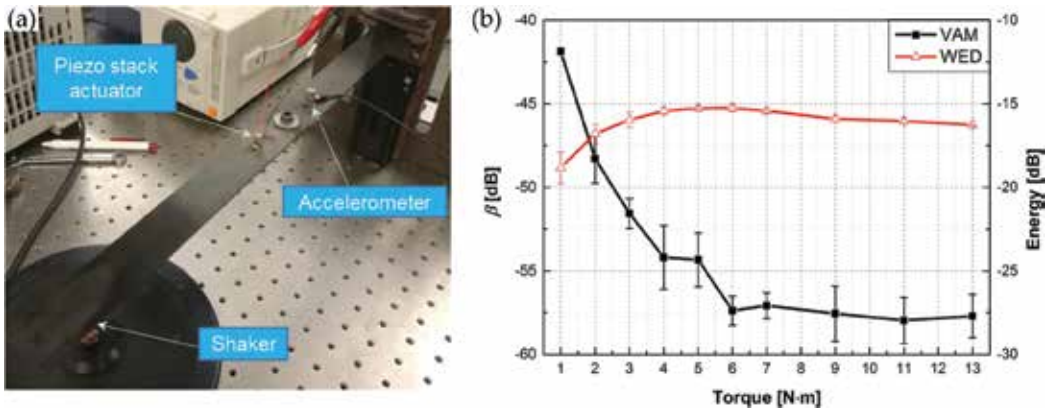

Figure 11. Preload monitoring of bolted composite joint using VAM method [17]: (a) experimental setup for VAM method and (b) comparison of VAM and WED methods.

both second-order harmonics index and sideband index to assess the tightening state of a bolted structure, and the assessment results of the two methods are similar. On the other hand, Zhang Z et al. [16] also compared the high-order harmonics and sideband methods and demonstrated that the stability of spectral sideband-based method is better. Spectral sideband can also be generated by impact modulation. Meyer and Adams [44] proposed an impact modulation-based method to detect bolt loosening in an aluminum joint. However, the sideband amplitudes are sensitive to test parameters including impact amplitude and location, probing force amplitude and frequency, and sensor location. One common disadvantage of these above spectral sideband methods is that it needs two different actuators and one sensor for each joint monitored [27]. Meanwhile, the saturation phenomena have not been completely removed, and the detection sensitivity still needs to be improved at the early stage of bolt loosening.

4.2. Phase shift

Apart from transmitted wave energy and CAN, the phase shift of guided wave has also been used for quantifying bolt torques. Zagrai et al. [45] estimated bolt torques by measuring delays of guided wave transmitted across bolt joint. Their experimental results demonstrated that bolt torque is proportional to phase shift of the guided waves, as shown in **Figure 12**.

In addition, Zagrai et al. [45] tried to explain the experiment results by acousto-elastic theory and presented a simplified theoretical approach to calculate phase shift of the propagating elastic wave. However, their approach gives approximately an order of magnitude underestimation for pulse delays. Subsequently, Doyle et al. [46, 47] further studied phase shift of guided wave propagating in a complex structure analogous to a typical satellite panel containing 49 bolt joints using an array of piezoelectric sensors sparsely distributed. The results show that the time at which this shift occurs is related to the distance between the location of loosening bolt and the primary wave propagation path. Thereby, using only two or three possible paths, it is possible to obtain a realistic estimate of the location of damage in the form of single bolt loosening [47]. On this basis, Zagrai et al. [48] tried to develop a baseline-free method utilizing

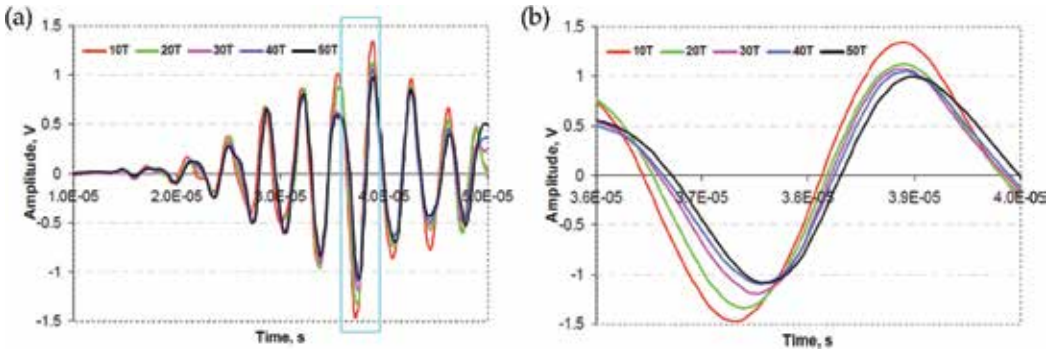

Figure 12. Guided wave signals recorded at different bolt torques: (a) full records and (b) zoomed-in segments [45].

signals of different initial phases to assess bolt loosening. Unfortunately, it does not work in structures with complicated geometries and large number of bolts. Furthermore, changes of the phase shift induced by a bolted joint are rather small and require sensitive equipment with advanced signal-processing capabilities [46]. In addition, because received guided waves are very complex, it is difficult to select the correct time window and the corresponding wave speed to calculate phase shift and the distance between wave path and damage.

4.3. Chaotic ultrasonic excitation

In addition to stimulate the nonlinear characteristics of the jointed structure, another research idea is to directly use nonlinear ultrasonic excitation. At this time, artificially introducing a nonlinear component in the ultrasonic excitation signal can be used to sensitively estimate the change of structural parameters caused by loosened bolts. Chaotic signal is a well-known nonlinear signal, but chaotic signals generated by most well-known chaotic systems are unsuitable for guided wave monitoring which is more sensitive to small-scale damage.

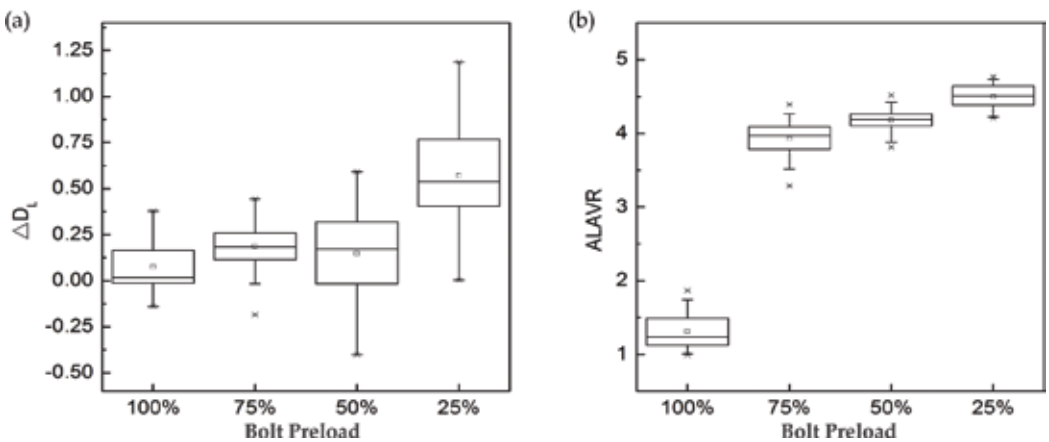

Figure 13. Looseness indexes versus bolt preload [51]: (a) Lyapunov dimension and (b) ALAVR.

Clayton et al. [20] proposed a bolt preload monitoring approach combining a chaotic excitation method with ultrasonic guided waves. In this method, the chaotic signal is upconverting to an ultrasonic frequency band, and the ultrasound signal with chaotic characteristics is generated to stimulate the bolted structure. The response signal is reconstructed to analyze the phase space, and the nonlinear characteristic quantitatively representing the bolt looseness is extracted. Fasel et al. [49, 50] used similar methods to identify bolt preload in simulations and experiments on single and multi-bolt structures. Recently, based on the chaotic ultrasonic excitation method, Wu and Xu [51] take both Lyapunov dimension and the ratio of averaged local attractor variance (ALAVR) as looseness indexes, which can be used to characterize an attractor's whole features and local features. Experimental results show that ALAVR is better for bolt preload monitoring, as displayed in **Figure 13**.

5. Conclusions

Ultrasonic guided wave is an effective technique to monitor the preload of bolts. The research status of this field is reviewed in this chapter. At present, considerable advancements have been made in this area in the past two decades. Both linear and nonlinear features of guided waves introduced by bolted joints have been used for bolt preload monitoring. In particular, the transmitted wave energy as a linear feature is the most extensively used for preload monitoring in single bolt and multi-bolt structures. For this reason, the wave energy dissipation method (WED) based on the above features is experimentally compared with time reversal method (TR). The results show that the detection sensitivity of WED method is not very good, especially at the early stage of bolt loosening, and the TR method is more sensitive to bolt loosening. Meanwhile, this chapter also reviews a variety of monitoring methods based on nonlinear features, including contact acoustic nonlinearity (CAN), phase shift caused by acoustic-elastic, and chaotic ultrasound. The above methods can improve the detection sensitivity, but there are also several disadvantages. For example, both acoustic and vibrational excitations are always required for CAN-based methods, and high-frequency sampling frequencies are required for phase shift-based method. The open areas of research, which might need attention, are outlined as follows:

1. Accurate and efficient numerical models should be further developed to simulate wave propagation in bolted joints. For example, acoustic-elastic are currently believed to cause the phase shift of transmitted guided-wave signal. However, the current simplified model based on acoustic-elastic cannot effectively explain the phase shift phenomenon. In the meantime, it is very difficult to consider the micro-topography of contact surfaces in FEM models now. Therefore, the establishment of a more accurate and efficient numerical model is expected to fully study the interaction between jointed interface and guided wave theoretically.
2. Improving bolt preload monitoring method is still required. Although bolt preload monitoring methods such as TR and VAM methods can effectively improve the preload detection sensitivity, the detection sensitivity of these methods is not still very good at the early stage of bolt loosening. Moreover, almost all the methods currently require baseline

signals from healthy structures. Therefore, the establishment of a baseline free monitoring method with a high detection sensitivity is an important step for moving toward the goal of real-life in-service implementation.

3. Bolt-loosening detection methods considering environmental factors for multi-bolt structures should be further developed. Current research limited to a flat lap joint with a single bolt. However, bolted joints with complex structure and multiple bolts are more common in real structures. Meanwhile, little attention has been paid to preload monitoring considering environmental factors which have significant effect on guided wave monitoring. Hence, loosening detection method considering environmental factors for multi-bolt structures is also very important for realizing the application of bolt preload monitoring in real engineering structures.

Acknowledgements

This study is supported by the National Natural Science Foundation of China (Grant Nos. 51705422 and 11372246). This study is also supported by China NSAF Project (Grant No. U1530139) and Fundamental Research Funds for the Central Universities (Grant No. 3102017OQD004).

Nomenclature

ALAVR	ratio of averaged local attractor variance
CAN	contact acoustic nonlinearity
DOF	degree of freedom
FEM	finite element method
IM	impact modulation
K_1, K_2	contact stiffness
PZT	piezoelectric transducers
SHM	structural health monitoring
TR	time reversal
TI_Ω	tightness index
VAM	vibro-acoustic modulation
WED	wave energy dissipation
β	sideband index
ΔD	tightness index based on Lyapunov dimension

Author details

Fei Du[1], Chao Xu[1]*, Huaiyu Ren[2] and Changhai Yan[2]

*Address all correspondence to: chao_xu@nwpu.edu.cn

1 School of Astronautics, Northwestern Polytechnical University, Xi'an, China

2 Science and Technology of Space Physics Laboratory, China Academy of Launch Vehicle Technology, Beijing, China

References

[1] Peairs DM, Park G, Inman DJ. Practical issues of activating self-repairing bolted joints. Smart Materials & Structures. 2004;**13**:1414

[2] ARP S. Guidelines for Implementation of Structural Health Monitoring on Fixed Wing Aircraft. Warrendale: Society of Automotive Engineers; 2013

[3] Yang J, Chang F-K. Detection of bolt loosening in C–C composite thermal protection panels: I. Diagnostic principle. Smart Materials and Structures. 2006;**15**:581-590

[4] Todd MD, Nichols JM, Nichols CJ, Virgin LN. An assessment of modal property effectiveness in detecting bolted joint degradation: Theory and experiment. Journal of Sound and Vibration. 2004;**275**:1113-1126

[5] Madhav AVG, Kiong SC. Application of electromechanical impedance technique for engineering structures: Review and future issues. Journal of Intelligent Material Systems & Structures. 2010;**21**:41-59

[6] Peairs DM, Inman DJ. Improving accessibility of the impedance-based structural health monitoring method. Journal of Intelligent Material Systems & Structures. 2004;**15**:129-139

[7] Mascarenas DL, Park G, Farinholt KM, Todd MD, Farrar CR. A low-power wireless sensing device for remote inspection of bolted joints. Proceedings of the Institution of Mechanical Engineers Part G Journal of Aerospace Engineering. 2009;**223**:565-575

[8] Kuznetsov S, Pavelko I, Panidis T, Pavelko V, Ozolinsh I. Bolt-joint structural health monitoring by the method of electromechanical impedance. Aircraft Engineering & Aerospace Technology. 2014;**86**:207-214

[9] Zagrai A, Doyle D, Gigineishvili V, Brown J, Gardenier H, Arritt B. Piezoelectric wafer active sensor structural health monitoring of space structures. Journal of Intelligent Material Systems and Structures. 2010;**21**:921-940

[10] Parvasi SM, Ho SCM, Kong Q, Mousavi R, Song G. Real time bolt preload monitoring using piezoceramic transducers and time reversal technique—A numerical study with experimental verification. Smart Materials and Structures. 2016;**25**:085015

[11] Raghavan AC, Cesnik CES. Review of guided-wave structural health monitoring. Shock & Vibration Digest. 2007;**39**:91-114

[12] Mitra M, Gopalakrishnan S. Guided wave based structural health monitoring: A review. Smart Materials & Structures. 2016;**25**:053001

[13] An Y-K, Sohn H. Integrated impedance and guided wave based damage detection. Mechanical Systems and Signal Processing. 2012;**28**:50-62

[14] Popov VL. Contact mechanics and friction. Berlin: Springer Berlin Heidelberg; 2010;**225**: 341-344

[15] Hong M, Su Z, Wang Q, Cheng L, Qing X. Modeling nonlinearities of ultrasonic waves for fatigue damage characterization: Theory, simulation, and experimental validation. Ultrasonics. 2014;**54**:770-778

[16] Zhang Z, Liu M, Liao Y, Su Z, Xiao Y. Contact acoustic nonlinearity (CAN)-based continuous monitoring of bolt loosening: Hybrid use of high-order harmonics and spectral sidebands. Mechanical Systems and Signal Processing. 2018;**103**:280-294

[17] Zhang Z, Xu H, Liao Y, Su Z, Xiao Y. Vibro-acoustic modulation (VAM)-inspired structural integrity monitoring and its applications to bolted composite joints. Composite Structures. 2017;**176**:505-515

[18] Zhang Z, Liu M, Su Z, Xiao Y. Quantitative evaluation of residual torque of a loose bolt based on wave energy dissipation and vibro-acoustic modulation: A comparative study. Journal of Sound and Vibration. 2016;**383**:156-170

[19] Zhang M, Shen Y, Xiao L, Qu W. Application of subharmonic resonance for the detection of bolted joint looseness. Nonlinear Dynamics. 2017;**88**:1643-1653

[20] Clayton EH, Kennel MB, Fasel TR, Todd MD, Stabb MC, Arritt BJ. Active ultrasonic joint integrity adjudication for real-time structural health monitoring. In: The 15th International Symposium on: Smart Structures and Materials & Nondestructive Evaluation and Health Monitoring, International Society for Optics and Photonics; 2008. pp. 69350M-69350M-69311

[21] Doyle D, Reynolds W, Arritt B, Taft B. Computational setup of structural health monitoring for real-time thermal verification. In: ASME 2011 Conference on Smart Materials, Adaptive Structures and Intelligent Systems; 2011. pp. 447-453

[22] Bao J, Giurgiutiu V. Effects of fastener load on wave propagation through lap joint. SPIE Smart Structures and Materials+ Nondestructive Evaluation and Health Monitoring. International Society for Optics and Photonics; 2013. pp. 869521-869521-869512

[23] Bao J, Shen Y, Giurgiutiu V. Linear and Nonlinear Finite Element Simulation of Wave Propagation Through Bolted Lap Joint, 54th AIAA/ASME/ASCE/AHS/ASC Structures, Structural Dynamics, and Materials Conference; 2013

[24] Shen Y, Bao J, Giurgiutiu V. Health monitoring of aerospace bolted lap joints using nonlinear ultrasonic spectroscopy: Theory and experiments. In: Proceedings of the 9th International Workshop on Structural Health Monitoring. Stanford University; 2013. pp. 2333-2340

[25] Yang J, Chang F-K. Detection of bolt loosening in C–C composite thermal protection panels: II. Experimental verification. Smart Materials and Structures. 2006;**15**:591-599

[26] Wang T, Song G, Wang Z, Li Y. Proof-of-concept study of monitoring bolt connection status using a piezoelectric based active sensing method. Smart Materials and Structures. 2013;**22**:087001

[27] Amerini F, Meo M. Structural health monitoring of bolted joints using linear and nonlinear acoustic/ultrasound methods. Structural Health Monitoring. 2011;**10**:659-672

[28] Yang B, Xuan FZ, Xiang Y, Li D, Zhu W, Tang X, Xu J, Yang K, Luo C. Lamb wave-based structural health monitoring on composite bolted joints under tensile load. Materials. 2017;**10**:652

[29] Haynes C, Yeager M, Todd M, Lee J-R. Monitoring bolt torque levels through signal processing of full-field ultrasonic data. Health Monitoring of Structural and Biological Systems 2014. International Society for Optics and Photonics; 2014. pp. 906428

[30] Kedra R, Rucka M. Research on assessment of bolted joint state using elastic wave propagation. Journal of Physics: Conference Series. 2015;**628**:012025

[31] Jalalpour M, El-Osery AI, Austin EM, Reda Taha MM. Health monitoring of 90° bolted joints using fuzzy pattern recognition of ultrasonic signals. Smart Materials and Structures. 2014;**23**:015017

[32] Montoya AC, Maji AK. An assessment of joint rigidity with ultrasonic wave energy. Journal of Nondestructive Evaluation. 2011;**30**:122-129

[33] Montoya A, Doyle D, Maji A, Dumm H-P. Ultrasonic evaluation of bolted connections in satellites. Research in Nondestructive Evaluation. 2014;**25**:44-62

[34] Mita A, Fujimoto A. Active detection of loosened bolts using ultrasonic waves and support vector machines. In: Proceeding of the 5th International Workshop on Structural Health Monitoring; 2005. pp. 1017-1024

[35] Liang D, Yuan S-f. Decision fusion system for bolted joint monitoring. Shock and Vibration. 2015;**2015**:1-11

[36] Ing RK, Fink M. Time-reversed lamb waves. IEEE Transactions on Ultrasonics, Ferroelectrics, and Frequency Control. 1998;**45**:1032-1043

[37] Poddar B, Kumar A, Mitra M, Mujumdar PM. Time reversibility of a lamb wave for damage detection in a metallic plate. Smart Materials and Structures. 2011;**20**:025001

[38] Park HW, Sohn H, Law KH, Farrar CR. Time reversal active sensing for health monitoring of a composite plate. Journal of Sound and Vibration. 2007;**302**:50-66

[39] Watkins R, Jha R. A modified time reversal method for lamb wave based diagnostics of composite structures. Mechanical Systems and Signal Processing. 2012;**31**:345-354

[40] Zeng L, Lin J, Huang L. A modified lamb wave time-reversal method for health monitoring of composite structures. Sensors. 2017;**17**:955

[41] Mustapha S, Lu Y, Li J, Ye L. Damage detection in rebar-reinforced concrete beams based on time reversal of guided waves. Structural Health Monitoring. 2014;**13**:347-358

[42] Wang T, Liu S, Shao J, Li Y. Health monitoring of bolted joints using the time reversal method and piezoelectric transducers. Smart Materials and Structures. 2016;**25**:025010

[43] Huo L, Wang F, Li H, Song G. A fractal contact theory based model for bolted connection looseness monitoring using piezoceramic transducers. Smart Materials and Structures. 2017;**26**:104010

[44] Meyer JJ, Adams DE. Theoretical and experimental evidence for using impact modulation to assess bolted joints. Nonlinear Dynamics. 2015;**81**:103-117

[45] Zagrai A, Doyle D, Arritt B. Embedded nonlinear ultrasonics for structural health monitoring of satellite joints. Proceedings of SPIE. 2008;**6935**:693505

[46] Doyle D, Zagrai A, Arritt B, Çakan H. Damage detection in bolted space structures. Journal of Intelligent Material Systems and Structures. 2010;**21**:251-264

[47] Doyle D, Zagrai A, Arritt B. Bolted joint integrity for structural health monitoring of responsive space satellites. In: Proceedings of 50th AIAA SDM Conference; 2009

[48] Zagrai A, Gigineishvili V, Kruse WA, Murray A, Doyle D, Reynolds W, Arritt B, Gardenier H. Acousto-elastic measurements and baseline-free assessment of bolted joints using guided waves in space structures. In: Proceedings of SPIE; 2010. p. 765017

[49] Fasel TR, Olson CC, Todd MD. Optimized guided wave excitations for health monitoring of a bolted joint. In: The 15th International Symposium on: Smart Structures and Materials & Nondestructive Evaluation and Health Monitoring. International Society for Optics and Photonics; 2008. pp. 69351N-69351N-69358

[50] Fasel TR, Kennel MB, Todd MD, Clayton EH, Stabb MC, Park G. Bolted joint damage assessment using chaotic probes. In: Proceedings of the 26th International Modal Analysis Conference (IMACXXVI); 2008

[51] Wu G, Xu C. Study of bolt looseness detection based on chaotic ultrasonic excitation. Journal of Vibration and Shock. 2018;**37**:208-213. (In Chinese)

Edited by Magd Abdel Wahab, Yun Lai Zhou and Nuno Manuel Mendes Maia

Structural health monitoring (SHM) has attracted more attention during the last few decades in many engineering fields with the main aim of avoiding structural disastrous events. This aim is achieved by using advanced sensing techniques and further data processing. SHM has experienced booming advancements during recent years due to the developments in sensing techniques. The reliable operation of current, sophisticated, man-made structures drives the development of incipient reliable damage diagnosis and assessment. This book aims to illustrate the background and applications of SHM from both sensing and processing approaches. Its main objective is to summarize the advantages and disadvantages of SHM methodologies and their applications, which may provide a new perspective in understanding SHM for readers from diverse engineering fields.

Published in London, UK

IntechOpen

ISBN 978-1-83881-713-8